## Aim and Scope

The Journal of Multifunctional Composites is dedicated to identifying and publishing original work on multifunctional composite materials and structures. It welcomes analytical, experimental and computational studies of multifunctional composites covering topics such as design and manufacturing; processing and transport; characterization and properties; interface and damage mechanics; microstructural characterization; modeling and simulation; testing; performance and commercial applications.

Of particular interest are studies of composite materials that include the effects of statistical variability in microstructure and constituent material properties, bridge the length scales from the molecular to the macro scale, and consider performance under extreme environments that span quasi-static to ballistic strain rates and sub-freezing to very high operating temperatures. Composite materials include synthetic, natural and biological fibers and particle reinforcements in polymer, metal, and ceramic matrices—and hybrid variants. While studies that address only a single functionality are also welcomed, of particular interest are biomimetic, self-healing, self-cooling, active morphing, functionally graded, nano, green and smart composite structures.




**JOURNAL OF MULTIFUNCTIONAL COMPOSITES** is published by DEStech Publications, Inc., 439 North Duke Street, Lancaster, PA 17602, U.S.A., 717-290-1660; http://www.destechpub.com.

Publication frequency: Inaugural year - April and October, then published quarterly - January, April, July and October.
Subscriptions: Annual Online only - $450.00; Print only - $470.00; Combined Print and Online - $480.00 Single copy price - $130.00
Non U.S. print or combined subscriptions add $45.00 for postage

ISSN: 2168-4286 doi: 10.12783/issn. 2168-4286

DEStech Publications, Inc.

# Journal of Multifunctional Composites

October 2014 Volume 2, Number 4 ISSN 2168-4278

Journal of Multifunctional Composites

journal homepage: http://jmc.destechpub.com

# Letter from the Guest Editor—Dr. Jandro L. Abot

Dear Colleagues:

Several nondestructive evaluation and structural health monitoring techniques are available to inspect and ensure the reliability of composite materials and structures. However, most of them are complex, expensive, and require the structural component or vehicle be taken out of service for inspection. There is thus a significant need for novel sensing concepts and approaches in composite materials that are able to provide information about the structure without the need for complex external equipment. Ideally, miniaturized integrated sensors that were able to detect microscale damage or incipient failure would facilitate the development of structural health monitoring techniques that could be implemented in actual structures.

The Journal of Multifunctional Composites is dedicated to identifying and publishing original work on multifunctional materials and structures including experimental, analytical and computational studies of multifunctional composites covering topics such as design and manufacturing; processing and transport; characterization and properties; interface and damage mechanics; microstructural characterization; modeling and simulation; testing; performance and commercial applications. Sensing in composite materials, in particular, is critical to ensure their integrity and detect any damage that may lead to the failure of a component or structure. The goal of this Special Issue is to present about novel sensor concepts, experimental techniques and modeling approaches to monitor strain or detect initiating damage in composites including some preliminary results that show the feasibility of the proposed concepts.

The six articles in this Special Issue focus on piezoresistive-based and integrated sensing in three types of polymeric composites including nanocomposites, nano/micro hybrid composites and microfiber laminated composites. They demonstrate the ability to monitor damage and failure and constitute an advancement towards self-sensing in composites. In some cases, the sensitivity of the proposed techniques allows the prediction of impending damage and could be used for actuation purposes also. Certainly, significant challenges remain regarding the achievement of simplicity and robustness of these techniques and crucially, their ability to relay structural health data in real time and without requiring a baseline. Sensing approaches that are based on piezoelectric, capacitive, optical, thermal, magnetic or others effects may be complementary and considered in the future. Success in these sensing endeavors may lead to a qualitative leap in the maintenance of composite structures, which could be instead based on the actual condition of the structure and not its amount of use.

Sincerely yours,

Jandro L. Abot, Ph.D.
Associate Professor, Department of Mechanical Engineering
The Catholic University of America
E-mail: abot@cua.edu
Office: G21 Pangborn Hall
Mail: 620 Michigan Ave. NE
Washington, DC 20064
Telephone: (202) 319-4382
Facsimile: (202) 319-5173
URL: http://faculty.cua.edu/abot


doi:10.12783/issn. 2168-4286/3.1

*Journal of Multifunctional Composites*, 2 (2014) 171–181

Journal of Multifunctional Composites

journal homepage: http://jmc.destechpub.com

# Tailored Self-sensing of Failure Mechanisms in Glass Fiber/Carbon Nanotube/Vinyl Ester Multiscale Hierarchical Composites Loaded in Tension

J.J. KU-HERRERA[1,*], B. PINTO[2], V. LA SAPONARA[2], R.H.R. CASTRO[3] and F. AVILÉS[1,*]

[1]*Centro de Investigación Científica de Yucatán A.C., Unidad de Materiales, Calle 43 No.130, Col. Chuburná de Hidalgo. C.P. 97200, Mérida, Yucatán, Mexico*
[2]*University of California, Davis, Dept. of Mechanical and Aerospace Engineering, One Shields Ave, Davis, CA 95616, USA*
[3]*University of California, Davis, Dept. of Chemical Engineering and Materials Science, One Shields Ave, Davis, CA 95616, USA*

**KEYWORDS**

carbon nanotubes
hierarchical composites
piezoresistivity
damage sensing

**ABSTRACT**

The damage sensing capabilities of a glass fiber/carbon nanotube/vinyl ester multiscale composite containing a tailored electrically conductive network of multiwall carbon nanotubes (MWCNTs) is investigated. The tailored MWCNT network is achieved by manufacturing the composite into two architectures depending on the location of the MWCNTs within the composite: (1) randomly dispersed within the matrix, or (2) deposited onto the glass fibers. The former architecture was achieved by dispersing MWCNTs within the uncured vinyl ester resin, while the later architecture by depositing MWCNTs onto the glass fibers by using an ultrasonic-aided dipping deposition method. The damage sensing capabilities of the composite were investigated under quasi-static tension loading by using specimens with fibers oriented at 0° and 90° with respect to the load direction for both composite architectures. *In situ* measurements of electrical resistance while loading the composite show distinctive features, which allow discerning between fiber breakage from matrix or fiber/matrix interfacial damage, depending on the composite's architecture and failure mode.



## 1. INTRODUCTION

The use of fiber reinforced polymer composites (FRPCs) has progressively increased for aerospace, marine, automotive and renewable energy industries, due mainly to their corrosive resistance and high specific strength and stiffness [1–3]. However, during their service life, such composites are subjected to certain loading conditions that risk their structural integrity and performance. This demands the development of structural health monitoring (SHM) techniques that provide live information. A promising approach for SHM of FRPCs consists in making the composite sensitive or "intelligent", providing information on its own structural health status [4,5]. One of the most promising techniques of *in situ* SHM of FRPCs consists in making the composite electroconductive and piezoresistive, i.e. for an applied stress/strain the composite experiences changes in its electrical resistance which can be correlated to its state of stress/strain or structural damage [1,4,6–13]. With this aim, several approaches have been used to obtain polymer composites with strain and damage sensing capabilities, earlier by using carbon fibers [10] and, more recently, other electroconductive nanofillers such as carbon nano-fibers [14], carbon black nanoparticles [15], carbon nanotubes (CNTs) [4,7,8,13–15] and exfoliated graphite oxide [16]. In the particular case of carbon nanotubes, by the addition of small amounts of CNTs (typically <1 wt %) into a polymer matrix, an electrically percolated network can be obtained, sensitive to stress and strain. Given that the dimensional scale of CNTs are three orders of magnitude smaller than that of conventional structural fibers, they can be used to fabricate minimally invasive multiscale hierarchical composites [4,7].

*Corresponding authors. E-mail: jesuskuh@live.com.mx, faviles@cicy.mx, Tel: (+52) 999 9438330 (Ext 388)


doi:10.12783/issn. 2168-4286/2.4/Ku-Herrera

Since the failure mechanisms of advanced composites are complex and depend on the loading scenarios, it is desirable that the multiscale hierarchical composite provide specific information on the damage occurring at the matrix, fiber or fiber/matrix interface. In this sense, although several works have implemented this technique [7,17], limited research has been devoted to tailor the sensitivity of the electrical network for specificity, i.e. to be more sensitive to damage of the matrix, fiber or their interface. The selectivity in sensing fiber or matrix damage using CNTs has not yet been fully achieved. Furthermore, the relationship between the damage mechanisms occurring at the nano- and microscales and the macroscopic changes of electrical resistance at the composite level is not yet fully understood. Given this motivation, this work investigates the capability of multiwall carbon nanotube (MWCNT)/glass fiber/vinyl ester composites with a tailored electrical MWCNT network, to self-sense damage when the composite is subjected to quasi-static tension loading, identifying the failure mechanisms. In order to tailor the composite's electrical sensitivity, the multiscale hierarchical composites are manufactured into two architectures depending on the location of the MWCNTs: (1) with MWCNTs randomly dispersed within the matrix, and (2) with MWCNTs deposited onto the glass fibers.

## 2. MATERIALS AND METHODS

### 2.1. Materials

Commercial E-glass fibers (Owens Corning, Ohio, USA) with an average diameter of 15 μm and density of 2.54 g/cm$^3$ in the form of fiber tows (~4000 filaments/tow) were used in this study. Commercial multiwall carbon nanotubes with purity > 95%, 30–50 nm outer diameter, 5–10 nm inner diameter, and a length distribution with a spread of 1–6 μm were used. The MWCNTs were oxidized using a solution of $H_2SO_4/HNO_3$ at 3.0 M for 2 h, following the procedure reported in Ref. [18]. An epoxy vinyl ester Hetron 992 FR resin from Ashland composites (Dublin, Ohio, US) was used as the thermosetting matrix for composite manufacturing. Cobalt naphthenate (CoNap) in a proportion of 0.2 wt % and 0.6 wt % of methyl ethyl ketone peroxide (MEKP) were employed to manufacture the composites.

### 2.2. Carbon Nanotube Deposition onto Glass Fibers

The composites investigated here comprise of two architectures depending on the location of the MWCNTs in the composite. One of such architectures consisted in having MWCNTs bonded to the surface of the glass fibers prior to composite manufacturing. For such a configuration, a prerequisite is to deposit the MWCNTs onto the glass fibers, which was achieved following the procedure depicted in Figure 1. First, 70 mg of MWCNTs were added to 1 L of deionized water (step 1) and dispersed for 2 h using an ultrasonic bath (step 2) operated at 42 kHz and 70 W. Following these steps, 14 g of glass fibers (14 cm long tows) were immersed in the MWCNT/water solution (step 3). This mixture was further dispersed in the same ultrasonic bath for 2 h (step 4). Finally, the glass fibers with deposited MWCNTs were removed from the closed container (step 5) and dried in a convection oven at 100°C overnight (step 6).

### 2.3. Scanning Electron Microscopy

The morphology of the glass fibers before and after MWCNT deposition as well as the fractured surface of the multiscale composites after mechanical testing were analyzed by scanning electron microscopy (SEM). For the analysis of fibers, a sample of a randomly selected glass fiber tow was fixed onto a SEM support using conductive carbon tape, and micrographs were taken at different magnifications. After the quasi-static tensile characterization up to fracture of the hierarchical composite (either with MWCNTs bonded to the glass fibers or located within the matrix), the fractured specimens were also analyzed by SEM. The conventional (1,2,3) material coordinate system was used to indicate the fiber (1), in-plane transverse (2) and through-the-thickness (3) directions, see Figure 2. Specimens with fiber direction aligned with the load direction [0° specimens, Figure 2(a)] and perpendicular to the load direction [90° specimen, Figure 2(b)] were investigated. Following this convention, the

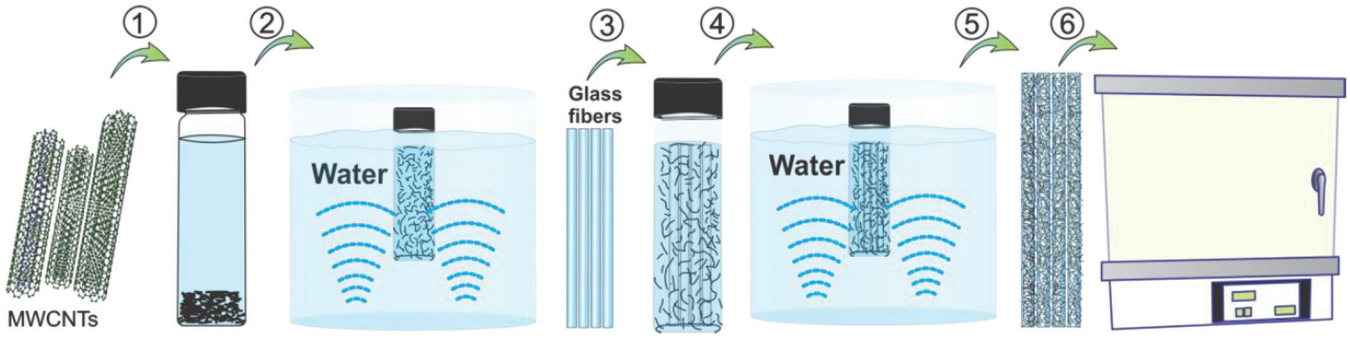


***Figure 1.*** *Ultrasonic procedure used to deposit MWCNTs onto glass fibers.*

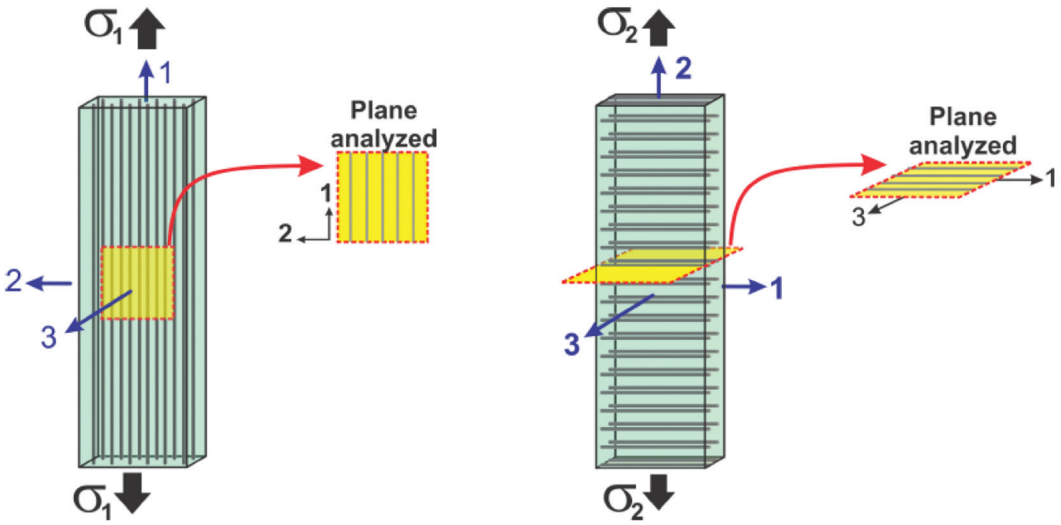


***Figure 2.*** *Schematic of the fractured specimens analyzed by SEM. (a) 0° specimen, (b) 90° specimen.*

SEM examination was conducted over the 1-2 plane of the broken 0° specimens [Figure 2(a)], and on the 1-3 plane for the 90° specimens [Figure 2(b)].

### 2.4. Electrical Resistance of Single Glass Fibers with Carbon Nanotubes

One key challenge in this research was to achieve sufficient electrical conductivity on the fibers through the deposition of MWCNTs. Therefore, the electrical resistance of individual fibers and fiber tows (~4000 filaments/tow) was characterized. For individual glass fibers, the electrical resistance was measured as a function of the electrode separation, employing 1 mm, 3 mm and 5 mm electrode separation. For this purpose, 10 individual glass fibers were randomly selected from a tow and cut to a 10 mm constant length. Following this, 2 mm long electrodes were instrumented using conductive silver paint leaving 1 mm, 3 mm or 5 mm electrode separation as depicted in Figure 3. A Keithley 6517B electrometer was used for DC electrical resistance measurements.

For the electrical resistance measurement of the glass fiber tows, 10 samples consisting of 40 mm long glass fibers tows with 10 mm long electrodes placed 20 mm apart (gage length of 20 mm) were used.

### 2.5. Composite Manufacturing

In order to tailor their electrical sensitivity, the hierarchical composites were manufactured following the two architectures illustrated in Figure 4, viz. with MWCNTs randomly dispersed within the vinyl ester matrix ("architecture *m*"), and with MWCNTs bonded to the glass fibers ("architecture *f*").

Unidirectional composite laminates have well recognized failure modes under quasi-static tension loading and were thus selected for this investigation. To manufacture the multiscale laminate, a layup consisting of three layers of 14 cm long glass fibers was used. For the composite architecture *m*, the preform was made of as-received glass fibers, while for architecture *f*, the preform was made of glass fibers covered with MWCNTs.

Both composite architectures defined in Figure 4 were manufactured by vacuum assisted resin transfer molding. For the composites with architecture *m*, a modified matrix with dispersed MWCNTs was used to impregnate the neat glass fiber preform. Such a matrix containing the dispersed MWCNTs was obtained by mixing 0.5 wt % of MWCNTs with the vinyl ester resin prior to infusion. The dispersion

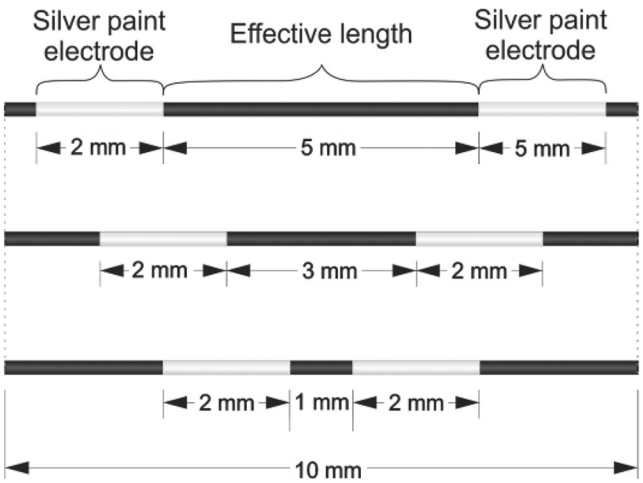


***Figure 3.*** *Specimens used for electrical resistance measurements of individual glass fibers with deposited MWCNTs.*

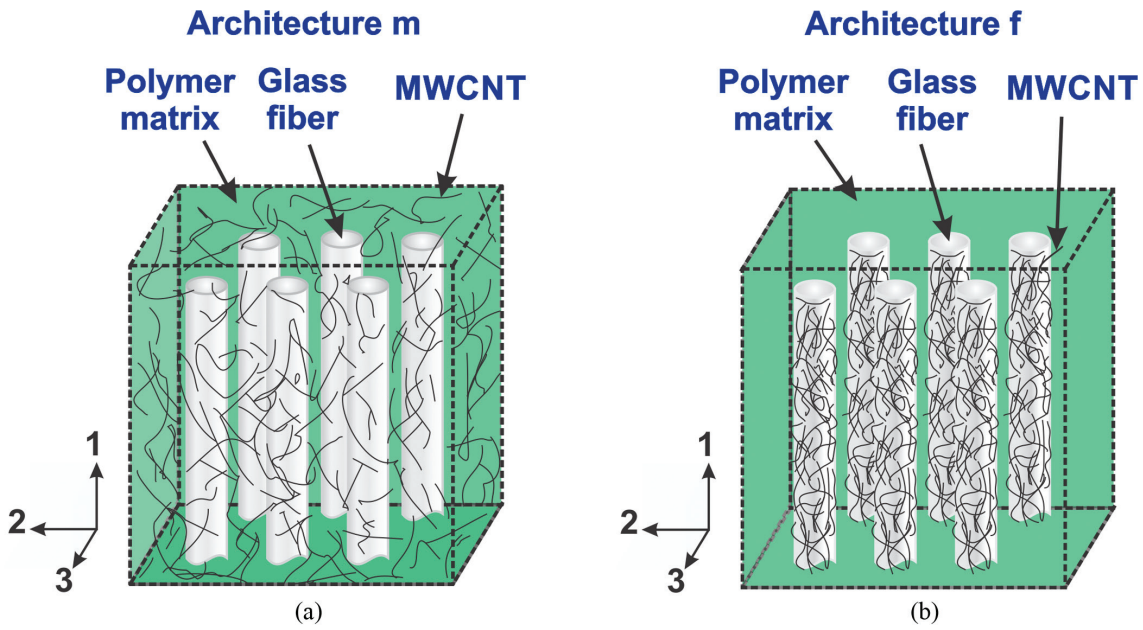


***Figure 4.*** *Multiscale hierarchical composite architectures. (a) Composite architecture m, MWCNTs dispersed within the matrix, (b) composite architecture f, MWCNTs deposited onto the glass fibers.*

of MWCNTs in the vinyl ester prior to infusion and curing was conducted following the procedure depicted in Figure 5. This procedure consisted in mixing 0.5 g of oxidized MWCNTs in 100 g of the vinyl ester resin and homogenizing this mixture for 1 h using a mechanical stirrer. Then, the MWCNTs were dispersed within the vinyl ester using and ultrasonic bath operated at 42 kHz an 70 W for 2 h.

For the composite architecture *f*, a conductive mixture of MWCNT/vinyl ester with a concentration of 0.5 wt % MWCNTs was applied at the ends of the preform, to promote electrical contact among fibers and to consolidate the electrodes. Then the glass fiber preform with the defined electrodes was impregnated with neat vinyl ester resin (without MWCNTs) by resin infusion. The resin was infused into the fiber preform assisted by vacuum at a rate of 10 mL/min. The laminate was left for curing at room temperature for 2 h, then taken out of the mold and postcured for 4 h at 82ºC in a convection oven.

### 2.6. Specimen Instrumentation

The specimen's instrumentation for the electromechanical characterization involved tabbing the laminates, bonding strain gages and electrodes instrumentation. The specimens' dimensions and instrumentation are schematized in Figure 6. For the fibers aligned with the load direction (0° specimens), 30 mm long tabs made of glass fibers/epoxy were adhesively bonded at the ends of the laminate [Figure 6(a)], while 20 mm long tabs were used for the specimens with fibers aligned perpendicularly to the loading direction [90° specimens, Figure 6(b)]. 0° and 90° tensile specimens were obtained by cutting the hierarchical composite laminates with dimensions scaled down (ratio of 1:2) from the dimensions recommended by the ASTM standard D3039 [19]. The 0° specimens were 120 mm long and 7 mm wide, with a thickness of ~1.0 mm defined by the 3 laminas employed. Likewise, the 90° specimens were 90 mm long, 12 mm wide and

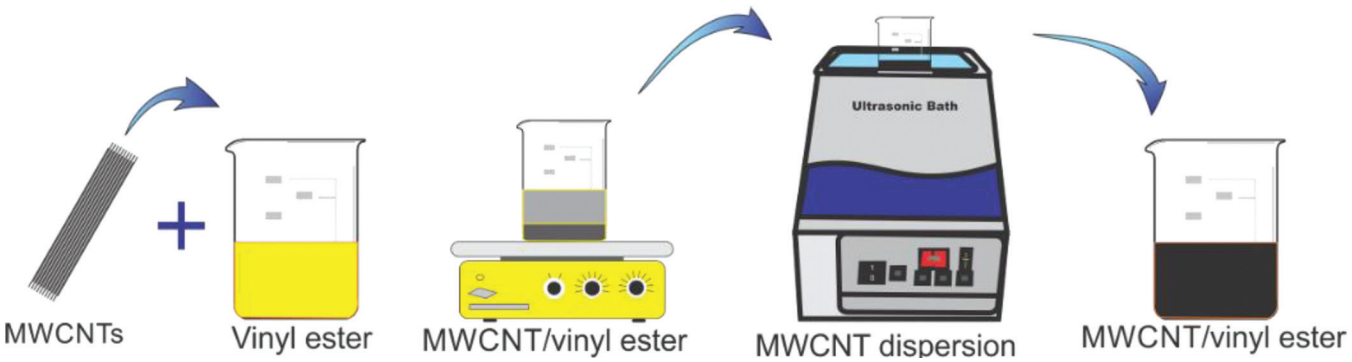


***Figure 5.*** *Procedure used to disperse MWCNTs within the vinyl ester resin prior to resin infusion and curing for composite with architecture m.*

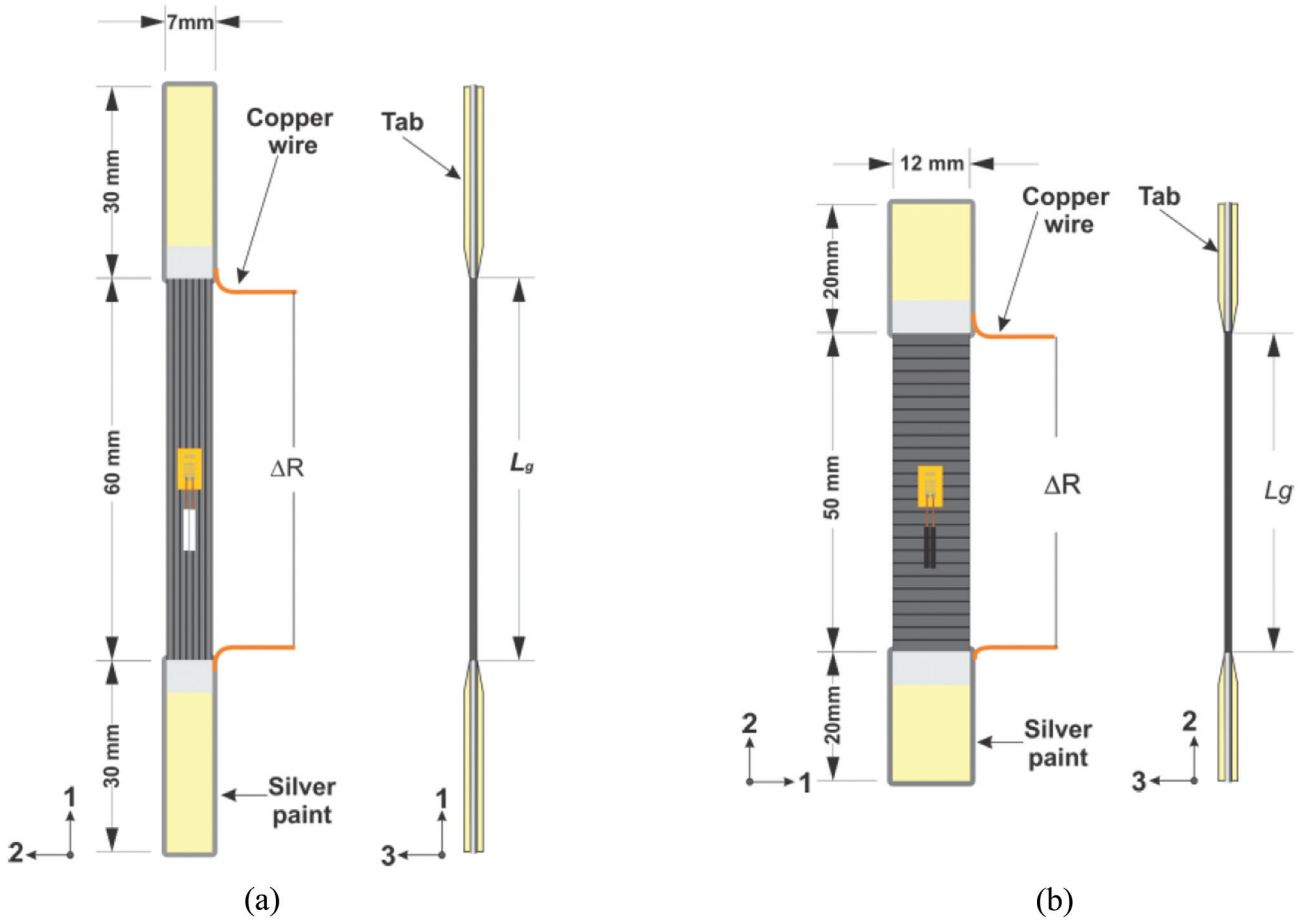


***Figure 6.*** *Tensile specimens dimensions and instrumentation. (a) 0° specimen, (b) 90° specimen.*

~1.0 mm thick. A silver paint strip was placed on each end of the specimen, close to the end tabs as indicated in Figure 6. Notice that silver paint is placed all around the sample ends at the onset of the tabbed region, leaving the gage length as the effective distance between electrodes.

### 2.7. Mechanical Testing

A Shimadzu AG-I universal testing machine was employed for quasi-static tensile loading up to failure using a 20 kN load cell as force sensor for the 0° specimens, and a 5 kN load cell for the 90° specimens. The crosshead displacement rate was 1 mm/min for all tests. The specimens' strain was recorded by means of unidirectional strain gages using a Vishay P3 strain indicator. The change in electrical resistance ($\Delta R$) of the sample was measured during testing using an advanced Agilent SMU 2911A source-meter, synchronizing all instruments using an in-house data acquisition software. Four replicates per group of the 0° and 90° specimens for each composite architecture, were tested. The axial stress ($\sigma_1$, $\sigma_2$), longitudinal or transverse strains ($\varepsilon_1$, $\varepsilon_2$) and the electrical resistance ($R$) of the samples were acquired simultaneously.

## 3. RESULTS

### 3.1. Characterization of Glass Fibers with Deposited Nanotubes

#### *3.1.1. Morphological Analysis*

Optical and SEM micrographs of a representative tow of glass fibers, both with and without deposited MWCNTs, are shown in Figure 7. The tows of the as-received glass fibers show the typical white color at the macroscale [Figure 7(a), left], and a relative smooth surface [Figure 7(a), center and right]. After deposition of MWCNTs, the glass fibers appear uniformly black at the macroscale [Figure 7(b), left], indicating the uniform presence of MWCNTs on their surface. Microscale SEM images [Figure 7(b), center and right] confirm the presence of the MWCNTs, which are rather uniformly distributed onto the glass fibers.

#### *3.1.2. Electrical Resistance*

The as-received E-glass fibers are electrical insulators with a volume resistivity in the order of ~$10^{25}$ Ωcm [20]. A

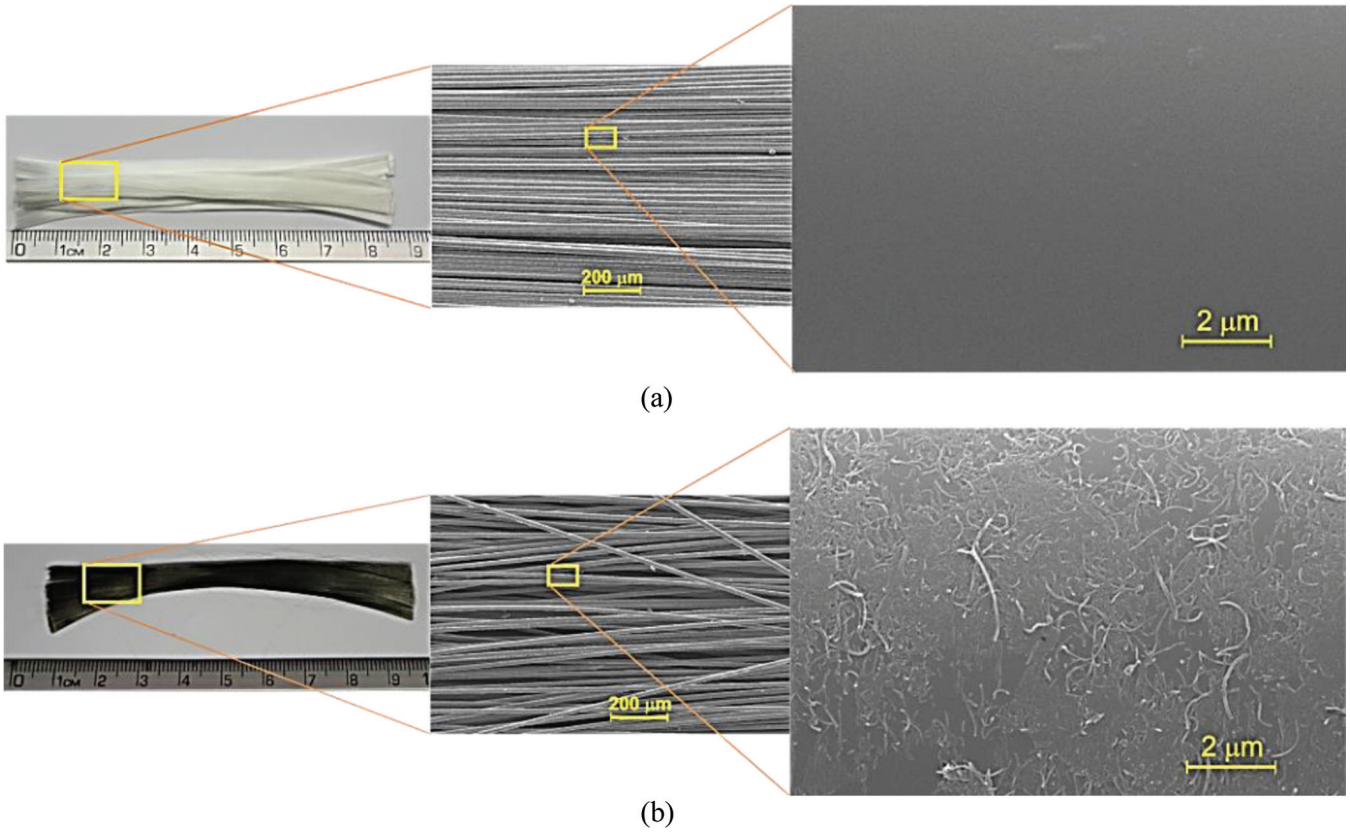


***Figure 7.*** *Optical and SEM images of the glass fibers before and after MWCNT deposition. (a) As-received glass fibers and (b) glass fibers with deposited MWCNTs.*

key property for damage sensing of the glass fibers with deposited CNTs is to form a continuous electrically percolated network. To investigate this issue, the electrical resistance ($R$) of individual fibers as a function of the electrode separation was measured, and the results are shown in Figure 8.

In general, the electrical resistance of individual fibers containing MWCNTs was in the order of 1–$10^3$ MΩ, as seen in Figure 8. A similar range of electrical resistances and scattering values has been reported for glass fibers with deposited MWCNTs in Ref. [21], using either electrophoretic or dip deposition. In the current work, the lowest measured electrical resistance is ~1 MΩ, corresponding to an electrode separation of 1 mm (Figure 8). When the electrodes are 3 mm apart, the electrical resistance increases to ~10–100 MΩ. For an electrode separation of 5 mm, the electrical resistance is in the order of ~10 MΩ–1 GΩ. Additionally, the electrical resistance of tows of glass fibers (~4000 filaments) containing MWCNTs was also measured. In spite of the scattered values of the electrical resistances of individual glass fibers, when the fibers are arranged in tows, the average and standard deviation of the measured electrical resistance of 10 samples with 20 mm electrode separation was 0.55 ± 0.06 MΩ. The decrease in electrical resistance of the fiber tows and the significantly lower scatter with respect to the measured electrical resistance of individual fibers are associated to the formation of additional conductive pathways from lateral contacts between adjacent fibers. These results indicate that a conductive MWCNT network was achieved on the glass fibers, and such MWCNT-coated glass fibers are suitable to manufacture composites with damage sensing capabilities.

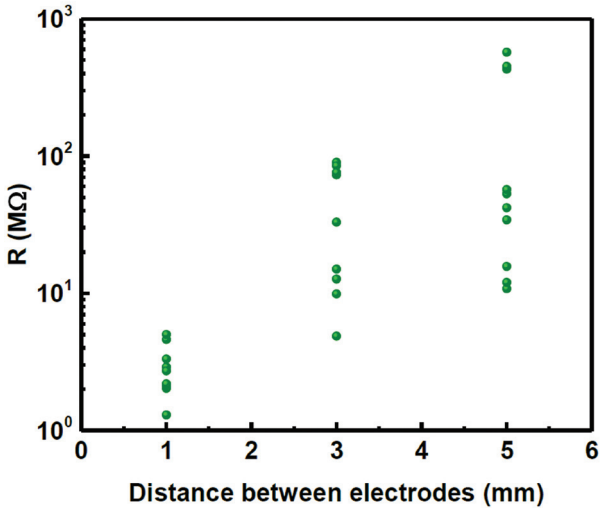


***Figure 8.*** *Electrical resistance of individual glass fibers with deposited MWCNTs as a function of the distance between electrodes*

### 3.2. Analysis of the 0° and 90° Fractured Specimens and Confirmation of MWCNT Location

#### *3.2.1. Analysis of Fracture Surfaces*

In order to analyze the fracture mechanism of the specimens, macroscopic images and SEM micrographs were taken from the fractured specimens tested under tension as indicated in Figure 2. The final fracture of a unidirectional composite is the result of the accumulation of various mechanisms such as fiber fracture, transverse matrix cracking, longitudinal matrix cracking and/or fracture of the fiber-matrix interface. Those mechanisms develop according to the nature of the materials and conditions of the mechanical loading imposed [22]. In general, for unidirectional 90° specimens, the fracture is produced by matrix fracture or by debonding of the fiber/matrix interface. If the fiber/matrix interface is strong, the failure mechanism is matrix-dominated, since the tensile strength of the matrix is reached before the interfacial shear strength of the fiber/matrix interface. In contrast, when the fiber/matrix interface is weak, the failure occurs mainly due to the shear stress developed at the interface region, which reaches the interfacial shear strength of the fiber/matrix. Figure 9 shows the 90° fractured specimens for composite architecture *m* [Figure 9(a)] and composite architecture *f* [Figure 9(b)]. In Figure 9(a) (left), two arrows indicate the failure region of the specimen (plane 1-3). At higher magnifications [Figure 9(a) center and right], the region at the glass fiber/matrix interface shows that the specimen failed due to fiber/matrix debonding and due to the formation of cracks in the interface region, which suddenly propagated through the matrix given its brittle nature [23]. Similarly, a representative 90° fractured specimen of the composite architecture *f* is shown in Figure 9(b). SEM observations of the specimen's fracture surface show debonding of the fiber/matrix interface, suggesting that the composite also failed due to a weak interface.

Figure 10 shows a representative 0° fractured specimen for architecture *m* [Figure 10(a)] and architecture *f* [Figure 10(b)]. For both architectures, broken fibers and shattered failure are clearly seen in the macroscale pictures of Figure 10 (left). Fiber breakage is also evident in the SEM micrographs of Figure 10 (center and right). Fiber fracture produces stress concentrations in the vicinity of the fracture which propagates the crack through the matrix, if the matrix is not capable to absorb the energy released [22]. For architecture *m*, at a higher magnification [Figure 10(a), right], some MWCNTs protruding from the matrix further confirm the tailored MWCNT location within the polymer matrix. For architecture *f*, at a higher magnification [Figure 10(b),

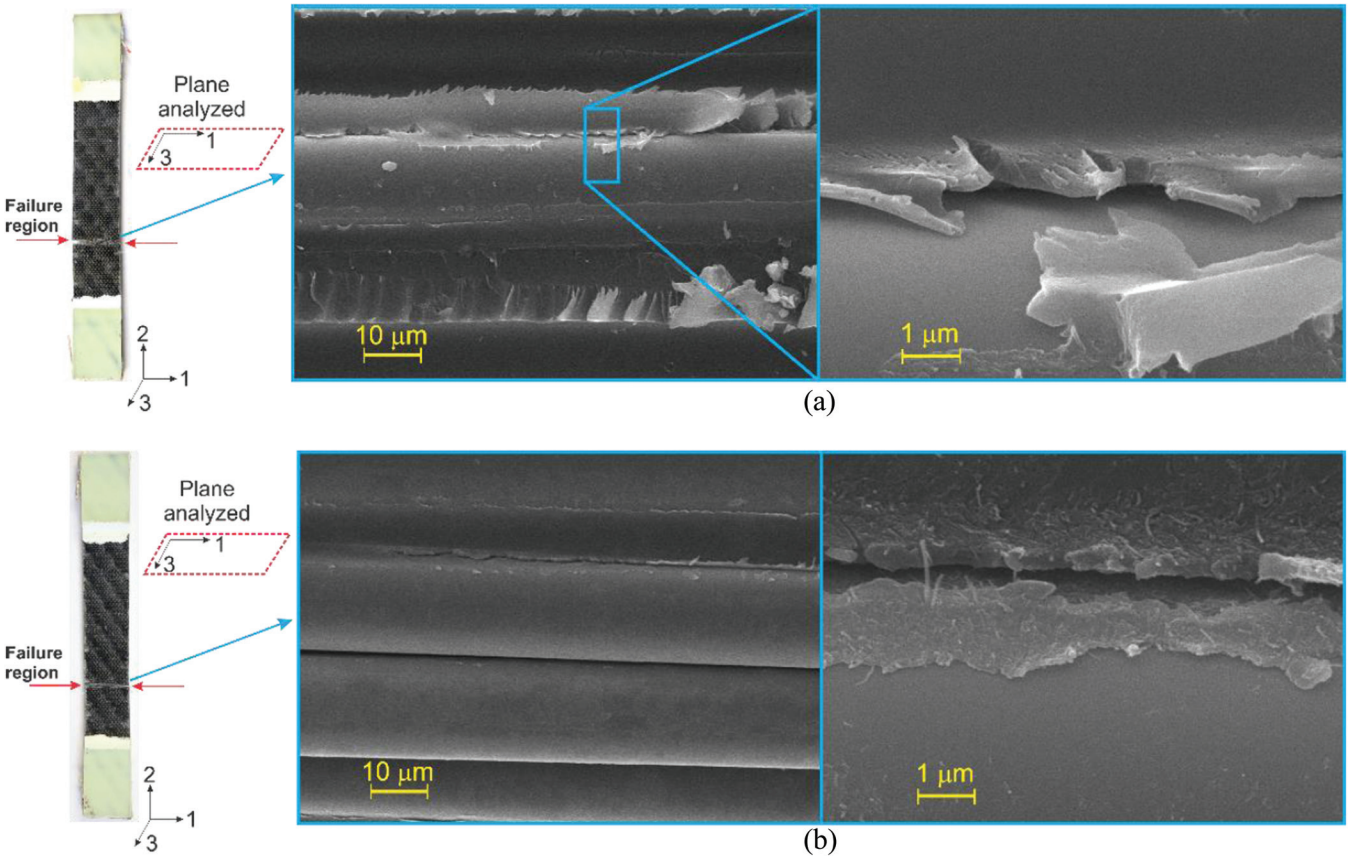


***Figure 9.*** *Fracture surface of the 90° specimen. (a) Composite architecture m, (b) composite architecture f.*

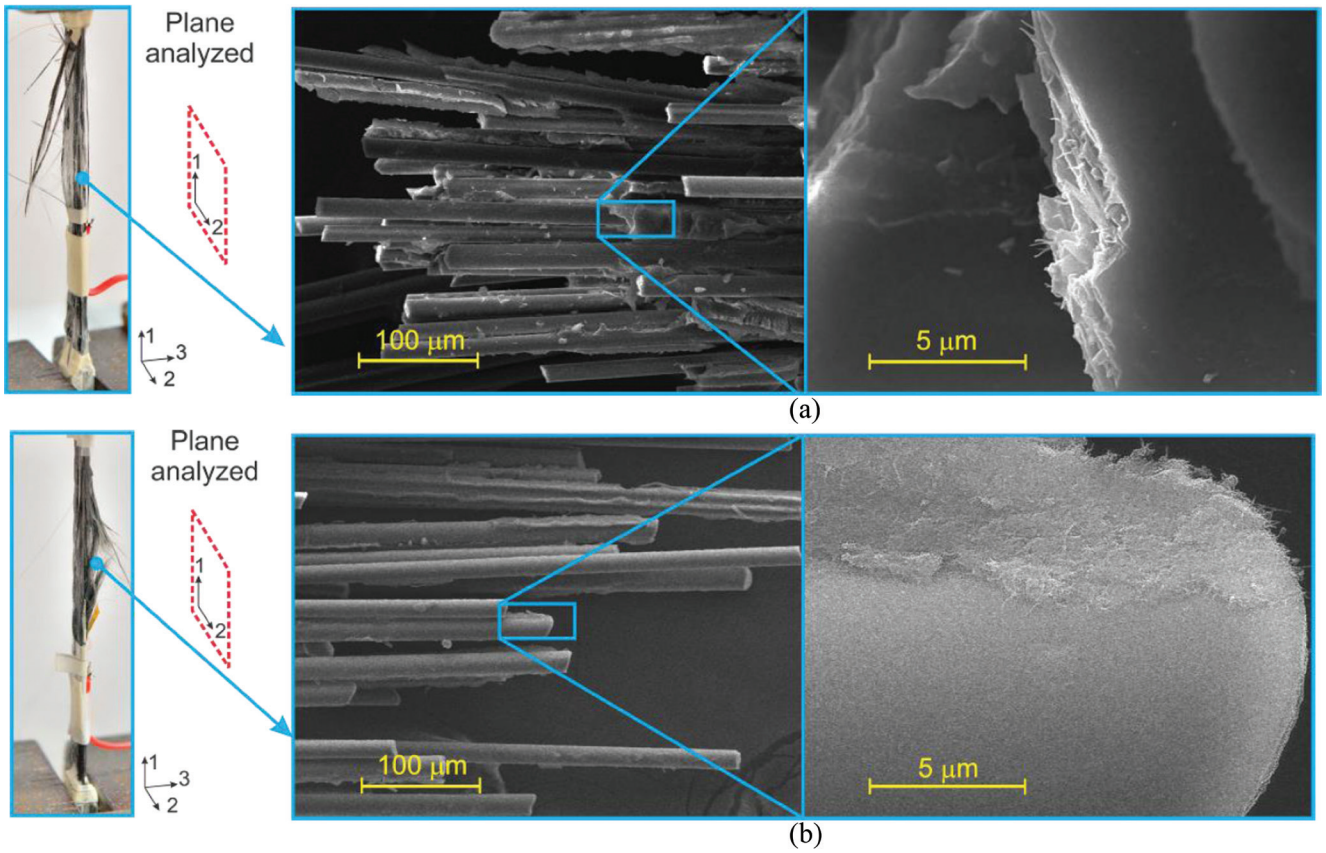


***Figure 10.*** *Fracture surface of the 0° specimen. (a) Composite architecture m and (b) composite architecture f.*

right], a number of MWCNTs are observed on the fiber, indicating the success of the intended location of the MWCNTs within this composite.

### 3.3. Self-sensing of Failure Mechanisms in Composites

#### *3.3.1. Failure of 90° Specimens*

The strain and damage sensitivity of both composite architectures ("*f*" and "*m*", see Figure 4) to detect either matrix and/or fiber/matrix interfacial failure mechanisms was investigated by subjecting the 90° samples to quasi-static tension loading up to failure. The representative axial stress, which is transverse to the fibers ($\sigma_2$, left axis), and normalized change in electrical resistance ($\Delta R/R_0$, right axis) vs. transverse strain ($\varepsilon_2$) of the 90° specimens under tension loading for both composite architectures are shown in Figure 11(a) (architecture *m*) and 11(b) (architecture *f*). Plotting the normalized change in electrical resistance ($\Delta R/R_0$), instead of just $\Delta R$, enables the analysis of different specimen responses regardless of the initial electrical resistance ($R_0$). In the electromechanical behavior ($\Delta R/R_0$ vs. $\varepsilon_2$), the normalized change in electrical resistance of the 90° composites for both architectures experiences a quite linear trend with the applied strain, and follows closely the stress-strain behavior up to fracture. For these composites with fibers oriented at 90° with respect to the loading direction, there is no sudden change in stress (associated to fiber break up), i.e., fiber break up did not occur (see Figure 9) and the concomitant $\Delta R/R_0$ signal also does not present abrupt changes. The $\Delta R/R_0$ vs. $\varepsilon_2$ curves of Figures 11(a) and 11(b) are also quite smooth, which is associated to the deformation of the electrically percolated network within the composites (on the fibers for composite architecture *f* and within the matrix for architecture *m*). Therefore, the electrical signal is consistent with the mechanical behavior and with fiber/matrix interface and matrix failure mechanisms observed in Figure 9.

Given this mechanical behavior and the coupled increase of $R$ with increased strain, the linear relationship between $\Delta R/R_0$ and $\varepsilon_2$ of up to fracture of the 90° specimens in Figure 11 is considered piezoresistivity. This allows to quantify the sensitivity of the composite material by a metric known as the gage factor ($K$), defined as the slope of the $\Delta R/R_0$ vs. $\varepsilon_2$ curve. The average and standard deviation of the gage factors for 90° specimens ($K_{90}$) and 0° specimens ($K_0$, to be discussed in Section 3.3.2) calculated from four replicates loaded in tension are listed in Table 1.

Both composite architectures are capable to self-sense their own deformation up to failure, although a higher sensitivity to strain for the 90° specimens was experienced by

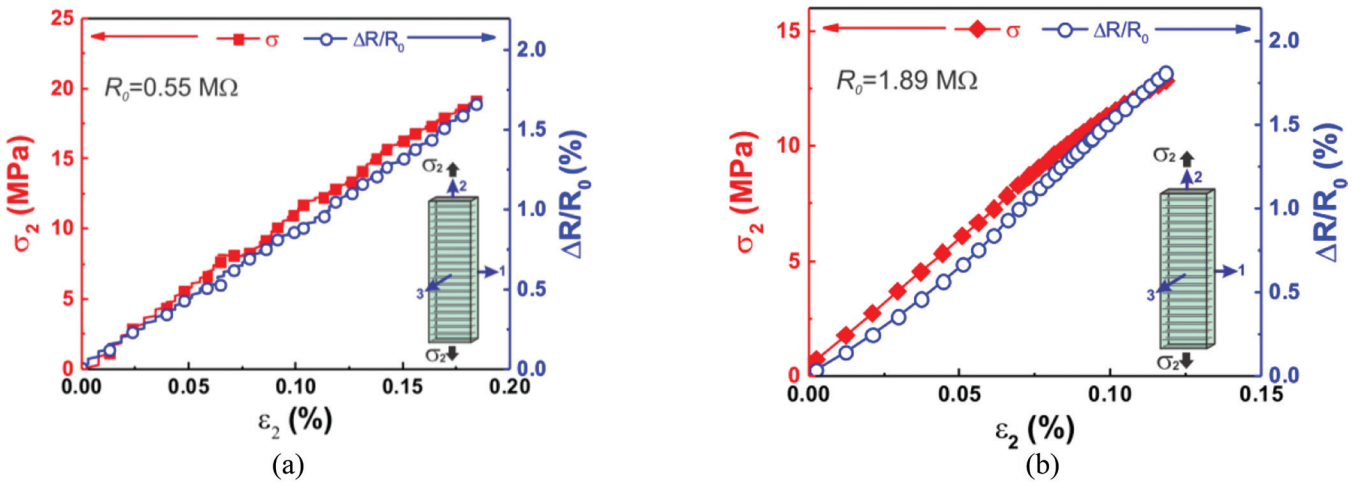


***Figure 11.*** *Representative mechanical (solid squares) and electromechanical (hollow circles) responses of the 90° specimens. (a) Composite architecture m, (b) composite architecture f.*

the composite architecture *f*. The highest average gage factor was $K_{90}$ = 19.3, corresponding to the 90° composite with MWCNTs deposited onto the fibers. This gage factor is ~9 times higher than the gage factor of commercial metallic strain gages. The higher (average) sensitivity ($K_{90}$ = 19.3) of the composite architecture *f* with respect to that of the composite architecture *m* ($K_{90}$ = 12.6) in 90° composites may be attributed to the increase in the fiber-to-fiber transverse distance with applied load, which is not very relevant for changes in *R* when the nanotubes are dispersed within the matrix (architecture *m*). For the composite architecture *m*, changes in *R* are mainly attributed to the deformation of the MWCNT network located within the polymer matrix. On the other hand, for the composite architecture *f*, changes in *R* upon loading come not only from the deformation of the MWCNT network formed on the fibers, but also from the increase in the transverse distance between adjacent glass fibers (covered with MWCNTs). As seen from Table 1, the gage factors of both composite architectures have a relatively small standard deviation, since the conductivity of the specimens comes from the fiber tows, rather than from individual fibers. As seen in Figure 9, failure of the 90° specimens is a matrix/interface dominated process.

### 3.3.2. *Failure of 0° Specimens*

The electrical sensitivity to fiber failure of the tailored composites was investigated by using 0° composites, i.e. unidirectional composites with the continuous fiber oriented along the fiber direction. Representative electromechanical behavior of the 0° specimens for both composite architectures is shown in Figure 12(a) (architecture *m*) and 12(b) (architecture *f*).

As for Figure 11, in Figure 12 the longitudinal stress ($\sigma_1$, left vertical axis) and the normalized change in resistance ($\Delta R/R_0$, right vertical axis) are simultaneously plotted as functions of the applied longitudinal strain ($\varepsilon_1$). For composite architecture *m*, Figure 12(a), the initial linear increase in electrical resistance at low strain ($\varepsilon_1 < 0.5\%$, region a-b) is dominated by the elastic deformation of the composite, and hence can be considered piezoresistivity. The average gage factor of the 0° specimen of architecture *m* calculated at

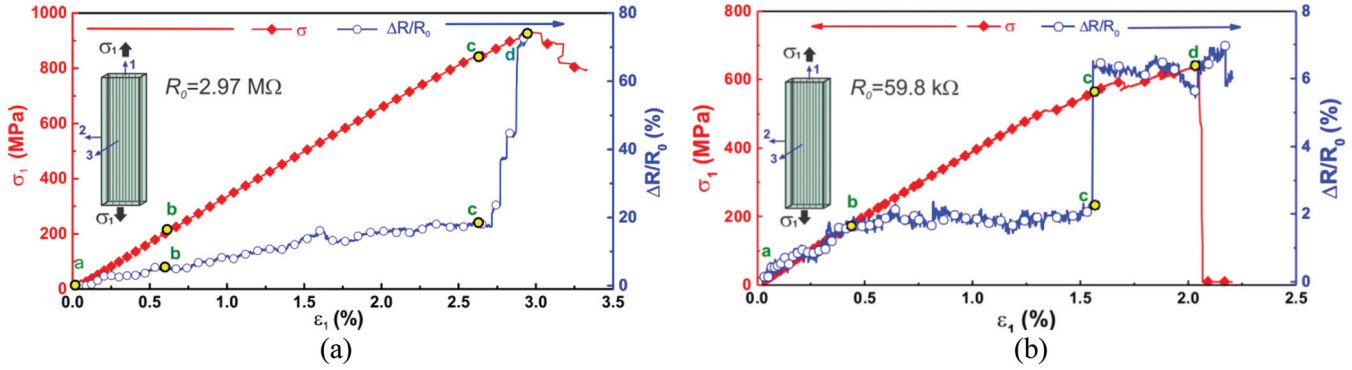


***Figure 12.*** *Representative mechanical (solid squares) and electromechanical (hollow circles) responses of the 0° specimens. (a) composite architecture m and (b) composite architecture f.*

***Table 1. Gage Factors for the 90° Specimens ($K_{90}$) Calculated at $\varepsilon_2$ = 0–0.1% and for the 0° Specimens ($K_0$) Calculated at $\varepsilon_1$ = 0–0.5% for Both Composite Architectures.***

| | Gage Factor | |
|---|---|---|
| **Composite Architecture** | $K_{90}$ | $K_0$ |
| Architecture *m* | 12.6 ± 2.3 | 5.2 ± 0.4 |
| Architecture *f* | 19.3 ± 1.6 | 2.7 ± 0.6 |

$\varepsilon_1$ = 0–0.5 % is $K_0$ = 5.2 (see Table 1), twice the gage factor of commercial metallic strain gages. For small deformations, the tensile strain applied to the composite deforms the electrical percolating network of the MWCNTs located within the matrix, inducing a change in electrical resistance of the composite at the macroscale. With small oscillations, the electrical resistance of the composite continues increasing rather linearly until $\varepsilon_1$ ~2.7% [point c in Figure 12(a)], when a sudden increase in $R$ is observed, just before the final collapse of the specimen [point d in Figure 12(a)]. This sudden increase in $R$ is associated to (late) fiber breakage immediately followed by collapse. For the composite architecture *f* [Figure 12(b)], the initial linear region [$\varepsilon_1 < 0.5\%$, region a-b in Figure 12(b)] can also be attributed to piezoresistivity. The sensitivity of this composite architecture in the linear region ($K_0$ = 2.7) is lower than that of the composite architecture *m* in the same region ($K_0$ = 5.2), but is still in the range of the gage factor of commercial metallic strain gages ($K$ ~2). For small deformations, the tensile strain applied to the composite equally stretches the matrix and fibers, which modifies the separation of the MWCNT network on the fibers, yielding an increase in $R$. From point b to c ($0.5 < \varepsilon_1 < 1.5$), relatively small changes in $R$ are observed in this composite until $\varepsilon_1$ ~1.5 %, when an abrupt increase in $R$ is observed [point c in Figure 12(b)]. This abrupt increase in $R$ is associated to the onset of fiber breakage. Thereafter, the fibers continue to randomly break until the final collapse of the composite [point d in Figure 12(b)]. This failure mode detected by the electrical signal (fiber breakage) coincides with what is expected for a 0° specimen [22] and with the failure mode indicated by the post-mortem observations of Figure 10. Notice that the onset of fiber breakage detected by the composite with architecture *f* at $\varepsilon_1$ ~1.5 % is not clearly detected by the composite with architecture *m*. Rather, the composite with architecture *m* does detect fiber breakage, but only once the stress/strain level is close to composite collapse. For composite architecture *m*, since the MWCNT network is within the matrix, only when enough fiber breakage induces significant damage in the surrounding matrix, an important change $R$ is observed [see Figure 12(a)]. Optical and SEM observations (Figure 10) support the hypothesis that for the composite architecture *f* under axial tensile loading, glass fibers breakage is followed by the disruption of effective conductive pathways, which induce macroscopic changes in the electrical resistance of the composite. Therefore, even though both hierarchical composite types are able to self-sense their own deformation and damage, the composite with MWCNTs on the fibers is more sensitive to detect the onset of fiber breakage.

## 4. CONCLUSIONS

A multiscale glass fiber/multiwall carbon nanotube/vinyl ester composite with a tailored location of electrically conductive multiwall carbon nanotube (MWCNT) network was developed. Such hierarchical composites were manufactured with two architectures distinguished by the location of the carbon nanotubes, viz. (1) within the matrix, (2) on the glass fibers. The capability of these composite architectures to self-sense their own strain and damage was investigated, identifying the corresponding failure mechanisms under uniaxial quasi-static tension loading. A homogeneous deposition of MWCNTs onto the glass fibers was successfully achieved and used to manufacture composites with such an intended architecture. The electrical resistance of 1–5 mm long individual glass fibers with MWCNTs on their surface was in the order of $1–10^3$ MΩ. The tows of glass fibers with 20 mm electrode separation showed an electrical resistance <1 MΩ. Analysis of the specimen's fracture surface showed that for laminated composites with fibers oriented 90° with respect to the loading direction, composite failure initiated at the fiber/matrix interface and propagated through the matrix, while for the unidirectional composites whose fibers were aligned along the loading direction (0° specimens) the main failure mechanism was fiber breakage. In the tensile electromechanical characterization of laminated composites with fibers oriented 90° with respect to the loading direction, a linear piezoresistive response was observed, dominated by the matrix strain. Both composite architectures (with MWCNTs within the matrix or on the fibers) were able to sense their own strain up to failure and the highest gage factor (19.3 ± 1.6) was observed for the composites where the MWCNTs are located onto the fibers. For the 0° unidirectional composites whose continuous fibers were aligned with respect to the loading direction, both composite architectures were also able to self-sense their own strain and damage; however, the composites with MWCNTs deposited on the fibers capture more adequately the onset of fiber breakage than the composites with MWCNTs dispersed within the matrix. The hierarchical composites developed in this research provide a promising alternative to real time detection of strain, premature and severe damage of advanced composites.

## ACKNOWLEDGEMENTS

This research was supported by CONACYT, Mexico, grant number 220513 under the direction of Dr. Avilés. Ad-

ditional support from a 2013-2015 grant by the University of California Institute for Mexico and the United States (UC MEXUS) and CONACYT is also acknowledged. Dr. La Saponara acknowledges the support of the National Science Foundation (grant number CMMI-1200521) and of the Office of Naval Research (grant N00014-13-1-0604, managed by Dr. Yapa Rajapakse). The authors also want to thank the technical support of Serena Ferraro and Md. Hasan from UC Davis, as well as Alejandro May and Santiago Duarte from CICY.

## REFERENCES

[1] Alexopoulos ND, Bartholome C, Poulin P, Marioli-Riga Z. Structural health monitoring of glass fiber reinforced composites using embedded carbon nanotube (CNT) fibers. *Composites Science and Technology*. 2010; 70(2): 260–71.

[2] Gay D, Hola SV, Tsai SW, eds. Composite Materials Design and Applications. Boca Raton, FL: CRC Press 2003.

[3] Mouritz AP, Gellert E, Burchill P, Challis K. Review of advanced composite structures for naval ships and submarines. *Composite Structures*. 2001; 53(1): 21–42. http://dx.doi.org/10.1016/S0263-8223(00)00175-6

[4] Gao L, Thostenson ET, Zhang Z, Chou T-W. Coupled carbon nanotube network and acoustic emission monitoring for sensing of damage development in composites. *Carbon*. 2009; 47(5): 1381–8. http://dx.doi.org/10.1016/j.carbon.2009.01.030

[5] Yun Y-H, Inpil K, Sachin J, Atul M, Suhasini N, Goutham K, *et al.* Nanoscale Intelligent Materials and Structures. *Nanoengineering of Structural, Functional and Smart Materials*: CRC Press 2005.

[6] Balageas D. Introduction to Structural Health Monitoring. Structural Health Monitoring: ISTE 2010, p. 13–43.

[7] Gao Sl, Zhuang RC, Zhang J, Liu JW, Mäder E. Glass Fibers with Carbon Nanotube Networks as Multifunctional Sensors. *Adv Funct Mater*. 2010; 20(12): 1885–93. http://dx.doi.org/10.1002/adfm.201000283

[8] Gao S-l, Zhuang R-C, Zhang J, Liu J-W, Mäder E. Glass Fibers with Carbon Nanotube Networks as Multifunctional Sensors. *Advanced Functional Materials*. 2010; 20(12): 1885–93. http://dx.doi.org/10.1002/adfm.201000283

[9] Schueler R, Joshi SP, Schulte K. Damage detection in CFRP by electrical conductivity mapping. *Composites Science and Technology*. 2001; 61(6): 921–30. http://dx.doi.org/10.1016/S0266-3538(00)00178-0

[10] Schulte K, Baron C. Load and failure analyses of CFRP laminates by means of electrical resistivity measurements. *Composites Science and Technology*. 1989; 36(1): 63–76. http://dx.doi.org/10.1016/0266-3538(89)90016-X

[11] Sebastian J, Schehl N, Bouchard M, Boehle M, Li L, Lagounov A, *et al.* Health monitoring of structural composites with embedded carbon nanotube coated glass fiber sensors. *Carbon*. 2014; 66(0): 191–200. http://dx.doi.org/10.1016/j.carbon.2013.08.058

[12] Wang X, Chung DDL. Self-monitoring of fatigue damage and dynamic strain in carbon fiber polymer-matrix composite. *Composites Part B: Engineering*. 1998; 29(1): 63–73. http://dx.doi.org/10.1016/S1359-8368(97)00014-0

[13] Yesil S, Winkelmann C, Bayram G, La Saponara V. Surfactant-modified multiscale composites for improved tensile fatigue and impact damage sensing. *Materials Science and Engineering: A*. 2010; 527(27–28): 7340–52. http://dx.doi.org/10.1016/j.msea.2010.07.105

[14] Kang I, Heung YY, Kim JH, Lee JW, Gollapudi R, Subramaniam S, *et al.* Introduction to carbon nanotube and nanofiber smart materials. *Composites Part B: Engineering*. 2006; 37(6): 382–94. http://dx.doi.org/10.1016/j.compositesb.2006.02.011

[15] Wichmann MHG, Buschhorn ST, Gehrmann J, Schulte K. Piezoresistive response of epoxy composites with carbon nanoparticles under tensile load. *Physical Review B*. 2009; 80(24): 245437. 13

[16] Kim Y-J, Cha JY, Ham H, Huh H, So D-S, Kang I. Preparation of piezoresistive nano smart hybrid material based on graphene. *Current Applied Physics*. 2011; 11(1, Supplement): S350–S2. http://dx.doi.org/10.1016/j.cap.2010.11.022

[17] Grammatikos SA, Paipetis AS. On the electrical properties of multi scale reinforced composites for damage accumulation monitoring. *Composites Part B: Engineering*. 2012; 43(6): 2687–96. http://dx.doi.org/10.1016/j.compositesb.2012.01.077

[18] Avilés F, Cauich-Rodríguez JV, Moo-Tah L, May-Pat A, Vargas-Coronado R. Evaluation of mild acid oxidation treatments for MWCNT functionalization. *Carbon*. 2009; 47(13): 2970–5. http://dx.doi.org/10.1016/j.carbon.2009.06.044

[19] ASTM standard D3039 / D3039M. Standard Test Method for Tensile Properties of Polymer Matrix Composite Materials, *ASTM International*. West Conshohocken, PA 2014.

[20] Wallenberger F. Commercial and Experimental Glass Fibers. In: Wallenberger FT, Bingham PA, eds. *Fiberglass and Glass Technology*: Springer US 2010, p. 3–90. http://dx.doi.org/10.1007/978-1-4419-0736-3_1

[21] Gao Sl, Zhuang RC, Zhang J, Liu JW, Mäder E. Glass Fibers with Carbon Nanotube Networks as Multifunctional Sensors. *Advanced Functional Materials*. 2010; 20(12): 1885–93. http://dx.doi.org/10.1002/adfm.201000283

[22] Berthelot J-M. Fracture Mechanisms and Damage of Composite Materials. *Composite Materials*: Springer New York 1999, p. 228–64.

[23] Hull D, Clyne. TW. *An Introduction to Composite Materials*: Cambridge University Press; 1996. http://dx.doi.org/10.1017/CBO9781139170130

*Journal of Multifunctional Composites*, 2 (2014) 183–194

Journal of Multifunctional Composites

journal homepage: http://jmc.destechpub.com

# Piezoresistive Sensing of Strain and Damage in Carbon/Epoxy Rectangular and I-shaped Cross-section Beams in Flexure

B. PINTO[1], J.J. KU-HERRERA[2], S. KERN[1], V. LA SAPONARA[1,*] and F. AVILÉS[2]

[1]*University of California, Davis, Department of Mechanical and Aerospace Engineering, One Shields Ave., Davis, CA 95616, USA*
[2]*Centro de Investigación Científica de Yucatán A.C., Unidad de Materiales, Calle 43 No.130, Col. Chuburná de Hidalgo. C.P. 97200, Mérida, Yucatán, Mexico*

**KEYWORDS**

carbon fiber
I-beam
piezoresistivity
flexural loading

**ABSTRACT**

The strain and damage sensing capabilities of a carbon fiber/epoxy composite subjected to monotonic and incremental cyclic flexural loading is investigated using the electrical resistance approach. The piezoresistive sensitivity of the carbon fiber/epoxy composites were first characterized using rectangular cross-section specimens and then application of the electrical resistance approach was extended to an I-shaped cross-section laminated composite. The change in the electrical resistance of the specimens was simultaneously monitored on both the tensile and compressive sides while the specimens were tested under flexural loading. On the tensile side, the positive electrical resistance change ($\Delta R$) showed a linear trend for small deformations (less than 0.3% strain) and increased in a nonlinear fashion for larger deformations. In contrast to the tensile side, $\Delta R$ on the compressive side showed a nonlinear and non-monotonic behavior. Initially, $\Delta R$ decreased for low values of deformation (less than 0.3% strain), leveled off at the onset of the specimen's compressive failure, and then increased up to complete failure. Correlations between abrupt changes in $\Delta R$ and indications of composite damage are confirmed with scanning electron microscopy. Carbon fibers in both rectangular and I-shaped cross-section carbon/epoxy specimens are capable of sensing tensile and compressive strain, and adequately capture the onset and progression of failure by fiber micro-buckling, formation of kink bands, and delamination. The cross-section properties (e.g. stiffness and layup sequence) affect the piezoresistive and damage sensitivity, with the stiffer I-shaped cross-section being less sensitive to $\Delta R$ than standard specimens of rectangular cross-section. $\Delta R$ under cyclic flexural loading for both tensile and compressive sides showed a permanent change with applied deformation after each cycle, indicating first the release of residual stresses and then damage.



## 1. INTRODUCTION

An increased use of carbon fiber (CF) composites for the aerospace, civil, naval, transportation and wind energy industries has been observed in the last decades. Starting as CF filaments used for Edison's electrical bulb [1,2], CF's are now consistently adopted for applications requiring high specific strength and stiffness through fiber-reinforced polymer composites (FRPCs). With the growing use of CF composites for structural applications, it is necessary to establish structural health monitoring (SHM) techniques that can provide information on the structural integrity of a composite in real time and thus maintain structural safety during its lifecycle. A promising feature of CFs, over other (electrically insulating) fiber reinforcements, is their intrinsic electrical conductivity and piezoresistive properties. When used in FRPCs, such a feature can render a coupled electrome-

*Corresponding author. E-mail: vlasaponara@ucdavis.edu. W: +1-530-754-8938


doi:10.12783/issn. 2168-4286/2.4/Pinto

chanical response to the composite, which can be exploited to monitor its own strain and damage in real time [3]. The piezoresistive behavior of individual CFs when subjected to tensile strains along the fiber direction was initially observed by Owston [4]. Since then, several investigations have been performed to exploit the intrinsic CF ability to sense strain and damage based on the electrical resistance change of CF/polymer composites under several loading scenarios, including quasi-static uniaxial tension [5] and compression [6], impact [7], fatigue [8–10], and flexure [11,12].

Condition-based maintenance in large composite assemblies utilizing composite structural components, such as wind turbines and aircraft, is commonly carried out through non-destructive testing methods such as acoustic emission, ultrasonics, eddy currents, radiography, fiber optics, and other surface-mounted or embedded sensors [13,14]. Acoustic emission is a well-established technique used to monitor damage in real time within composite structures; however only new accumulated damage can be detected [15], the equipment necessary to implement such a technique is expensive, and the technique is sensitive to external noise [16,17], which may lead to the generation of false positives. Eddy currents are another alternative approach for small scale structures but their implementation for large scale structures is still in development [18]. Embedded sensors, e.g. piezoelectric transducers, optic fibers, fiber Bragg grating sensors, have been also explored for SHM. Their ability to successfully monitor damage in composites is counteracted by the fact that their embedment within composites may induce stress concentrations that compromise the structural integrity [19,20]. A smaller size of the sensors with respect to the composite ply thickness would alleviate this problem (see for example discussion on optic fibers and fiber Bragg grating sensors in [20]). Surface-mounted sensors such as strain gauges only measure localized surface deformations limiting their use for SHM. Additionally, metal-foil strain gauges have gauge factors of ~2 [21], while CF/polymer composites can achieve gauge factors up to ~50 [22], confirming the potential of CFs as SHM (piezoresistive) sensors.

Although there are several investigations on the piezoresistive self-monitoring of CF/polymer composites using standard specimens with rectangular cross-section [5,10–12,22–24], very few attempts have been made to utilize CFs as strain sensors for structural composite components [25], such as an I-shaped cross-section. Hence, further efforts should be conducted to extend the electrical resistance approach to more complex-shapes and realistic scenarios suitable for structural applications. The group of Deborah Chung has thoroughly investigated this area using CF for piezoresistive-based sensing in composites [7–9,11,22,26,27]. They have investigated for example, the piezoresistive behavior of a filament wound CF/epoxy cylinder subjected to drop impacts [27]. The electromechanical behavior of uniaxial tensile and compressive tests often starts with simple rectangular cross-section specimens as discussed in Ref. [22,23,28,29]. To characterize the behavior of a structural component, such as an I-shaped beam, knowledge of its flexural behavior is of paramount importance. In an effort to further extend this technique towards more realistic applications in structural components, this work investigates the effectiveness of the electrical resistance technique applied to a composite beam of I-shaped cross-section under monotonic and cyclic flexural loading scenarios. Conventional specimens of rectangular cross-section are also examined as a reference. Given the complex nature of flexural loading, the composite's piezoresistive response of both the bottom (tensile) and top (compressive) surfaces are simultaneously monitored. Dedicated microscopic analysis is used to assist in correlating the observed electrical resistance changes with the composite's failure.

## 2. MATERIALS AND METHODS

### 2.1. Materials

Specimens with rectangular and I-shaped cross-sections were manufactured using Torayca T700SC 12K (Soller Composites, NH, USA) uniaxial woven CF and an epoxy polymer matrix LAM125/LAM237 (Pro-Set, MI, USA). According to the manufacturer, the CF has a nominal electrical resistivity of ~$1.6 \times 10^{-3}$ Ω.cm with a filament diameter of ~7 μm [30]. As suggested by the manufacturer, a 100:28 epoxy/hardener ratio was used to manufacture all composites.

### 2.2. Manufacturing of Rectangular and I-shaped Cross-section Specimens

A vacuum-assisted resin transfer molding procedure was utilized to fabricate the CF/epoxy specimens of rectangular cross-section with a layup of $[0]_{13}$. Prior to infusion the epoxy/hardener mixture was degassed for 25 min to help remove air bubbles and reduce voids within the composite. The rectangular specimens were cured at room temperature for 14 h and then post-cured at 82°C for an additional 8 h in a convection oven. The cured laminates were cut into individual specimens, to nominal dimensions of 183 mm (length) × 25 mm (width) × 3.5 mm (thickness), using a water-cooled diamond impregnated saw blade.

A wet hand layup procedure was used to fabricate the CF/epoxy specimens with I-shaped cross-section. To produce the I-shaped cross-section, an aluminum mold was constructed in which the web and flanges were cured together as a single piece. This mold produced a 1.2 m long I-shaped beam. Figure 1 shows a schematic of the ply orientations and a section (25 mm/228 mm of total length) of the final I-shaped specimen. The fabrication procedure begins by thoroughly coating the interior of the aluminum mold surface

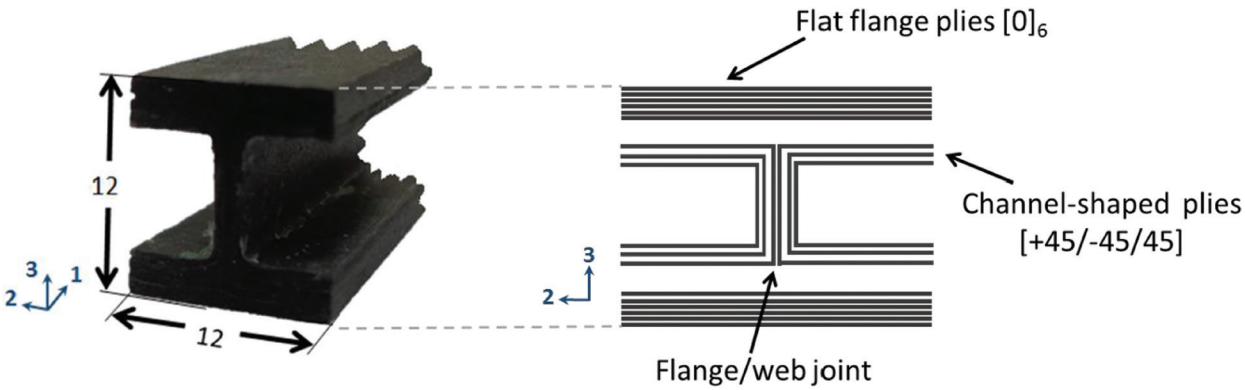


***Figure 1.*** *Picture of cropped I-shaped specimen (left) and schematic of ply orientations (right). Dimensions in mm (not to scale).*

with wax to ease the separation of I-shaped beam from the mold after curing. Flat flange plies (see Figure 1) comprised of six 0° plies are stacked upon the bottom of the mold. Using the side mold inserts, channel-shaped plies are formed using ±45° off-axis plies as indicated in Figure 1. These channel-shaped plies extend from the web into the flanges. To improve the fiber continuity at the web/flange joints (see Figure 1), four CF tows were inserted at this junction, as suggested by Zhou and Hood [31]. Another set of flat flange plies are stacked before closing the mold to form the top flange. Finally, the impregnated plies within the mold were held under uniform pressure in the horizontal and vertical directions using clamps and cured in an oven at 50°C for 8 h. The resulting 1.2 m I-beam was cut into 5 individual specimens to nominal dimensions of 228 mm (length) × 12 mm (width) × 12 mm (height), as in Figure 1.

### 2.3. Electrode Instrumentation

Electrodes were attached to the top (compressive side) and bottom (tensile side) surfaces of both types of specimen using two electrical contacts at each surface. An electrode separation of 25 mm for the rectangular and 50 mm for the I-shaped specimens were used as indicated in Figure 2. In order to instrument such electrodes, the specimen's surface was first lightly sanded to expose the CF. After sanding the specimens, a strip of silver paint (Ted Pella Inc., CA, USA) was applied to define each electrode contact and provide a conductive pathway across the CF tows. Finally, a strip of conductive silver epoxy paste (MG Chemicals, Surrey, B.C., Canada) was used to attach 30 AWG copper wires to function as electrodes for electrical resistance measurements.

### 2.4. Test Setup and Instrumentation

A hydraulic material testing system (MTS 810) equipped with a 244 kN load cell was used to load the specimens placed on a four-point bending fixture (WTF-FL-52 Wyoming Test Fixtures, UT, USA) as shown in Figure 2. Following procedure B of ASTM standard D7264 [32], all specimens had the loading points centered and spaced with a distance equal to one-half the support span (i.e. 76 mm for the rectangular and 92 mm for the I-shaped specimens as indicated in Figure 2). These dimensions correspond to support span-to-thickness ratios of respectively 40:1 (for rectangular) and 16:1 (for I-shaped). All tests were conducted at a displacement rate of 1 mm/min, including monotonic and cyclic loadings. Recorded data included force measurements obtained from the MTS load cell and displacement from the MTS linear variable differential transformer. Surface-based electrical resistance (R) measurements were collected using two digital multimeters (DMM) (Agilent 34401A and 34410A) using the internal four-wire setting (Kelvin measurement) and recorded using Agilent's Benchvue data acquisition software. Since the specimens are under flexural loading, one surface is under compressive stress/strain while the opposite surface is under tensile stress/strain, volume based electrical resistance measurements commonly utilized for uniaxial tensile/compression tests would not be suitable. One DMM was allocated to measure the electrical resistance of the specimen's side under tensile strain, and the other DMM was allocated for the specimen's side under compressive strain. To pre-

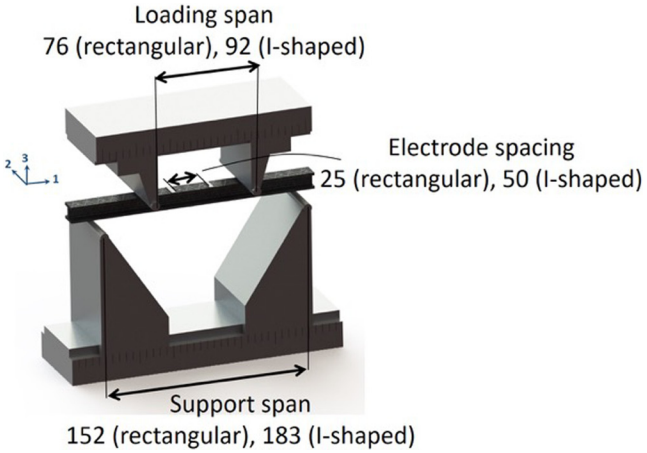


***Figure 2.*** *Schematic of four-point bending setup and electrode spacing for specimens with rectangular and I-shaped cross-sections (all dimensions in mm).*

vent potential electrical current leakage, electrically insulated tape was placed between the specimens' surface and the contact points of the four-point bending fixture. In order to synchronize data obtained from both the MTS and Agilent Benchvue data acquisitions, post-processing of the data sets was performed through linear interpolation.

For the cyclic tests, three specimens for each cross-section were tested for 30 cycles, increasing the maximum applied displacement after every 10th cycle. For specimens with rectangular cross-section, the first ten cycles reached a maximum displacement amplitude of 2.5 mm, followed by an increase in amplitude to 5 mm for ten more cycles, and finally to 7.5 mm for the last ten cycles. For the specimens with I-shaped cross-section, the maximum displacements for each set of ten cycles were 0.75 mm, 1.5 mm and 2.25 mm, applied sequentially. These set maximum displacement amplitudes were chosen based on the response of the monotonic flexural loading tests.

### 2.5. Calculation of Gauge Factors

In order to characterize the piezoresistive response of the CF/epoxy composites, a metric of strain sensitivity known as a gauge factor ($K$) was used. A gauge factor is defined as the (linear) relationship between the fractional electrical resistance change ($\Delta R/R_0$) and strain ($\varepsilon$) [21]. The fractional electrical resistance is defined as the relative change in electrical resistance ($\Delta R = R - R_0$) with respect to the resistance at zero strain ($R_0$). Under flexural loading, a specimen will simultaneously undergo tensile and compressive longitudinal strains, which are maximum at opposite surfaces. Therefore, within a fixed strain region which was approximately linear, tensile ($K_T$) and compressive ($K_C$) gauge factors were calculated for each rectangular and I-shaped specimen. Both $K_T$ and $K_C$, for all rectangular and I-shaped cross-section specimens, were calculated from a fixed strain range of 0.05% to 0.3%. In order to calculate $K_T$ and $K_C$, the instantaneous strain $\varepsilon$ (instead of machine cross-head displacement, $\delta$) is required. The relationship between $\delta$ and the longitudinal strain ($\varepsilon$) is a function of the specimen's thickness ($h$) and the support span length ($L$) used, i.e.,

$$\varepsilon = \frac{4.36\delta h}{L^2} \tag{1}$$

This equation may suffer from some inaccuracies, given the finite compliance of the machine and test apparatus, as well as the fact that it was derived from isotropic beam theory. Therefore, initial tests were conducted using strain gauges to directly measure $\varepsilon$, on both tensile and compressive sides, while simultaneously recording $\delta$. This procedure allowed for $\varepsilon$ to be obtained from $\delta$ and correct for such inaccuracies. The corrected values of $\varepsilon$ were found to be always within ~10% error for rectangular and ~3% for I-shaped cross section specimens with respect to the strain directly calculated from Equation (1).

### 2.6. Scanning Electron Microscopy

A Phillips FEI XL30 scanning electron microscope (SEM) using a field emission gun electron source was utilized to obtain images which enabled the study of failure mechanisms of the CF/epoxy rectangular specimens. After flexural testing, the rectangular specimens were trimmed in order to fit inside the SEM chamber. A layer of gold was sputtered onto the specimen's surface to improve the image quality and to prevent the buildup of electrical charge within the specimens. Micrographs taken on the analyzed specimens were collected by setting an accelerating voltage of 20 kV with a 40 μm aperture. While sub-surface damage can be assumed to have occurred in all rectangular specimens tested, identification of evident failure of the composites at their exposed surface (where the micrographs were taken) was not possible for all specimens analyzed. Therefore, a total of 14 replicates were observed and analyzed to provide meaningful correlations.

## 3. RESULTS AND DISCUSSION

### 3.1. Strain and Damage Sensing Under Monotonic Flexural Loading

#### *3.1.1. Specimens with Rectangular Cross-section*

Representative load-displacement curves are shown in Figure 3 for the specimens with rectangular cross-section tested under flexural loading, along with the coupled electromechanical response on both top and bottom surfaces. In Figure 3, the applied load (left vertical axis) and the fractional resistance change ($\Delta R/R_0$, right vertical axis) are plotted as a function of the machine's cross-head displacement ($\delta$), for the bottom [Figure 3(a)] and top [Figure 3(b)] surfaces. On the tensile side [Figure 3(a)], $\Delta R/R_0$ increases monotonically until the specimen's collapse. For small displacements ($\delta < 4$ mm), $\Delta R/R_0$ increases in a nearly linear fashion with increasing $\delta$. This behavior can be attributed to the intrinsic piezoresistivity of the stretched CFs, enhanced by a reduction in the density of fiber contacts (i.e. increase in the lateral distance between adjacent fibers) [11,26]. In addition, it is assumed that residual compressive stresses on the CF, initially created from the mismatch of the CF and epoxy thermal expansion properties, are slowly released, dictating the gradual increase $\Delta R/R_0$ for small displacement [3]. From approximately $4 < \delta < 6$ mm, the slope of $\Delta R/R_0$ increases at a slightly faster rate in a nonlinear fashion, conceivably due to the onset of fiber damage within the composite. Finally, for $\delta > 6$ mm, $\Delta R/R_0$ continues to increase linearly until the specimen collapses, which is attributed to the increased

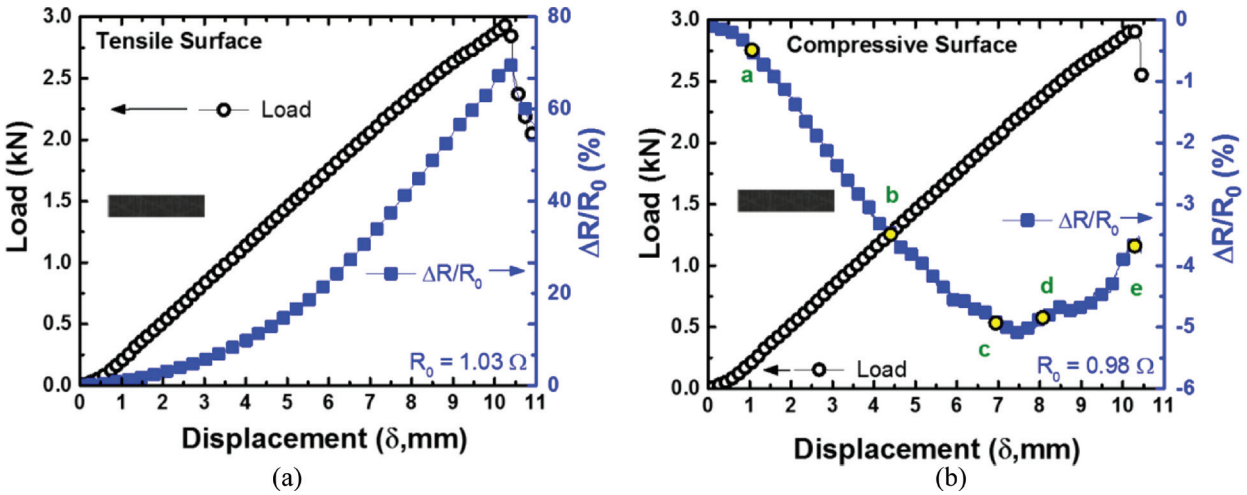


***Figure 3.*** *Monotonic flexural response of a representative specimen with rectangular cross-section until failure: (a) tensile surface (b) compressive surface.*

damage within the composite [22]. During the linear $\Delta R/R_0$ region, seen at small deformation ($\delta < 6$ mm), it is assumed that the composite behaves elastically and $\Delta R$ is mainly due to strain; as such the calculation of gauge factors is appropriate in that region. Gauge factors were thus computed using the strain-displacement relation in Equation (1), along with the correction factor described in Section 2.5. For the tensile side, the piezoresistive response yielded an average value of $K_T = 31.5 \pm 13.9$ (see Table 1), which is one order of magnitude higher than the value previously reported for an individual CF ($K_T = 1.3 – 1.7$ [4]) and comparable to that reported for the transverse (with respect to the loading direction) resistance of a continuous CF/epoxy composite ($K_T = 34.2 – 48.7$ [22]) under uniaxial tension. The high variation of $K_T$ in our results could stem from variation in the initial degree of fiber alignment from specimen to specimen (which can render differences in the initial density of fiber contacts), differences in residual stresses during composite curing, and the complex nature of such a coupled phenomenon.

The behavior of $\Delta R/R_0$ on the compressive side, Figure 3(b), is quite different to that of the tensile side [Figure 3(a)]. For the compressive side, the global behavior of $\Delta R/R_0$ is nonlinear and non-monotonic, first decreasing and then increasing. After a small toe adjustment [region 0-a in Figure 3(b)], $\Delta R/R_0$ linearly decreases with the applied deformation ($\delta < 4$ mm, region a-b in Figure 3(b). This region a-b is assumed to be within the elastic region of the composite, and thus the associated metric of piezoresistivity ($K_C$) for the rectangular cross-section specimen under compression was quantified in such a region. For the compressive side, the piezoresistive response yielded an average value of $K_C = 9.1 \pm 3$ (see Table 1), which is three times less than the $K_T$ listed in Table 1 for a rectangular cross-section. This piezoresistive response is expected to be driven by an increase in the density of CF lateral contacts forming new conductive pathways [11]. Following this linear region [$4 < \delta < 7$ mm, region b-c in Figure 3(b)], $\Delta R/R_0$ continues decreasing at a slightly different rate, which is attributed to the onset of fiber breakage for a few fibers. The first strong indication of significant fiber damage on the compressive side is seen at the region $7 < \delta < 8$ mm [region c-d in Figure 3(b)], where $\Delta R/R_0$ forms a valley and reaches a minimum value. After reaching this minimum [$\delta > 8$ mm, region d-e in Figure 3(b)] the $\Delta R/R_0$ response increases, suggesting fiber rupture and permanent damage which coincides with a load drop representing the loss of the composite's load-bearing capability.

The composite's failure was identified to occur on the compressive side. In general, for a FRPCs, several indications of compressive-dominated failure exist, including crushing, shearing, crack growth within the matrix, and fiber micro-buckling [33,34]. In order to investigate the damage progression and how the compressive electromechanical response correlates to specific failure mechanisms, SEM micrographs of the rectangular specimens were taken at increasing levels of $\delta$. Figure 4 shows the compressive load-displacement and corresponding $\Delta R/R_0$ for rectangular

***Table 1. Rectangular and I-shaped Cross-section Gauge Factors.***

| Specimen Cross-section | Number of Replicates | Average | | Median | |
|---|---|---|---|---|---|
| | | $K_T$ | $K_C$ | $K_T$ | $K_C$ |
| Rectangular | 16 | 31.5 ± 13.9 | 9.1 ± 3.0 | 30.3 | 8.7 |
| I-shaped | 5 | 20.0 ± 5.1 | 3.2 ± 1.7 | 19.0 | 3.0 |

specimens tested up to a maximum displacement of $\delta_{max} = 6$, 8 and 9 mm, as well as a reference (pristine) specimen which was not loaded. *Post-mortem* SEM micrographs were taken at the 1-3 plane on the specimen which was within the "pure bending" region as shown in Figure 4(a). Lettered markers (a,b,c,d,e) help to highlight specific regions of the $\Delta R/R_0$ response and correspond to those described in Figure 3(b). As a reference, Figure 4(a) shows a SEM picture of a specimen which was not loaded, portraying the undamaged state of the rectangular cross-section specimen. For the maximum displacement of 6 mm shown in Figure 4(b), $\Delta R/R_0$ decreases until point "c" and the corresponding SEM micrograph in Figure 4(b) (right) was taken. At this state, the micrograph shows slightly bent fibers indicating fiber micro-buckling closer to the compressive surface, but without indications of fracture. This observation shows that the rectangular specimen is accumulating damage induced by the distortion of the fibers and forming kink bands [35]. In addition, it has been shown by Parry and Wronski [36], that kink band propagations lead to the formation of interlaminar cracks and eventual delamination of CF/epoxy under flexure. A second rectangular specimen tested to a maximum displacement of 8 mm is shown in Figure 4(c). Herein, the $\Delta R/R_0$ response decreases until point "c", leveling off and forming a valley (minimum region) between points "c" and "d". Region "c-d" corresponds to a change in trend as indicated in Figure3(b). The corresponding micrograph [Figure 4(c)] shows an interlaminar crack propagating along the fiber direction triggering delamination among the plies. This evidence of damage is directly correlated to the abrupt change in $\Delta R/R_0$ at $\delta \sim 8$mm in the electromechanical response shown in Figure 4(c). Delamination reduces the density of fiber contacts in the through-thickness direction, and hence it is expected to cause the observed inversion of the $\Delta R/R_0$ trend (from negative to positive). Finally, in Figure 4(d) the steep increase in $\Delta R/R_0$ close to $\delta \sim 9$ mm (region "d-e") is evidently associated to a drop in load and the specimen's collapse.

#### *3.1.2. Specimens with I-shaped Cross-section*

Figure 5 shows the representative mechanical and electromechanical behavior of a CF/epoxy specimen with I-shaped cross-section corresponding to the tensile [Figure 5(a)] and compressive surfaces [Figure 5(b)]. The load (left vertical axis) and $\Delta R/R_0$ (right vertical axis) are simultaneously plotted as a function of $\delta$ in the same fashion for the specimens with rectangular cross-section. Comparing the mechanical behavior of the specimens with I-shaped cross-section (Figure 5) to those of rectangular cross-section (Figure 3), it is clear that the I-shaped cross-section is structurally stiffer and fails at lower levels of displacement. Similar to the specimens of rectangular cross-section, the electromechanical behavior of the I-shaped specimens shows a linear increase of $\Delta R/R_0$ on the tensile side [Figure 5(a)], with the electrical behavior almost replicating the mechanical behavior indicating an outstanding straightforward electromechanical correlation. On the other hand, the behavior of $\Delta R/R_0$ on the compressive side is somewhat different, as the signal is noisier and $\Delta R/R_0$ is less sensitive to strain/displacement than for the tensile side. However, the compressive $\Delta R/R_0$ response still shows a clear correlation with the mechanical loading, initiating with a nearly linear zone (at the elastic region, $\delta < 2$ mm, where gauge factors are calculated), leveling off at the onset of damage ($2 \text{ mm} < \delta < 3$ mm) and reversing its trend once the load-displacement curve shows a clear indication of damage ($\delta > 3$ mm). Gauge factors for low strain levels ($0.1\% < \varepsilon < 0.3\%$) for specimens with I-shaped cross-section were also obtained to assess the strain sensitivity for both the tensile and compressive sides of the I-shaped specimen and are summarized in Table 1. Similar to the specimens with rectangular cross-section, the I-shaped cross-section $K_T = 20 \pm 5.1$ (tensile) is significantly larger than $K_C = 3.2 \pm 1.7$ (compressive). For the tensile response, the maximum change in $\Delta R/R_0$ of the representative rectangular specimen reaches $\Delta R/R_0 \sim 70\%$ (at $\delta \sim 10$ mm), whereas for the representative I-shaped specimens $\Delta R/R_0$ reaches only up to $\Delta R/R_0 \sim 7\%$ (at $\delta \sim 2.5$ mm). On the compressive side, a minimum value of $\Delta R/R_0 \sim -5\%$ (at $\delta \sim 7.5$ mm) is obtained for the representative rectangular specimen, while a value of $\Delta R/R_0 \sim -1\%$ (at $\delta \sim 3$ mm) is reached for the representative I-shaped specimen. It should be observed that there is quite a lot of scatter in $K_T$ for specimens with rectangular cross section, so box plots (see Appendix A) may suggest statistical equivalence of the strain sensitivity for both cross-sections. However, the differences shown in the overall $\Delta R/R_0$ magnitude changes clearly demonstrate a reduction in the strain sensitivity from the specimens with rectangular to I-shaped cross section. The reasoning behind this lowered strain sensitivity of the I-shaped cross-section can be made further evident by comparing the mechanical behavior (load versus deflection curves) of the I-shaped and the rectangular cross-section response after reaching the maximum load. For rectangular specimens, the failure of the specimens is accompanied by a drastic drop in load [see Figure 3(a)], whereas the specimens with I-shaped cross-section are significantly stiffer and after they reach their maximum load they are still capable of carrying relatively high loads [see Figure 5(a)], given the significant amount of still unbroken fibers.

### 3.2. Strain and Damage Sensing under Incremental Cyclic Loading

#### *3.2.1. Specimens with Rectangular Cross-section*

In order to determine the progressive electromechanical behavior under cycling flexural loading, rectangular specimens were first cycle loaded at incrementally increasing displacement amplitudes of 2.5 mm (cycles 1-10), 5 mm

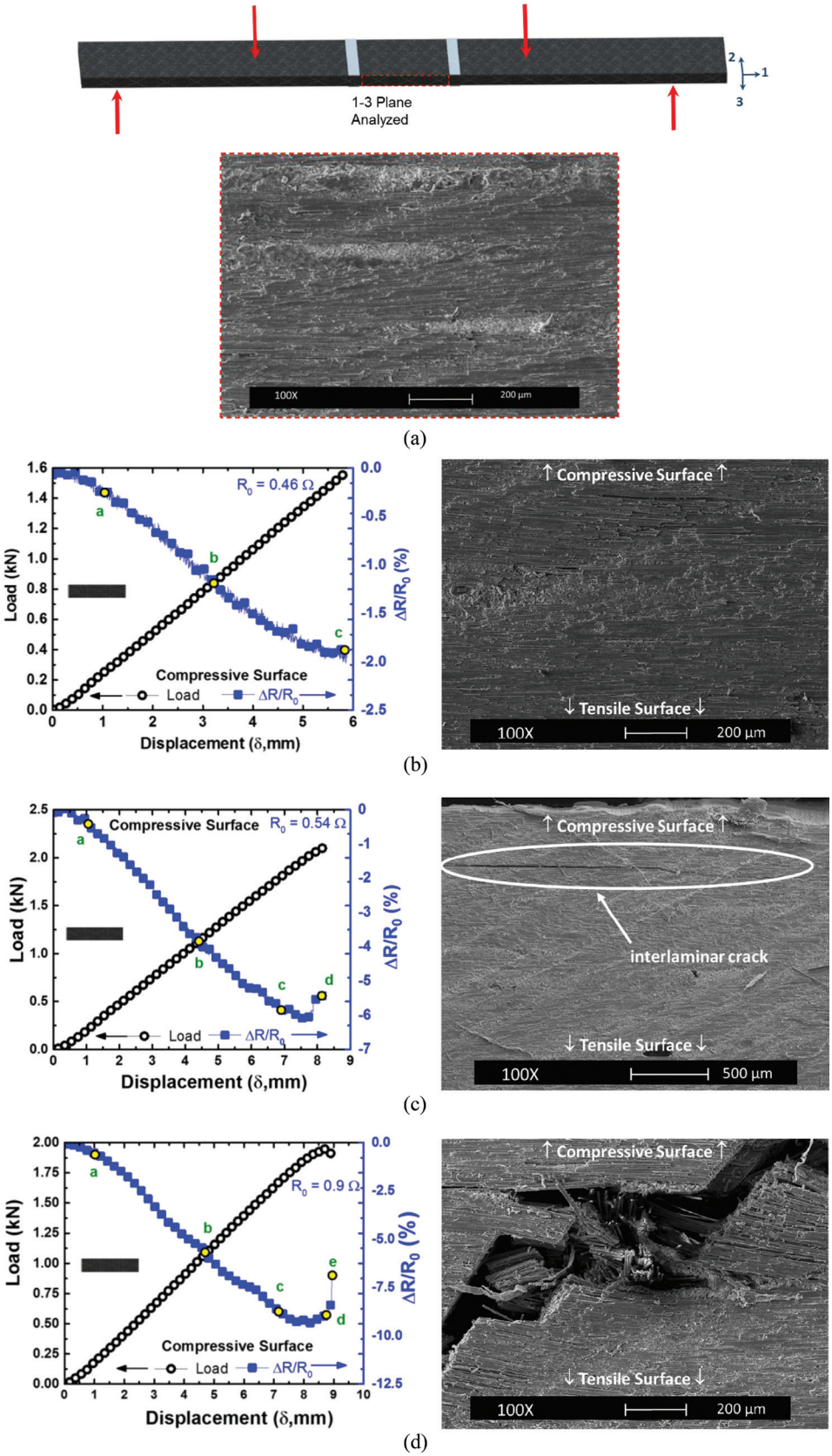


***Figure 4.*** *Sequential load-displacement and $\Delta R/R_0$-displacement curves with corresponding SEM analysis of rectangular cross-section specimens tested under increasing displacement. (a) Baseline (pristine) specimen, (b) $\delta_{max}$ = 6 mm, (c) $\delta_{max}$ = 8 mm (d) $\delta_{max}$ = 9 mm.*

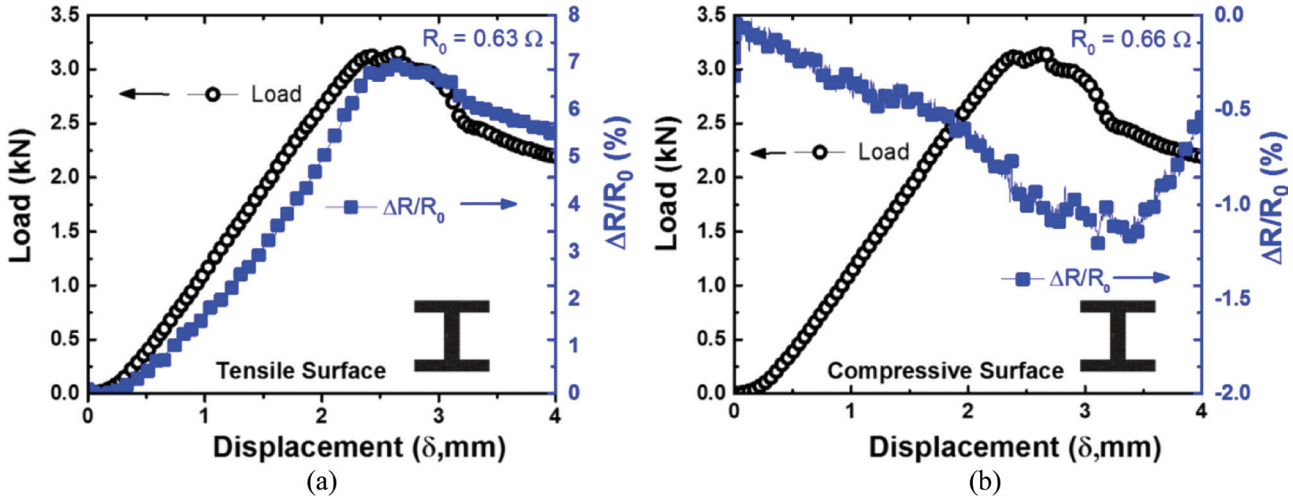


***Figure 5.*** *Monotonic flexural response of a representative specimen with I-shaped cross-section until failure on (a) tensile side and (b) compressive side.*

(cycles 11-20) and 7.5 mm (cycles 21-30). Figure 6 shows the displacement (left vertical axis) and fractional resistance response (right vertical axis) as a function of time for the tensile [Figure 6(a)] and compressive [Figure 6(b)] sides of a rectangular cross-section, tested under cyclic flexural loading. The $\Delta R/R_0$ signal shows an instantaneous dependence with applied deformation, with increasing displacement amplitudes corresponding to increasing $\Delta R/R_0$ amplitudes.

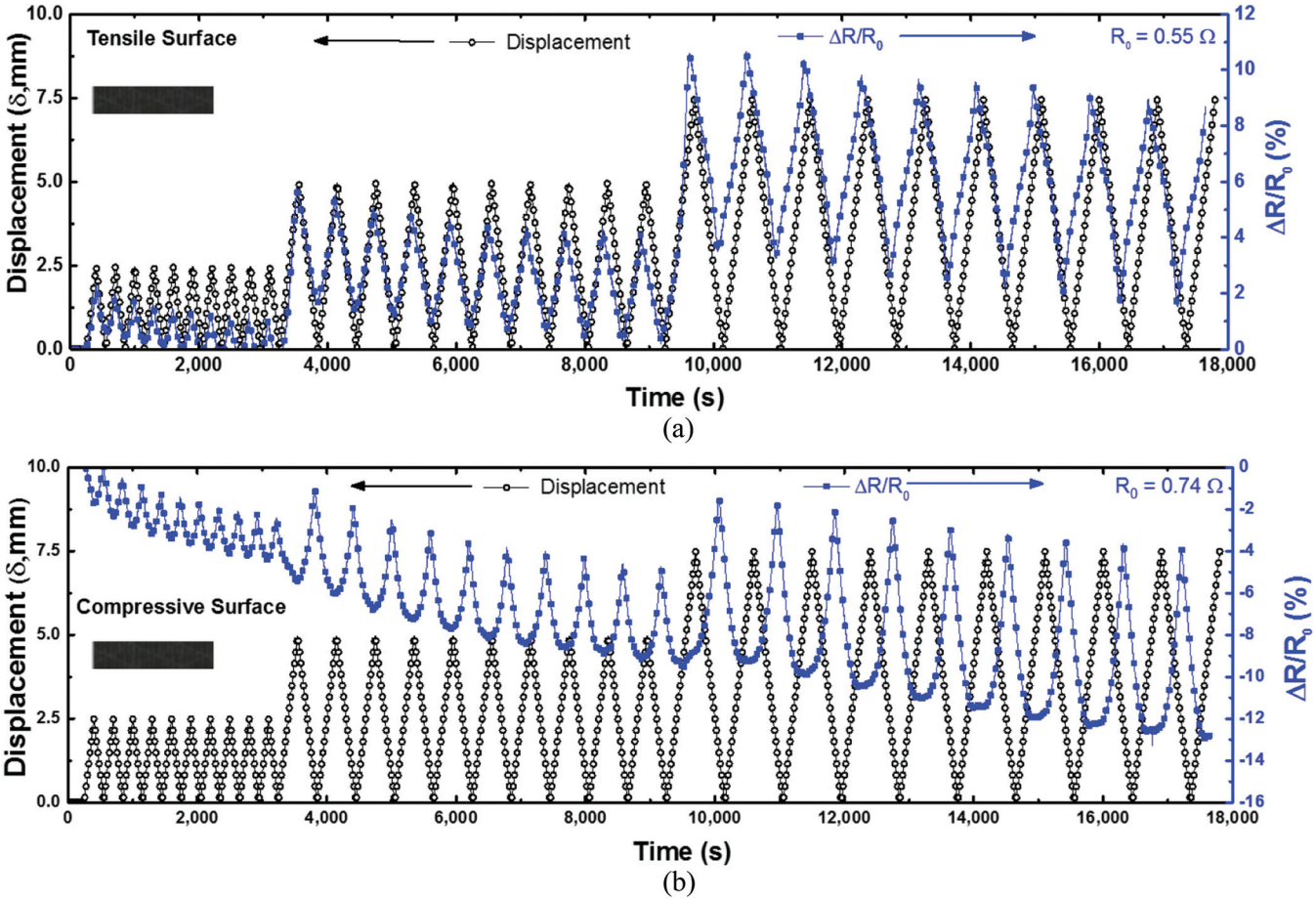


***Figure 6.*** *Cyclic flexural loading at incremental displacement amplitudes for a representative specimen with rectangular cross-section on (a) tensile side and (b) compressive side.*

Starting with the loading segment of cycle 1 for the tensile response [Figure 6(a)], the rectangular specimen is deformed up to 2.5 mm with a corresponding $\Delta R/R_0$ peak amplitude of ~2%. Immediately upon the following unloading segment of cycle 1, $\Delta R/R_0$ begins to decrease. Although the applied displacement returns to zero, the $\Delta R/R_0$ response does not. Cycles 2 to 10 repeat this pattern with the $\Delta R/R_0$ peak values at 2.5 mm displacement progressively decreasing for increasing number of cycles, seeming to level off after the 7th cycle. This irreversible response of $\Delta R/R_0$ is thought to originate from the release of compressive residual stresses introduced during the curing and post-curing steps, as pointed out previously by other authors [3]. This irreversible response should be distinguished from the irreversible response due to the composite's damage, as it is assumed the mechanical loading up to 2.5 mm is within the elastic range. Further evidence which supports that these irreversible changes in $\Delta R$ comes from the release of compressive residual stresses is that the $\Delta R$ signal seems to level off after several repetitions (~7) of the loading cycle, becoming reproducible and returning to almost zero thereafter. For the second group of cycles (cycles 11-20), the tensile $\Delta R/R_0$ response increases to a $\Delta R/R_0$ peak amplitude of ~4%, corresponding to 5 mm displacement. Similar to the first group, $\Delta R/R_0$ peak values also gradually decrease for increasing number of cycles. A similar behavior is observed for cycles 21-30 with an applied displacement of 7.5 mm, indicating damage accumulation as inferred from the SEM micrographs of Figure 4.

For the compressive response [Figure 6(b)], at the first cycle $\Delta R/R_0$ decreases to ~ –2% for an applied displacement of 2.5 mm. Upon unloading $\Delta R/R_0$ returns back to the $R_0$ value, which only occurs for the first cycle. Upon subsequent loading at the same displacement amplitude (cycle 2-10), $\Delta R/R_0$ follows the same pattern maintaining a $\Delta R/R_0$ amplitude of ~ –2%, but shifted towards more negative values of $\Delta R/R_0$. This behavior is similar to the quasi-isotropic CF/epoxy specimens under cyclic flexural loading observed in Ref. [11]. For cycles 11-20, the compressive $\Delta R/R_0$ response cycles with an amplitude of ~ –4%, with minimum values progressively decreasing for increasing number of cycles. The $\Delta R/R_0$ response in Figure 4 indicates that damage at the compressive side occurs earlier than at the tension side. Based on this, it is suggested that the irreversible nature of $\Delta R/R_0$ not returning to zero is an indication of initial composite damage such as fiber micro-buckling and occurrence of shear bands, as shown in Figure 4(b). Finally for cycles 21-30, $\Delta R/R_0$ cycles with an amplitude of ~ –8%, with each cycle's minimum value continuing to decrease for increasing number of cycles. This consistent irreversible nature highlights the conductive CF ability to provide information on pre-existing damage and accumulation of new damage by measurement of the instantaneous $R$ and knowledge of the referenced $R_0$.

### *3.2.2. Specimens with I-shaped cross-section*

The electromechanical behavior was also investigated for specimens with I-shaped cross-section loaded under flexural cycling incremental displacement amplitudes of 0.75 mm (cycles 1-10), to 1.5 mm (cycles 11-20), and 2.25 mm (cycles 21-30). Figure 7 shows the displacement (left vertical axis) and fractional resistance response (right vertical axis) as a function of time for the tensile [Figure 7(a)] and compressive [Figure 7(b)] sides. Similar to the rectangular specimens, during a given loading segment the $\Delta R/R_0$ response increases on the tensile side and decreases on the compressive side of the I-shaped specimen for increasing displacement, such that displacement peaks correspond to $\Delta R/R_0$ peak values. Starting with the tensile response of the loading segment corresponding to the first cycle [Figure 7(a)], the I-shaped specimen is deformed up to 0.75 mm with a corresponding $\Delta R/R_0$ small increase of ~1%. Immediately, upon the following unloading segment $\Delta R/R_0$ decreases. The maximum $\Delta R/R_0$ peak values of cycles 1-10 on the tensile surface [Figure 7(a)] continue to decrease irreversibly for increasing number of cycles with an average $\Delta R/R_0$ peak amplitude of ~0.5% throughout the cycles. An increase in the displacement amplitude from 0.75 mm to 1.5 mm (cycles 11-20) and then to 2.25 mm (cycles 21-3) corresponds to an increase in the $\Delta R/R_0$ peak amplitude to ~2% and ~3%, respectively. As before, the amplitudes of $\Delta R/R_0$ clearly show a dependency with applied strain and signs of irreversible damage. Consistent with the monotonic results of Figure 5(a), the I-shaped specimens tested under cyclic loading show a reduction in the $\Delta R/R_0$ sensitivity to applied deformation in contrast to the cyclic response of the rectangular cross-section specimens.

The $\Delta R/R_0$ compressive response of the I-shaped specimen [Figure 7(b)] is qualitatively quite similar to that of the rectangular specimen [Figure 6(b)] but consistently less sensitive to an applied strain. Similar to the rectangular cross-section specimens, the I-shaped cross-section compressive $\Delta R/R_0$ response mirrors the $\Delta R/R_0$ tensile response, yielding minimum $\Delta R/R_0$ values at the compressive side that coincide to the peak (maximum) $\Delta R/R_0$ values at the tensile side. For increased displacement, the magnitude of the compressive $\Delta R/R_0$ response decreases such that the displacement peaks correspond to minimum $\Delta R/R_0$ values. Similar to the cyclic response of specimens with I-shaped cross-section, $\Delta R/R_0$ amplitudes correspond to increasing displacement amplitudes, and indicate damage with irreversible residual electrical resistance changes.

## 4. CONCLUSIONS

The piezoresistive behavior and the ability of the electrical resistance signal to monitor damage in continuous carbon fiber/epoxy composites under flexural loading was

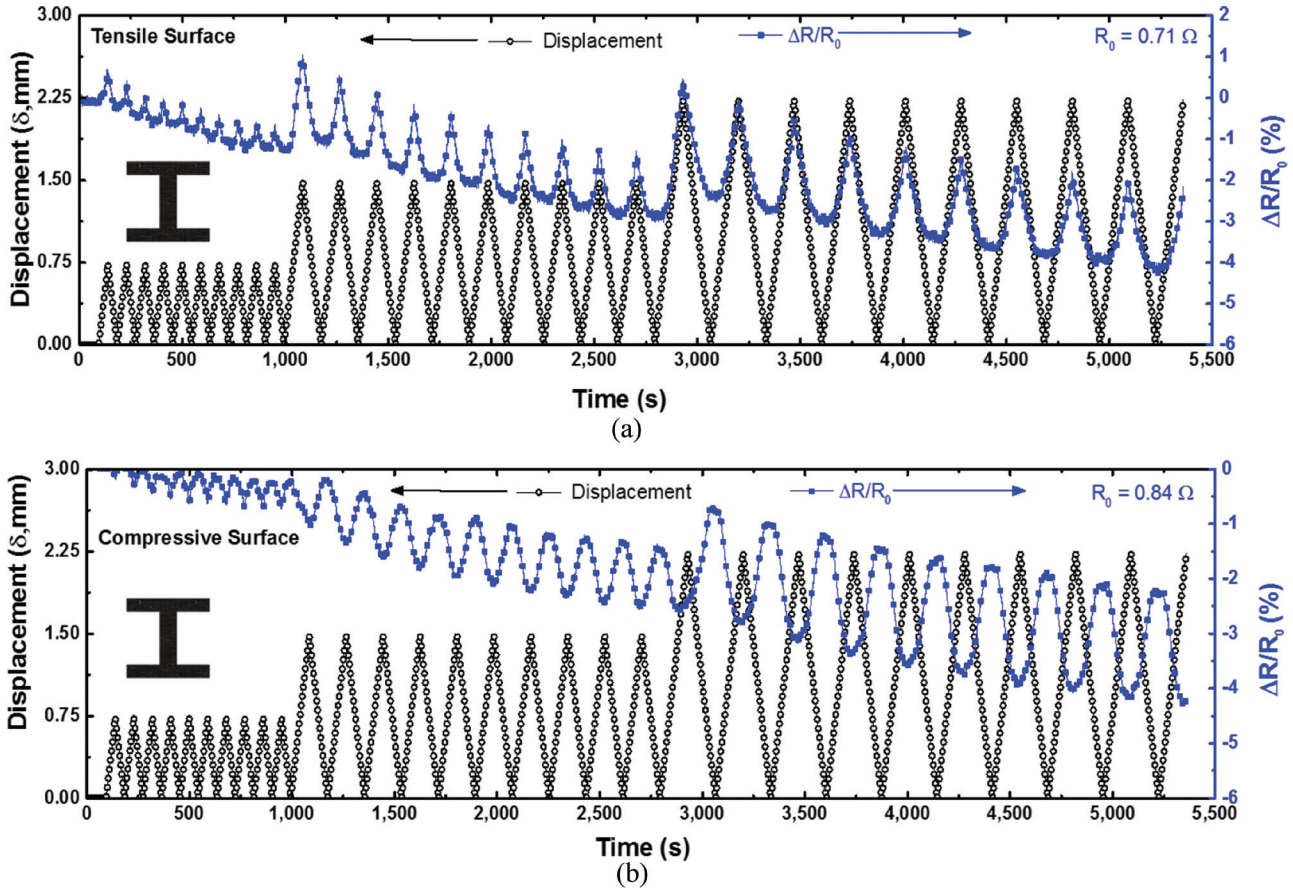


***Figure 7.*** *Cyclic flexural loading at incremental displacement amplitudes for a representative specimen with I-shaped cross-section on (a) tensile side and (b) compressive side.*

analyzed for specimens with rectangular and I-shaped cross-sections. For both the rectangular and I-shaped cross-sections, the fractional change in electrical resistance ($\Delta R/R_0$) at the tensile side of the specimen yields a nonlinear response that increases monotonically up to failure. In contrast, the $\Delta R/R_0$ compressive behavior is highly nonlinear and also non-monotonic. This compressive behavior initially decreases linearly for small deformations, then further decreases at a different rate leveling off to a minimum value such that a valley is formed, and finally reverses its trend and increases upon significant composite damage up to the complete collapse of the specimen. Using the electrical resistance approach specimens with both rectangular and I-shaped cross-sections produced responses which demonstrate their ability to self-sense tensile and compressive strain and composite damage. Given the observed failure mechanisms of both specimens, the compressive side proved to be particularly sensitive to failure events such as fiber micro-buckling, fiber deformation by formation of matrix shear bands and occurrence of transverse cracking. The I-shaped cross-section specimens showed a reduced strain and damage sensitivity, which indicates that the geometry and stiffness of a structural member should be taken into account in order to extend the application of the electrical resistance approach to practical operation of composite structures. Irreversible $\Delta R/R_0$ changes after each cycle of the flexural cyclic loading either at the tensile or compressive sides are associated to irreversible mechanical phenomena indicated by changes in the $\Delta R/R_0$ peaks for each cycle. This irreversible phenomena occurs first due to the release of residual stresses occurred during composite manufacturing, then to the re-orientation and rearrangement of the fibers upon loading, and finally due to the occurrence of failure mechanisms within the composite at elevated loads. This damage accumulated under cycling loading, also indicated by the cumulative residual electrical resistance changes in the composite, yields a hysteretic electromechanical behavior.

It is thus concluded that the electrical resistance approach to monitor structural integrity can be extended to structural members such as an I-beam, but the response may depend on many factors such as the cross-section thickness and geometry, curing conditions and lamination sequence. Therefore, detailed characterization, calibration and analysis are needed for varying geometric cross-sections and composite fiber orientations of a composite structural member.

## 5. ACKNOWLEDGMENTS

The authors thank Angelo Magliola, Nicolas Marinkovich, Daniel Reid, Christopher O'Keefe, Stephanie Zhu, and Miguel Duran (Advanced Composites Research, Engineering and Science, ACRES, UC Davis) for helping in the manufacturing of I-shaped specimens used in this work. We are also thankful to Dr. Ricardo Castro (Materials Science and Engineering, UC Davis) for the loan of a DMM, and Mr. Fred Hayes (Advanced Materials Characterization and Testing Lab of Materials Science and Engineering, UC Davis) for his help with the SEM. Dr. La Saponara acknowledges the support of the US National Science Foundation (grant number CMMI-1200521) and of the Office of Naval Research (grant number N00014-13-1-0604) managed by Dr. Y. Rajapakse. Partial support of the University of California Institute for Mexico and the United States (UC MEXUS) and CONACYT (project number 220513) is also acknowledged.

## 6. REFERENCES

[1] Edison TA. Electric lamp. US Patent 223898 Jan. 1880.

[2] Chand S. Carbon fibers for composites. *Journal of Materials Science.* 2000;35(6):1303-13. http://dx.doi.org/10.1023/A:1004780301489

[3] Wang X, Fu X, Chung DDL. Strain sensing using carbon fiber. *Journal of Materials Research.* 1999;14(3):790-802. http://dx.doi.org/10.1557/JMR.1999.0105

[4] Owston CN. Electrical Properties of Single Carbon Fibers. *Journal of Physics D-Applied Physics.* 1970;3(11):1615-26. http://dx.doi.org/10.1088/0022-3727/3/11/309

[5] Schulte K, Baron C. Load and failure analyses of CFRP laminates by means of electrical resistivity measurements. *Composites Science and Technology.* 1989;36(1):63-76. http://dx.doi.org/10.1016/0266-3538(89)90016-X

[6] Liu W, Hubert P. Self-sensing of Strain in Carbon Nanotube Modified Carbon Fibre Reinforced Composites. 55th AIAA/ASMe/ASCE/AHS/SC Structures, *Structural Dynamics, and Materials Conference.* 2014.

[7] Wang S, Chung DDL, Chung JH. Impact damage of carbon fiber polymer-matrix composites, studied by electrical resistance measurement. *Composites Part A—Applied Science and Manufacturing.* 2005;36(12):1707-15. http://dx.doi.org/10.1016/j.compositesa.2005.03.005

[8] Wang S, Chung DDL. Sensing delamination in a carbon fiber polymer-matrix composite during fatigue by electrical resistance measurement. *Polymer Composites.* 1997;18(6):692-700. http://dx.doi.org/10.1002/pc.10322

[9] Wang X, Chung DDL. Self-monitoring of fatigue damage and dynamic strain in carbon fiber polymer-matrix composite. *Composites Part B (Engineering)*. 1998;29B(1):63-73. http://dx.doi.org/10.1016/S1359-8368(97)00014-0

[10] Vavouliotis A, Paipetis A, Kostopoulos V. On the fatigue life prediction of CFRP laminates using the Electrical Resistance Change method. *Composites Science and Technology.* 2011;71(5):630-42. http://dx.doi.org/10.1016/j.compscitech.2011.01.003

[11] Wang S, Chung DDL. Self-sensing of flexural strain and damage in carbon fiber polymer-matrix composite by electrical resistance measurement. *Carbon*. 2006;44(13):2739-51. 13

[12] Abry JC, Bochard S, Chateauminois A, Salvia M, Giraud G. In situ detection of damage in CFRP laminates by electrical resistance measurements. *Composites Science and Technology*. 1999;59(6):925-35. http://dx.doi.org/10.1016/S0266-3538(98)00132-8

[13] Ciang CC, Lee J-R, Bang H-J. Structural health monitoring for a wind turbine system: a review of damage detection methods. *Measurement Science & Technology*. 2008;19(12):20. http://dx.doi.org/10.1088/0957-0233/19/12/122001

[14] Diamanti K, Soutis C. Structural health monitoring techniques for aircraft composite structures. *Progress in Aerospace Sciences*. 2010;46(8):342-52. http://dx.doi.org/10.1016/j.paerosci.2010.05.001

[15] Gao LM, Thostenson ET, Zhang ZG, Chou T-W. Coupled carbon nanotube network and acoustic emission monitoring for sensing of damage development in composites. *Carbon*. 2009;47(5):1381-8. http://dx.doi.org/10.1016/j.carbon.2009.01.030

[16] Hamstad MA. A Review - Acoustic-Emission, A tool for composite materials studies. *Experimental Mechanics*. 1986;26(1):7-13. http://dx.doi.org/10.1007/BF02319949

[17] Rizzo P. *Acoustic Emission of Composites. Smart Composites*: CRC Press 2013, p. 273-98.

[18] Adams RD, Cawley P. A review of defect types and nondestructive testing techniques for composites and bonded joints. *NDT International*. 1988;21(4):208-22. http://dx.doi.org/10.1016/0963-8695(88)90113-2

[19] Tang H-Y, Winkelmann C, Lestari W, La Saponara V. Composite Structural Health Monitoring Through Use of Embedded PZT Sensors. *Journal of Intelligent Material Systems and Structures*. 2011;22(8):739-55. http://dx.doi.org/10.1177/1045389X11406303

[20] Kuang KSC, Cantwell WJ. Use of conventional optical fibers and fiber Bragg gratings for damage detection in advanced composite structures: a review. *Applied Mechanics Review*. 2003;56(5):493-513. http://dx.doi.org/10.1115/1.1582883

[21] Kobayashi AS, Mechanics SfE. *Handbook on experimental mechanics*: VCH; 1993.

[22] Wang X, Chung DDL. Continuous carbon fibre epoxy-matrix composite as a sensor of its own strain. *Smart Materials and Structures*. 1996;5(6):796-800. http://dx.doi.org/10.1088/0964-1726/5/6/009

[23] Todoroki A, Yoshida J. Electrical resistance change of unidirectional CFRP due to applied load. *JSME International Journal Series A Solid Mechanics and Material Engineering*. 2004;47(3):357-64. http://dx.doi.org/10.1299/jsmea.47.357

[24] Inoue H, Ogi K. Piezoresistance behavior of CFRP cross-ply laminates with transverse cracking. *Key Engineering Materials*. 2007;334-335:961-4. http://dx.doi.org/10.4028/www.scientific.net/KEM.334-335.961

[25] Chung DDL. Structural health monitoring by electrical resistance measurement. *Smart Materials and Structures*. 2001;10(4):624-36. 14

[26] Chung DDL, Wang SK. Self-sensing of damage and strain in carbon fiber polymer-matrix structural composites by electrical resistance measurement. *Polymers & Polymer Composites*. 2003;11(7):515-25.

[27] Wang S, Chung DDL, Chung JH. Self-sensing of damage in carbon fiber polymer-matrix composite cylinder by electrical resistance measurement. *Journal of Intelligent Material Systems and Structures*. 2006;17(1):57-62. http://dx.doi.org/10.1177/1045389X06056072

[28] Wang X, Chung DDL. Inherently smart laminates of carbon fibers in a polymer matrix. *Layered Materials for Structural Applications Symposium*. 1996:299-304.

[29] Wang D, Chung DDL. Through-thickness piezoresistivity in a carbon fiber polymer-matrix structural composite for electrical-resistance-based through-thickness strain sensing. *Carbon*. 2013;60:129-38. http://dx.doi.org/10.1016/j.carbon.2013.04.005

[30] T700S Technical Data Sheet No. CFA-005: Toray Carbon Fibers America, Inc.

[31] Zhou G, Hood J. Design, manufacture and evaluation of laminated carbon/epoxy I-beams in bending. *Composites Part A: Applied Science and Manufacturing*. 2006;37(3):506-17. http://dx.doi.org/10.1016/j.compositesa.2005.01.005

[32] ASTM D7264 / D7264M-07, Standard Test Method for Flexural Properties of Polymer Matrix Composite Materials. West Conshohocken, PA: ASTM International 2007.

[33] Jelf PM, Fleck NA. Compression failure mechanisms in unidirectional composites. *Journal of Composite Materials*. 1992;26(18):2706-26. http://dx.doi.org/10.1177/002199839202601804

[34] Hull D, Clyne. TW. *An Introduction to Composite Materials*: Cambridge University Press; 1996. http://dx.doi.org/10.1017/CBO9781139170130

[35] Sutcliffe MPF, Fleck NA. Microbuckle propagation in carbon fibre-epoxy composites. *Acta Metallurgica Et Materialia*. 1994;42(7):2219-31. http://dx.doi.org/10.1016/0956-7151(94)90301-8

[36] Parry TV, Wronski AS. Kinking and tensile, compressive and interlaminar shear failure in carbon-fibre-reinforced plastic beams tested in flexure. *Journal of Materials Science*. 1981;16(2):439-50. http://dx.doi.org/10.1007/BF00738635

## APPENDIX A

The measured gauge factors are listed in Table A1 for specimens with rectangular cross-section and Table A2 for the I-shaped ones.

In order to display the variability of the gauge factors of individual specimens, box plots were computed for tensile and compressive gauge factors, respectively shown in Figures A1 and A2. A common hypothesis test such as the t-test would require the data sets to be normally distributed. In the case of the data shown in Tables A1 and A2, one normality test (Lilliefors test) indicated the data to be normal, with 95% confidence, while another normality test (Kolmogorov-Smirnov test) gave the opposite outcome. On the other hand, box plots are not parametric (i.e., they allow comparisons among sets, independent of their distribution), and were thus used in this case. The data is shown in a box, with its top and bottom lines being respectively the 75 percentile and the 25 percentile of the data. The center of the box is the median and the 50 percentile. The box extends to the maximum and minimum values through so-called whiskers. Outliers are represented by a symbol (for example, a cross). The result from Figure A1 indicates that the two sets of samples may have statistically similar gauge factors with 95% confidence.

***Table A1. Gauge Factors for Specimens with Rectangular Cross-section.***

| Specimen | $K_T$ | $K_C$ |
|---|---|---|
| 1 | 13.9 | 8.0 |
| 2 | 32.0 | 7.0 |
| 3 | 29.3 | 9.7 |
| 4 | 23.6 | 7.4 |
| 5 | 14.4 | 7.1 |
| 6 | 27.6 | 6.2 |
| 7 | 34.3 | 11.4 |
| 8 | 50.6 | 8.5 |
| 9 | 32.1 | 3.0 |
| 10 | 28.8 | 12.7 |
| 11 | 15.2 | 9.0 |
| 12 | 20.2 | 8.7 |
| 13 | 31.4 | 7.9 |
| 14 | 16.8 | 5.0 |
| 15 | 40.8 | 10.3 |
| 16 | 63.4 | 17.1 |

***Table A2. Gauge Factors for Specimens with I-shaped Cross-section.***

| Specimen | $K_T$ | $K_C$ |
|---|---|---|
| 1 | 19.0 | 3.0 |
| 2 | 27.0 | 6.0 |
| 3 | 22.9 | 1.9 |
| 4 | 14.2 | 1.9 |
| 16 | 16.6 | 3.4 |

This outcome is most likely due to the large scatter. When reviewing the actual sensitivity of the two sets over the entire life spans of the specimens, it is clear that the rectangular cross-sections have a much higher sensitivity with respect to the I-shaped cross-sections. The box plot in Figure A1 is provided for sake of completeness and reproducibility. In Figure A2, the interpretation of the box plot is that the two sets are statistically different, which is indeed supported by the different sensitivity on the compressive side of the specimens.

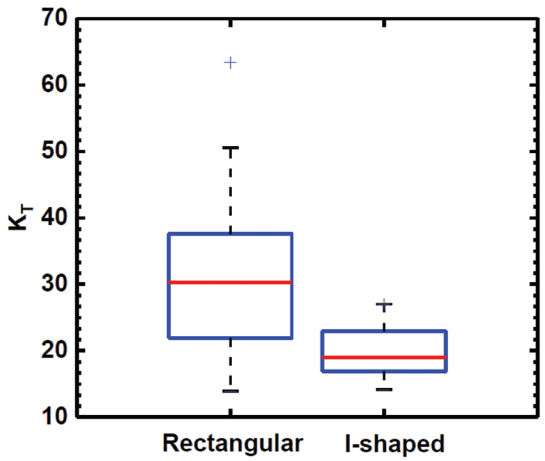


***Figure A1.*** *Box plot of tensile gauge factors for specimens with rectangular and I-shaped cross-section.*

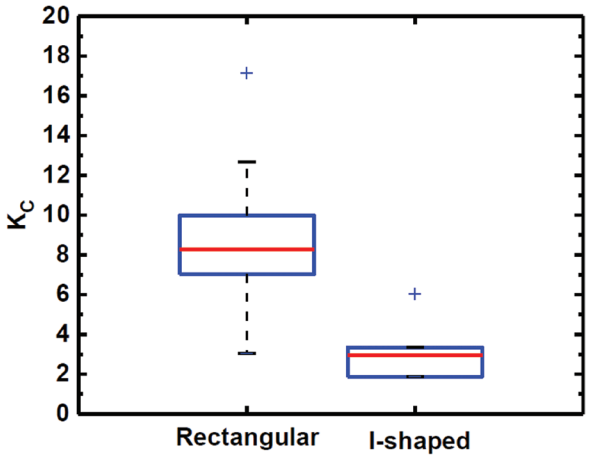


***Figure A2.*** *Box plot of compressive gauge factors for specimens with rectangular and I-shaped cross-section.*

*Journal of Multifunctional Composites,* 2 (2014) 195–206

Journal of Multifunctional Composites

journal homepage: http://jmc.destechpub.com

# Carbon Based Nanostructures Hybrids for Composites Materials: The Graphene—Carbon Nanotubes Interaction Investigation

ANTONIO F. ÁVILA, VIVIANE C. MUNHOZ, ALINE M. OLIVEIRA and ELVIS C. MONTEIRO

*Universidade Federal de Minas Gerais, Belo Horizonte, Minas Gerais, 31270-901, Brazil*

**ABSTRACT**

Two different carbon based nanostructures, multiwall carbon nanotubes and multi-layered graphene, were incorporated to carbon epoxy laminates. X-ray diffractometry indicates an average particle size of 22 nm for the multi-layer graphene (MLG) nanostructures. TEM observations revealed a thickness of 10 graphene layers, and a hybrid nanostructure where MWNT interpenetrated the MLG nanostructure. To be able to disperse more efficiently the carbon based nanostructures two different surfactants were employed, i.e. Sodium dodecylbenzenesulfonate (SDBS) and Polyoxyethylene nonylphenyl ether (IGEPAL CO890). The dispersion of surfactants associated to graphene led to increase on stiffness and strength, for both tensile and bending loads. If on the top of these surfactants/graphene additions, CNTs are added, the improvement is even better. For tensile tests, the average peak stress increase from 542.76 MPa (blank specimen) to 667.51 MPa (CO 890 and graphene/CNT), while for bending the peak stress improved from 369.40 MPa (blank specimen) to 584.15 MPa (CO 890 and graphene/CNT). The association of carbon based nanostructures (graphene and CNT) associated to surfactants seems to be a promising route to improve carbon/epoxy composites. Finally, the addition of carbon based nanostructures increased the hybrid composites toughness between 39.59% (from 4.712 to 6. 578 J/m$^3$ x 10$^4$) and 180.65% (from 4.712 to 13. 225 J/m$^3$ x 10$^4$).



## 1. INTRODUCTION

Carbon based materials uniqueness is well known. As discussed by Zhu *et al.* [1], carbon has unique hybridization properties as a result of its structure capabilities to morphing due to changes in synthesis conditions. Moreover, Mauter and Elimelec [2] pointed out those tailor-made manipulations of these carbon based materials can reach a degree not yet matched by inorganic nanostructures. Among the most important carbon based nanostructures, carbon nanotubes (CNTs) and graphene nanosheets (GN) are truly the most important ones. Saito *et al.* [3] defined carbon nanotube as a honeycomb lattice rolled into a cylinder. As discussed by Carley *et al.* [4], carbon nanotubes have been the center of many researches due to their dimensions and remarkable electro-mechanical properties. In general, a CNT diameter has a nanometer size and its length can be more than 1 μm. Its large aspect ratio (length/diameter) is appointed as one of the reasons for the CNTs notable properties. Kalamkarov *et al.* [5] were able to model singlewalled nanotubes (SWNTs) and predict specific strength around 600 times larger than steel. It is worth to mention that SWNT's density is approximately 1/8 of steel. CNT capabilities have been observed experimentally and verified by numerical analysis. Frankland *et al.* [6], Jin and Yuan [7] and Agrawal *et al.* [8] are among those researchers who employed molecular dynamics for analyzing CNTs. The atomistic simulation approach was employed by Belytschko *et al.* [9], Lurie *et al.* [10], Gates *et al.* [11], while the nano-mechanics modeling was described by Liu *et al.* [12], Ruoff and Pugno [13], Li and Chou [14], Ávila *et al.* [15]. The basic difference between the two groups of

*Corresponding author. E-mail: avila@demec.ufmg.br; W: +1-530-754-8938


doi:10.12783/issn. 2168-4286/2.4/Avila

modeling is the approach employed. The molecular mechanics ones are based on finite element simulations where beam elements replaced the covalent bonds while Van der Waals bonds were represented by spring elements. The atomistic modeling employed chemical potentials, e.g. the Moore's one, to describe the carbon-carbon bonds. Although CNTs have tremendous potential in a large variety of applications, e.g. aerospace and medical industries, there is no consensus about their exact mechanical properties. The experiments performed up to now have presented large variability due to the inherent complexity of manipulating these materials. However, their potential is unquestionable, in special for composites.

The recent developments on CNT synthesis led to dramatically decreased into its cost. As a consequence, the number of researchers using carbon based nanostructures increased, and the results on nano-reinforcement of composites laminates are encouraging. Among those researchers are Kim *et al.* [16] whom described no significant increase on tensile properties of the addition of CNTs to carbon fibers/epoxy laminates. Nonetheless, they noticed an enhancement on flexural modulus (≈12%) and strength (≈18%) with the addition of 0.3 wt. % of CNT to the epoxy system. These properties enhancement can be attributed to changes into flexural failure mechanisms. Following the same idea, Chou *et al.* [17] discussed the influence of CNTs into the failure of laminates composites. They even proposed the concept of a multi-phase inter-laminar architecture that can bridge inter-laminar cracks. Wicks *et al.* [18] actually produced the multi-phase nano reinforced laminated composites proposed by Chou *et al.* [17]. In Wicks' laminate, CNTs were grown in situ in all fibers leading to a "fuzzy" fibers configuration. As mentioned by Wicks, aligned CNTs bridges the plies interfaces, which can lead to an increase on toughness, for the steady state condition, 76% higher than the conventional laminated systems. Notice that for the interlayer nano reinforcement some issues must be considered, i.e. the interfacial bonds between carbon nanotubes, fiber/matrix system and the length effect into this "grip condition". To understand the failure mechanism, Shokrieh and Rafiee [19] modeled the CNT length effect on reinforcement effectiveness. Moreover, they concluded that for carbon nanotubes with length less than 100 nm, the improvement on stiffness for CNT/polymeric systems is negligible. Experimental data provided by Ma *et al.* [20] demonstrated the limitations of using CNTs with aspect ratio smaller than 100 into polymeric systems. The "fuzzy" fibers configuration developed by Wicks *et al.* [18] is also limited as all plies have to be loaded with carbon nanotubes. This increase on "fiber density" due to the "CNTs loads" can lead to manufacturing limitations, e.g. a severe decrease on resin flow channels into vacuum assisted impregnation. It is clear that alternative techniques must be developed.

The CNT dispersion into composite materials has being attempted using different techniques, e.g. sonication, high shear mixing, etc. . The CNT infusion into laminated composites and its alignment by applying an electric field after the infusion was studied by Domingues *et al.* [21]. The major criticism on Domingues' work is the amount of CNT dispersed which is around 0.1 wt.%. Another approach tried to link CNTs to laminated composites was implemented by Yan *et al.* [22]. Wu's work was based on electrochemical grafting of CNTs on carbon fibers surface. Although the technique described by Wu *et al.* [22] seems to be effective, it is limited to the CNT concentration into the solution.

Moreover, as noticed by Wu, there were "preferential regions" for CNTs direct attachment to carbon fibers. These preferred sites were fibers' grooves and edges. This phenomenon led to a non-uniform distribution of CNT on carbon fibers surface. Another technique used to attaching CNTs to carbon fibers was studied by De Riccardis *et al.* [23] and Vilatela *et al.* [24]. In their case, the chemical vapor deposition (CVD) technique was employed for directly grown CNTs into carbon fibers. De Riccardis' work was based on deposition of nickel clusters and later on the CNTs were grown by hot filament chemical vapor deposition (HFCVD) technique. By using ferrocene as precursor, and CVD as the growing process, Vilatela was also able to obtain good quality CNTs. Moreover, the CVD technique employed by Vilatela *et al.* [24] seems to be much simpler and easier to control. Although the results presented by De Riccardis *et al.* [23] and Vilatela *et al.* [24] seem to be encouraging, much work has to be done for applications to laminated composites, in special high performance carbon fiber/epoxy systems. It is clear that CNTs can be used as potential reinforcement for nanocomposites and/or multi-scale composites, but recently graphene nanosheets are emerging as another option to CNTs.

Another class of carbon based materials was described by Gein and Novoselov [25], i.e. graphene nanosheets. They defined graphene as a single layer of carbon atoms tightly packed into a two-dimensional (2D) honeycomb lattice. This carbon atom monolayer array is the building block for graphitic materials. Furthermore, Lee *et al.* [26] mentioned that graphene effective elastic modulus follows a normal distribution with a peak close to 1.0 TPa, which is equivalent to the SWNT. This high stiffness and elevated strength (Zhang *et al.* [27] reported a 130 GPa value), can be attributed to two factors, i.e. the elevated specific surface area (≈ 2600 $m^2/g$) and the strong carbon-carbon covalent bonds. Odegard *et al.* [28] investigated these properties using molecular dynamics simulations and based on his results, it was possible to postulate that they are valuable options for improving mechanical properties of composites laminates. Furthermore, these reinforcements at micro/nano scale can be used for creating a new class of composite materials, i.e. multi-scaled composites (MSC). The MSC are multi-phase reinforced composites, i.e. in addition to traditional reinforcement carbon

fibers; the matrix is replaced by nanocomposites. As commented by Joshi and Dikshirt [29], nanocomposites can be obtained by dispersing nanoparticles/nanostructures into the polymeric matrix. The dispersion process can create inside the polymeric matrix three different nanostructures, i.e. intercalated, exfoliated and mixed. As discussed by Gouda *et al.* [30], the exfoliated nanostructured are the ones with best mechanical performance due to the largest surface area. Furthermore, Ávila *et al.* [31] pointed out that carbon based nano-structures, i.e. carbon nanotubes and graphene nanosheets (GN) can be combined to traditional composites for a multi-scale reinforcement.

One of the pioneers on graphite platelets and graphene research is Yasmin *et al.* [32], they stated that graphene based nanocomposites can be an alternative option for engineering applications due to their outstanding specific strength and stiffness. However, the different routes to obtain graphene nanosheets and their dispersion processes can lead to large variety of mechanical properties. The first route for obtaining graphene nanosheets (GN) was based on mechanical cleavage. Nevertheless, as discussed by Balandin *et al.* [33], this technique is time consuming and a series of defects can be introduced during this process. An alternative to mechanical cleavage is the chemical route. A large variety of chemical routes is also combined with thermal effects, e.g. thermal shock. The work developed by Stankovich *et al.* [34] is one example. They pointed out that a common route for graphite platelets, which can be used as graphene nanosheets precursor, is based on graphite expansion. The expanded graphite is produced from graphite intercalation compounds thru intercalant rapid evaporation at elevated temperature. Once the expanded graphite is obtained, techniques as ultrasonication and/or ball milling can be used to obtain graphite nanoplatelets and later on graphene nanosheets. These graphite nanoplatelets consist of hundreds of stacked graphene layers. Few layers of graphene can be obtained by dispersing the graphite nanoplatelets into an aqueous solution using ultra sonication followed by ultracentrifugation. To overcame this extra procedure, Ruoff's research group [34] proposed the use of graphite oxide (GO) instead of expanded graphite (EG). As observed by Allen *et al.* [35], the advantages of GO method are the low-cost and massive scalability. However, the major criticism to GO method is the use of hydrazine for GO's chemical reduction. Cooper *et al.* [36] pointed out the hydrazine high toxicity and the environmental concerns about its use. As noted by Stankovich *et al.* [34], the chemical reduction has the objective of restoration of graphitic network of $sp^2$ bonds and consequently increases on electrical conductivity. However, coagulation can occur during the reduction of exfoliated graphene oxide nanoplatelets, which makes virtually impossible to disperse these nanostructures within polymeric matrices. Another problem was detected by Dreyer *et al.* [37]. According to them, the degree of oxidation caused by differences in starting graphite sources or oxidation protocol can cause substantial variations in the GO structure and properties. This was the case of the work reported by Marcano *et al.* [38]. By introducing a modification on Hummer's method, i.e. they used a mix of $H_2SO_4/H_3PO_4$ at ratio of 9:1 and by excluding the $NaNO_3$, they were able to obtain a larger amount of GO. However, the use of hydrazine for GO reduction was present. Again, this harmful chemical component was employed, which is the major criticism of their work. A possible solution for hydrazine use was proposed by Shahil and Balandin [39]. They proposed a methodology based on natural graphite ultra-sonication on an aqueous solution of sodium chlorate followed by centrifugation and mechanical exfoliation by ultra-sonication and high shear mixing. This methodology can lead to multilayer graphene (MLG) consisting of 1–10 stacked atomic monolayers. However, this procedure does not guarantee the homogeneity required for engineering applications. Moreover, it is possible source of voids due to air bubbles entrapment during the mixing/cure procedure. A possible solution for this problem was proposed by Ávila *et al.* [31]. They employed N, N Dimethylformamide (DMF) as a solvent. No aqueous solution of sodium chlorate was used. Ultra sonication (20 KHz for 2 hours) followed by a high shear mixing at 17400 RPM (2 hours) lead to MLG with the number of graphene monolayers stacked between 2–50. After the DMF evaporation, the nanocomposite consolidation was made by dispersing the MLGs into the epoxy resin again using the high shear mix procedure under restrict temperature control (< 50°C). Another dispersion procedure was employed by Yang *et al.* [40]. Yang's work, however, took the advantage of the hydrophilic condition of GO nanoplatelets after oxidation. Therefore, they first dispersed the GO nanoplatelets into an aqueous (they employed a 1mg/mL concentration) solution using ultra sonication and later on the resulting solution was added to the polyvinyl alcohol (PVA) solution. This procedure can only be employed due to the special nature of such nanocomposite (both PVA and GO are hydrophilic). Their mechanical results indicated an increase on tensile strength around 30% with addition of 3.5% graphene. This increase on tensile strength could be related to the decrease on crystallinity reported by Yang and co-workers [40]. It is a well-known fact that high degree of crystallinity makes polymer brittle and stiffer. By observing fracture surfaces, Yang *et al.* [40] noticed layered-structures with uniformly dispersed graphene nanosheets into PVA matrix. Moreover, the graphene dispersion into PVA matrix leads to a change into the overall macroscopic behavior from brittle to ductile. This phenomenon can be related to the decrease on crystallinity. A much higher increase on tensile strength was reported by Kuilla *et al.* [41], where the addition of 0.7% by weight of GO lead to an improvement on tensile strength closes to 150%. This substantial increase seems to be related to crystallinity changes, and the solution blending technique employed. According to Wang *et al.*

[42], an "extra" exfoliation is provided by this technique due to GO's swelling. Young *et al.* [43], however, provided another explanation for such increase. They recalled that GO's individual nanoplatelets are often wrinkled, which provides an additional superficial area. Rafiee *et al.* [44] went further, as they were able to link this "extra" superficial area effect into matrix toughening (in their case epoxy). It is important to point out that superficial area is not the only issue that must be considered. The total number of layers (which can be translated into total thickness), separation of graphene layers and shape are also important, as they can influence the matrix toughness by controlling the crack propagation. Moreover, as discussed by Mukhopadhyay and Gupta [45], the surface energy is also another issue, as high surface energy help to improve dispersion into polymeric matrices. Unfortunately, a much easier dispersion provided by high surface energy also leads to a decrease on conductivity. This trade-off is the key issue for polymeric matrix/graphene nanocomposites. All these techniques have a problem in common, i.e. the cluster formation.

To avoid the graphene/CNT cluster/agglomerates Tkalya *et al.* [46] suggested the usage of surfactants. According to them, during the dispersion process by sonication (by bath or horn) carbon based nanostructures are exfoliated into individual nanostructure. This debundle/exfoliation process is due to the mechanical energy provided by sonication which overcomes the Van der Waals interactions between CNTs bundles or graphene platelets. If this energy is removed, the individual nanostructures have the tendency to agglomerate. The usage of surfactants during the sonication promotes the surfactant molecules adsorption onto individual exfoliated nanostructures and consequently avoiding agglomeration. The idea of using surfactants into aqueous solution to disperse carbon based nanostructures and later on incorporate the exfoliated nanostructures into polymeric solution was proposed by Pu *et al.* [47]. The called the attention that pristine graphene is naturally hydrophobic, therefore, producing a stable suspension (graphene in water or organic solvent) is a critical issue during the nanocomposite synthesis. Both Tkalya *et al.* [46] and Pu *et al.* [47] investigated the usage of surfactants as carbon based nanostructures (graphene or CNTs) dispersion "facilitator". As discussed by them, from the large number of surfactants two can be considered the most promising, i.e. nonylphenylether (CO890) and Sodium dodecylbenzenesulfonate (SDBS). According to Mital [48], the usage of surfactants not only create a stable solution (graphene in water or organic solvent) but it is also allows the network formation inside the polymer matrix. This percolation process can lead to multifunctional composites, which includes electrical conductivity.

This paper focuses on investigation of surfactant effects on carbon/epoxy composites nano-modified by graphene and carbon nanotubes. The key parameters evaluated are mechanical properties under tension and bending as function of surfactant employed and carbon based nanostructures.

## 2. EXPERIMENTAL PROCEDURES

This research final goal is to understand how the surfactants changes the dispersion process of carbon nanotubes and/or graphene into epoxy systems and its effect on the overall carbon/epoxy composite materials behavior. To achieve such goal, a series of hybrid composite materials was manufactured and tested under tensile and bending loadings. The nanostructures formed were composed of multi-layered graphene and/or multiwall carbon nanotubes (MWNT). The MWNT were grown by CVD as described by Lacerda *et al.* [49], while the multi-layered graphene were produced from expandable graphite using the technique developed by Avila *et al.* [50]. As discussed by Avila *et al.* [51], the optimum concentration for MWNT dispersion into epoxy system seems to be around 0.3 wt. %. Silva Neto *et al.* [52] argues that multi-layered graphene (MLG) dispersion into epoxy systems has a saturation limit close to 2 wt.%. Therefore, the amount of MLG employed in this research will be up to 0.3 wt.%, the same quantity of carbon nanotubes.

Based on Tkalya *et al.* [46] and Pu *et al.* [47] results, two surfactants were selected, i.e. nonylphenylether (CO890) and Sodium dodecylbenzenesulfonate (SDBS). The graphene aqueous solutions were prepared at 200 ppm and 300 ppm for SDBS and CO890, respectively. According to Tkalya *et al.* [46], these are the optimum concentrations. A bath sonication system at 42 KHz was employed for at least 30 minutes. After the graphene was completely dispersed, the aqueous solution was dried in a vacuum oven for 24 hours. The dried powder was later on dispersed into the epoxy system following the process described in Ávila *et al.* [53], i.e. horn sonication at 20 KHz for 60 minutes followed by high shear mixing at 17400 RPM for 60 minutes. During the dispersion process, the temperature was kept constant (≈ 36°C) by iced water. The laminate is a four layer symmetric and balanced composite, where the fibers are plain weave carbon woven fabric with 200 g/m$^2$ areal density supplied by Texglass Inc. The resin is a DBGA epoxy system AR300/AH30-150 provided by Barracudatec Inc. with a gel time of 30 minutes and average viscosity (resin+hardner) of 1000 cps. The laminate consolidation after a hand lay-up was cure on air for 24 hours followed by a post-cure, i.e. a uniform pressure of 1.0 atm at 80°C for 6 hours. Nine plates, with fiber/resin weight fraction of approximately 50/50, were prepared and its configurations were listed on Table 1. From each plate, twelve samples, i.e. six for tensile and six for three point bending tests, were cut using diamond saw.

The code system can be described as follows: 15G-SDBS-00N stands for 0.15 wt.% of multi-layer graphene dispersed with SDBS surfactant and mixed into a pure epoxy system (0.0 wt.% of multi-walled carbon nanotubes). The 30G-CO890-30N represents a 0.30 wt.% of MLG dispersed

*Table 1. Testing Groups Characteristics.*

| Group ID | MWNT [wt. %] | MLG [wt. %] | CO890 [ppm] | SDBS [ppm] |
|---|---|---|---|---|
| Baseline | 0.0 | 0.0 | 0.0 | 0.0 |
| 15G-SDBS-00N | 0.0 | 0.15 | 0.0 | 200 |
| 30G-SDBS-00N | 0.0 | 0.30 | 0.0 | 200 |
| 15G-SDBS-30N | 0.3 | 0.15 | 0.0 | 200 |
| 30G-SDBS-30N | 0.3 | 0.30 | 0.0 | 200 |
| 15G-CO890-00N | 0.0 | 0.15 | 300 | 0.0 |
| 30G-CO890-00N | 0.0 | 0.30 | 300 | 0.0 |
| 15G-CO890-30N | 0.3 | 0.15 | 300 | 0.0 |
| 30G-CO890-30N | 0.3 | 0.30 | 300 | 0.0 |

with CO890 and mixed into a epoxy system where 0.30 wt% of MWNT was previously dispersed using sonication.

The morphological investigation was performed using a FEG Quanta 200 FEI scanning electron microscopy (SEM) and a Tecnai G2-12 transmission electron microscopy (TEM), while the overall macroscopic behavior was evaluated tensile and short-beam three point bending tests. The tensile test follows the ASTM D3039 standard [54], while the short-beam bending tests followed the ASTM D 790 standard [55]. The three point bending tests were performed using an aspect ratio L/d (support spam/specimen depth) of 16:1, close to the ASTM recommendation for high performance composites. As described by the ASTM D 3039 an electronic extensometer was used to obtain the Young's modulus. However, to avoid damage to the extensometer the tests were paused at 50% of the failure and the extensometer was removed and the test was reinitiated. The same procedure was adopted to the tensile tests based on ASTM D638 standard [56]. Furthermore, an LVDF (linear variable differential transformer) was employed to obtain mid-span displacement for the ASTM D790 tests. Finally, an atomic force microscopy (Asylum MFP-3ASA) was employed to observe the carbon based nanostructures dispersion inside the polymeric system.

## 3. EXPERIMENTAL DATA AND ANALYSIS

A morphological analysis on carbon nanotube and graphene interaction is observed in Figure 1. It shows the CNT somehow "entered" the MLG layers. These interlocking structures can provide the extra grip for increasing strength. The same hybrid nanostructure (CNTs+MLG) was observed in Figures 1(c)–(d). Notice that multi-layered graphene spotted varied from 8–12 layers. The darker spot in Figure 1(a), which indicates a much larger number of layers has an aspect ratio (length/width) of 2 while the lighter areas present aspect ratio from 6 to 12. All of this indicates the presence of Van der Waals forces, which is the possible interaction force between CNTs and MLG. According to Zhu *et al.* [1] carbon nanotubes and graphene share similar surface feature and many properties are common. The hypothesis of Van der Waals bonds is based on these carbon based nanostructures (graphene and carbon nanotubes) are not functionalized, i.e. used as growth. However, the presence of some "free chemical bonds" cannot be discarded but is unlike to occur. The presence of surfactant can also be an important factor. Tkalya *et al.* [46] discussed the "wrapping" mechanism as possible explanation for this complex interaction. The TEM observation on Figure 1(b) seems to be this case where layers of graphene surrounded carbon nanotubes. An overall micrograph of this three dimensional nanostructure is shown in Figure 1(c). As commented before, it is clear the evidence of different layers of graphene surrounding/wrapping nanotubes. But, when a much higher magnification is placed in one of the edges, an interesting phenomenon seems to be spotted. In Figure 1(d), like a needle a sharp edge of a multi-layer graphene seems to penetrate a carbon nanotube wall. It seems an evidence of interactions between the two types of carbon based nanostructures and the polymeric matrix around them. The same idea was proposed by O'Connell *et al.* [57] when considering the carbon nanotube and the polymeric matrix.

Although the morphological analysis via TEM seems to indicate an interaction between the two nanostructures, the surfactants and the epoxy resin. The resulting nanostructure can act as barriers during crack formation/propagation when the composite is under loading. The AFM representation on Figure 2(a) can give an estimation of the 3D nanostructures formed. For example, for the CO890 surfactant and the graphene (0.15 wt.%) and carbon nanotube (0.30 wt.%), this 3D nanostructure has a height peak of 205 nm [Figures 3(a)–(b)], which is equivalent of 600 atomic layers of carbon. This value seems not to be compatible with the two original carbon based nanostructures (multi-layer graphene and multiwall carbon nanotubes) employed. Therefore, the only reason for such height is the surfactant interaction. A more detailed analysis of such 3D nanostructure must be performed.

A complete analysis, however, must include a mechanical testing of such composite material. By performing mechanical tests, it will be possible to correlate the composite overall mechanical behavior and the nanostructures formed inside the epoxy system and its interactions with the carbon fibers.

The first set of mechanical experiments is based on three point bending tests. By observing the mechanical behavior under bending and its failure mode, it is possible to understand how the carbon based nanostructures associated to different surfactants affect stiffness and strength. Figure 4(a) shows the flexural elastic moduli, while the bending strength is represented by Figure 4(b). The surfactant usage seems to improve both stiffness and strength, when compared against the blank samples (carbon fiber/epoxy with surfactant or carbon based nanostructures). Considering the surfactant effect, the SDBS dispersion into the epoxy system lead to an aver-

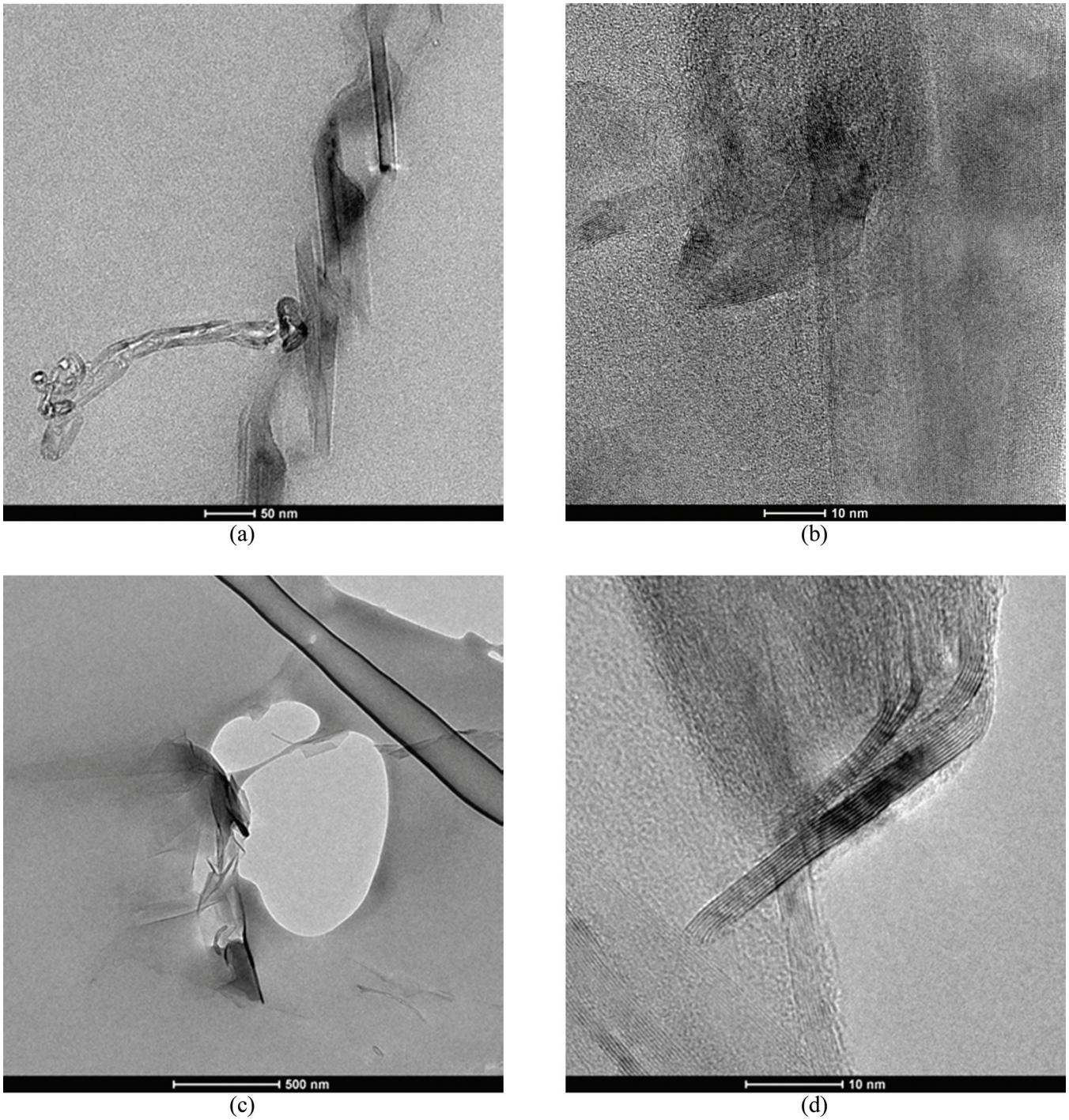


***Figure 1.*** *TEM observations of MWNT-MLG interactions.*

age increase on stiffness close to 90.69%, while the strength improvement was around 55.66%. The average mechanical properties enhancement with the addition of CO890, the second surfactant, was 92.69% and 58.13%, for stiffness and strength respectively. These improvements can be attributed to failure mode changes as shown in Figure 5. Another important issue is the interaction between graphene and carbon nanotubes. As it can be observed in Figure 6, the stress-strain curves, the addition of carbon nanotubes in presence of surfactant, either SDBS or CO890, improved both mechanical properties, i.e. stiffness and strength. This is an indication of interactions between graphene and carbon nanotubes as shown in Figures 1(a)–(d). The wrapping hypothesis can explain, at least at nanoscale, the mechanical behavior.

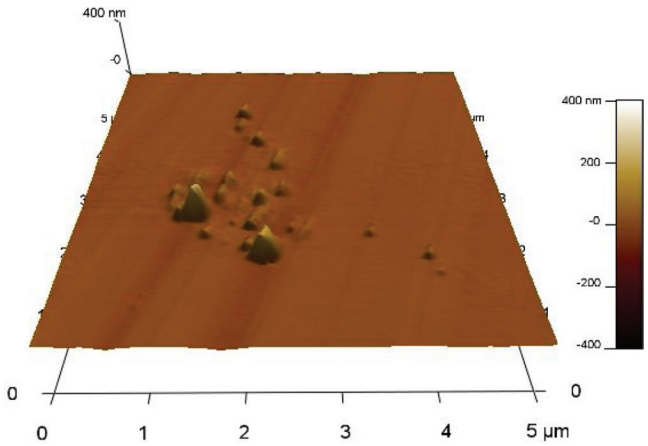


***Figure 2.*** *AFM 3 D representation of graphene, nanotube and surfactant interaction.*

Notice that such 3D nanostructures, the ones enfolded, seems to act as barriers for crack propagation, which leads to a much higher energy release. As it can observed from the previous figures, the addition of surfactant (SDBS and CO890) and graphene could be the reason for mechanical properties enhancement (stiffness ≈ 59.78%, strength ≈ 39.57%, for SDBS and stiffness ≈ 63.82%, strength ≈ 46.38%, for CO890), the additional improvement seems to be provided by the carbon nanotubes and its interaction with the graphene. From Figure 6, another hypothesis can be formulated. The CO890 surfactant appears to be more efficient regardless the carbon nanostructure. Notice that Figure 6 is composed by curves/data from the tests, which can be considered representative of the samples overall behavior. These curves are experimental data adjoining to the average overall samples behavior for each set studied.

The next step is the tensile properties evaluation. Figures 7(a)–(b) describe the stiffness and strength variation based on surfactant type and carbon nanostructure. As it can be noticed, the usage of surfactants as a carbon based nanostructure dispersant "facilitator" seems to be effective. The SDBS surfactant/graphene addition leads to an average increase on tensile elastic moduli close to 8.84%. However, if the CNT contribution is also considered, the SDBS+graphene+CNT addition promoted a stiffness improvement close to 55.26%. A similar trend was observed when the CO890 effect is analyzed. The stiffness increase for the CO890 addition without CNT was around 69.06%. However, the addition of CNT led to a much smaller increase on stiffness, i.e. ≈10.85%. It was expected, like in bending, the addition of CNTs should lead to a much higher increase on stiffness. One possible explanation for such behavior could be problems during the tensile tests, i.e. tab delamination. When the tensile strength is analyzed, the following trend can be identified. An average increase on tensile strength with addition of SDBS/graphene

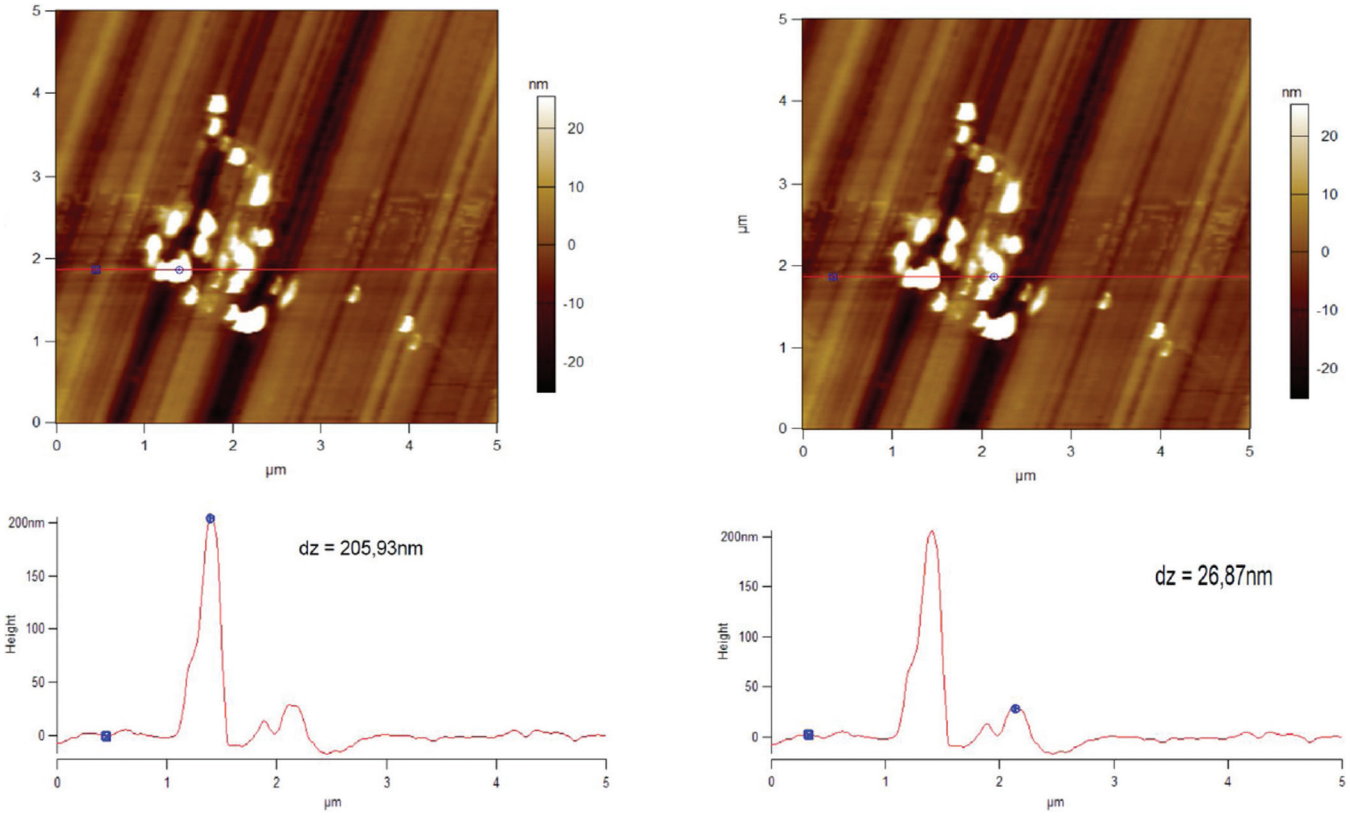


***Figure 3.*** *AFM measurements of nanostructures formed.*

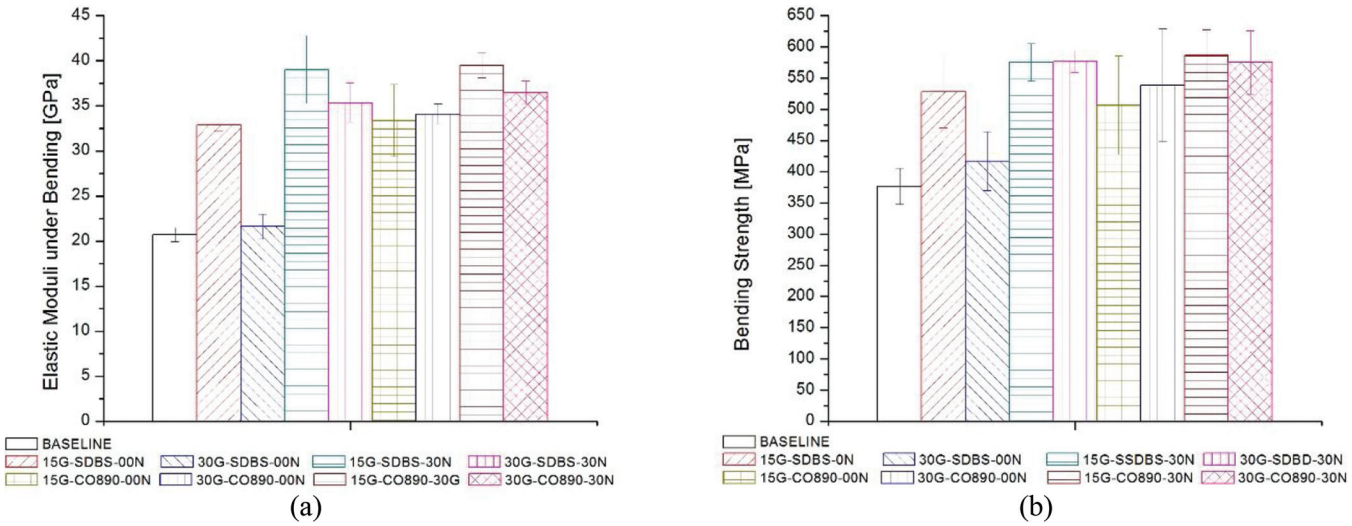


***Figure 4.*** *Three point Bending results. (a) Elastic moduli; (b) Flexural strength.*

was close to 7.66% and, and an increase nearly 27.97% was notice for the CO890/graphene composition. When the addition of CNT is considered on the top of SDBS/graphene and CO890/graphene, the increase was close to 27.02% and 22.98%, respectively. Notice that in both cases (SDBS and CO890 surfactants) the largest increase was observed for the 0.15 wt.% graphene addition. Figure 8 shows the stress-strain curves where two distinct groups can be identified. Changes on epoxy matrix behavior from brittle to ductile can be the reason for such good behavior. A typical ductile epoxy/carbon fiber fracture is represented in Figure 9. To have a complete analysis of the these hybrid laminates, the toughness is calculated for each group. The addition of carbon based nanostructures lead to an increase on toughness in all cases. The range on toughness improvement was between 39.59% (15G-CO890-00N) and 180.65% (30G-SDBS-00N), for more details see Figure 10.

To be able to verify the brittle-ductile transition a series of tensile tests based on ASTM D 638 were performed. The stiffness and strength variations based on those results were shown in Figure 11.

A complete analysis of the mode failure transition will not be complete without the stress-strain curve. Figure 12 shows the representative curves for the tensile tests of the dogbone shape specimens. By analyzing Figures 11 and 12 some conclusions can be drawn. First, a decrease on stiffness was also followed by an increase on displacement. Second, this increase on displacement at failure can be described as a transition from fragile to ductile failure behavior. The group

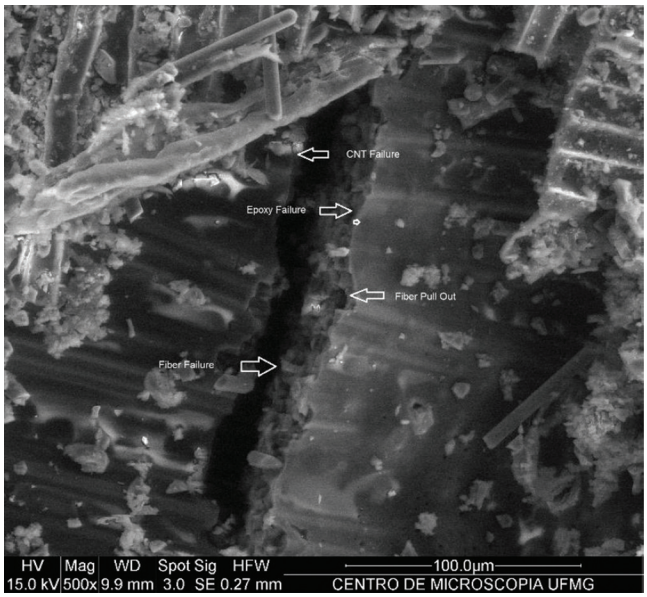


***Figure 5.*** *SEM observation of a fracture on bending with the presence of surfactant.*

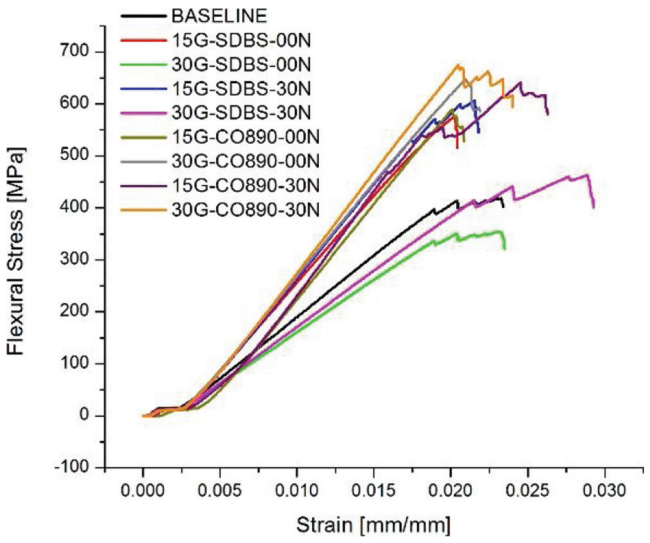


***Figure 5.*** *Stress-Strain curves under bending loads.*

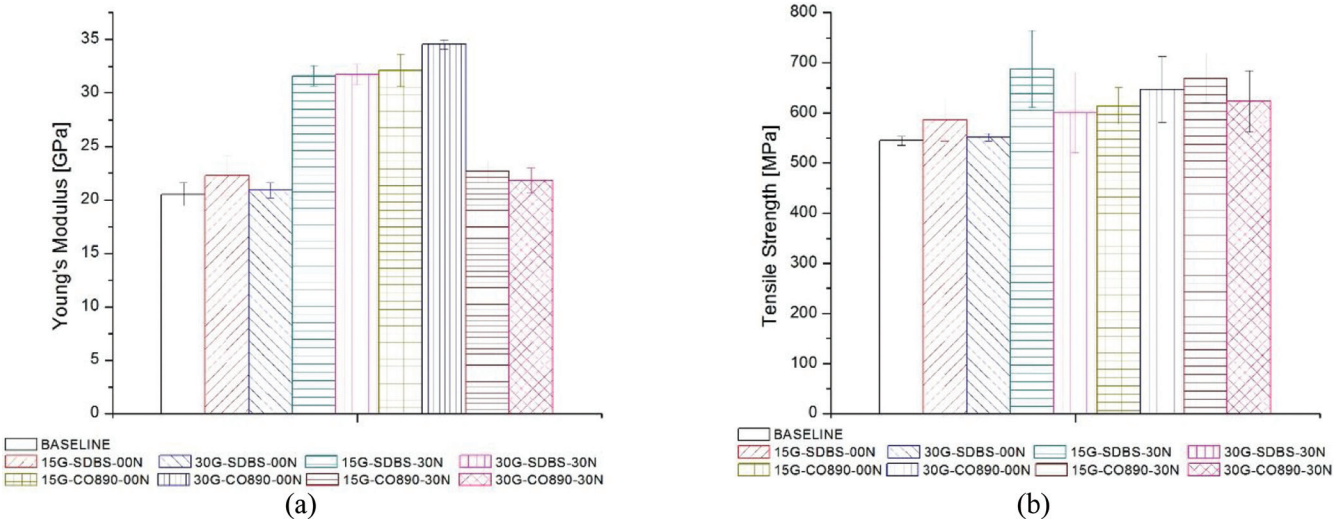


***Figure 7.*** *Tensile test results. (a) Stiffness; (b) Strength.*

made of 0.30 wt.% graphene with SDBS and no carbon nanotube (30G-SDBS-00N) is a representative set of this brittle-ductile transition. Noticie that in this case, a decrease on stiffness was followed by an increase of displacement at failure. Figure 13 shows two micrographs, the first one of the baseline sample and the second one is the 30G-SDBS-00N sample. As it can be notice, in the second case the fracture is ductile, as the necking formation is unmistakable observed.

## 4. CONCLUSION

Two different carbon based nanostructures, multiwall carbon nanotubes and multi-layered graphene, were incorporated to carbon epoxy laminated. X-ray diffractometry indicates an average particle size of 22 nm for the multilayer graphene (MLG) nanostructures. TEM observations revealed a thickness of 10 graphene layers, and a hybrid nanostructure where MWNT interpenetrated the MLG nanostructure. To be able to disperse more efficiently the carbon based nanostructures two different surfactants were employed, i.e. Sodium dodecyl sulfate (SDBS) and Polyoxyethylene nonylphenyl ether (IGEPAL CO890). The dispersion of surfactants associated to graphene led to increase on stiffness and strength, for both tensile and bending loads. If on the top of these surfactants/graphene additions, CNTs are added, the improvement is even better. For tensile tests, the average peak stress increase from 542.76 MPa (blank specimen) to 667.51 MPa (CO 890 and graphene/CNT), while for bending the peak stress improved from 369.40 MPa (blank specimen) to 584.15 MPa (CO 890 and graphene/CNT) . The association of carbon based nanostructures (graphene

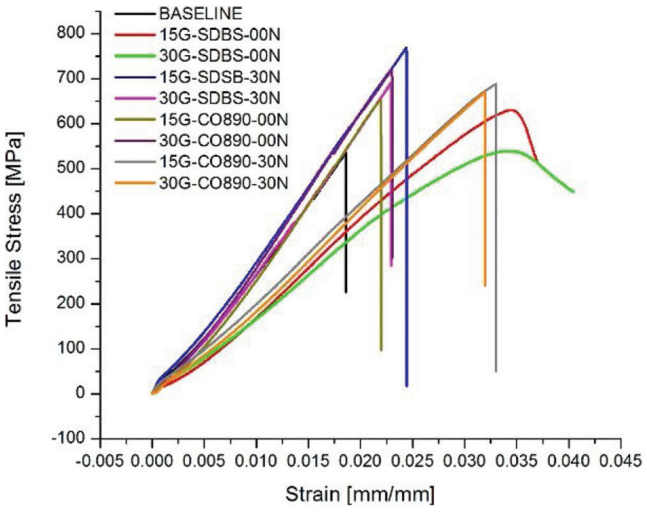


***Figure 8.*** *Stress-strain curves. Tensile tests.*

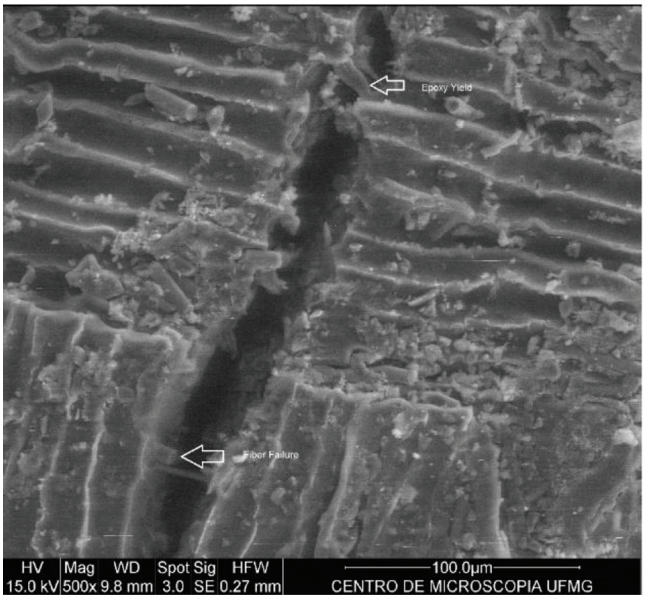


***Figure 9.*** *Ductile fracture micrograph.*

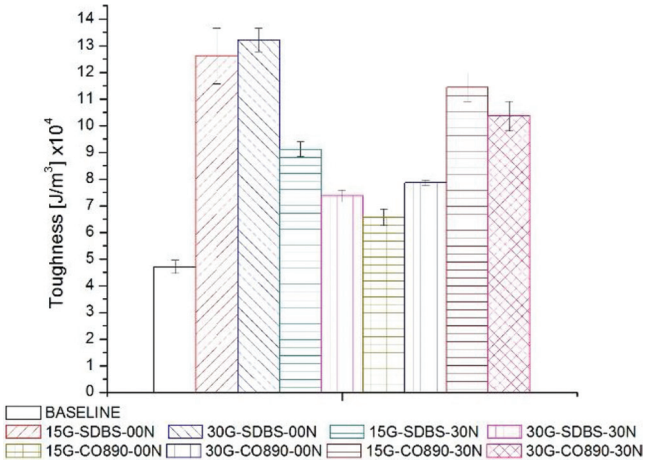


***Figure 10.*** *Toughness data for hybrid laminates.*

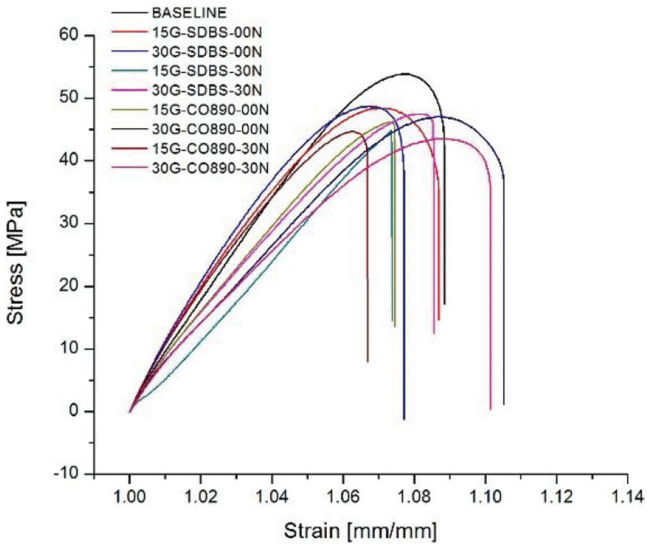


***Figure 12.*** *Dogbone shape specimens stress-strain curves.*

and CNT) associated to surfactants seems to be a promising route to improve carbon/epoxy composites. The average increase on flexure elastic moduli reach a peak of 92.62% while for tensile elastic moduli was up to 69.06%. In all cases, this increase can be attributed to two factors. The first one could be due to the formation of a wrapped 3D nanostructure (CNTs surrounded by graphene nanosheets), which can act as barriers to crack formation/propagation. This issue is critical in bending loads. For the tensile tests, the second factor is the change on epoxy behavior from brittle to ductile. In sum, the addition of carbon based nanostructures (CNTs and graphene) associated to surfactants could be a viable route to improve even more carbon/epoxy composites.

## 5. ACKNOWLEDGMENTS

This research was supported in part by the Brazilian Research Council (CNPq) under grants number 303447/2011-7, 472583/2011-5 and the Air Force Office of Scientific Research grant FA9550-14-1-0377. The authors are grateful to the UFMG's Center of Microscopy and Microanalysis for the technical support and the Nacional Grafite Incorporated for supplying the graphite from which the graphene blocks were obtained.

## 6. REFERENCES

[1] Zhu, J., Chen, M., He, Q., Shao, L., Wei, S., Guo, Z., "An overview of the engineered graphene nanostructures and nanocomposites", *Royal Society of Chemistry Advances*, Vol. 109, No. 3, 2013, pp. 22790–22824. http://dx.doi.org/10.1039/c3ra44621b

[2] Mauter, M.S. and Elimelech, M., "Environmental applications of carbon-based nanomaterials," *Environmental Science and Technology*, Vol. 42, No. 16, 2008, pp. 5843–5859. http://dx.doi.org/10.1021/es8006904

[3] Saito, R., Dresselhaus, G., and Dresselhaus, M.S., *Physical Proper-*

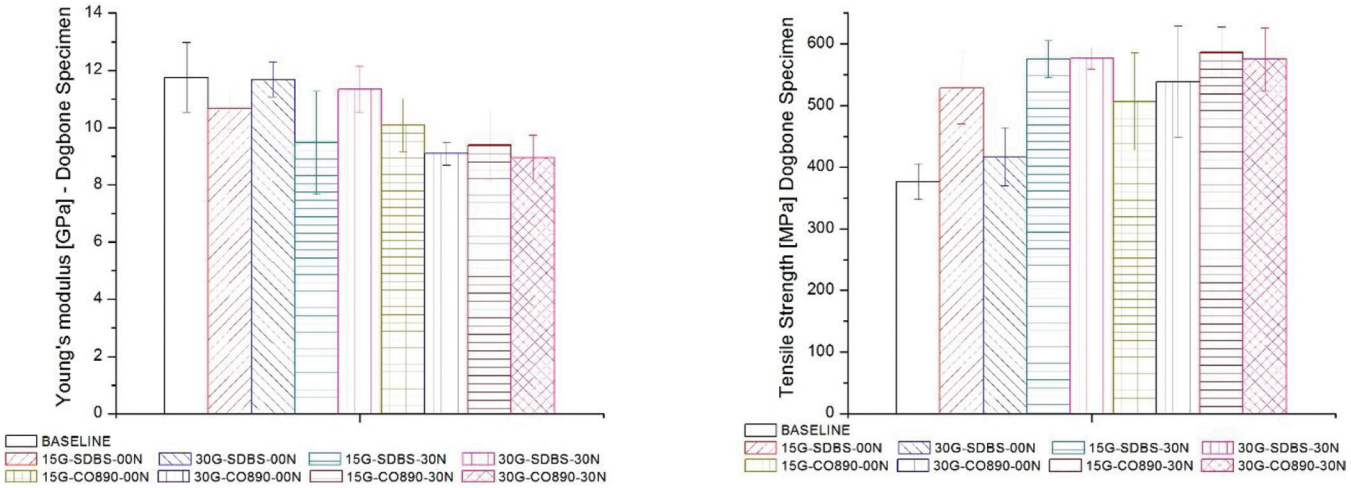


***Figure 11.*** *Dogbone specimens data. (a) stiffness; (b) strength.*

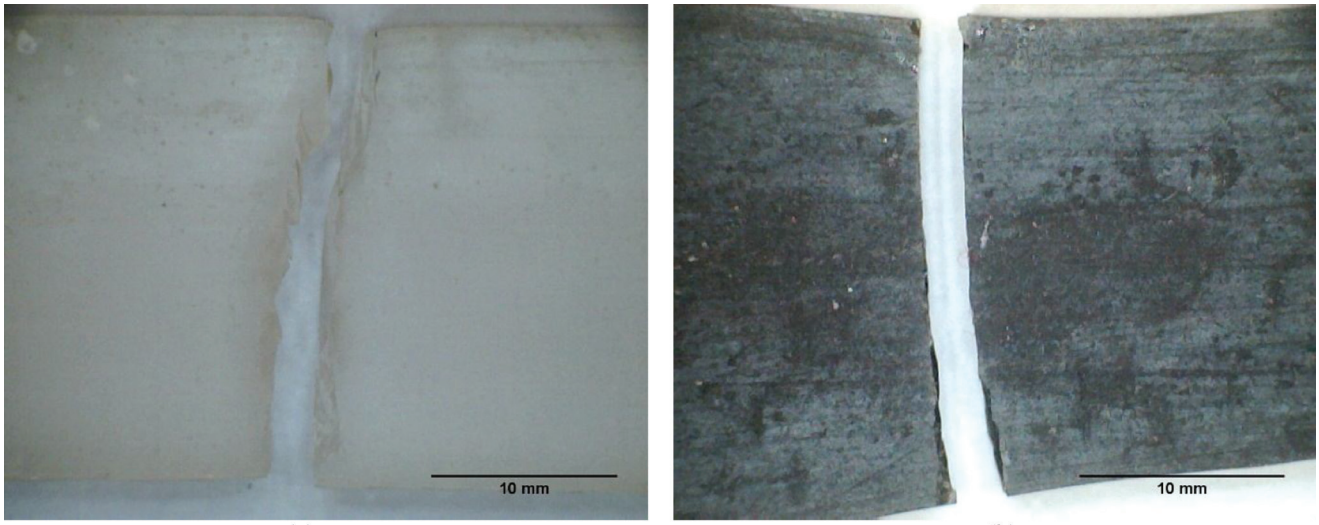


***Figure 13.*** *Dogbone specimen failure mode. (a) Baseline (Brittle); (b) 30G-SDBS-00N (ductile)*

*ties of Carbon Nanotubes*, Imperial College Press, London, UK, 2005, Chaps. 2–3.

[4] Carley, G., Moraes, V. G., Avila, A.F, Oliveira, S., "Nano-engineered composites: Interlayer carbon nanotubes effect", *Materials Research*, Vol. 16, No. 5, 2013, pp. 628–634. http://dx.doi.org/10.1590/S1516-14392013005000034

[5] Kalamkarov, A.L., Georgiades, A.V., Rokkam, S.K., Veedu, V.P., and Ghasemi Nejhad, M.N., "Analytical and numericaltechniques to predict carbon nanotubes properties," *International Journal of Solids and Structures*, Vol. 43, No. 22–23, 2006, pp. 6832–6854. http://dx.doi.org/10.1016/j.ijsolstr.2006.02.009

[6] Frankland, S.J.V., Harik, V.M., Odegard, G.M., Brenner, D.W., and Gates, T.S., "The stress–strain behavior of polymer–nanotube composites from molecular dynamics simulation," *Composites Science and Technology*, Vol. 63, No. 11, 2003, pp. 1655–1661. http://dx.doi.org/10.1016/S0266-3538(03)00059-9

[7] Jin, Y., and Yuan, F.G., "Simulation of elastic properties of single-walled carbon nanotubes," *Composites Science and Technology*, Vol. 63, No. 11, 2003, pp. 1507–1515. http://dx.doi.org/10.1016/S0266-3538(03)00074-5

[8] Agrawal, P.M., Sudalayandi, B.S., Raff, L.M., and Komanduri, R., "A comparison of different methods of Young's modulus determination for single-wall carbon nanotubes (SWCNT) using molecular dynamics simulations," Computational Materials Science, Vol. 38, No. 2, 2005, pp. 271–281. http://dx.doi.org/10.1016/j.commatsci.2006.02.011

[9] Belytschko, T., Xiao, S.P., Schats, G.C., and Ruoff, R.S., "Atomistic simulations of nanotube fracture," *Physics Review B*, Vol. 65, No. 4, 2002, pp. 2354301–2354308. http://dx.doi.org/10.1103/PhysRevB.65.2354030

[10] Lurie, S., Belov, P., Volkov-Bogorodsky, D., and Tuchkova, N., "Nanomechanical modeling of the nanostructures and dispersed composites," *Computational Materials Science*, Vol. 28, No. 4, 2003, pp. 529–539. http://dx.doi.org/10.1016/j.commatsci.2003.08.010

[11] Gates, T.S., Odegard, G.M., Frankland, S.J.V., and Clancy, T.C., "Computational materials: Multi-scale modeling and simulation of nanostructured materials," *Composites Science and Technology*, Vol. 65, No. 15–16, 2005, pp. 2416–2434. http://dx.doi.org/10.1016/j.compscitech.2005.06.009

[12] Liu, W.K., Karpov, E.G., Zhang, S., and Park, H.S. 2004. "An introduction to computational nanomechanics and materials," *Computational Methods in Applied Mechanics and Engineering*, Vol. 193, No. 17–20, 2004, pp. 1529–1578. http://dx.doi.org/10.1016/j.cma.2003.12.008

[13] Ruoff, R.S., and Pugno, N., Mechanics of Nanostructures in: T.S. Chuang *et al.* (Eds.) Nanomechanics of Materials and Structures, Springer, New York, 2006, pp. 199–203. http://dx.doi.org/10.1007/1-4020-3951-4_19

[14] Li, C., and Chou, T-W. 2003. "A structural mechanics approach for the analysis of carbon nanotubes," *International Journal of Solids and Structures*, Vol. 40, No. 10, 2003, pp. 2487–2499. http://dx.doi.org/10.1016/S0020-7683(03)00056-8

[15] Ávila, A.F., Eduardo, A.C., and Silva Neto, A., "Vibrational analysis of graphene based nanostructures," Computers and Structures, Vol. 89, No. 11–12, 2011, pp. 878–892. http://dx.doi.org/10.1016/j.compstruc.2011.02.017

[16] Kim, M., Park, Y-B., Okoli, O.I., and Zhang, C., "Processing, characterization, and modeling of carbon nanotubereinforced multi-scale composites," *Composites Science and Technology*, Vol. 69, No. 3–4:, 2009, pp. 335–342. http://dx.doi.org/10.1016/j.compscitech.2008.10.019

[17] Chou, T-W., Gao, L., Thostenson, E., Zhan, Z., and Byun, J-H., "An assessment of the science and technology of carbon nanotube-based fibers and composites," *Composites Science and Technology*, Vol. 70, No. 1, 2010, pp. 1–19. http://dx.doi.org/10.1016/j.compscitech.2009.10.004

[18] Wicks, S.S., Villanova, R.G., and Wardle, B.L. "Interlaminar and intralaminar reinforcement of composite laminates with aligned carbon nanotubes," *Composites Science and Technology*, Vol. 70, No. 1, 2010, pp. 20–28. http://dx.doi.org/10.1016/j.compscitech.2009.09.001

[19] Shokrieh, M.M., and Rafiee, R. "Investigation of nanotube length effect on the reinforcement efficiency in carbon nanotube based composites," *Composite Structures*, Vol. 92, No. 10, 2010, pp. 2415–2420. http://dx.doi.org/10.1016/j.compstruct.2010.02.018

[20] Ma, P-C., Siddiqui, N.A., Marom, G., and Kim, J.K. "Dispersion and functionalization of carbon nanotubes for polymer based nanocomposites: A review," *Composites Part A*, Vol. 41, No, 10, 2010, pp. 1345–1367. http://dx.doi.org/10.1016/j.compositesa.2010.07.003

[21] Domingues, D., Logakis, E., and Skordos, A.A. "The use of an electric field in the preparation of glass fiber/epoxy composites containing carbon nanotubes," *Carbon*, Vol. 50, No. 7, 2012, pp. 2493–2503. http://dx.doi.org/10.1016/j.carbon.2012.01.072

[22] Yan, L., Zhou, G., Ishaq, A., Zhou, X. "Improving the electrical conductivity of multi walled carbon nanotube networks by H ion beam irradiation," *Carbon*, Vol. 49, No. 6, 2011, pp. 2141–2144. http://dx.doi.org/10.1016/j.carbon.2010.12.067

[23] De Riccardis, M.F., Carbone, D., Makris, Th. D., Giorgi, R., Lisi, N.,

and Salernitano, E. "Anchorage of carbon nanotubes grown on carbon fibers," Carbon, Vol. 44, No. 4, 2006, pp. 671–674. http://dx.doi.org/10.1016/j.carbon.2005.09.024

[24] Vilatela, J.J., Deng, L., Kinloch, I.A., Young, R.J., and Windle, R.D. "Structure of and stress transfer in fibers spun from carbon nanotubes produced by chemical vapor deposition," *Carbon*, Vol. 49, No. 12, 2011, pp. 4149–4158. http://dx.doi.org/10.1016/j.carbon.2011.05.045

[25] Gein, A.K. and Novoselev, K.S. "The rise of graphene" *Nature Materials*, Vol. 6, No. 1, 2007, pp. 183–191.

[26] Lee, C., Wei, X., Kysar, J.W., and Hone, J. "Measurements of the elastic properties and intrinsic strength of monolayer graphene," *Science*, Vol. 321, No. 5887, 2008, pp. 385–388. http://dx.doi.org/10.1126/science.1157996

[27] Zhang, T., Xue, Q., Zhang, S., Dong. M., "Theoretical approaches to graphene and graphene-based materials", *Nano Today*, Vol. 7, No. 1, 2012, pp. 180–200. http://dx.doi.org/10.1016/j.nantod.2012.04.006

[28] Odegard, G.M., Gates, T.S., Wise, K.E., Park, C, and Siochi, E.J. "Constitutive modeling of nanotube-reinforced polymer composites," *Composites Science and Technology*, Vol. 63, No. 12, 2003, pp. 1671–1687. http://dx.doi.org/10.1016/S0266-3538(03)00063-0

[29] Joshi, S.C. and Dikshit, V. "Enhancing interlaminar fracture characteristics of woven CFRP prepreg composites through CNT dispersion", *Journal of Composite Materials*, Vol. 46, No. 8, 2012, pp. 665–675. http://dx.doi.org/10.1177/0021998311410472

[30] Gouda, P.S.S, Kulkarni, R., Kurbet, S.N., and Jawali, D. "Effects of multi walled carbon nanotubes and graphene on the mechanical properties of hybrid polymer composites," *Advanced Materials Letters*, Vol. 4, No. 4, 2013, pp. 261–270. http://dx.doi.org/10.5185/amlett.2012.9419

[31] Ávila, A.F., Yoshida, M.I., Carvalho, M.G.R., Dias, E.C., and Ávila Jr., J. "An investigation on post-fire behavior of hybrid nanocomposites under bending loads," *Composites Part B*, Vol.,41, No. 5, 2010, pp. 380–38. http://dx.doi.org/10.1016/j.compositesb.2010.02.002

[32] Yasmin, A., Luo J-J, and Daniel, I.M. "Processing of expanded graphite reinforced polymer nanocomposites," *Composites Science and Technology*, Vol. 66, No. 10, 2006, pp. 1182–1189. http://dx.doi.org/10.1016/j.compscitech.2005.10.014

[33] Balandin, A.A., Ghosh, S., Bao, W., Calizo, I., Teweldebrhan, D., Miao, F., and Lau, C.N. "Superior thermal conductivity of single-layer graphene," *Nano Letters*, Vol. 8, No. 3, 2008, pp. 902–907. http://dx.doi.org/10.1021/nl0731872

[34] Stankovich, S., Dikin, D.A., Piner R.D., Kohlhaas, K.A., Kleinhammes, A., Jia, Y., Wu, Y., Nguyen, S.T., and Ruoff, R.S. "Synthesis of graphene-based nanosheets via chemical reduction of exfoliated graphite oxide," *Carbon*, Vol. 45, No. 10, 2007, pp. 1558–1565. http://dx.doi.org/10.1016/j.carbon.2007.02.034

[35] Allen, M.J., Tung, V.C., and Kaner, R.B. "Honeycomb carbon: A review of graphene," *Chemical Review*, Vol. 110, No. 1, 2010, pp. 132–145. http://dx.doi.org/10.1021/cr900070d

[36] Cooper, D.R., D'Anjou, B., Ghattamaneni, N., Harack, B., Hilke, M., Horth, A., Majlis, N., Massicotte, M., Vandsburger, L., Whiteway, E., and Yu, V. "Experimental review of graphene," Condensed Matter Physics, Vol. 63, No. 1, 2012, pp. 1–56. http://dx.doi.org/10.5402/2012/501686

[37] Dreyer, D.R., Park, S., Bielawski, C.W., and Ruoff, R.S. "The chemistry of graphene oxide," *Chemistry Society Review*, Vol. 4, No. 8, 2010, pp. 228–240. http://dx.doi.org/10.1039/B917103G

[38] Marcano, D.C., Kosynkin, D.V., Berlin, J.M., Sinitskii, A., and Sun, Z. "Improved synthesis of graphene oxide," *ACS Nano*, Vol. 4, No. 8, 2010, pp. 4806–4814. http://dx.doi.org/10.1021/nn1006368

[39] Shahil, K.M.F., and Balandin, A.A. "Graphene-multilayer graphene nanocomposites as highly efficient thermal interface materials," *Nano Letters*, Vol. 12, No. 2, 2012, pp. 861–867. http://dx.doi.org/10.1021/nl203906r

[40] Yang, X., Li, L., Shang, S., and Tao, X-M. "Synthesis and characterization of layer-aligned poly(vinyl alcohol)/graphene nanocomposites," *Polymer*, Vol. 51, No. 15, 2010, pp. 3431–3435. http://dx.doi.org/10.1016/j.polymer.2010.05.034

[41] Kuilla, T., Bhadra, S., Yao, D., Kim, N.H., Bose, S., and Lee, J.H. "Recent advances in graphene based polymer composites," *Progress in Polymer Science*, Vol. 35, No. 12, 2010, pp. 1350–1375. http://dx.doi.org/10.1016/j.progpolymsci.2010.07.005

[42] Wang, M., Cheng, Y., and Lin, M. "Graphene nanocomposites," *Composites and Their Properties*, Vol. 3, No.1, 2012, pp. 17–36. http://dx.doi.org/10.5772/50840

[43] Young, R.J., Kinloch, I.A., Gong, L., and Novoselov, K.S. "The Mechanics of graphene nanocomposites: A review," *Composites Science and Technology*, Vol. 72, No. 12, 2012, pp. 1459–1476. http://dx.doi.org/10.1016/j.compscitech.2012.05.005

[44] Rafiee, M.A., Rafiee, J., Srivastava, I., Wang, Z., Song, H., Yu, Z-Z., and Koratkar, N. "Fracture and fatigue in graphene nanocomposites," *Small*, Vol. 6, No. 2, 2010, pp. 179–183. http://dx.doi.org/10.1002/smll.200901480

[45] Mukhopadhyay, P., and Gupta, R.K. "Trends and frontiers in graphene-based polymer nanocomposites," *Plastics Engineering*, Vol. 6, No.1, 2011, pp. 32–42.

[46] Tkalya, E., Ghislandi, M., de With, G., Koning, C.E., "The use of surfactants for dispersing carbon nanotubes and graphene to make conductive nanocomposites", Current Opinion in Colloid & Interface Science, Vol. 17. No. 1, 2012, pp. 225–232. http://dx.doi.org/10.1016/j.cocis.2012.03.001

[47] Pu, N-W, Wang, C-A, Liu, Y-M, Sung, Y, Wang, D-S, and Ger, M-D. "Dispersion of graphene in aqueous solutions with different types of surfactants and the production of graphene films by spray or drop coating", *Journal of the Taiwan Institute of Chemical Engineering*, Vol. 43, No. 1, 2012, pp. 140–146. http://dx.doi.org/10.1016/j.jtice.2011.06.012

[48] Mittal, V. "Functional polymer nanocomposites with graphene: A review", *Macromolecular Materials Engineering*, Vol. 299. No. 8, 2014, pp. 906–931. http://dx.doi.org/10.1002/mame.201300394

[49] Lacerda, R.G., Teo, K.B.K, The, A.S., Yang, M.H, Dalal, S.H., Jefferson, D.A., Durrell, J.H., Rupesingle, N.L., Roy, D.,Amaratunga, G.A.J., Milne, W.I., Wyczisk, F., Legagneux, P., and Chhowlla, M. "Thin-film metal catalyst for production of multi-wall and single-wall carbon nanotubes", *Journal of Applied Physics*, Vol. 96, No.8, 2004, pp. 4456–4462. http://dx.doi.org/10.1063/1.1794359

[50] Ávila, A.F., Peixoto, L.G. Z. de O., Silva Neto, A., de Ávila Jr., J., Carvalho, M.G.R. "Bending investigation on carbon fiber/epoxy composites nano-modified by graphene," *Journal of the Brazilian Society of Mechanical Science and Engineering*, Vol. 34, No. 3, 2012, pp. 269–275. http://dx.doi.org/10.1590/S1678-58782012000300007

[51] Ávila, A.F. Carley, G., Geraldo, V., Oliveira, S. "Multi-Phase Carbon Fiber-MWNT/Epoxy Composites", *International Journal of Composite Materials*, Vol. 3, No. 1–2, 2013, pp. 1–9. http://dx.doi.org/10.5923/x.cmaterials.2013.09.01

[52] Silva Neto, A., da Cruz, D.T.L., Ávila, A.F. "Nano-modified Adhesive by Graphene: The Single Lap-Joint Case," *Materials Research,* Vol.16, No. 3, 2013, pp. 592–596. http://dx.doi.org/10.1590/S1516-14392013005000022

[53] Ávila, A.F., Silva Neto, A., Nascimento Jr. H. "Hybrid nanocomposites for mid-range ballistic protection", *International Journal of Impact Engineering*, Vol. 38, No. 5m 2011, pp. 669–676. http://dx.doi.org/10.1016/j.ijimpeng.2011.03.002

[54] ASTM D 3039. "Standard Test Method for Tensile Properties of Polymer Matrix Composite Materials", *ASTM Standards*, Vol. 15, No. 3, 2011, pp. 1–13.

[55] ASTM D 2344. "Standard Test Method for Short-Beam Strength of Polymer Matrix Composite Materials and Their Laminates", *ASTM Standards*, Vol. 15, No. 3, 2010, pp. 1–8.

[56] ASTM D 638. "Standard Test Method for Tensile Properties of Plastics", *ASTM Standards*, Vol. 15, No. 3, 2014, pp. 1–17.

[57] O'Connell, M.J., Boul, P., Ericson, L.M., Huffman, C., Wang, Y.H., Haroz, E., Kuper, C., Tour, J., Ausman, K.D., and Smalley, R.E. "Reversible water-solubilization of single-walled carbon nanotubes by polymer wrapping," *Chemical Physics Letters*, Vol.342, No. 2–3, 2001, pp. 265–271. http://dx.doi.org/10.1016/S0009-2614(01)00490-0

*Journal of Multifunctional Composites*, 2 (2014) 207–215

Journal of Multifunctional Composites

journal homepage: http://jmc.destechpub.com

# Self-sensing of Matrix Damage using Mechanophore-based Smart Polymer in Fiber Reinforced Composites

JIN ZOU[1], YINGTAO LIU[2,*], ADITI CHATTOPADHYAY[1] and LENORE DAI[1]

[1]*School for Engineering of Matter, Transport, and Energy, Arizona State University, Tempe, AZ, USA 85287*
[2]*School of Aerospace and Mechanical Engineering, University of Oklahoma, Norman, OK, USA 73019*

**KEYWORDS**

self-sensing
glass fiber
composite
mechanophore
fluorescence
smart polymer

**ABSTRACT**

Polymer matrix composites (PMCs) are widespread in engineering applications due to their superior mechanical properties at low weight. However, they are susceptible to damage due to their low interlaminar mechanical properties and poor electrical and thermal conductivities in the transverse direction to the laminate. Moreover, methods to inspect the embedded damage and to ensure the reliability of composites are expensive and labor intensive. Recently, mechanophore-based smart polymer has attracted significant attention, especially for self-sensing of matrix damage in PMCs. A cyclobutane-based self-sensing approach using 1,1,1-tris (cinnamoyloxymethyl) ethane (TCE) and poly (vinyl cinnamate) (PVCi) has been studied in this paper. The developed TCE and PVCi based smart polymer blends were characterized to understand their thermal and mechanical properties. The self-sensing function was investigated at both the polymer level and composite laminate level. Fluorescence emissions from fiber reinforced composite laminate were observed on specimens subjected to low velocity impact load and low cycle fatigue load, indicating the presence of matrix cracks.



## 1. INTRODUCTION

The field of fiber reinforced composite materials has grown rapidly in the last decade such that over 20 million tons are now produced every year for a variety of applications including aerospace, civil, and mechanical infrastructures. However, concerns remain about the structural integrity of composite materials subject to fatigue and impact loading, as such materials are susceptible to cracks or delamination that form deep within the structure. In addition, the failure mechanisms of composite laminates are more complicated and damage detection is challenging. Damage accumulation in composites is progressive in nature, with damage initiation in the formation of microscale matrix cracks that lead to delamination and even fiber fracture. Matrix damage can cause significant reduction in load carrying capability of the laminate and early failure. The integrity of polymer matrices in composites is therefore critical for structural durability and operational safety.

Identification of matrix cracks and delamination in polymer composites is of significant importance so that preventative maintenance can be taken before catastrophic structural failure. Scientists and engineers have been developing damage detection technologies over many years, which are recognized as nondestructive evaluation (NDE) and structural health monitoring (SHM) techniques. Common NDE techniques include ultrasonics [1], acoustic emission [2,3], infrared thermography [4], etc. Although these techniques have been well validated in laboratory environments, in-field applications, especially real-time NDE (also referred to as SHM), are still difficult due to the bulky size of NDE equipment and the time-consuming data post-processing and decision making procedures. SHM techniques combining sensors and complex feature extraction algorithms have been well studied [5–8]. Piezoelectric ceramic sensors have been employed to record guided waves or impedance data for local and global damage awareness [9–11]. The application of

*Corresponding author. E-mail: yingtao@ou.edu; Phone: 1 405 325-3663; Fax: 1 405 325-1088


doi:10.12783/issn. 2168-4286/2.4/Zou

advanced sensors, such as optic fibers [12,13] and wireless sensors [14], and vibration based diagnostic methodologies [15] have been reviewed and summarized in literature. However, current sensor based data driven SHM techniques are incapable of early damage detection.

Nanoscale materials and smart materials provide the potential solutions for real-time matrix crack detection in polymer composites. Multiple nanoscale materials, such as uniformly dispersed pristine carbon nanotubes and functionalized carbon nanotubes [16,17], aligned carbon nanotube forests [18], carbon nanotube thread [19,20], graphene [21], and nanoscale piezoelectric ceramics [22], have been integrated within polymer matrix systems. By measuring the tailored material properties, such as electrical impedance and resistance, the local strain field and damage conditions can be estimated for laminated composites under simple uniaxial load conditions [23]. However, it is still difficult to detect the matrix crack initiation at the early damage state under complex fatigue and impact load conditions.

Recently, mechanophore-based polymers have received increasing attention for damage detection in composites. Such materials are able to translate mechanical energy to a chemical transformation so that the damage can be detected by measuring a visible color change. Piermattei et al. reported an optic activated mechanophore-linked polymer, which could mechanically induce luminescence emission at low stress level [24]. Such polymers incorporating the bis(adamantly)-1,2-dioxetanes unit enabled the transduction of force into luminescence by opening the four-membered dioxetane ring with subsequent ketone product relaxation from its excited state to the ground state. However, the time for monitoring the mechanically induced luminescence was short, which restricted its use in practical applications. Pyran-based organic compounds, like spiropyrans, spirooxazines, and naphthopyrans, are well known chromogenic materials whose structure changes accompanied by a color change induced by temperature or light. Davis *et al.* synthesized spiropyran-linked elastomeric polymers which could act as force sensors in response to stress loading [25]. They applied tensile testing and simultaneous optical spectroscopy to examine force-induced scissile transformation. Force distribution was detected by monitoring the color change due to a mechanically induced 6-electrocyclic ring-opening reaction from colorless spiropyran to colored merocyanine conformations. Our research group recently reported a cyclobutane-based polymer for early damage detection in epoxy [26]. To our best knowledge, the color change mechanisms have not been applied for early damage detection in fiber reinforced composites.

Although mechanophore-linked polymers have provided tremendous new opportunities, especially in the areas of stress sensing and early crack/failure detection, many unknown fundamentals as well as unexplored applications remain. Current research gives greater emphasis to pure and bulk traditional polymers; synthesis relies solely on an individual chemistry/reaction mechanism that is often limited and complicated. In this paper we have designed and synthesized a mechanically responsive composite material system by integrating cyclobutane-containing polymer into an epoxy matrix and further extended this approach to identify low-cycle fatigue damage in glass fiber reinforced polymer composites through mechanically induced fluorescence generation.

## 2. CONCEPTS OF SELF-SENSING POLYMER MATERIALS

### 2.1. Self-sensing Concept using Fluorescence Based Smart Polymer

Integrating smart materials within conventional composite matrix systems is a practical way to monitor and detect the matrix crack damage in laminate composites. In particular, we applied cyclobutane as mechanophore functional group to epoxy; the matrix system in the composite. Both 1,1,1-tris(cinnamoyloxymethyl) ethane (TCE) and poly (vinyl cinnamate) (PVCi) were studied. TCE was dimerized into cyclobutane rings under photoirradiation. This cyclic product has been proved to efficiently generate fluorescence emission upon the cleavage of the cyclobutane ring [27]. TCE has trifunctional mer units on each molecule. It forms three-dimensional networks under UV photoirradiation. For comparison, a second polymer, poly (vinyl cinnamate) (PVCi) with the functional group as the side chain on the polymer to form a cross-linked polymer, was selected. PVCi is commercially available and very prominent in photochemistry with some attractive characteristics [28,29].

The cyclobutane-based polymer was produced by photodimerization of the C=C bond from the cinnamoyl function group of TCE and PVCi, respectively. Cyclobutane-based polymers were dispersed in the epoxy as self-sensing crack sensors. When the polymer blends undergo crack formation and propagation, the cyclobutane is mechanochemically cleaved to afford the chemicals that are capable of strong fluorescence emission, indicating the location of the crack in the epoxy, as shown in Figure 1. In this work, the effect of the functionalization of two different cyclobutane-based cross-linked polymers on the thermal and mechanical properties of new epoxy matrix composites was investigated and the relationship of the stress-spectroscopic signals of the composites was also studied.

### 2.2. Material Preparation and Characterization

In this work, all of the following listed materials and reagents were used as received. 1,1,1-tris(hydroxymethyl) ethane (99%), cinnamoyl chloride (98%), tetrahydrofuran (≥ 99.9%), 4-(dimethylamino)pyridine (≥ 99%), dichloromethane (≥ 99.8%), ethanol (≥ 99.5%), and poly(vinyl

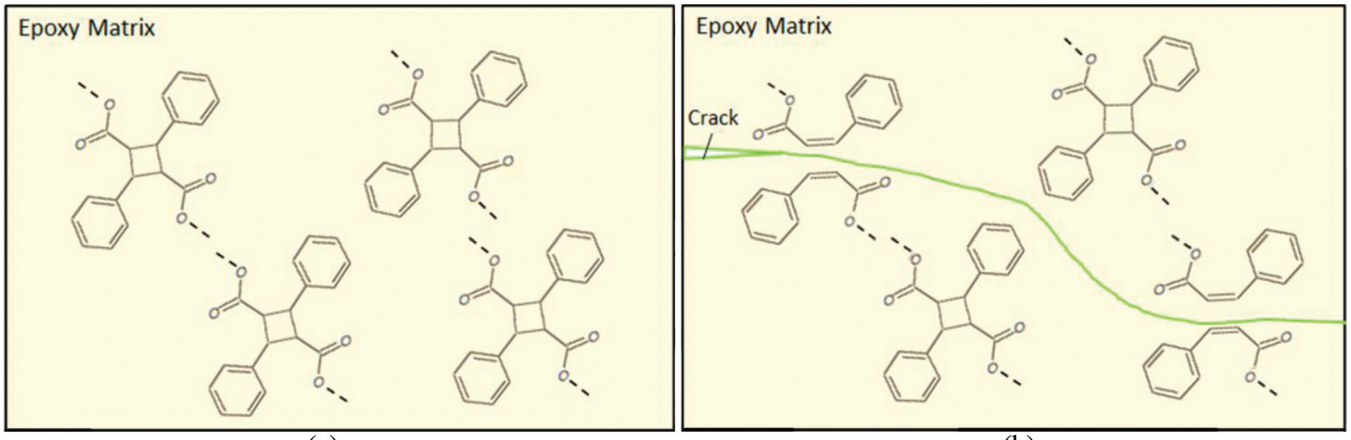


***Figure 1.*** *Depiction of the blending approach to create a stress-sensitive material. (a) before crack formation; (b) after crack formation [23].*

cinnamate) (PVCi, average Mn 45,000–55,000) were purchased from Sigma-Aldrich. Sodium chloride (≥ 99%) and water (HPLC) were purchased from Fisher Scientific. Epoxy resin FS-A23 (digycidylether of bisphenol F, DGEBPF) and epoxy hardener FS-B412 (diethylenetriamine, DETA) were purchased from Epoxy System Inc.

The TCE polymers or PVCi polymers were prepared using the following procedure. Solid TCE or PVCi was first dissolved in $CH_2Cl_2$. The solution was then applied on a clean silicon mold to form a thin film and placed in a vacuum to evaporate the excess $CH_2Cl_2$. After the evaporation, the thin film was photoirradiated under a UV light source at 302 nm for 4 h. All of the silicon molds and glass slides used for preparation of samples were pretreated with a mold release agent.

To prepare polymer/epoxy polymer blends, the TCE or PVCi solution was added to DGEBPF and thoroughly dispersed by using an ultrasonic probe sonicator (Sonics VibraCell, 500W model) for 20 seconds. The mixture was then placed in a vacuum chamber at 50°C to evaporate the $CH_2Cl_2$ until the mass of the mixture remained unchanged, indicating that the excess $CH_2Cl_2$ had evaporated. The resin mixture was cooled to room temperature before DETA was added and mixed ($M_{TCE}$ or $M_{PVCi}$: $M_{Epoxy}$ = 1:10; $M_{DGEBPF}$: $M_{DETA}$ = 100:27). The mixture was sonicated in an ice bath to prevent any premature curing. After the mixture became homogenous, the mixture was poured into the silicon molds and moved into a vacuum chamber to degas for 30 min, followed by photoirradiation conducted by a UV lamp of 302 nm wavelength (UVP, UVM-28). According to the manufacturer's data, the light density was approximately 1300 $\mu Wcm^{-2}$ at a distance of 3 cm. The sample was exposed to UV light for 4 hours and cured overnight at room temperature at atmospheric pressure. A neat epoxy sample followed a similar procedure for comparison. After simple machining, the sample was ready for testing. The average dimension of the cubic sample was 3 × 4 × 8 $mm^3$.

The glass fiber reinforced composites laminate was fabricated using the wet layup method. A polymer blend containing uncured epoxy and 10 w.t.% TCE was first mixed thoroughly. The uncured composite was cured under a load of 50 kg for 10 minutes and photoirradiation for four hours under UV light at 302 nm wavelength. In order to achieve further improved performance, the composites were posted-cured at 60°C overnight in an oven and allowed to cool gradually. The composite laminate sample size was 30 × 80 × 0.4 $mm^3$.

To characterize the mechanical and thermal properties of the proposed polymer matrix system, differential scanning calorimeter (DSC) thermal analysis, thermogravimetric analysis (TGA), and dynamic mechanical analysis (DMA) were conducted. The effect of the addition of the cross-linked polymer to the epoxy on glass transition temperature ($T_g$) was studied using DSC. The experiments were performed in a nitrogen atmosphere using TA Instruments Q20. TGA monitors the amount and rate of change in the mass of a sample as a function of temperature or time as a sample is heated at a programmed rate in a controlled atmosphere. The measurements are used primarily to determine the thermal stabilities of materials. DMA was used to measure the glass transition temperature, storage modulus, loss modulus. Cross-link density of the neat epoxy, the epoxy blended with TCE polymer, and the epoxy blended with PVCi polymer was calculated through DMA. Experiments were performed in a tension mode using a TA Instruments Q800. The detailed property characterization results have been reported in [26].

## 3. MECHANICAL STRESS INDUCTED SELF-SENSING POLYMER

The self-sensing capability of the proposed polymer was first investigated at the polymer level. The goal for the application of the cyclobutane-based polymer was to demonstrate mechanochemical cleavage of a covalent bond and investigate the use of these cyclobutane polymers blended with

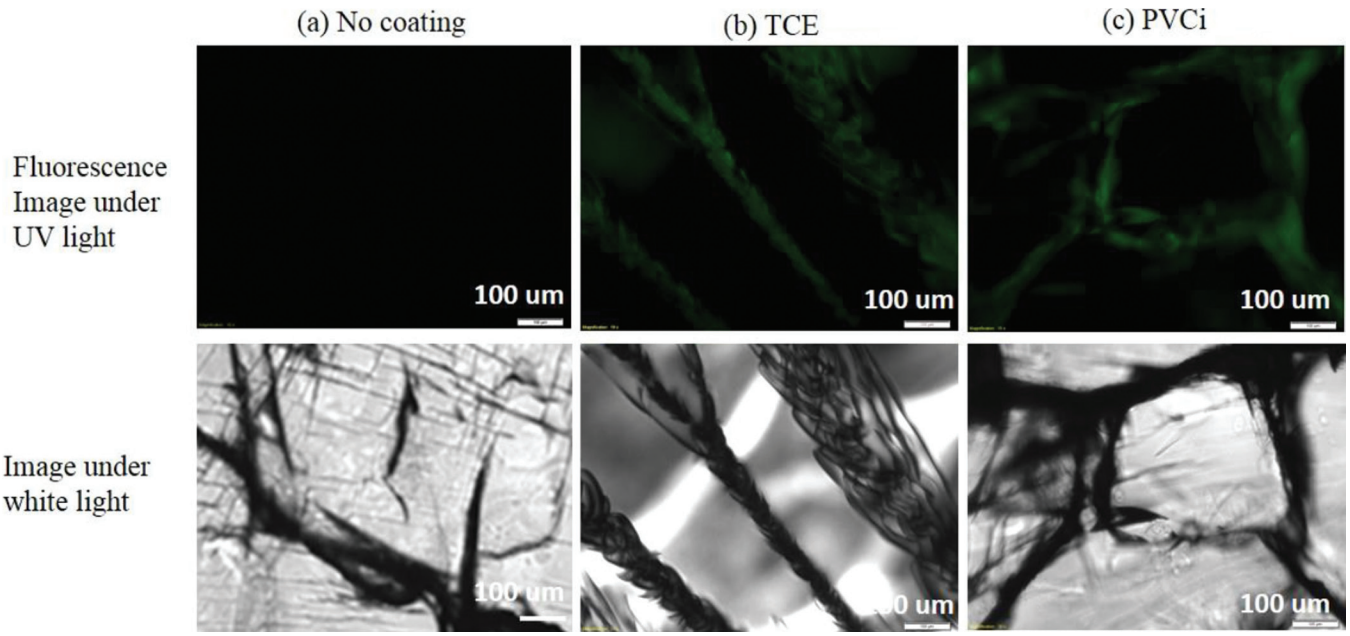


***Figure 2.*** *Microscopic images of cracks generated by hammer hit on (a) a clean polystyrene substrate, (b) a polystyrene substrate coated with cross-linked TCE and (c) PVCi polymer under a UV light. Images in second row were the corresponding images under a white light.*

epoxy as damage sensors by visual detection for composite laminates. Here, we applied a simple and direct method for detecting mechanochemical reactions with UV microscopy. The fluorescence response was first confirmed by coating cross-linked TCE polymer film on a polystyrene substrate. The cracks were generated by low velocity impacts using a hammer and observed using UV microscopy, as shown in Figure 2. Under the microscope with white light, the cracks were observed both on the polystyrene and polystyrene with coating. But the fluorescent signal was only detected on the polystyrene coated with cross-linked TCE polymer exposed to UV light. Furthermore, the cross-linked PVCi polymer was coated on the polystyrene substrate. The fluorescence emission was observed along the crack as well. The results indicated that the mechanochemical cleavage of cyclobutane occurred along the crack propagation and induced the fluorescence generation.

To further understand the self-sensing capabilities of the proposed smart polymer system, experiments were conducted under a quasi-static compression load condition using polymer cubic samples fabricated by the following procedures in Section 2.2. When the cracks were generated by external force on the polymer blends with different amounts of the cross-linked TCE polymer, fluorescence emission from the cracks was clearly observed under UV and white light both, as shown in Figure 3. The fluorescent signal was

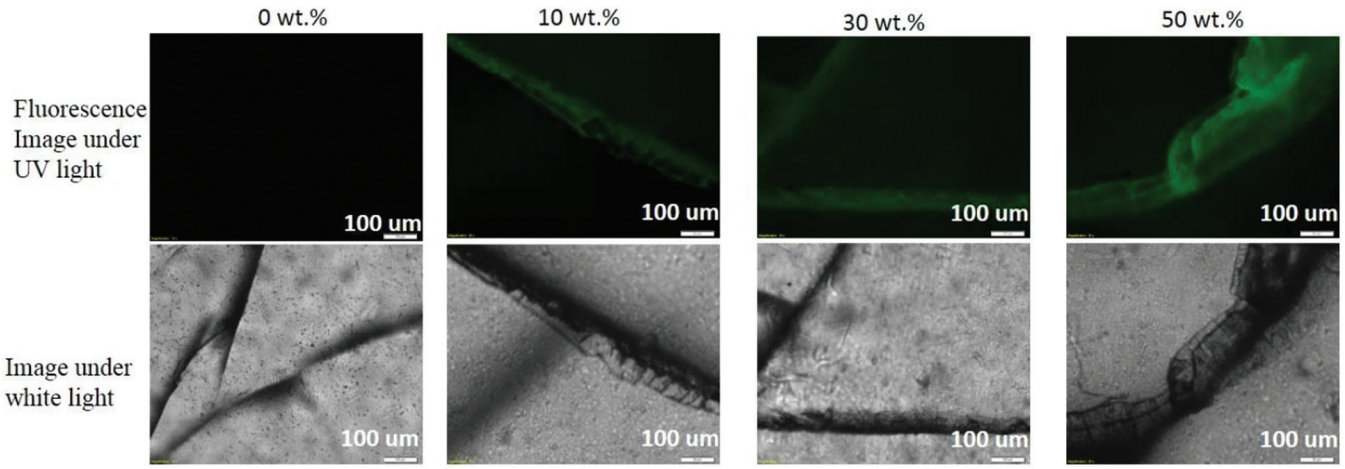


***Figure 3.*** *Microscopic images of fluorescence emission along cracks generated by hammer hit on polymer blends (a) 0 wt.% (b) with 10 wt.% (c) 30 wt. % (d) 50 wt.% cross-linked TCE polymer. Images in the second row were the corresponding images under white light.*

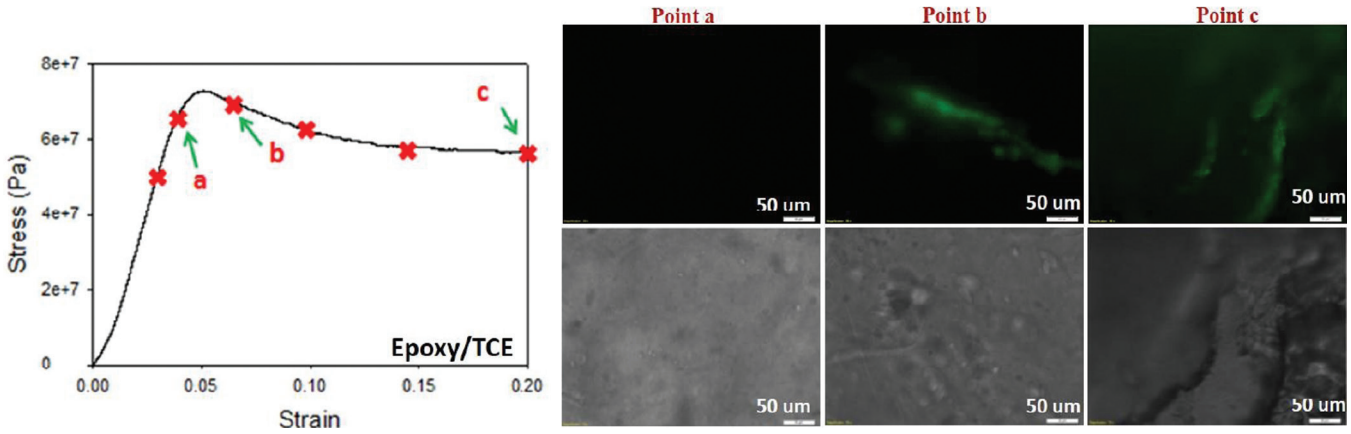


***Figure 4.*** *Microscopic images of fluorescence emission in response to different strains of epoxy with 10 wt.% cross-linked TCE polymer blends.*

further augmented with increasing amounts of cross-linked TCE polymer (30 w.t.% and 50 w.t.%) blended with epoxy. No fluorescence emission was found on neat epoxy in the same experimental conditions. From the images, epoxy with 10 wt.% cross-linked TCE polymer gave strong enough fluorescent emission to detect the damage. Thus, the content of 10 wt.% was used for the following fluorescence tests. Comparing the images under white light and UV light, it is noted that the proposed cyclobutane-based smart polymers were able to clearly identify the existence of polymer cracks when mixed with structural epoxy. The detailed crack shape and crack depth were represented by the intensity of fluorescence lights. The green light intensity of fluorescence images became stronger as more cracks existed in the polymer matrix system.

Neat epoxy and smart polymer samples were compressed to different strains, respectively. As shown in Figure 3, no fluorescence was detected on the neat epoxy. The evolution of induced fluorescence emission on the epoxy samples mixed with 10 wt.% TCE is shown in Figure 4. For all the polymer samples, limited fluorescence was observed before the stress passing yield point. However, the intensity of fluorescence emission from the proposed polymer significantly increased right after stress passing the yield point and microcracks starting to form. Those cracks could not be clearly observed under white light, indicating that the fluorescence emission could provide a higher sensitivity and easier detection for the location of cracks, especially cracks at the micro scale. It is also notable that fluorescence emission along the crack intensified with strain after the yield point. Similar results were observed using epoxy samples mixed with 10 wt.% PVCi smart polymers, as shown in Figure 5. In addition, through characterization of both TCE and PVCi smart polymers, it is shown that PVCi based smart polymers have a higher glass transition temperature, which results in better thermal stability and more potentials for practical applications in fiber reinforced composites.

In order to further explore the relationship between the strains and their corresponding fluorescence response, ten fluorescent micrographs were processed by ImageJ. The average fluorescence densities and related deviation for each mechanical load state were calculated. The density change as a function of strain was plotted in Figure 6. As expected, the densities increased with the accumulation of strain, which indicates that the more cleavages of cyclobutane were activated as strained increased.

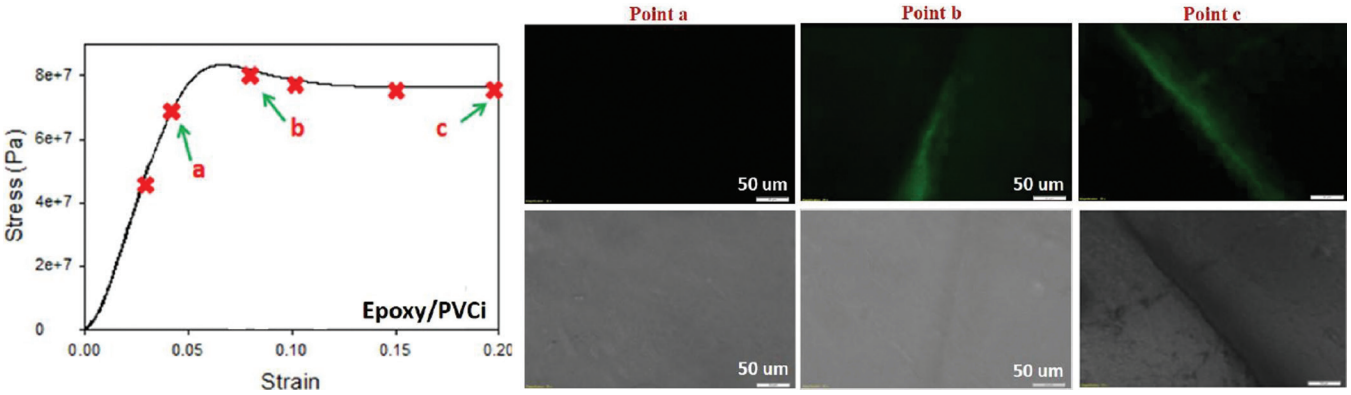


***Figure 5.*** *Microscopic images of fluorescence emission in response to different strains of epoxy with 10 wt.% cross-linked PVCi polymer blends.*

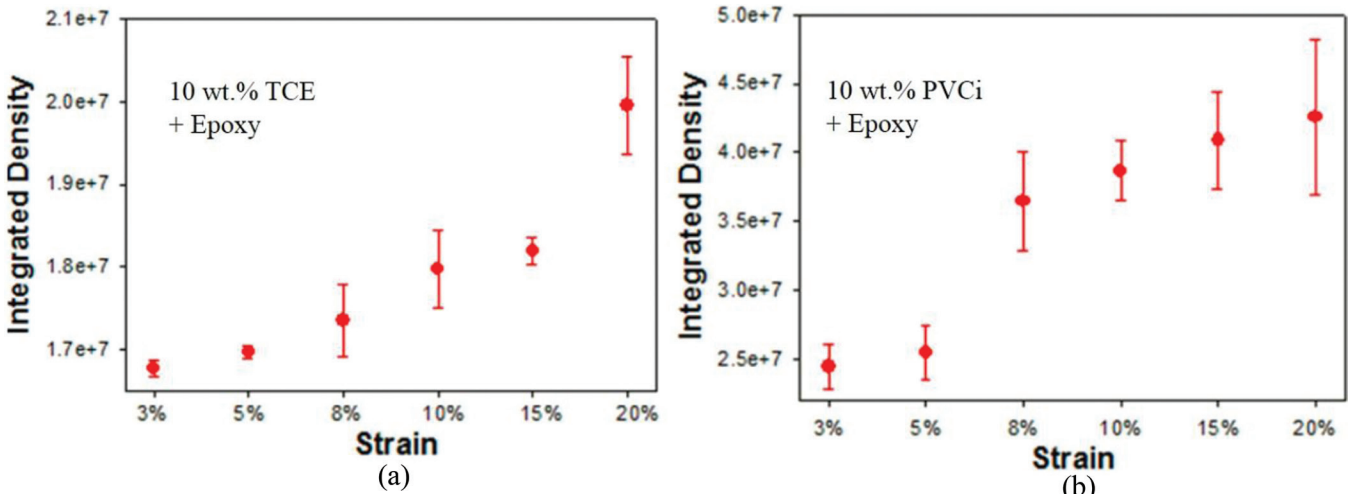


***Figure 6.*** *Integrated density of fluorescence emission in response to different strains of epoxy w/ 10 wt.% cross-linked (a) TCE and (b) PVCi polymer blends.*

## 4. SELF-SENSING OF LOW CYCLE FATIGUE DAMAGE IN COMPOSITE LAMINATE

In general, fatigue of fiber reinforced composite materials is a complex phenomenon. Multiple parameters, including fiber type, matrix type, load conditions, and boundary conditions, can significantly influence the fatigue performance of composites. Fatigue damage starts very early and the extent of the damage zones grows steadily, but the damage type in these zones can change. For example, small matrix cracks can lead to large size delamination as damage accumulates. Therefore, being able to efficiently detect early matrix cracks in composite laminates are critical for the structural safety and reliability of composites. The proposed self-sensing method using cyclobutane based smart polymers was further studied under low fatigue cycle load conditions.

The fluorescence response on the glass fiber reinforced composite (GFRC) was first validated by the damage applied with a hammer. A circle was marked and the damage was made by the hammer impacted on one side of the single sheet within the circle, as seen in Figure 7 (right). The images within the circle before and after the damage were collected and compared. Obviously, the fluorescence was observed along the fiber after the damage was applied, as seen in Figure 7 (left).

The fatigue tests were performed on a glass fiber reinforced composite (GFRC) sheet under uniaxial tensile load conditions. A 4 mm wide hole in the center of the specimen

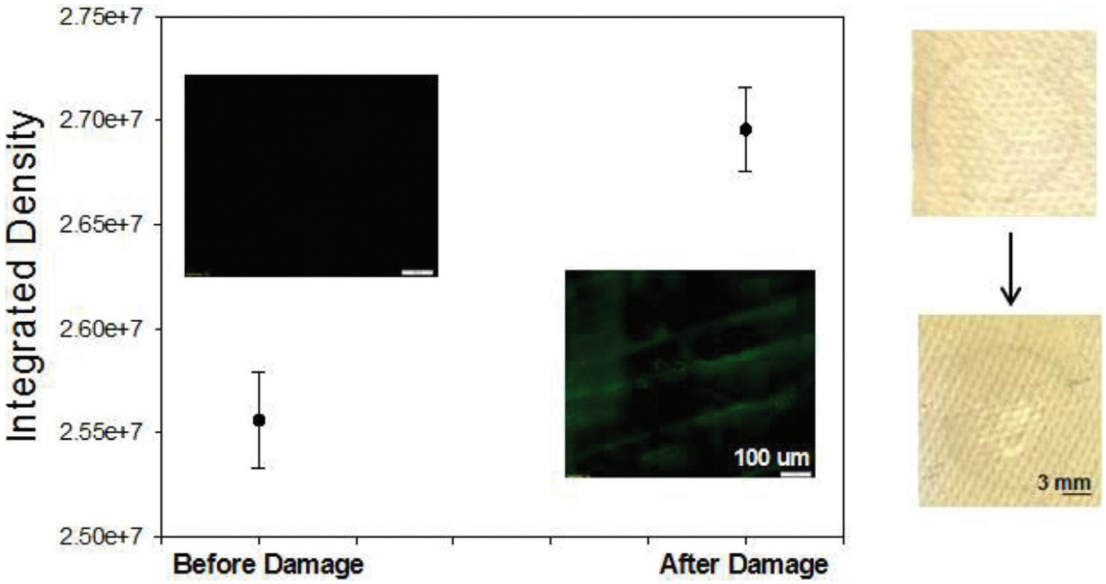


***Figure 7.*** *(Left) Fluorescence density of fiberglass epoxy composite with 10% TCE before and after damage was applied. (right) GFRC specimen under a white light.*

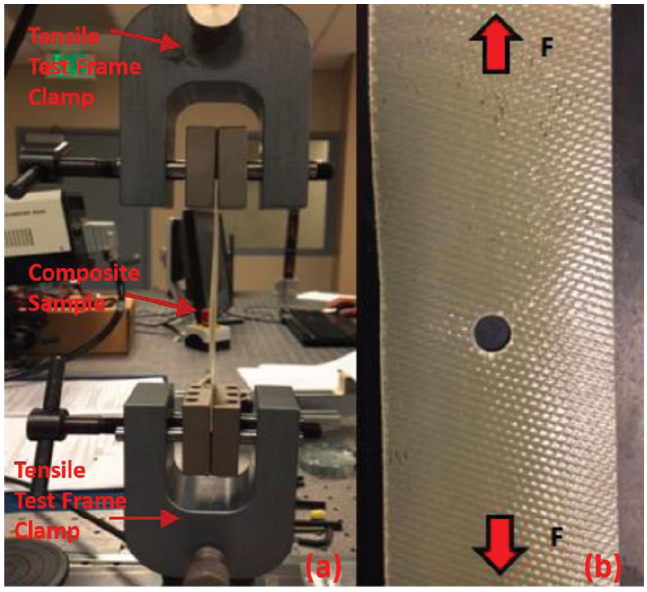


***Figure 8.*** *(Left) Experimental setup of the unidirectional tensile fatigue test using GFRC sample; (Right) GFRC sample with tensile load.*

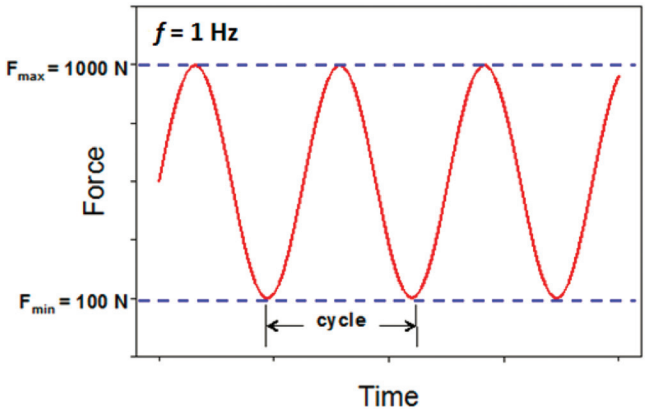


***Figure 9.*** *Low cycle fatigue load history applied in the experiment.*

was introduced before the fatigue test to create a stress concentrate area and the fatigue damage was expected to initiate around the hole. A TestResource 800L mechanical testing system was used in the experiment, as shown in Figure 8. The specimen was cycled in a load-controlled mode at stress ratio (R), $\sigma_{min}/\sigma_{max} = 0.1$ on a uniaxial fatigue frame operating with a sinusoidal waveform at a frequency of 2 Hz, as seen in Figure 9. Maximum stress (1000 N) and minimum stress (100 N) was constant for each cycle of a test. The number of fatigue cycles was recorded. After the application of a certain number of load cycles, the test was stopped. The specimen was removed from the fatigue frame and photographed under white light and a UV microscope. Then the specimen was remounted and fatigue cycles continued. The fluorescent intensity at each fatigue cycle loading was calculated through ImageJ. The average data against cycles are shown in Figure 9. The fatigue fracture surface of the specimen was sputter coated with a thin layer of gold to observe the fatigue crack growth under the scanning electron microscope (SEM). The specimens for SEM were sputter coated with gold and viewed by SEM-XL30 (FEI). The specimens for SEM experiments were prepared by placing a piece of GFRC sheet onto a newly cleaved mica substrate and applying Au coating of 10–15 nm thick using a sputter coater.

In order to monitor the crack growth on the GFRC specimen, SEM characterization of the specimen was carried out. Figure 10 shows the matrix cracks, matrix crack and fiber breakage on the GFRP specimen surface. Figure 10 (left) shows micro-cracks on the matrix after 500 cycles. The exposure of glass fibers after 1,000 cycles in Figure 10 (middle) shows interface debonding. These exposed glass fibers tend to fracture under cyclic tensile force. After 1350 fatigue cycles, more breakage of glass fibers was observed as well as matrix cracks, causing a noticeable propagation along the longitudinal direction, as shown in Figure 10 (right). The corresponding macroscopic images are shown in Figure 10 (inset). With increasing fatigue cycles, the cracks developed in the 0° direction and became visible. The higher the number of fatigue cycles, the more cracks formed. UV microscopic images of fluorescence emission at different fatigue stages are shown in Figure 11. The damages were first formed

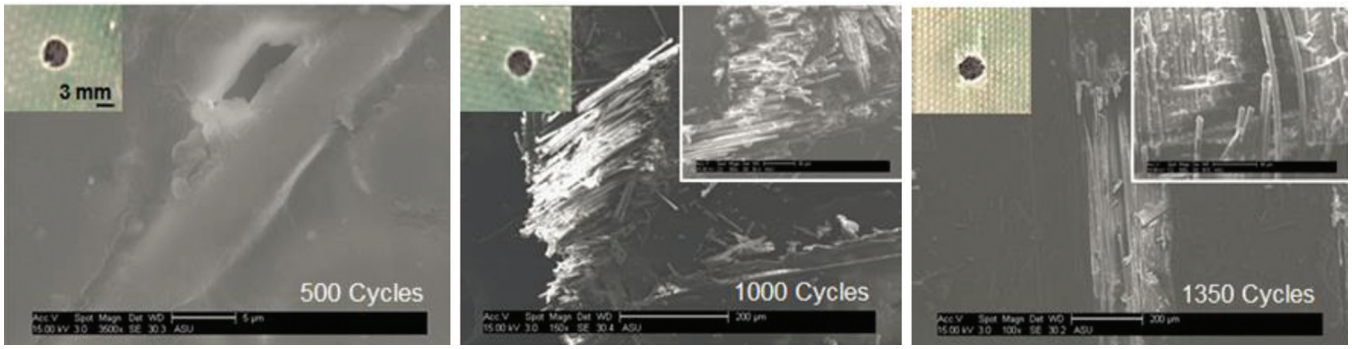


***Figure 10.*** *SEM micrographs of glass fiber reinforced epoxy composite with 10% TCE at different fatigue cycle stages. insets are the images under white light.*

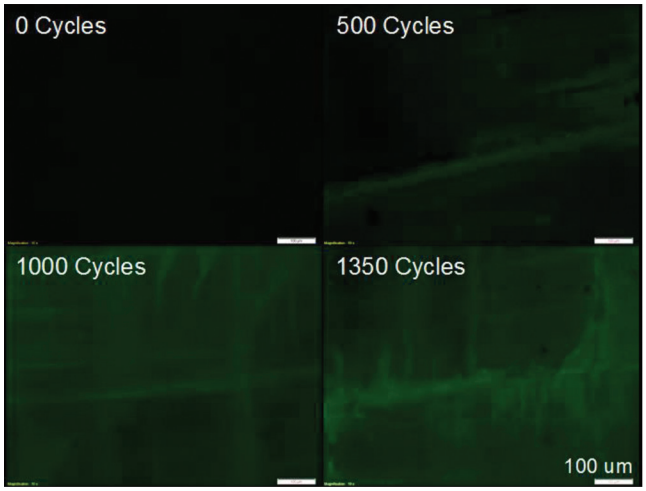


***Figure 11.*** *Microscopic images of fluorescence emission on GFRC in response to different fatigue cycle stages.*

along the glass fibers in the 0° direction. With cycles, the fluorescence emission became more obvious and the cracks along the glass fibers at 90° direction grew as well. Fluorescent micrographs at different fatigue cycles were processed through ImageJ and the average fluorescence densities were calculated. The corresponding fluorescence density change was plotted in Figure 12. As expected, the density intensified as cycles increased, indicating that there were more cyclobutane molecules cleaved into cinnamate molecules due to the weaker bond strength on the cyclobutane ring than on the other bonds.

## 5. CONCLUSION

In this paper, a novel self-sensing approach is developed to detect the matrix cracking in composite laminates. The cyclobutane based smart polymers were synthesized and integrated within conventional epoxies. Once external forces were applied on the smart polymer and composites, fluorescence emissions were observed under UV microscope. Both TCE and PVCi based smart polymers were investigated. Compared to smart polymers with TCE, polymers integrated with PVCi showed stronger fluorescence intensity at the same stress level, which lead to stronger sensing capabilities to stress and matrix crack damage. The smart polymers were further applied to GFRP composites to detect the low cyclic fatigue damage. Significant fluorescence emissions were measured as the damage accumulated during the experiments. The developed self-sensing approach provided a new method to efficiently detect matrix cracks in composites without using any bulky NDE equipment or complicated SHM sensors. This developed self-sensing method provides a practical approach to identify structural damage in composites under complex load conditions.

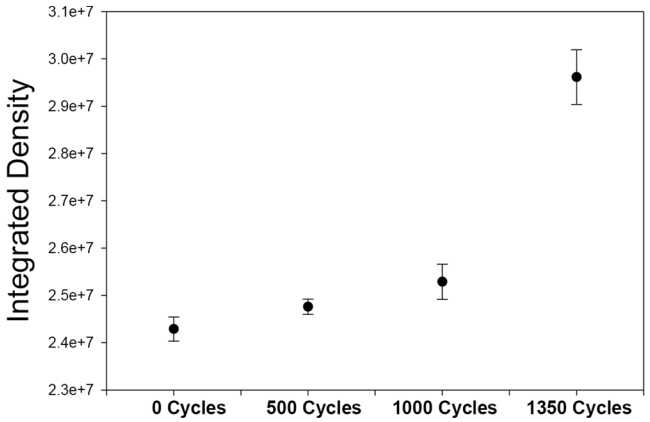


***Figure 12.*** *Microscopic images of fluorescence emission on GFRC in response to different fatigue cycle stages.*

## 6. ACKNOWLEDGEMENT

The authors are grateful for the financial support of the Air Force Office of Scientific Research (AFOSR), grant number: FA9550-12-1-0331. Dr David Stargel is the program manager.

## 7. REFERENCES

[1] Aymerich, F. and S. Meili, Ultrasonic evaluation of matrix damage in impacted composite laminates. *Composites Part B: Engineering,* 2000. 31(1): p. 1–6. http://dx.doi.org/10.1016/S1359-8368(99)00067-0

[2] De Oliveira, R. and A. Marques, Health monitoring of FRP using acoustic emission and artificial neural networks. *Computers & structures*, 2008. 86(3): p. 367–373. http://dx.doi.org/10.1016/j.compstruc.2007.02.015

[3] Godin, N., S. Huguet, R. Gaertner, and L. Salmon, Clustering of acoustic emission signals collected during tensile tests on unidirectional glass/polyester composite using supervised and unsupervised classifiers. *NDT & E International*, 2004. 37(4): p. 253–264. http://dx.doi.org/10.1016/j.ndteint.2003.09.010

[4] Toubal, L., M. Karama, and B. Lorrain, Damage evolution and infrared thermography in woven composite laminates under fatigue loading. *International journal of Fatigue*, 2006. 28(12): p. 1867–1872. http://dx.doi.org/10.1016/j.ijfatigue.2006.01.013

[5] Sohn, H., C.R. Farrar, F.M. Hemez, D.D. Shunk, D.W. Stinemates, B.R. Nadler, and J.J. Czarnecki, A review of structural health monitoring literature: 1996–2001. 2004: Los Alamos National Laboratory Los Alamos, NM.

[6] Liu, Y., M.Y. Fard, A. Chattopadhyay, and D. Doyle, Damage assessment of CFRP composites using a time–frequency approach. *Journal of Intelligent Material Systems and Structures*, 2012. 23(4): p. 397-413. http://dx.doi.org/10.1177/1045389X11434171

[7] Liu, Y., S.B. Kim, A. Chattopadhyay, and D.T. Doyle, Application of system-identification techniquest to health monitoring of on-orbit satellite boom structures. *Journal of Spacecraft and Rockets*, 2011. 48(4): p. 589–598. http://dx.doi.org/10.2514/1.51818

[8] Liu, Y., S. Mohanty, and A. Chattopadhyay, Condition based structural health monitoring and prognosis of composite structures under uniaxial and biaxial loading. Journal of Nondestructive Evaluation, 2010. 29(3): p. 181–188. http://dx.doi.org/10.1007/s10921-010-0076-2

[9] Park, G., H.H. Cudney, and D.J. Inman, Impedance-based health monitoring of civil structural components. *Journal of infrastructure systems*, 2000. 6(4): p. 153–160. http://dx.doi.org/10.1061/(ASCE)1076-0342(2000)6:4(153)

[10] Giurgiutiu, V., A. Zagrai, and J.J. Bao, Piezoelectric wafer embedded active sensors for aging aircraft structural health monitoring. Structural Health Monitoring, 2002. 1(1): p. 41–61. http://dx.doi.org/10.1177/147592170200100104

[11] Liu, Y. and A. Chattopadhyay, Low-velocity impact damage monitoring of a sandwich composite wing. *Journal of Intelligent Material Systems and Structures*, 2013. 24(17): p. 2074–2083. http://dx.doi.org/10.1177/1045389X12453964

[12] Li, H.-N., D.-S. Li, and G.-B. Song, Recent applications of fiber optic sensors to health monitoring in civil engineering. *Engineering structures,* 2004. 26(11): p. 1647–1657. http://dx.doi.org/10.1016/j.engstruct.2004.05.018

[13] Majumder, M., T.K. Gangopadhyay, A.K. Chakraborty, K. Dasgupta, and D.K. Bhattacharya, Fibre Bragg gratings in structural health monitoring—Present status and applications. *Sensors and Actuators A: Physical*, 2008. 147(1): p. 150–164. http://dx.doi.org/10.1016/j.sna.2008.04.008

[14] Lynch, J.P. and K.J. Loh, A summary review of wireless sensors and sensor networks for structural health monitoring. *Shock and Vibration Digest*, 2006. 38(2): p. 91-130. http://dx.doi.org/10.1177/0583102406061499

[15] Doebling, S.W., C.R. Farrar, M.B. Prime, and D.W. Shevitz, Damage identification and health monitoring of structural and mechanical systems from changes in their vibration characteristics: a literature review. 1996, Los Alamos National Lab., NM (United States). http://dx.doi.org/10.2172/249299

[16] Li, C., E.T. Thostenson, and T.-W. Chou, Sensors and actuators based on carbon nanotubes and their composites: A review. *Composites Science and Technology*, 2008. 68(6): p. 1227–1249. http://dx.doi.org/10.1016/j.compscitech.2008.01.006

[17] Liu, Y., A. Rajadas, and A. Chattopadhyay, A biomimetic structural health monitoring approach using carbon nanotubes. *JOM*, 2012. 64(7): p. 802–807. http://dx.doi.org/10.1007/s11837-012-0357-6

[18] Veedu, V.P., A. Cao, X. Li, K. Ma, C. Soldano, S. Kar, P.M. Ajayan, and M.N. Ghasemi-Nejhad, Multifunctional composites using reinforced laminae with carbon-nanotube forests. *Nature materials*, 2006. 5(6): p. 457–462. http://dx.doi.org/10.1038/nmat1650

[19] Abot, J.L., Y. Song, M.S. Vatsavaya, S. Medikonda, Z. Kier, C. Jayasinghe, N. Rooy, V.N. Shanov, and M.J. Schulz, Delamination detection with carbon nanotube thread in self-sensing composite materials. *Composites Science and Technology*, 2010. 70(7): p. 1113–1119. http://dx.doi.org/10.1016/j.compscitech.2010.02.022

[20] Abot, J.L., M.J. Schulz, Y. Song, S. Medikonda, and N. Rooy, Novel distributed strain sensing in polymeric materials. *Smart Materials and Structures*, 2010. 19(8): p. 085007. http://dx.doi.org/10.1088/0964-1726/19/8/085007

[21] Li, W., A. Dichiara, and J. Bai, Carbon nanotube–graphene nanoplatelet hybrids as high-performance multifunctional reinforcements in epoxy composites. *Composites Science and Technology*, 2013. 74: p. 221–227. http://dx.doi.org/10.1016/j.compscitech.2012.11.015

[22] Ahuja, T. and D. Kumar, Recent progress in the development of nanostructured conducting polymers/nanocomposites for sensor applications. *Sensors and Actuators B: Chemical*, 2009. 136(1): p. 275–286. http://dx.doi.org/10.1016/j.snb.2008.09.014

[23] Thostenson, E.T. and T.W. Chou, Carbon nanotube networks: sensing of distributed strain and damage for life prediction and self healing. *Advanced Materials*, 2006. 18(21): p. 2837–2841. http://dx.doi.org/10.1002/adma.200600977

[24] Piermattei, A., S. Karthikeyan, and R.P. Sijbesma, Activating catalysts with mechanical force. *Nature chemistry*, 2009. 1(2): p. 133–137. http://dx.doi.org/10.1038/nchem.167

[25] Davis, D.A., A. Hamilton, J. Yang, L.D. Cremar, D. Van Gough, S.L. Potisek, M.T. Ong, P.V. Braun, T.J. Martínez, and S.R. White, Force-induced activation of covalent bonds in mechanoresponsive polymeric materials. *Nature*, 2009. 459(7243): p. 68–72. http://dx.doi.org/10.1038/nature07970

[26] Zou, J., Y. Liu, B. Shan, A. Chattopadhyay, and L.L. Dai, Early damage detection in epoxy matrix using cyclobutane-based polymers. *Smart Materials and Structures*, 2014. 23(9): p. 095038. http://dx.doi.org/10.1088/0964-1726/23/9/095038

[27] Cho, S.-Y., J.-G. Kim, and C.-M. Chung, A fluorescent crack sensor based on cyclobutane-containing crosslinked polymers of tricinnamates. *Sensors and Actuators B: Chemical*, 2008. 134(2): p. 822–825. http://dx.doi.org/10.1016/j.snb.2008.06.042

[28] Iimura, Y., S. Kobayashi, T. Hashimoto, T. Sugiyama, and K. Katoh, Alignment control of liquid crystal molecules using photo-dimerization reaction of poly (vinyl cinnamate). *IEICE Transactions on Electronics*, 1996. 79(8): p. 1040–1046.

[29] Song, Y.-K., K.-H. Lee, W.-S. Hong, S.-Y. Cho, H.-C. Yu, and C.-M. Chung, Fluorescence sensing of microcracks based on cycloreversion of a dimeric anthracene moiety. *Journal of Materials Chemistry*, 2012. 22(4): p. 1380–1386. http://dx.doi.org/10.1039/C1JM13709C

*Journal of Multifunctional Composites*, 2 (2014) 217–226

Journal of Multifunctional Composites

journal homepage: http://jmc.destechpub.com

# Localized Detection of Damage in Laminated Composite Materials Using Carbon Nanotube Yarn Sensors

J. L. ABOT[1,*], K. WYNTER[1], S. P. MORTIN[1], H. BORGES DE QUADROS[1], H. H. LE[1], D. C. RENNER[1] and K. BELAY[2]

[1]*Department of Mechanical Engineering, The Catholic University of America, Washington, DC 20064, USA*
[2]*Department of Physics, Florida A&M University, Tallahassee, FL 32307, USA*

**KEYWORDS**

carbon nanotubes
smart materials
delamination
damage
non-destructive testing

**ABSTRACT**

Carbon nanotube yarns are lightweight, stiff, strong, ductile and electrically conductive fiber-like materials that exhibit a piezoresistive response. This piezoresistive characteristic of the carbon nanotube yarns is being tapped to measure strain in polymeric and laminated composite materials through resistance measurements without adding much weight or altering the integrity of the host material. Furthermore, the same principle is being used to detect damage and delamination in laminated composite materials. This paper includes the experimental results of a study about damage detection in laminated polymeric composite materials using carbon nanotube yarn sensors. A combination of sensor configurations including yarns stitched through the thickness direction of the composite laminate and yarns placed straight cross wide to the laminate are used to detect the presence of damage as well as its extent and propagation pattern. As the laminated composite is mechanically loaded, the yarn sensors capture instantaneously delamination as demonstrated by their resistance response. Crucially, the yarn sensors are sensitive enough to provide a significant resistance increase output that serves as an indication of an impending delamination. Minor damage such as porosity or other fabrication details are also captured as evidenced by a small increase in the resistance of the yarn sensor. The experimental results also show the ability of a combination of different yarn sensors to detect the exact location and extent of the delamination throughout the entire loading process. Damage detection using carbon nanotube yarns may offer a highly adaptive, practical, and sensitive structural health monitoring method.



## 1. INTRODUCTION

Monitoring the structural health of composite materials and structures has been the focus of research for several decades. Non-destructive evaluation (NDE) methods include acoustic monitoring, laser vibrometry, thermal imaging, piezoresistive carbon microfiber reinforcement, X-rays, and several other techniques [1]. They offer precise information regarding the structural integrity of a laminated composite but require costly, prolonged and complex procedures that make their use impractical in many applications. Structural health monitoring (SHM) methods provide constant and immediate feedback of the state of health of a structure including potential damage [2]. SHM methods may include vibration analysis, strain gauges, fiber optic sensors, stress wave propagation techniques as well as several other methods [2]. SHM methods that utilize micro-strain sensors can capture strain variation due to piezoresistive effects, resonance monitoring, piezoelectric effects, capacitance variation, or changes in optical properties [3].

Piezoresistive methods work on the principle of variations in strain being proportional to changes in resistance. Commonly used piezoresistive devices include metal alloy-polymeric films or metallic foil strain gauges. These strain gauges are able to capture very low fluctuations of strain with a maximum range of about 5% [3]. Similarly, semiconductor gauges rely on the piezoresistive properties of

*Corresponding author. Tel: 1 (202) 319-4382, Fax: 1 (202) 319-5173,
E-mail: abot@cua.edu.


doi:10.12783/issn. 2168-4286/2.4/Abota

silicone and germanium correlating the change in resistance with variations of stress instead of strain [4]. Although the semiconductor gauges are less expensive, more ductile, and operate with a gauge factor up to one hundred times higher than that of metallic foil gauges, they are significantly nonlinear in operation and suffer from high temperature sensitivity [4].

Despite the advantages of the previously mentioned piezoresistive-based SHM methods, they cannot detect initiating damage in composite materials with high compaction or multifaceted construction. More critically, they fail to achieve damage detection without altering the microstructure of the composite material. An alternative method of strain monitoring and damage detection that may offer the advantages of the previously mentioned methods without their drawbacks consists of the use carbon nanotube (CNT) yarns [5–9] that are intricately integrated into the fiber reinforcements of composite materials [10–14]. The concept is that CNT yarns are integrated in a laminated composite material forming a continuous sensor circuit, and their inherent piezoresistive sensitivity would capture small amounts of strain within the host material [10–13]. Unlike other SHM methods, integrated CNT yarn sensors may offer a non-destructive, simpler, easily customizable and robust alternative of damage detection in laminated composite materials.

Delamination in laminated composites consists of the separation of their layers and represents a significant risk to their integrity [15]. Delamination can occur at the edge, near the surface, or in the center of the laminated composite. Typically, edge delamination occurs because of loading perpendicular to the axis of a beam near its edge. While delamination may occur during processing of the material, interlaminar normal and shear loading cases typically lead to delamination when interlaminar shear stress components, $\tau_{13}$ and $\tau_{23}$, exceed their strength values under the maximum stress failure criterion, or when the strain energy release rate, $G_{ic}$, exceeds its maximum allowable value under the fracture mechanics criterion [15]. While the range in size of delamination and damage can vary drastically, it may elude the detection capabilities of most techniques that monitor change in material geometry such as metallic foil strain gauges, which are more suitable for surface strain detection, or optical fiber monitoring that requires complex equipment and data analysis. The ability of the CNT yarn sensors to detect mode II-dominated delamination in laminated composite materials had been previously shown by these authors [10]. This paper presents the results of an experimental study about the detection of delamination and minor damage including their exact location and extent using a combination of different types of integrated CNT yarn sensors. Furthermore, it provides a detailed explanation of the methodology and the mechanisms of capturing delamination using the CNT yarn sensors.

## 2. CARBON NANOTUBE YARN SENSOR

The CNT yarns in this study were dry-spun from the sides of 400 to 500 μm-high vertically aligned arrays composed of multi-walled carbon nanotubes (MWCNTs) grown by water-assisted Chemical Vapor Deposition (CVD) [16–19]. The CNT yarns are composed of one or three intertwined threads. The CNT yarns composed of three threads have a total diameter of about 25 μm, a density of about 0.9 g $cm^{-3}$, and the twist of the single thread varies between 558 and 868 $m^{-1}$. A Scanning Electron Microscopy (SEM) image of the 3-thread yarn is presented in Figure 1(a). The CNT yarns composed of one thread have a diameter of about 29 μm and a corresponding SEM image is shown in Figure 1(b). CNT yarns exhibit a piezoresistive response that depends on the exact construction of the material including the nanotube diameter, length and chirality, twist angle of the yarn, fabrication technique and other yarn characteristics [20,21]. The response of unconstrained 1-thread yarns subjected to quasi-static uniaxial tension loading exhibits a negative piezoresistivity [14]. The response of laterally constrained yarns is being determined and will be used to predict the response of the yarn sensors that are integrated in polymeric and composite materials. This piezoresistive characteristic of the CNT yarn is being used for sensing purposes and provide real time monitoring of the structural health of a polymeric or composite material through resistance measurements [10–13].

## 3. FABRICATION OF SELF-SENSING COMPOSITE MATERIALS

The fabrication of the self-sensing laminated polymeric composite samples with the integrated CNT yarn sensors comprises three stages: CNT yarn integration into the dry fabric layers, curing of the laminated composites, and preparation of the CNT yarn sensor circuits. It should be noted that in the case of integrating CNT yarns into a carbon fiber laminated composite, an additional step consisting of coating the CNT yarn would be necessary to prevent short-circuiting between the carbon fibers and the CNT yarns. In this study, the CNT yarns are integrated in a glass fabric/epoxy laminated composite and the following process is used to integrate the CNT yarns into the fabric reinforcement. The CNT yarn requires unwrapping from the spool and careful inspection for defects such as sharp bends or frays, which can degrade both its mechanical and electrical properties. The CNT yarn is then secured to the head of a sewing needle and securely stitched into four layers of the glass fabric, which constitute the central layers of the laminated composite consisting of six or eight layers in this study. Before the first stitch is made, an artificial delamination may be inserted between the two central layers to control the location of the initiation of delamination growth. After stitching the CNT

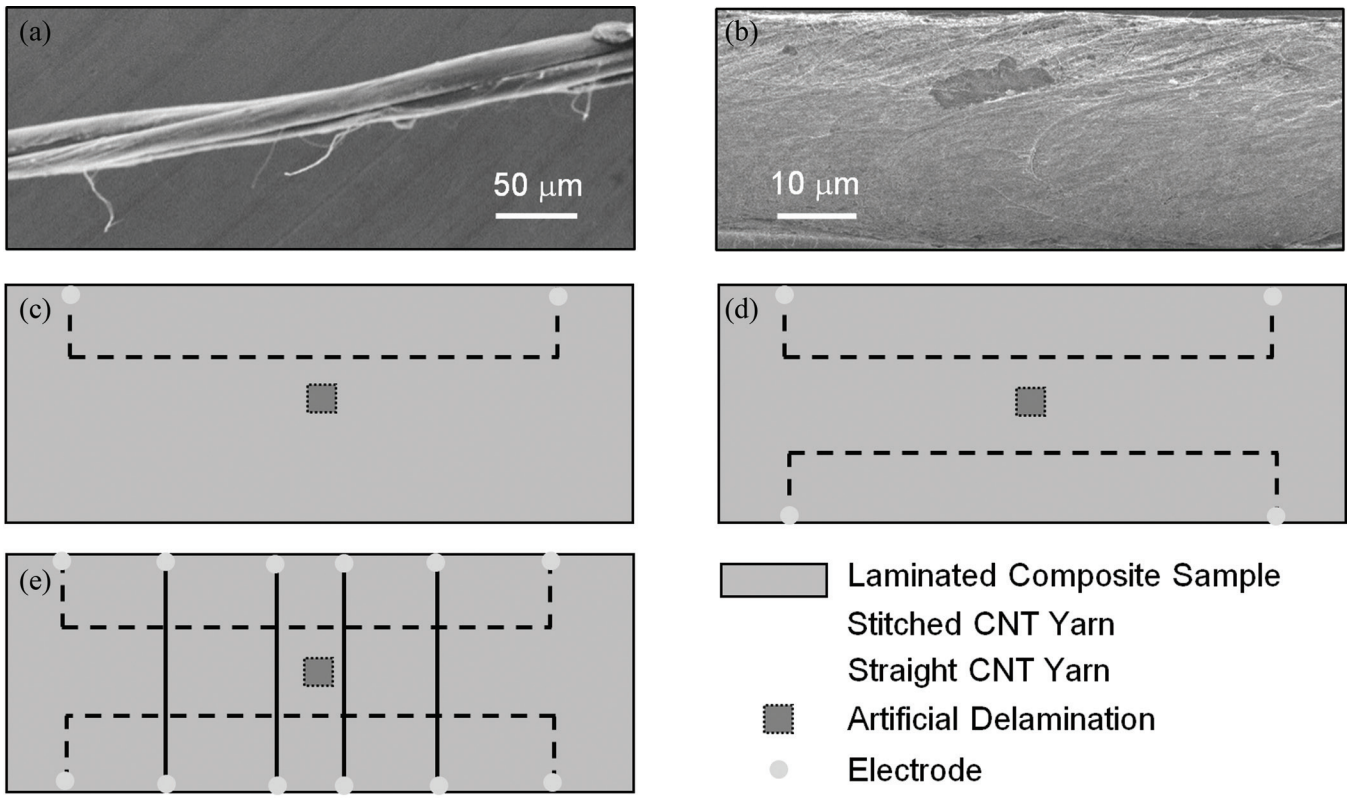


***Figure 1.*** *SEM images of CNT yarn used as the sensor in the self-sensing composite materials: (a) 3-thread yarn; (b) 1-thread yarn. Top view schematic configurations consisting of laminated composite samples instrumented with CNT yarn sensors: (c) single stitched yarn sensor; (d) dual stitched yarn sensor; (e) combined stitched and straight yarn sensors.*

yarns into the central layers, colloidal silver epoxy is applied at its ends to connect electrically the CNT yarns. The silver epoxy is applied in thin coats to the 3-mm-ends of CNT yarn and formed into a flat connector. Additional dry fabric layers are then added to complete the layup of the laminated composite. Figure 1(c)–(e) show schematics of the samples containing various configurations of the CNT yarn sensors. An optical image of a self-sensing laminated composite sample showing the silver epoxy electrodes is presented in Figure 2.

The next step in the composite fabrication process consists of the impregnation of the yarn sensor-integrated composite layers using a hand lay-up process. The polymeric phase consists of ToolFusion$^{TM}$, a room temperature-curing epoxy system composed of resin and hardener, which are combined in a 5:1 resin to hardener ratio. After impregnation, the layers are sandwiched between four layers of dry carbon fiber layers acting as bleeders in order to maintain an approximate 65% fiber volume fraction. The composite sample is then placed in a mold and cured under full vacuum and 480 kPa of pressure for ten hours. After the self-sensing composite sample is removed from the mold, the electrical connections are checked to make sure they are intact. At this point, more silver epoxy may be applied to the electrodes if needed.

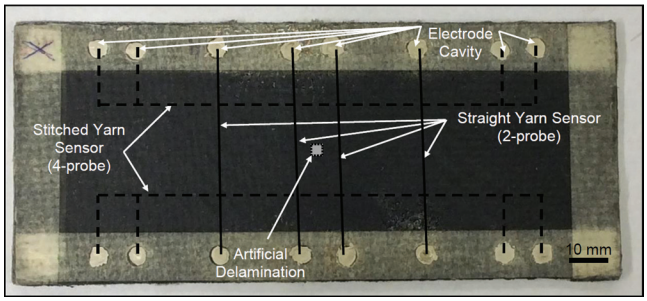


***Figure 2.*** *Optical image of a 6-layer glass/epoxy laminated composite sample and superimposed schematics of the integrated yarn sensors including stitched ones (through layers 2–5) and straight ones (between layers 2 and 3). Wires are later connected to the electrodes for resistance measurements.*

## 4. COUPLED MECHANICAL-ELECTRICAL MEASUREMENTS

The coupled mechanical and electrical characterization of the self-sensing composite samples requires accurate and sensitive testing equipment to capture load, displacement and resistance histories. An MTS Criterion 43, displacement-controlled mechanical testing platform fitted with a 30 kN-load cell, is used in combination with a 3-point bending fixture as shown in the schematic of Figure 3. Loading is

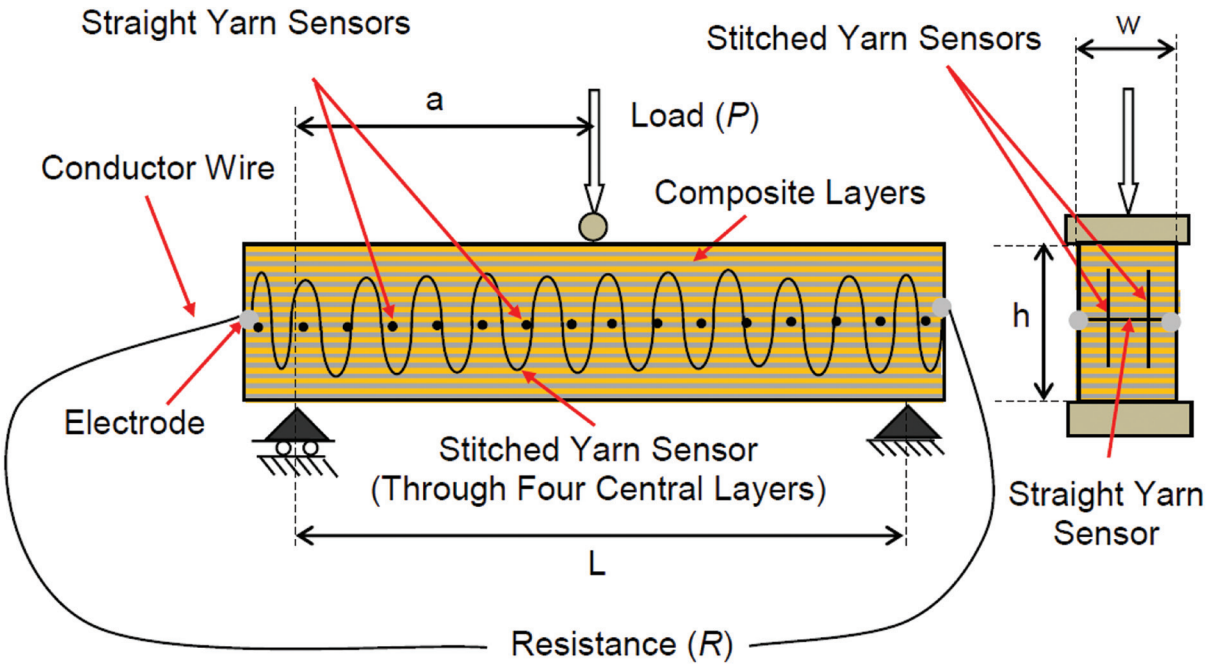


***Figure 3.*** *Schematic of experimental setup of self-sensing composite sample subjected to 3-point bending: side and end cross-sectional views of laminated composite beam sample instrumented with stitched and straight yarn sensors.*

monitored by a Testworks4 software controller that acquires load and displacement histories data at 1 Hz. To minimize the effect of the contact resistance, the two lower supports are positioned between the electrical connections of the stitched yarn sensor circuits, thus creating a zero stress area near the electrodes throughout the entire loading process. The self-sensing composite samples are loaded at a rate of 0.2 mm $min^{-1}$.

Electrical monitoring of the self-sensing composite samples requires a measurement system that can accommodate to the differences in the resistance ranges of each yarn sensor circuit. A National Instruments (NI) data acquisition chassis (DAq) Model 1978 equipped with a NI 9219 card is used along with a NI 4072 digital multi-meter (DMM) mounted on an NI PXI 1033 chassis. The DMM is capable of monitoring a single yarn sensor circuit at a time with a maximum resistance range of 1 MΩ while the DAq chassis can capture multiple yarn sensor circuits with a maximum range of 10.5 kΩ. The resistance monitoring is achieved with a NI LabVIEW Signal Express software program. After the self-sensing composite sample is secured in the 3-point bending fixture, electrical connections are made using small alligator clips. The resistance history data is acquired at a rate of 1 Hz.

## 5. DAMAGE DETECTION RESULTS

It has been demonstrated that CNT yarn sensors integrated in laminated composite materials are able to detect delamination [10]. The following results include the details of the damage detection and its localization and progression throughout the loading process in laminated composite materials. The mechanical/electrical response of self-sensing composite samples consisting of a glass plain weave architecture and sensor configurations like the ones indicated in Figure 1(c) and 1(d) is presented in Figures 4 to 7. Figure 4(a) shows the load, $P$, in terms of time, $t$, representing the load history and the resistance, $R$, in terms of time, $t$, representing the resistance history. Figure 4(b) shows the delta resistance, $\Delta R$, or the difference between the actual resistance and the initial resistance in terms of time, $t$, representing the delta resistance history. Delamination in the sample is identified by the sudden decrease of the maximum load in the load history curve (event A). Delamination is detected by the stitched yarn sensor as evidenced by the significant increase in the resistance and delta resistance (event B) and by the increase of the resistance to infinity (event C). The time delay between events A and B was 67 s. This delay apparently implies that the yarn sensor may not be able to capture the delamination instantaneously. However, as it can be observed in Figure 4(b), a significant change in delta resistance slope (event D) is noticeable 48 s before event A. The resistance increases by 137 Ω between events D and A, by 40 Ω between events A and B, and by 450 Ω between events B and E, where the significant increase in resistance immediately is halted after the delmination. This response of the yarn sensor demonstrates its ability to not only detect the delamination but also to anticipate it (event D) even before the load-history response of the laminated composite sample indicates it (event A). The corresponding deflections of this composite sample between events A and B is 0.68

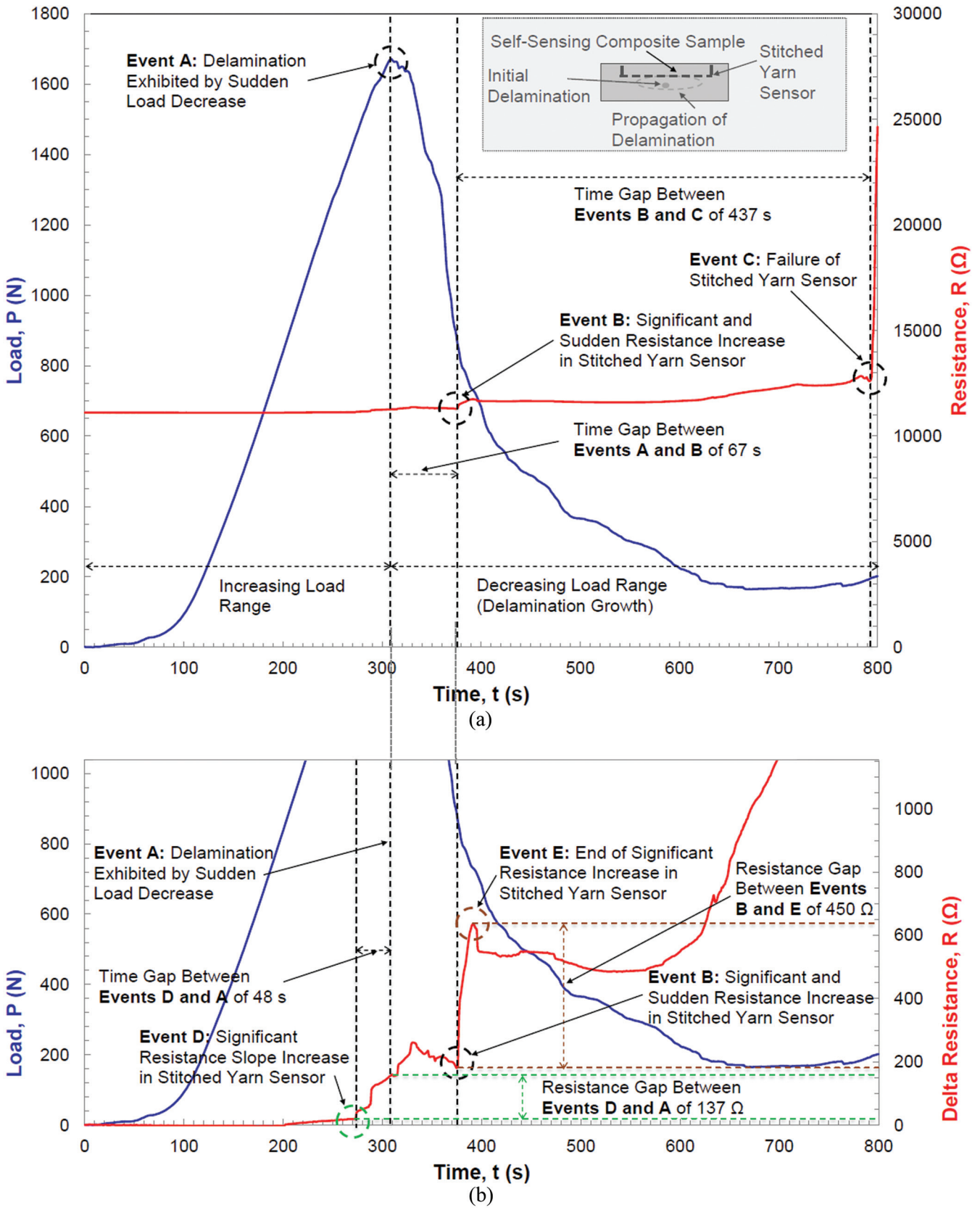


***Figure 4.*** *Detection of mode II-dominated delamination in 6-layer glass/epoxy laminated composite sample using a single stitched yarn sensor configuration. (a) Load and resistance versus time curves. (b) Load and delta resistance versus time curves.*

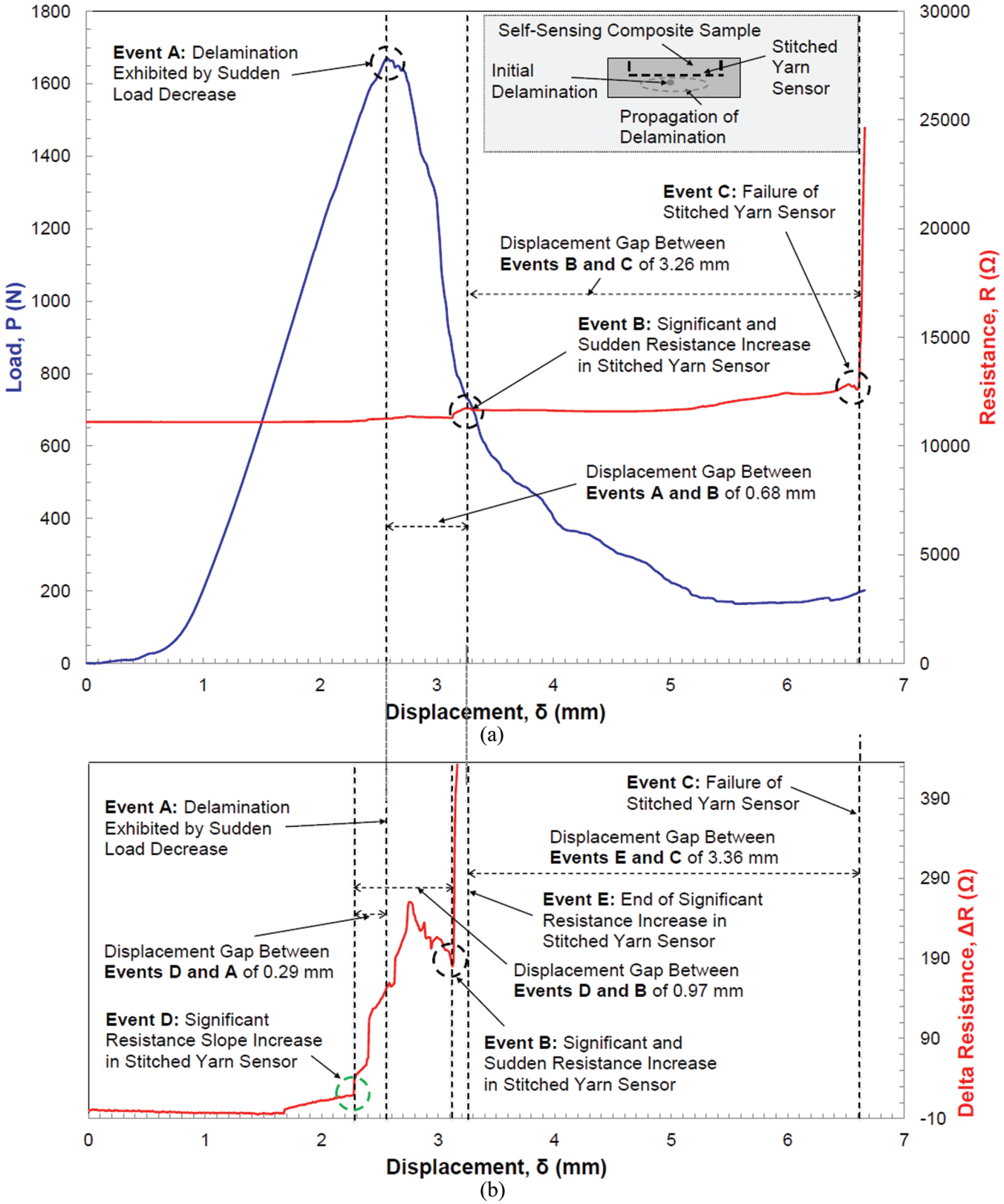


***Figure 5.*** *Detection of mode II-dominated delamination in 6-layer glass/epoxy laminated composite sample using a single stitched yarn sensor configuration. (a) Load and resistance versus displacement curves. (b) Delta resistance versus displacement curve.*

mm [Figure 5(a)], and 0.29 mm between events D and A [Figure 5(b)], respectively. In addition, the yarn sensor was able to withstand loading well in excess of the maximum load as well as capture the delamination without its circuit failing. The yarn sensor failed (event C) 504 s after event A as shown in Figure 4(a).

In order to detect minor damage prior to major delamination, the self-sensing composite samples were loaded and unloaded within the elastic region [13]. A small amount of internal damage occurred and it was revealed as a load reduction of 2 N (event F) as shown in Figure 6. It was also observed that the yarn sensor experienced an increase in the resistance of 1.2 Ω (between events G1 and H1) with a time delay of 14 s between events F and H1 (Figure 6). The corresponding deflection between these two events was determined to be 0.05 mm.

Since the laminated composite samples were subjected to bending loading, the sections of the yarn sensor in the upper portion of the beam (above the neutral axis) undergo compressive strains and those in the lower portion of the beam (below the neutral axis) undergo tensile strains. Consequently, the overall resistance of the stitched yarn sensor includes contributions to the resistance from the yarn sections under tension and from those under compression. It had been determined that the piezoresistive response of the unconstrained yarn under uniaxial tension exhibits a piezoresistivity that is dependent on the strain rate [14,22]. The piezoresistive response of the CNT yarn under uniaxial compression is currently being investigated. The corresponding responses of the CNT yarn embedded in a polymer under tension and compression are also being determined. The initial decrease in the overall resistance of the CNT yarn inside the composite beam may be explained once the previous responses are obtained and the corresponding modeling results become available.

In order to confirm the results obtained with one yarn sensor, a configuration like that in Figure 1(d) consisting of two yarn sensors was used to monitor damage and delamination. An artificial delamination of 1 cm in diameter was centered between the two yarn sensors allowing a gap of 2.5 mm be-

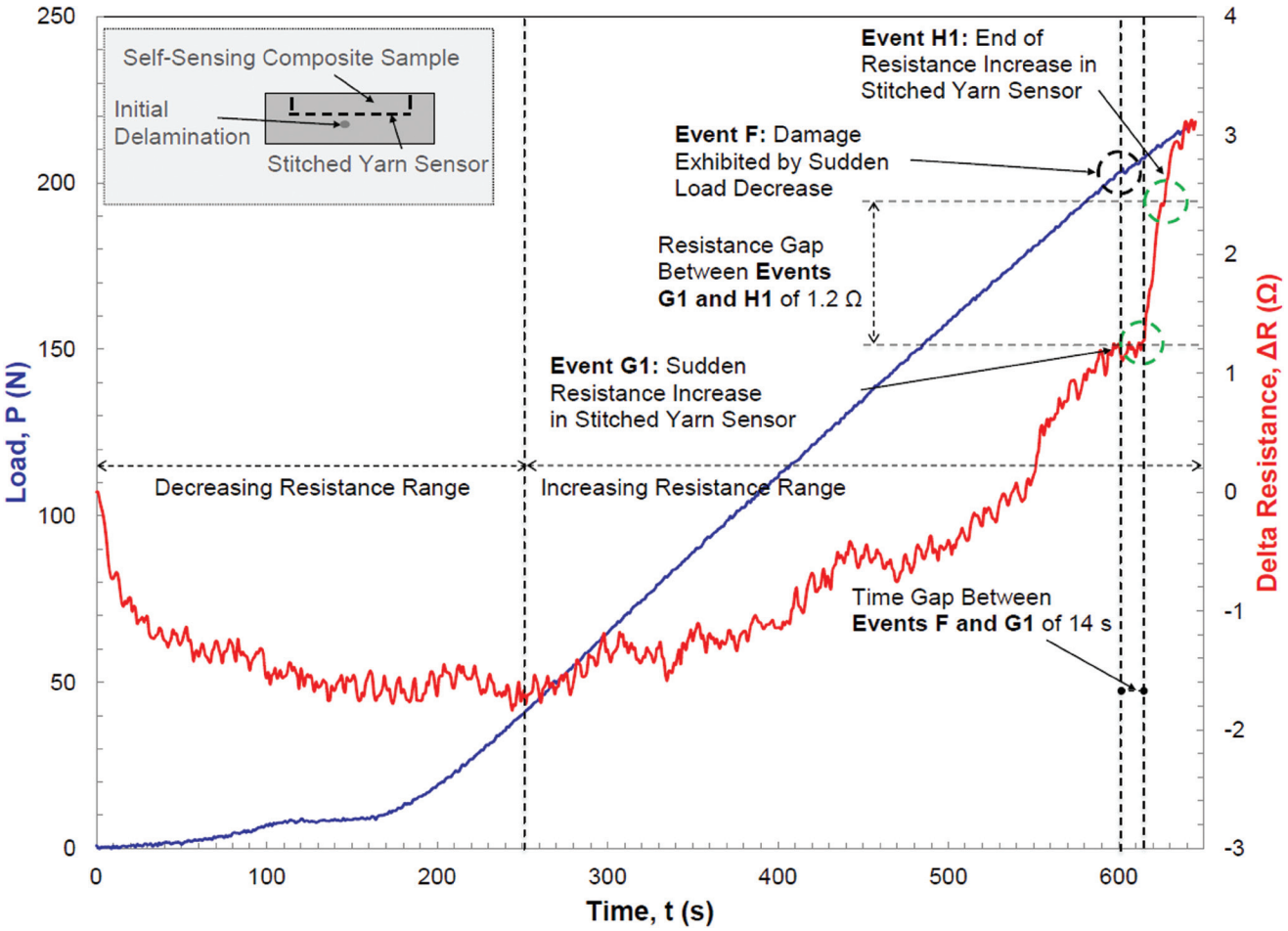


***Figure 6.*** *Detection of minor damage in 6-layer glass/epoxy laminated composite sample using a single stitched yarn sensor configuration: load and delta resistance versus time curves. The minute reduction in the load history curve indicates the presence of microscopic damage, which is detected by the yarn sensor after a few seconds in the form of a significant resistance increase.*

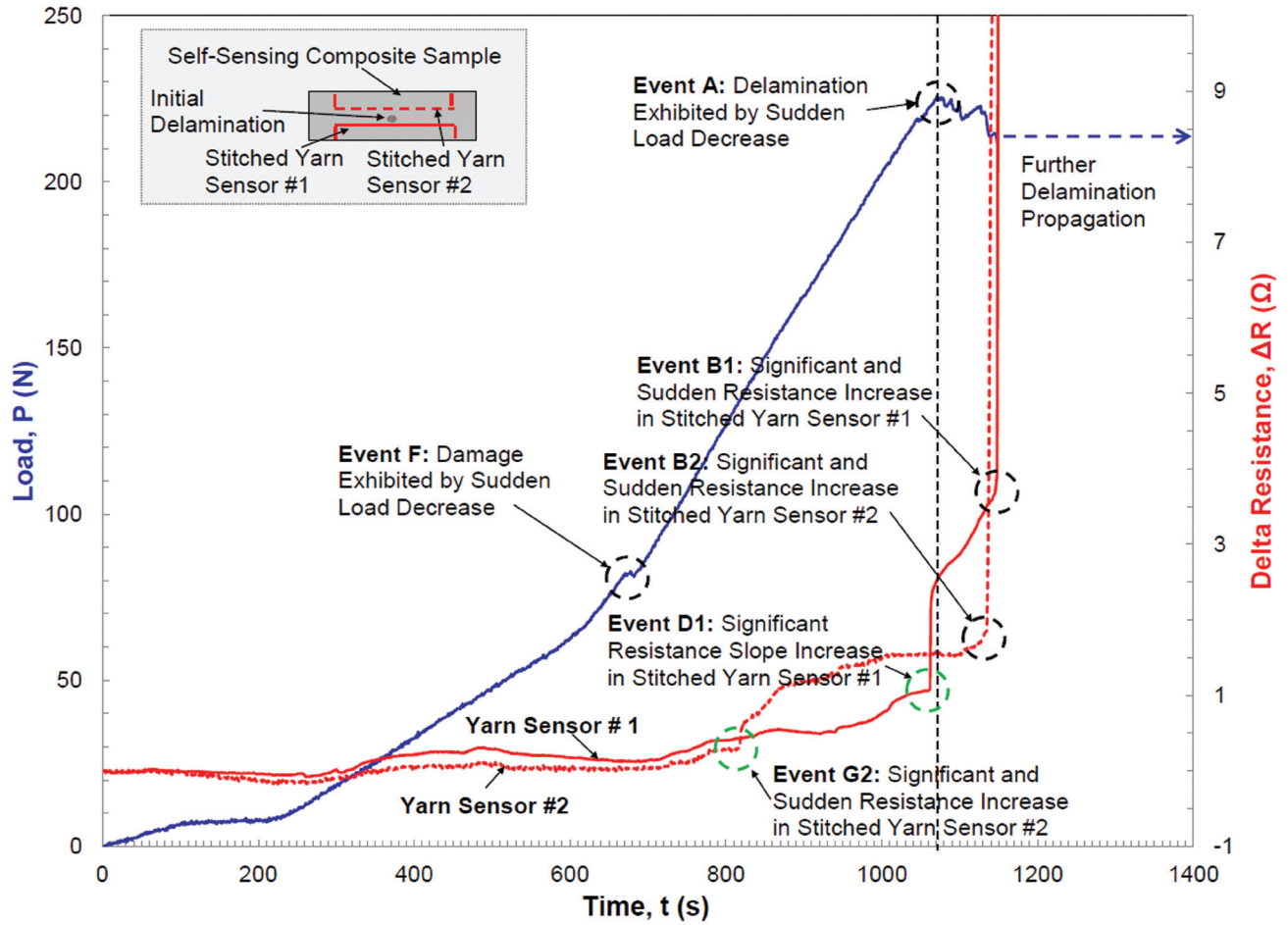


***Figure 7.*** *Detection of minor damage and mode II-dominated delamination in 6-layer glass/epoxy laminated composite sample using a double stitched yarn sensor configuration: load and delta resistance versus time curves. Both reductions in the load history curve indicating first, the presence of microscopic damage, and later, delamination, are detected by the stitched yarn sensors after a few seconds as demonstrated by events G2, D1 and B1 and B2.*

tween the yarn sensors and the delamination [13]. Figure 7 shows the load and the delta resistance histories of the two yarn sensors. It is observed that all the previously described events are also present and some occur almost simultaneously (time delay of 11 s between events B1 and B2). The D event, associated with the anticipation of an impending delamination, is obvious in CNT yarn sensor #1 (event D1). The G event, associated with the sensor's response to a minor damage in the sample, is obvious in CNT yarn sensor #2 (event G2). Both yarn sensors withstood the applied load and responded in a similar way demonstrating a relatively symmetrical growth progression of the initial delamination.

The determination of the exact location of delamination and its progression in the laminated composite samples can be achieved with a configuration consisting of a combination of different yarn sensors like the one shown in Figure 1e, which includes stitched yarn sensors and straight cross wide yarn sensors. The through-the-thickness stitched yarn sensors allow the determination of delamination but only additional straight yarn sensors parallel to the composite laminate layers and along the beam's width direction are able to detect the precise location of the delamination or the damage. Figure 2 shows an image of a fabricated self-sensing composite sample containing both types of yarn sensors. It is worth mentioning that the straight yarn sensors were configured for two point probe measurements but the stitched sensors were set up for four point probe measurements so that contact resistance does not play any role. It is worth mentioning that damage detection based on a significant delta resistance increase does not need to rely on minute resistance measurements and thus two probe measurements are deemed appropriate and sufficient. Figure 8 shows the load and resistance histories of all the yarn sensors.

The two stitched yarn sensors, indicated as continuous and dotted red lines, respectively (stitched yarn sensor #1 and #2) in Figure 8, show sensitivity to the deformation throughout the entire loading process of the laminated composite sample as indicated by the initial resistance decrease followed by a resistance increase. They both detect the de-

lamination as shown by the corresponding jumps in the resistance and the time delay between these events (B1 and B2) is 151 s. This time delay could be attributed to a slight asymmetric growth of the initial delamination. In these particular experiments, four straight yarn sensors were placed as indicated in the inset of Figure 8. All the straight yarn sensors increase their resistance output during the entire loading process and delamination progress. Straight yarn sensor circuit #4, indicated as a continuous brown line in Figure 8, exhibits a resistance increase of about 4.3 Ω before failing and when the delamination reaches its location at about 280 s before the delamination reaches the first stitched yarn sensor. The two outer straight yarn sensors, indicated as a continuous green line (straight yarn sensor circuit #5) and as a continuous yellow line (straight yarn sensor circuit #6) in Figure 8, exhibit an increasing resistance of several ohms over time. However, these outer straight yarn sensors do not fail because the delamination does not reach them before the sample experienced a significant deformation and the test is stopped. The yarn sensor that is proximate to the load application point (straight yarn sensor circuit #3) in Figure 8 tends to exhibit significant noise due to the transversely compressive load exerted at the center of the beam that applies pressure on the sensor.

Many experiments were run using shorter beam configurations and it was observed consistently that the straight yarn sensor closest to the delamination fails first and subsequently the other straight yarn sensors fail as the delamination propagates and reaches their locations. The straight yarn sensors are being placed between the central layers of the laminate, and are thus not subject to bending stresses but only shear stresses. The correlation between the stress level and the resistance of the yarn sensor requires further investigation.

## 6. CONCLUSIONS

An experimental study was conducted to evaluate the ability of piezoresistive-based, integrated and distributed, carbon nanotube yarn sensors to detect minor damage and

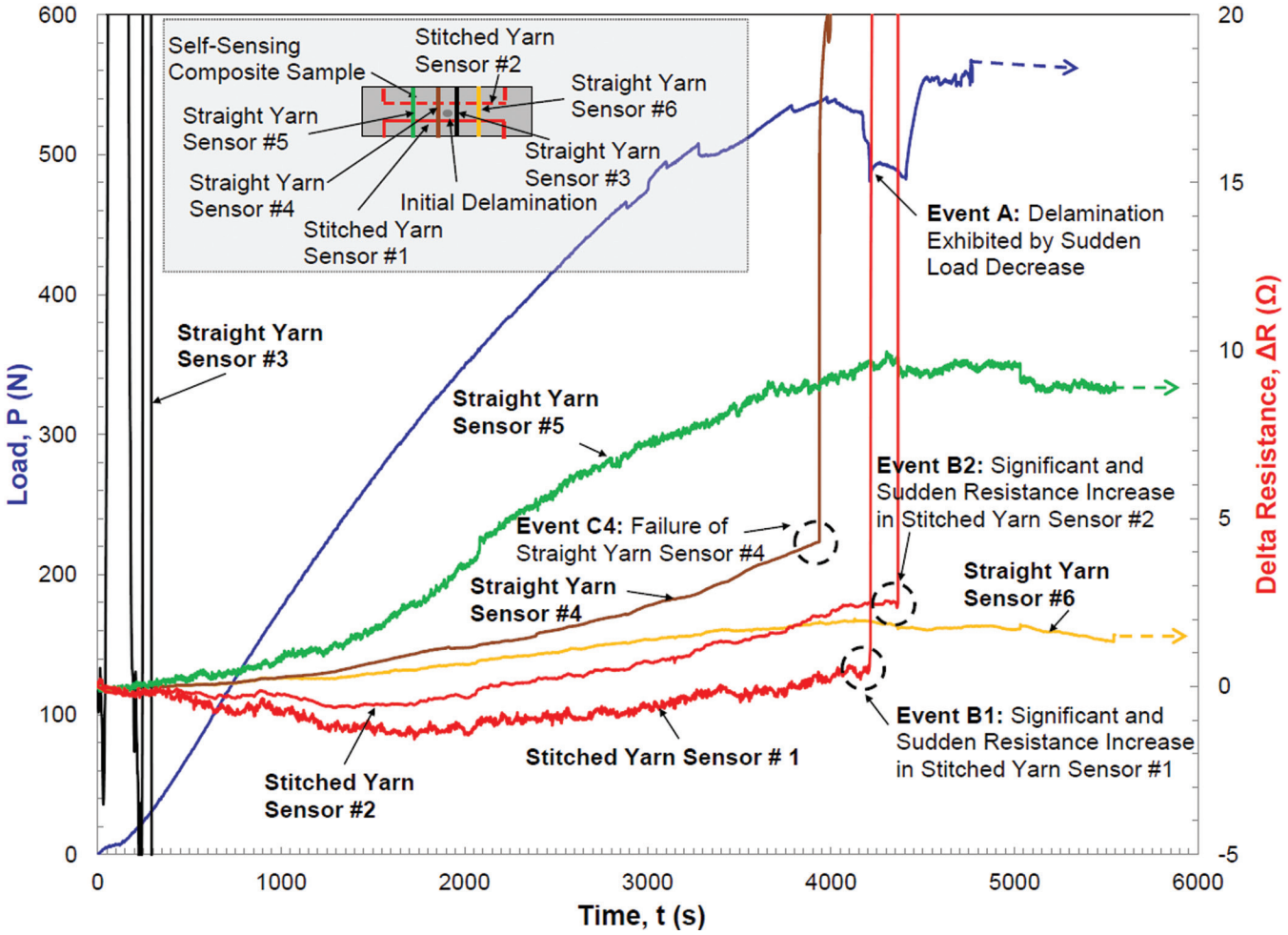


***Figure 8.*** *Localized detection of major delamination in 6-layer glass/epoxy composite sample using a combined stitched and straight yarn sensors configuration: load and delta resistance versus time curves.*

delamination in laminated composite materials, determine the specific location of the damage and delamination, and further understand the yarn sensors' response in this monitoring methodology. The study included monitoring the growth of preset delamination defects and randomly appearing damage during loading of glass fabric polymeric laminated composite samples using integrated yarn sensors. The study showed the ability of the yarn sensors to not only capture the delamination but also anticipate it as exhibited by a significant increase in the resistance of the stitched yarn sensors ahead of the delamination. The sensitivity of the yarn sensors is also exhibited by their ability to detect minor damage as demonstrated by a slight increase in their resistance immediately after the load experiences a small reduction. Despite the sensitivity of the integrated yarn sensors, they are able to sustain significant deformation and fail, as exhibited by their resistance increase to infinity, when the host laminated composite fails. The exact location and progression of a delamination was determined by additional straight yarn sensors that yield a higher resistance output when the delamination reaches their specific locations. All the previous findings further contribute to demonstrate the feasibility of a multi-sensor network of integrated and distributed carbon nanotube yarn sensors to monitor an entire designated area and pinpoint the exact location of damage. These carbon nanotube yarn sensors provide excellent piezoresistive response to loading without compromising the integrity of the laminated composite, offering thus the potential for developing a highly adaptive, practical, and sensitive structural health monitoring technique. However, many questions remain to be answered through more research including the correlation between the strain and the resistance in the yarn sensor for the different strain and damage levels in the host composite material.

## 7. ACKNOWLEDGEMENTS

The authors thank the following students at The Catholic University of America (CUA): Victor Casarotto, Tareq Alosh, Angeline Bajar, Michael-David Lamos, Edward Mitchell, Jason Quisberth and Alex Leo for their support to the experimental sections of this study; and also thank the machinist at CUA, Don Smolley, for the fabrication of testing fixtures. Abot and Belay acknowledge the financial support from the Air Force Office of Scientific Research (AFOSR) through Grants FA9550-10-1-0040 and FA9550-15-1-0177, both with program officer Dr. David Stargel.

## 8. REFERENCES

[1] Hellier C. Handbook of nondestructive evaluation, ed. 2. McGraw-Hill, Westminster, 2012.

[2] Boller C, Chang F−K, Fujino Y, editors. *Encyclopedia of structural health monitoring*. Wiley, Chichester, 2009. http://dx.doi.org/10.1002/9780470061626

[3] Dally JW, Riley WF. *Experimental stress analysis*, ed. 3. McGraw-Hill, New York, 1990.

[4] Middelhoek S, Audet SA. *Silicon sensors*. Delft University Press, Delft, 1994.

[5] Jiang KL, Li QQ, Fan SS. Nanotechnology: spinning continuous carbon nanotube yarns. *Nature* 2002;419(6909):801. http://dx.doi.org/10.1038/419801a

[6] Zhang M, Atkinson KR, Baughman RH. Multifunctional carbon nanotube yarns by downsizing an ancient technology. *Science* 2004; 306(5700):1358–1361. http://dx.doi.org/10.1126/science.1104276

[7] Behabtu N, Green MJ, Pasquali M. Carbon nanotube-based neat fibers. *Nano Today* 2008;3(5–6):24–34. http://dx.doi.org/10.1016/S1748-0132(08)70062-8

[8] Lu W, Zu M, Byun J–H, Kim B-S, Chou T–W. State of the art of carbon nanotube fibers: opportunities and challenges. *Advanced Materials* 2012; 24(14):1805–1833. http://dx.doi.org/10.1002/adma.201104672

[9] Park J, Lee K–H. Carbon nanotube yarns. *Korean Journal of Chemical Engineering* 2012;29(3):277–287. http://dx.doi.org/10.1007/s11814-012-0016-1

[10] Abot JL, Song Y, Sri Vatsavaya M, Medikonda S, Kier Z, Jayasinghe C, Rooy N, Shanov VN, Schulz MJ. Delamination detection with carbon nanotube thread in self-sensing composite materials. *Composites Science and Technology* 2010;70(7):1113–1119. http://dx.doi.org/10.1016/j.compscitech.2010.02.022

[11] Abot JL, Schulz MJ, Song Y, Medikonda S, Rooy N. Novel distributed strain sensing in polymeric materials. *Smart Materials and Structures* 2010;19(8):085007. http://dx.doi.org/10.1088/0964-1726/19/8/085007

[12] Jayasinghe C, Li W, Song Y, Abot JL, Shanov VN, Fialkova S, Yarmolenko S. Sundaramurthy S, Chen Y, Cho W, Chakrabarti S, Li G, Yun Y, Schulz MJ. Nanotube responsive materials. *MRS Bulletin* 2010;35(9):682–692. http://dx.doi.org/10.1557/mrs2010.680

[13] Wynter K. *Detecting failure in laminated composite materials using carbon nanotube yarn sensors*. Washington DC USA, Catholic University of America, MS thesis, 2013.

[14] Abot JL, Alosh T, Belay K. Strain dependence of electrical resistance in carbon nanotube yarns. *Carbon* 2014;70(4):95–102. http://dx.doi.org/10.1016/j.carbon.2013.12.077

[15] Daniel IM, Ishai O. *Engineering mechanics of composite materials*, ed. 2. Oxford, New York, 2006.

[16] Schulz M, Shanov V, Yin Z. *Nanotube superfiber materials: Changing engineering design*. Elsevier, Oxford, 2014.

[17] Jayasinghe C, Amstutz T, Schulz MJ, Shanov V. Improved processing of carbon nanotube yarn. *Journal of Nanomaterials* 2013;309617. http://dx.doi.org/10.1155/2013/309617

[18] Miao, M. Yarn spun from carbon nanotube forests: production, structure, properties and applications. *Particuology* 2013;11(4):378–393. http://dx.doi.org/10.1016/j.partic.2012.06.017

[19] Behabtu N, Young CC, Tsentalovich DE, Kleinerman O, Wang X, Ma AWK, Bengio EA, ter Waarbeek RF, de Jong JJ, Hoogerwerf RE, Fairchild SB, Ferguson JB, Maruyama B, Kono J, Talmon Y, Cohen Y, Otto MJ, Pasquali M. Strong, light, multifunctional fibers of carbon nanotubes with ultrahigh conductivity. *Science* 2013;339(6116):182−186. http://dx.doi.org/10.1126/science.1228061

[20] Lekawa-Raus A, Koziol KKK, Windle AH. Piezoresistive effect in carbon nanotube fibers. *ACS Nano* 2014;8(11):11214−11224. http://dx.doi.org/10.1021/nn503596f

[21] Lekawa-Raus A, Patmore J, Kurzepa L, Bulmer J, Koziol K. Electrical properties of carbon nanotube based fibers and their future use in electrical wiring, Advanced Functional Materials 2014;24(24):3661−3682. http://dx.doi.org/10.1002/adfm.201303716

[22] Anike, J.C., Bajar, A., and Abot, J.L. Time-dependent effects on the coupled mechanical-electrical response of carbon nanotube yarns under tensile loading. *J. Carbon Res.* (in press).

*Journal of Multifunctional Composites*, 2 (2014) 227–253

Journal of Multifunctional Composites

journal homepage: http://jmc.destechpub.com

# Experimental Characterization and Computational Modeling of Deformation and Damage Sensing through the Piezoresistive Response of Nanocomposite Bonded Surrogate Energetic Materials

ADARSH K. CHAURASIA[1], ENGIN C. SENGEZER[2], KRISHNA K. TALAMADUPULA[3], STEFAN POVOLNY[2] and GARY D. SEIDEL[2,*]

[1]*Department of Biomedical Engineering and Mechanics, Virginia Polytechnic Institute and State University, Blacksburg, VA 24061, USA*
[2]*Department of Aerospace and Ocean Engineering, Virginia Polytechnic Institute and State University, Blacksburg, VA 24061, USA*
[3]*Department of Mechanical Engineering, Virginia Polytechnic Institute and State University, Blacksburg, VA 24061, USA*

**KEYWORDS**

energetics
carbon nanotube
nanocomposite
piezoresistivity
cohesive zone
micromechanics

**ABSTRACT**

The current work aims to explore the potential for in-situ structural health monitoring in polymer bonded energetic materials through the introduction of carbon nanotubes (CNTs) into the binder phase as a means to establish a significant piezoresistive response through the resulting nanocomposite binder. The experimental effort herein is focused towards electro-mechanical characterization of surrogate materials in place of actual energetic (explosive) materials in order to provide proof of concept for the strain and damage sensing. The electrical conductivity and the piezoresistive behavior of samples containing randomly oriented, well dispersed MWNTs at concentrations of 0.09–0.6 %wt introduced into the epoxy binder of 70 %wt granulated sugar-epoxy hybrid composites are evaluated. In the computational modeling e.ort herein, the effective piezoresistive response of these nanocomposite bonded polymer explosives (NCBX) is evaluated using a computational micromechanics approach based on a 2-scale hierarchal model connecting the CNT-polymer nanocomposite scale (nanoscale) to the explosive grain structure scale (microscale). Scanning Electron Microscopy (SEM) based microstructure morphology of as-produced MWNT-sugar-epoxy hybrid composites is used to construct a representative microscale computational domain. The nanocomposite binding medium is modeled as electromechanical cohesive zones between adjacent explosive grains which are representative of effective electromechanical response of CNT-polymer nanocomposites. The effective electromechanical properties of CNT-polymer nanocomposites are obtained using the Mori-Tanaka method allowing for random and aligned orientations of CNTs within the binder. The real time in-situ electrical resistance measurements under quasi-static tensile loading obtained both experimentally and in computational modeling demonstrate the strain and damage sensing potential in hybrid composites.



## 1. INTRODUCTION

Energetic materials, such as polymer bonded explosives (PBXs) [1–9] which are composed of two phases, namely, the explosive material and a polymeric binder, are a class of composite materials designed to release high amounts of energy in response to a trigger. PBXs are used in various applications such as rocket propellants and detonators [10]. Typically, these energetic materials are comprised of explosive materials such as HMX (Octahydro-1,3,5,7-tetranitro-1,3,5,7-tetrazocine), RDX (1,3,5-Trinitroperhydro -1,3,5-triazine), PETN (pentaerythritol-tetranitrate), or TATB (triamino -trinitrobenzene) which are present in the composite in the form of small (~100 μm) crystals. Polymer binder materials, e.g. estane, are used in these composites

*Corresponding author. Phone: (540) 231-9897 Email: gary.seidel@vt.edu.


doi:10.12783/issn. 2168-4286/2.4/Chaurasia

*Journal of Multifunctional Composites*, 2 (2014) 227–253

Journal of Multifunctional Composites

journal homepage: http://jmc.destechpub.com

# Experimental Characterization and Computational Modeling of Deformation and Damage Sensing through the Piezoresistive Response of Nanocomposite Bonded Surrogate Energetic Materials

ADARSH K. CHAURASIA[1], ENGIN C. SENGEZER[2], KRISHNA K. TALAMADUPULA[3], STEFAN POVOLNY[2] and GARY D. SEIDEL[2,*]

[1]*Department of Biomedical Engineering and Mechanics, Virginia Polytechnic Institute and State University, Blacksburg, VA 24061, USA*
[2]*Department of Aerospace and Ocean Engineering, Virginia Polytechnic Institute and State University, Blacksburg, VA 24061, USA*
[3]*Department of Mechanical Engineering, Virginia Polytechnic Institute and State University, Blacksburg, VA 24061, USA*

**KEYWORDS**

energetics
carbon nanotube
nanocomposite
piezoresistivity
cohesive zone
micromechanics

**ABSTRACT**

The current work aims to explore the potential for in-situ structural health monitoring in polymer bonded energetic materials through the introduction of carbon nanotubes (CNTs) into the binder phase as a means to establish a significant piezoresistive response through the resulting nanocomposite binder. The experimental effort herein is focused towards electro-mechanical characterization of surrogate materials in place of actual energetic (explosive) materials in order to provide proof of concept for the strain and damage sensing. The electrical conductivity and the piezoresistive behavior of samples containing randomly oriented, well dispersed MWNTs at concentrations of 0.09–0.6 %wt introduced into the epoxy binder of 70 %wt granulated sugar-epoxy hybrid composites are evaluated. In the computational modeling e.ort herein, the effective piezoresistive response of these nanocomposite bonded polymer explosives (NCBX) is evaluated using a computational micromechanics approach based on a 2-scale hierarchal model connecting the CNT-polymer nanocomposite scale (nanoscale) to the explosive grain structure scale (microscale). Scanning Electron Microscopy (SEM) based microstructure morphology of as-produced MWNT-sugar-epoxy hybrid composites is used to construct a representative microscale computational domain. The nanocomposite binding medium is modeled as electromechanical cohesive zones between adjacent explosive grains which are representative of effective electromechanical response of CNT-polymer nanocomposites. The effective electromechanical properties of CNT-polymer nanocomposites are obtained using the Mori-Tanaka method allowing for random and aligned orientations of CNTs within the binder. The real time in-situ electrical resistance measurements under quasi-static tensile loading obtained both experimentally and in computational modeling demonstrate the strain and damage sensing potential in hybrid composites.



## 1. INTRODUCTION

Energetic materials, such as polymer bonded explosives (PBXs) [1–9] which are composed of two phases, namely, the explosive material and a polymeric binder, are a class of composite materials designed to release high amounts of energy in response to a trigger. PBXs are used in various applications such as rocket propellants and detonators [10]. Typically, these energetic materials are comprised of explosive materials such as HMX (Octahydro-1,3,5,7-tetranitro-1,3,5,7-tetrazocine), RDX (1,3,5-Trinitroperhydro -1,3,5-triazine), PETN (pentaerythritol-tetranitrate), or TATB (triamino -trinitrobenzene) which are present in the composite in the form of small (~100 μm) crystals. Polymer binder materials, e.g. estane, are used in these composites

*Corresponding author. Phone: (540) 231-9897 Email: gary.seidel@vt.edu.


doi:10.12783/issn. 2168-4286/2.4/Chaurasia

which typically constitute around 10% or less of the volume. The overall mechanical properties of the composite are largely determined by the polymer binder because of relatively larger compliance when compared to explosive grains. In addition, the polymer binder contributes significantly to the improvement of the toughness and impact tolerance of such composites [11].

Numerous experimental tests have been performed on energetics and mock/surrogate materials over the years of energetics development. These mock/surrogate materials have similar microstructural features and mechanical properties as the energetic crystals, but they are non-energetic which makes them safer to work with. Peeters [1] *et al.* performed tensile and compression testing for different strain rates at room temperature on PBX 9501, PBX 9502 and 900-10 mock materials, as wells as creep and cyclic tests for each material not only to provide a data set for energetic materials constitutive model development, but also to obtain a phenomenological characterization of energetics. Liu *et al.* [2] fabricated PBX 9502 specimens containing a cavity in order to investigate damage initiation, progression and cracking under compression. It was observed that the non-uniform stress distribution around cavity in the energetic material resulted in the development of microcracks under compression. Liu *et al.* [3] also examined the aging effects in high explosives. Brazilian disk samples made of pristine and artificially aged PBX 9501 materials were subjected to compression testing at different temperatures in conjunction with digital image correlation in order to observe microcrack initiation, propagation and accumulation. Aged PBX 9501 samples were much weaker and much more brittle than pristine ones, leading to easier macroscopic cracking. Liu *et al.* [4] investigated the fracture process of PBS 9501 sugar mock, a PBX 9501 high explosive simulant mock. The most dominat mechanical failure mechanism in high explosives of microcrack initiation and propagation was similarly observed in PBS 9501 sugar mock material. It was also observed that crystal interlocking and friction along with binder stretching contributed to the formation and extension of stress-bridging zones, leading to crack bridging processes. Liu *et al.* [5] also tested Mock 900-21, a PBX 9501 high explosive simulant which was subjected to monotonic and cyclic loading in order to assess the macroscopic crack formation and its extension in these materials. It was postulated that the heterogeneity in the microstructure of the energetic material led to macroscopic crack formation under cyclic loading at load levels which were below the failure stresses observed for monotonic strain to failure.

Seidel *et al.* [12,13] developed viscoelastic cohesive zone models for highly filled polymers such as LX17, with a phenomenological damage law. They observed that cohesive zone models captured nonlinear material behavior, formation and coalescence of microcracks into macrocracks, and eventual failure which are typically observed in the experimental results. Barua *et al.* [14–16] studied the deformation and damage of PBX materials subjected to dynamic loading conditions using a cohesive zone finite element formulation. They concluded that the main form of deformation is debonding at the grain-binder interface which further leads to cracking and sliding of the grains. In addition, Panchadhara and Gonthier [17,18] used a Lagrangian finite and discrete element technique to study compaction of HMX under uniaxial deformation waves and Hardin *et al.* used a finite element framework to investigate thermomechanical response of polycrystalline-HMX [19].

The explosive event in PBX is usually divided into various stages: ignition, the growth of deflagration (burning) and de.agration to detonation transition (DDT). Usually, a shock impact event results in adiabatic compression of the material which generates enough heat to trigger the desired chemical reaction which leads to detonation immediately [20]. However, in many situations which involve accidental low velocity impact during transportation and handling or tool drop, inadvertent ignition of the energetic material can occur [21]. In order to assess the structural integrity of the composite in terms of the current deformation and damage state and prognostication of remaining life, it is anticipated that the piezoresistive response of carbon nanotube(CNT)-polymer nanocomposites can be exploited by infusing CNTs in the polymer binder phase. The CNT-polymer nanocomposites have been experimentally shown to exhibit an inherent piezoresistive response [22–28]. Nanocomposite gauge factors between 1 and 20 have been typically reported in the literature [22–28] in comparison to commercially available (metallic) strain gauges with gauge factor of 2. In order to ascertain CNT orientation effects on nanocomposite piezoresistivity, Sengezer and Seidel [29,30] dispersed aligned SWNTs in a blend of two different photopolymerizable monomers which consisted of urethane dimethacrylate (UDMA) and 1,6-hexanediol dimethacrylate (HDDMA). It was observed that the electrical resistance change of as-produced aligned nanocomposites subjected to cyclic tensile loading followed the applied deformation with no lag and the transverse piezoresistive response sensitivity surpassed the axial piezoresistive response. On a larger scale, Gao *et al.* [31] premixed 0.5 %wt MWCNTs in EPON 862 epoxy resin and used vacuum assisted resin transfer molding to produce $[0/90]_2$ cross-ply E-glass fiber composite laminates. Using quasi-static tension tests, the composite laminates were quasi static monotonic loaded until failure and cyclic loaded while simultaneously monitoring changes in the electrical resistivity and taking acoustic emission data. Piezoresistive response outperformed acoustic emission measurements by not only detecting the onset of damage prior to noticeable effects in the stress strain response, i.e. measuring instances of new damage initiation, but also in being able to provide continuous assessment of the damage state between damage initiation events.

The piezoresistive response in CNT-polymer nanocomposites originiates primarily from three factors, i.e. the evolution of CNT networks at the microscale [32,33], nanoscale electron hopping/quantum tunneling [33–39] and inherent CNT piezoresistivity [32,40–44] . Several modeling efforts [32,33,35,45,46] have attempted to model the CNT-polymer piezoresistive response by idealizing the nanotubes as rigid members dispersed in the polymer medium forming a 2-D or 3D stick network. For the electrical problem, these nanotube networks are represented by an equivalent resistor network where each resistor represents either the CNT resistance or the intertube electron hopping/quantum tunneling resistance. These nanotube networks and corresponding resistance networks evolve on application of strains resulting in an effective piezoresistive response. Other modeling efforts [47–50] have tried to appropriately include the microstructure morphology and physical effects (e.g. Electron Hopping, inherent CNT piezoresistivity) starting at the nanoscale and transitioning them to the macroscale through micromechanics based homogenization schemes to explore the effective piezoresistive response of such nanocomposites.

In the current work, the electro-mechanical characterization of surrogate hybrid MWNT-sugar-epoxy composites is conducted in order to provide proof of concept for in-situ strain and damage sensing in nanocomposite bonded explosives. In addition, effective piezoresistive response of NCBX materials is studied computationally using a micromechanics based hierarchical multiscale framework where the nanocomposite binder is modeled through electromechanical cohesive zones representative of effective CNT-polymer piezoresistive response. It is expected that the results presented in the current work will provide basis to explore optimum NCBX microstructure for in-situ detection of strain and damage state.

## 2. EXPERIMENTAL INVESTIGATION

### 2.1. Fabrication of MWNT-sugar-epoxy Nanocomposites and Microstructural Morphology Assessment

In the present study, MWNTs and granulated sugar have been dispersed in 105 Epoxy Resin/206 Slow Hardener (West System) (being 5 parts 105 epoxy resin and 1 part 206 slow hardener). The epoxy system was selected as the binder for its general coating and bonding applications along with its low viscosity and very long working life at room temperature. The pristine MWNTs (PD15L15) (NanoLab) were reported to have a purity of more than 95%. The granulated pure cane sugar (Domino®) was used as a surrogate material in place of actual explosive materials. Neat sugar-epoxy samples were prepared with a weight ratio of 70/30 (corresponding to 72 %vol sugar) to obtain the neat sugar-epoxy mixture, with this ratio likewise being maintained in the preparation of hybrid binder samples having concentrations of 0.09, 0.15, 0.3 and 0.6 %wt MWNTs relative to the entire sugar-epoxy-MWNT sample (corresponding to 0.3, 0.5, 1 and 2 %wt MWNTs relative to the epoxy, respectively). In preparing hybrid composite samples, varying weight concentrations of MWNTs were added first to the lower viscosity (compared to epoxy) fast evaporating acetone solvent with 2.5 ml acetone used for each 0.01 grams of MWNTs. MWNTs were dispersed in acetone using a bath sonication for one hour with a QsonicaSonicator 4000 operating at 20 kHz and amplitude of 25% in order to obtain a more uniform initial dispersion of MWNTs. 105 Epoxy resin was added to the predispersed MWNTs-acetone solutions and resonicated for an additional hour with the same settings to obtain a homogeneous MWNT distribution within the epoxy. Acetone was evaporated from the solutions using a Buchi Rotavapor RII rotary evaporator with a heating bath at 35°C. The aforementioned curing agent and 70 %wt (72 %vol) surrogate material (granulated pure cane sugar) was then added to evaporated solution and blended thoroughly using mechanical stirring with tongue depressors. The prepared mixtures were cast into silicon molds and cured at room temperature for 24 hours. Figure 1(a) shows the resulting specimens prepared for quasi-static tensile testing. The neat sugar-epoxy and MWNTs-sugar-epoxy hybrid composite specimens have a gauge length of 11 mm, rescaled from ASTM standard D638 for specimen type IV, with the loading exerted in longitudinal direction at a distance of 28.2 mm between the grips.

Both the neat and hybrid surrogate material samples have inherently multiscale material architectures with microstructural features ranging the nanoscale (nanotubes) and the mesoscale (nanotube network) in the hybrid material to the microscale (grains) and macroscale of both the neat and hybrid samples. In order to assess key morphological features of the as-produced neat sugar-epoxy and hybrid MWNT-sugar-epoxy composites such as MWNT and surrogate crystal distribution, Scanning Electron Microscopy (SEM and FE-SEM) was used. Figure 1 provides the SEM micrographs of neat-72 %vol sugar-epoxy fracture surface where the sugar crystal can be observed with associated length scales of ~ 200 μm. Additionally, regions of crystal pull-outs are observed in contrast to the polymer coated crystal surfaces. The surfaces of these pull-outs appear to have epoxy polymer left behind during the fracture event indicating that the fracture appears to have occurred in the binder phase.

Figure 2 shows SEM micrographs taken using Neo-Scope JCM-5000 Benchtop SEM for 0.6 %wt MWNT (2 %wt relative to epoxy)-hybrid composite fracture surfaces. As with the neat sugar-epoxy samples, sugar crystals, pull-outs and the polymer binder are visible in Figure 2(a) and the zoomed versions Figures 2(b) and 2(c). It is not until the scale is reduced to the order of 5 μm in Figure 2(d) that bundles/agglomerations of CNTs are observed in the form

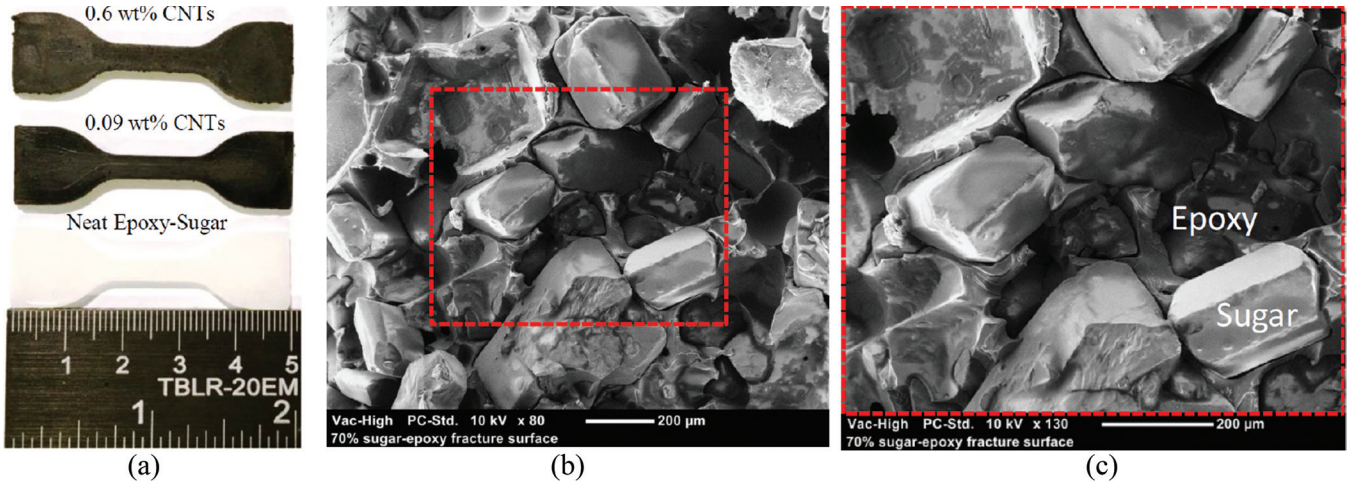


***Figure 1.*** *(a) As-produced, randomly oriented 0.6 wt%, 0.09 wt% MWNT-70 wt% sugar-epoxy, neat 70 wt% sugar-epoxy hybrid composites (wt% represents relative to the entire sugar-epoxy-MWNT sample), (b) and (c) SEM micrographs of neat-72 vol.% sugar-epoxy fracture surface.*

of white clouds/specs on the fracture surface in the local binder region. In order to confirm that the observed cloud-like structures are indeed bundles/agglomerations MWNTs, FE-SEM micrographs were taken using a LEO/Zeiss 1550 high-performance Schottky field-emission SEM as shown in Figure 3. Figures 3(a), 3(c) and 3(e) are micrographs taken of the fracture surface for the 0.09 %wt MWNT samples while Figures 3(b), 3(d) and 3(f) are taken from the fracture surface of a 0.6 MWNT %wt sample. It is observed that the FE-SEM provides the capability to go to 200 nm length scale

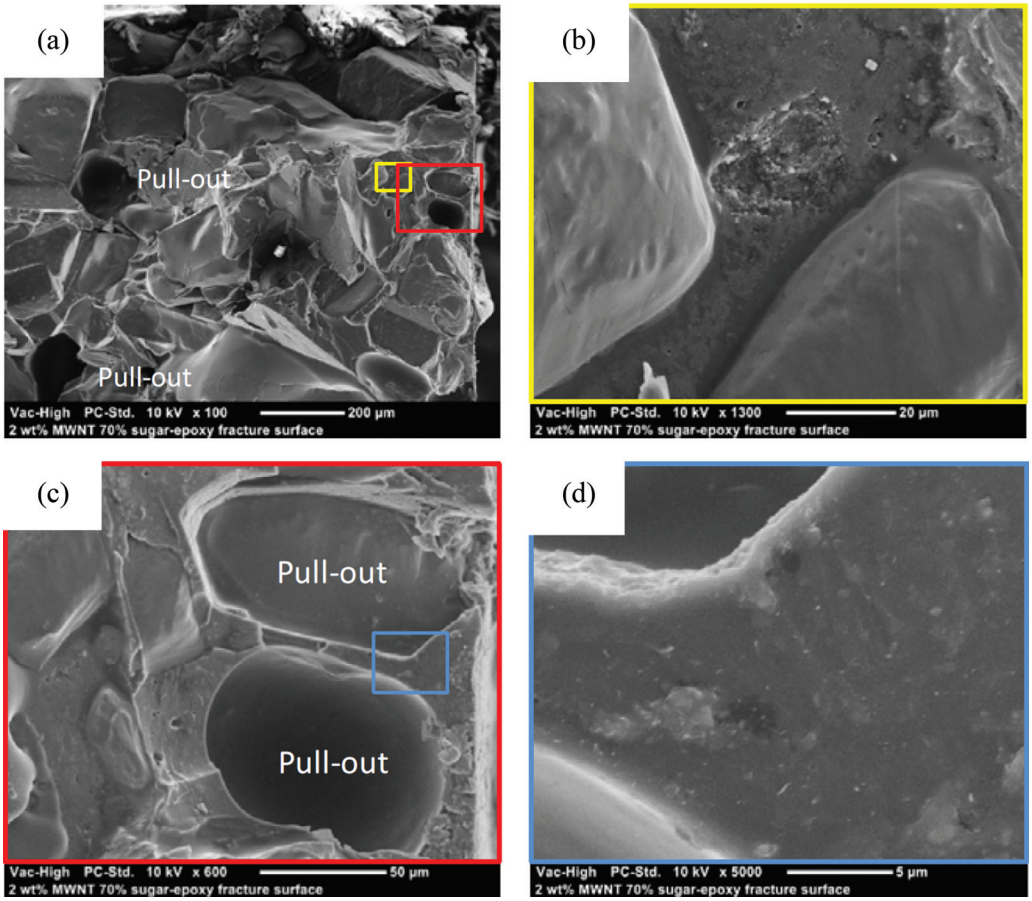


***Figure 2.*** *SEM photographs of hybrid composite fracture surface for 0.6 wt% MWNT (2 wt% relative to epoxy) samples at different zoomed scales. Pull-out refers to the surfaces left behind by sugar crystals pulling out during the fracture event.*

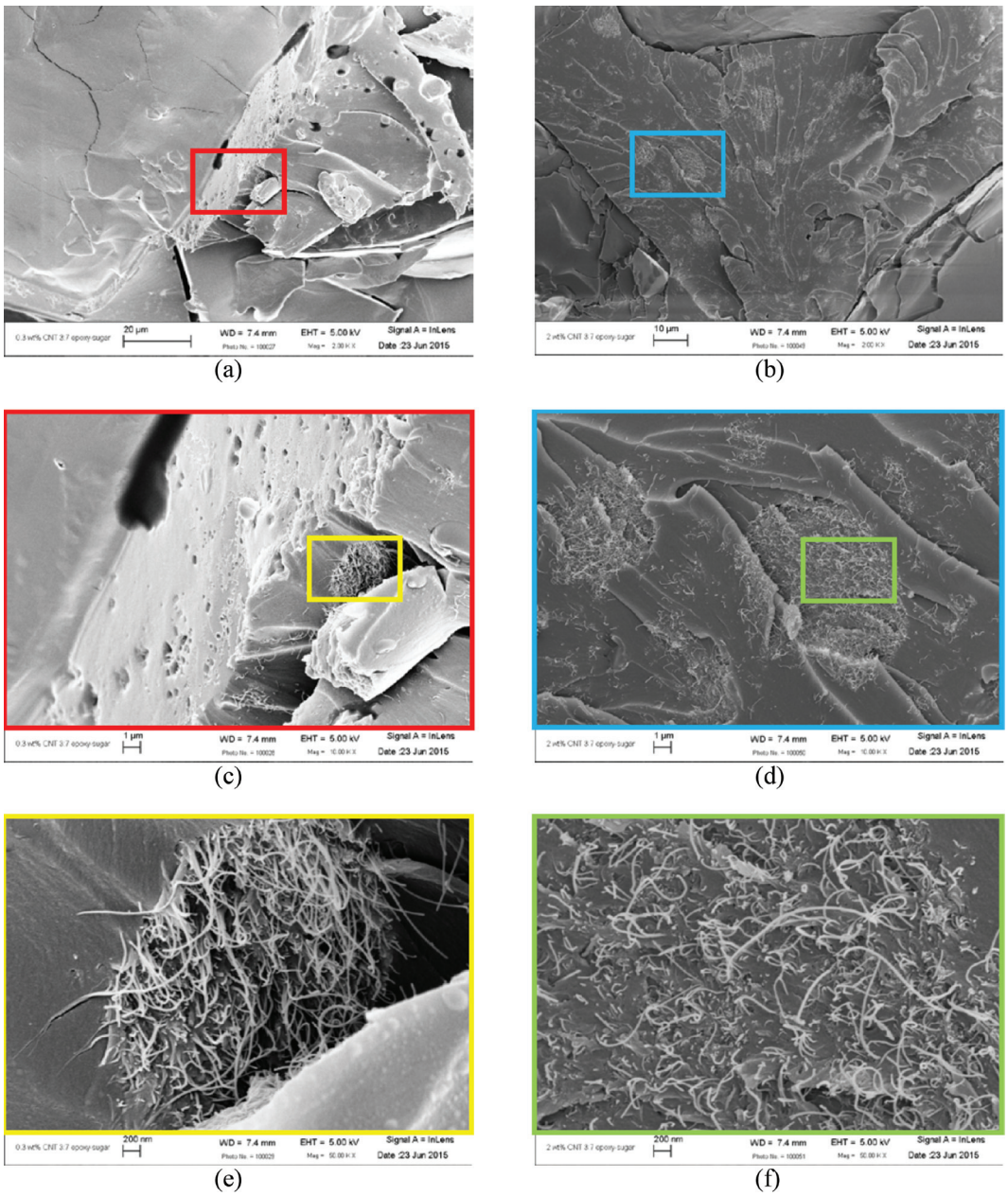


***Figure 3.*** *FE-SEM micrographs of fracture surface for (a),(c),(e) 0.09 %wt MWNT-sugar-epoxy (0.3 %wt relative to epoxy) samples, and (b),(d),(f) 0.6 %wt MWNT-sugar-epoxy (0.2 %wt relative to epoxy) samples.*

on the scale bars in Figures 3(e) and 3(f) which is much finer resolution (higher magnification) than the SEM pictures presented in Figure 2. The white cloud like structures observed in Figure 2 are also observed for both 0.09 and 0.6 %wt MWNT samples using the FE-SEM, as shown in Figures 3(a) and 3(b), respectively. On further zooming in to these clouds, a collection of individual MWNTs is observed where the MWNTs are sticking out of the fracture surface for each of the samples. It is to be noted that the white clouds comprised of a collection of MWNTs are more difficult to isolate for the 0.09 %wt as compared to the 0.6 MWNT %wt sample because of smaller weight concentration of MWNTs for the 0.09 %wt samples. It is further observed that the MWNTs are bundled/agglomerated in collections (local nanotube networks) within the local polymer binder which will have a significance in the measured macroscale properties of these nanocomposites.

### 2.2. Electrical Characterization of MWNT-Sugar-Epoxy Hybrid Nanocomposites

The electrical properties of as-produced neat sugar-epoxy and MWNT-sugar-epoxy hybrid composite samples were measured using an Agilent Technologies E4980A Preci-

sion LCR Meter. Conductive epoxy was used to connect the electrodes as shown in Figure 4. The conductive epoxy electrodes were cemented on top and bottom of the gauge section at distance 4 mm apart on alternate sides of the sample to obtain volume conductivity measurements. Figure 4 shows the log-log scale plot of the frequency dependence (range: 20 Hz–2 MHz) of absolute AC conductivity for as-produced hybrid composites. It is to be noted that the data presented in Figure 4 has error bars associated with each data point calculated by testing 8 different samples for each MWNT weight concentration. Neat sugar-epoxy composite conductivity is plotted to provide a baseline measurement to assess the effect of MWNT on the electrical conductivity.

For the neat sugar-epoxy samples, both the epoxy and the sugar crystals are expected to have very low conductivity and thus the effective composite displays strong insulator-like behavior, i.e. frequency dependence as a function of the input measurement frequency (20 Hz–2 MHz). The conductivity increases from ~2E-9 S/cm at low frequency (20 Hz) to 1E-5 S/cm at high frequency (1 MHz). On addition of highly conductive MWNTs, the conductivity of the MWNT-sugar-epoxy composite is observed to increase from that of the baseline sugar-epoxy composite. As an example, at 20 Hz input measurement frequency, the conductivity of the neat, 0.09, 0.15, 0.3 %wt MWNT hybrid composites is observed to be about 2E-9 S/cm, 6E-8 S/cm, 1E-7 S/cm and 4.4E-7 S/cm, respectively. The increase in effective conductivity is attributed to formation of conductive pathways within the local polymer binder (i.e. nanotube networks) which make the binder more conductive as MWNT weight concentration is increased. Large dependence of the conductivity on measurement frequency is still observed, therefore indicating that the as-produced MWNT-sugar-epoxy hybrid composites are still below percolation threshold[1], thus continuing to act more like an insulator than a conductor overall. In contrast, the effective conductivity for 0.6 %wt MWNT-sugar-epoxy hybrid composites demonstrated a four order of magnitude increase in conductivity at low measurement frequency (20 Hz) as compared to the neat sugar-epoxy samples corresponding to a value of 1E-5 S/cm. In addition, 0.6 %wt MWNT hybrid composites' conductivity was observed to be less frequency dependent as compared to the neat sugar-epoxy and the other MWNT weight concentration cases, which is an indication that the 0.6 %wt MWNT hybrid composites is transitioning towards percolation leading to a more conductive behavior. It is noted that at 20 Hz measurement frequency, conductivity measurements for the neat sugar-epoxy and low weight concentration (0.09, 0.15 %wt) CNT-sugar-epoxy hybrid composites show high degree of fluctuation because of their low conductivities. However, the observations made for 20Hz frequency remain

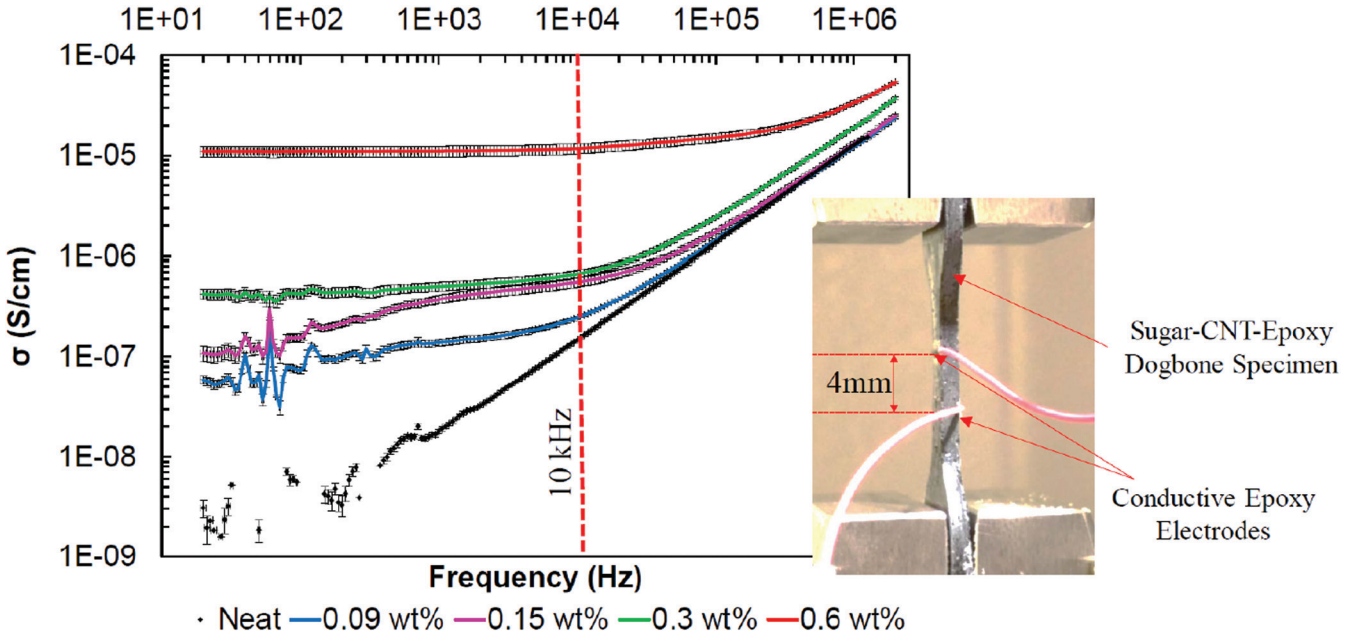


***Figure 4.*** *Assessment of neat and hybrid composite electrical conductivity at various measurement frequencies and at different MWNT concentrations. Inset shows conductive epoxy electrodes cemented on top and bottom of the gauge section of the dogbone specimen at a distance 4 mm apart to obtain volume conductivity measurements. The marked frequency (10kHz) indicates the frequency at which the resistance measurements were made during piezoresistive testing.*

[1]It is to be noted that percolation concentration mentioned here is for the entire MWNT-sugar-epoxy nanocomposite which is different from the local MWNT-epoxy percolation. Local percolation of the nanocomposite binder is difficult to assess from the macroscale testing performed herein. However, the percolation threshold for MWNT-epoxy nanocomposites has been reported in the literature to be in between 0.002 wt% to 5 wt% depending on the type of MWNT, aspect ratio and dispersion process [51].

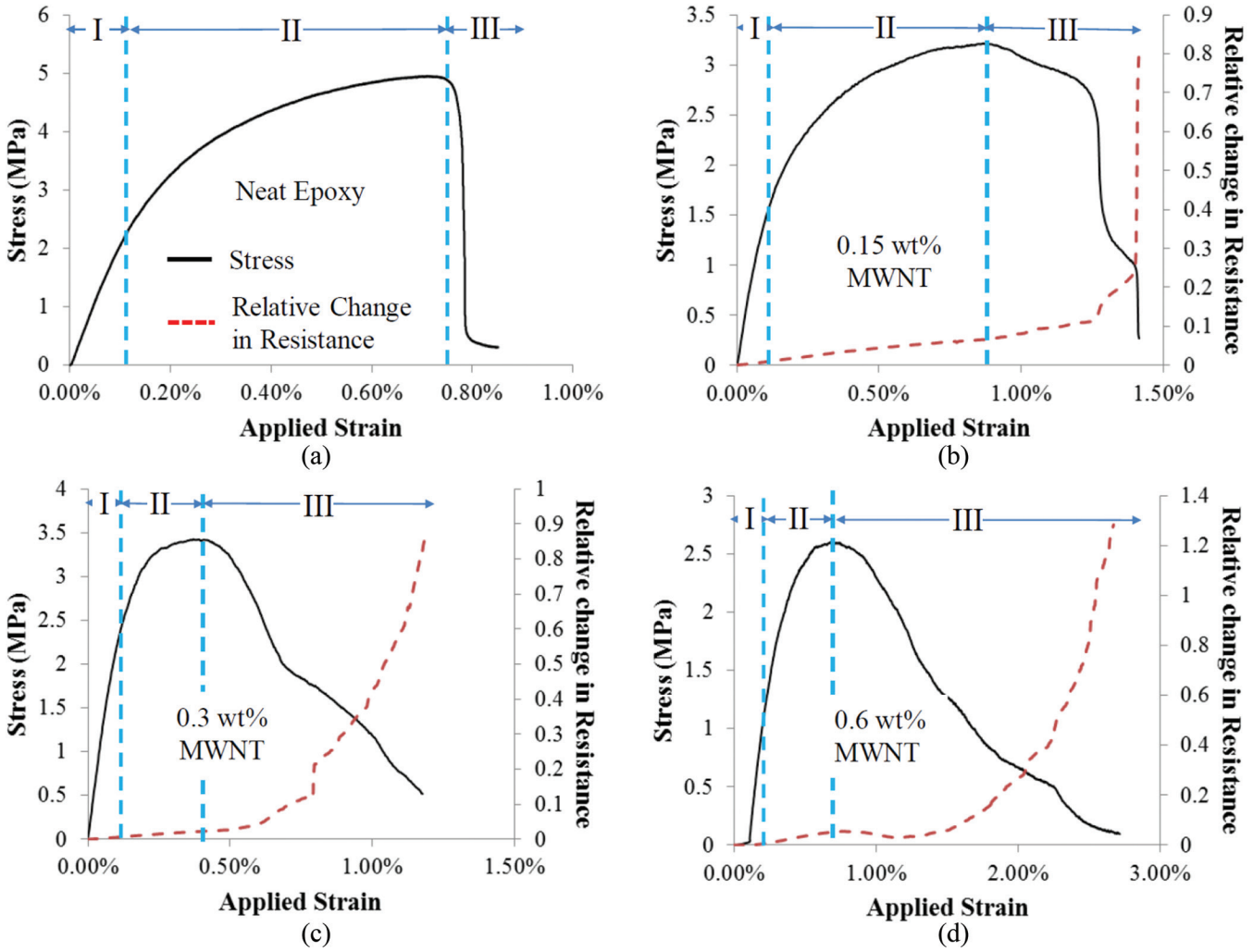


***Figure 5.*** *Stress-strain and relative change in resistance-strain response of as-produced hybrid composites (a) Neat sugar-epoxy, (b) 0.15 wt% MWNT hybrid composite (0.5 wt% relative to epoxy) $R_0$ = 16.53 MΩ, (c) 0.3 wt% MWNT hybrid composite (1 wt% relative to epoxy) $R_0$ = 11.7MΩ and (d) 0.6 wt% MWNT hybrid composite (2 wt% relative to epoxy) $R_0$ = 0.82 MΩ.*

true for larger frequencies. For example, at 1kHz applied frequency, the conductivity of the neat, 0.09, 0.15, 0.3 and 0.6 %wt MWNT concentration samples is observed to be about 1.1E-8 S/cm, 1.05E-7 S/cm, 1.3E-7 S/cm, 1.4E-7 S/cm and 1E-5 S/cm, respectively.

### 2.3. Piezoresistive Testing of MWNT-Sugar-Epoxy Hybrid Nanocomposites

The piezoresistive behavior of MWNT-sugar-epoxy hybrid composites was obtained using a two terminal method (volume resistivity test) applying 1 volt at 10 kHz, from an Agilent Technologies E4980A Precision LCR Meter while loading within an Instron testing system controlled by LabVIEW. Four specimens were tested for each MWNT weight concentration (0.15, 0.3 and 0.6%) for piezoresistivity measurements. The quasi-static tensile loading was applied at a constant rate of 0.025 mm/min which corresponds to a strain rate of 0.00089 mm/mm/min. An average resistance reading was obtained to detect strain and damage initiation as well as its progression under quasi-static loading. The volume piezoresistivity measurements were recorded in terms of relative resistance change ($\Delta R/R_0$) as the specimens underwent deformation, where $R_0$ was initial unstrained resistance. The piezoresistive sensitivity of randomly dispersed 0.15, 0.3 and 0.6 %wt MWNT-sugar-epoxy hybrid composites was quantified by defining the gauge factor as $G = (\Delta R/R_0)/\varepsilon$. It is to be noted that the symbol $G$ is reserved for gauge factors throughout the manuscript.

Figure 5(a) provides the baseline mechanical stress-strain response of neat sugar-epoxy samples. It is observed that the effective stress follows an initial linear elastic response up to about 0.1% applied strain, depicted by region I. The initial linear elastic stiffness of the neat sugar-epoxy composite is observed to be 2.08 ± 0.55 GPa, where the errors in initial stiffness are calculated by averaging over the initial response

of four different samples tested to ensure consistency of the experiments. Thereafter, the effective stress-strain response starts to deviate from the initial linear elastic behavior and the effective stiffness of the composite reduces monotonically in region II. The reduction in effective composite stiffness in region II is attributed to local damage in the polymer binder (microcracks) in response to local deformations on application of tensile strains which reduces the load carrying capacity of the composite. A peak stress of about 5MPa is observed at about 0.75% applied strain for the test presented here. Over four different samples, the peak stress was observed to be 4.60 ± 0.29MPa at an applied strain of 0.86 ± 0.26%. Finally, after the peak stress is reached, a sharp decline in effective stress is observed because of macroscale damage (macrocracks) of the composite dogbone specimen leading to complete failure at about 0.85% applied strain, as observed from region III in Figure 5(a)[2].

The effective stress-strain response of nanocomposite samples with addition of 0.15%wt of MWNTs to the epoxy binder are shown in Figure 5(b). The effective stress-strain response is observed to undergo an initial linear increase in effective stress (region I) on application of less than 0.1% strain. The initial stiffness averaged over four 0.15%wt MWNT samples is observed to be 1.76 ± 0.33GPa, which is about 18% smaller than the neat polymer samples in comparing the mean values. The stress-strain response undergoes a similar behavior as was observed for the neat polymer samples progressing through a non-linear region (region II) as the sample develops microcracks up to an average peak stress of about 3.29 ± 0.08MPa at an average strain of 1.06 ± 0.10%. While the average peak stress for the 0.15%wt MWNT samples is observed to be 40% smaller than that of the neat polymer samples, the strain to failure (region III) is observed to be 1.40% which is 64% larger than that observed for the neat epoxy shown in Figure 5(a).

In terms of the piezoresistive response of the 0.15%wt MWNT samples, the relative change in resistance follows a linear increase in initial linear elastic region I with a gauge factor ($G^I$) of 7.74 calculated at 0.1% applied strain. The observed relative change in resistance for region I can be attributed to the local deformations of the inherently piezoresistive MWNT-epoxy binder in absence of interfacial damage for low values of applied strains. It is to be noted that the inherent MWNT-polymer piezoresistivity is dependent on several factors including CNT network arrangement/morphology distribution [32,33] and electron hopping/quantum tunneling [33–39]. However, isolation of dominant piezoresistive mechanism in the local interfacial binder is diffcult based on the macroscale tests conducted herein. On further application of strain, a linear increase in relative change in resistance is observed in region II with the corresponding gauge factor ($G^{II}$) of 7.49 calculated at the strain corresponding to peak stress (0.9%). The observed gauge factor for region II starts to include the effect of local microcracks developing within the polymer binder medium and at the binder-crystal interfaces. Finally, development of macrocracks in region III leads to a non-linear evolution of relative change in resistance which can be closely correlated to the corresponding changes in the stress-strain response. An effective gauge factor ($G^{III}$) of 16.19 is observed just before the failure strain (1.4%) indicating large scale damage of the dog-bone specimen.

For the 0.3%wt MWNT samples, stress-strain response regions similar to those observed for 0.15%wt MWNT case are observed, i.e. linear elastic region I, microcracks based stiffness reduction in region II and macrocracks leading to eventual failure in region III, as shown in Figure 5(c). The averaged initial stiffness of the 0.3%wt MWNT samples is observed to be 2.50 ± 0.26GPa, with an averaged peak stress of 3.66 ± 0.33MPa at an average applied strain of 0.36 ± 0.05%. The change in resistance follows an initial linear increase through regions I and II with effective gauge factors ($G^I$ and $G^{II}$) of 5.81 and 5.78, respectively, again similar to the 0.15%wt MWNT sample. Finally, in region III, macrocracks develop in the dog-bone sample resulting in loss of load carrying capacity leading to eventual failure at around 1.2% applied strain. The relative change in resistance, in region III, increases non linearly with close correlation to the reduction in effective stress leading to a gauge factor of 71.04 just before failure.

Finally, the 0.6%wt MWNT sample features similar behavior as was observed for the 0.15%wt and 0.3%wt MWNT in the stress-strain and relative change in resistance. The averaged initial stiffness of the 0.6%wt MWNT samples is observed to be 1.21 ± 0.06GPa, with an averaged peak stress of 2.70 ± 0.19MPa at an average applied strain of 0.55 ± 0.07%. The key parameters associated with the response are shown in Table 1 along with the 0.15%wt, 0.3%wt MWNT and neat epoxy samples, averaged over four different tests on different samples. It is observed that the mechanical response of the hybrid composites is close to the PBX-polymer energetics published in the literature [10] where an ultimate tensile strength between 3–5 MPa is reported with effective stiffness between 0.5–5 GPa. One of the key differences in the relative change in resistance for the 0.6%wt MWNT sample is that it exhibits a non-monotonic behavior unlike the other 0.15%wt and 0.3%wt MWNT cases for which the relative change in resistance increases monotonically. For such composites with granular composite microstructure, it is difficult to constrain the developing microcracks to initiate in the gauge section for the dog-bone samples like the ones tested here. In some cases, microcracks can develop outside of the gauge section which relax the local stresses in the gauge section. While this information is not represented in the effective stress which is calculated from the load cells

[2]The piezoresistive response for the neat sugar-epoxy hybrid composites was not measured since the relative change in resistance is expected to be insignificant.

***Table 1. Measured Stiffness, Ultimate Tensile Strength, Strain at Maximum Load and Gauge Factors in the Three Identified Regions for Randomly Oriented-well Dispersed MWNTs Hybrid Composites Before and After Damage Initiation and Propagation.***

| Specimen Cross-section | Initial Stiffness (GPa) | Ultimate Tensile Strength (MPa) | Tensile Strain at Maximum Load (%) | $G^{I}$ | $G^{II}$ | $G^{III}$ |
|---|---|---|---|---|---|---|
| Neat | 2.08 ± 0.55 | 4.60 ± 0.29 | 0.86 ± 0.26 | – | – | – |
| 0.15 wt% | 1.76 ± 0.33 | 3.29 ± 0.08 | 1.06 ± 0.10 | 7.74 | 7.49 | 16.19 |
| 0.30 wt% | 2.50 ± 0.26 | 3.66 ± 0.33 | 0.36 ± 0.05 | 5.81 | 5.78 | 71.04 |
| 0.60 wt% | 1.21 ± 0.06 | 2.70 ± 0.19 | 0.55 ± 0.07 | 3.21 | 8.53 | 49.21 |

(i.e. always outside the electrode gauge section), the effective resistance can reduce because of local relaxation of the specimen within the gauge section. Similar piezoresistive responses were observed for a handful of samples in which macrocracks were noted to occur outside of the electrodes, though alternative sources of such behavior can include complex rearrangements of the current carrying pathways as the interfaces separate. More direct correlations for such observations would require in-situ monitoring of the microstructure which is beyond the scope of the current work, but some of these mechanisms will be explored in the subsequent modeling results.

## 3. COMPUTATIONAL MODELING

### 3.1. Model Description

#### *3.1.1. Modeling Assumptions and RVEs*

A modeling idealization of separation of scales in NCBX nanocomposites goes through an effective homogeneous macroscale medium transitioning through the explosive crystal grain structure at the microscale [10] to the nanocomposite binding medium which has microstructural features (CNTs and CNT bundles/agglomerates) at the nanoscale [47]. At the microscale explosive grains are bound together with polymer nanocomposite with large grain volume fractions as shown in Figure 1. Thus, the polymer nanocomposite binder medium can effectively be thought of as a thin interface connecting the explosive crystals. The effective electromechanical response of the binding interface should then represent the effective electromechanical response of the CNT-polymer nanocomposite.

In the current work, the effective properties of CNT bundles [47–50] will be used in a micromechanics based homogenization framework to allow for random/aligned orientations of these bundles within the polymer matrix. The effective electromechanical properties of randomly oriented/aligned CNT-polymer nanocomposites obtained are then used to appropriately model the interfacial nanocomposite binder response. For the computational modeling of the explosive grain structure at the microscale, representative volume elements (RVEs) are constructed based on (1) idealized Voronoi Tessellation and (2) based on the SEM micrograph obtained in the current work shown in Figre 1(b). Figure 6(a) shows an idealized 10-grain RVE generated using Voronoi Tessellation. Figure 6(b) shows the SEM micrograph presented in Figure 1(b) overlaid with the iden-

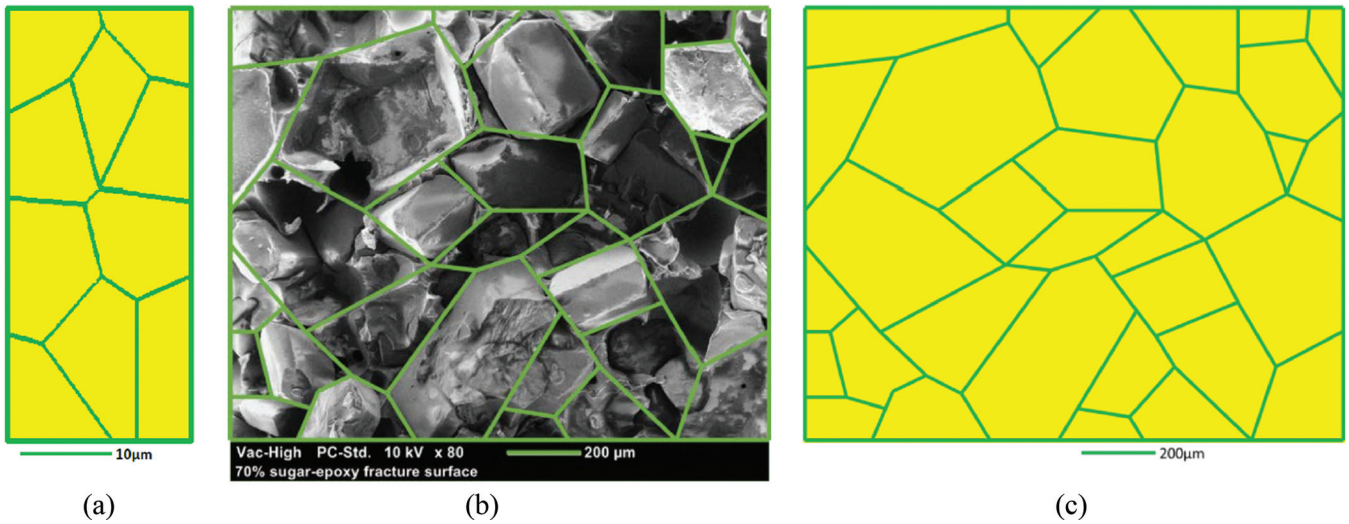


***Figure 6.*** *(a) An idealized 10-grain RVE generated using Voronoi Tesselation. (b) Identification of grains from SEM photographs of neat-72 %vol sugar-epoxy fracture surface, and (c) a 31-grain RVE inspired from the SEM microstructure morphology image in (b).*

tified crystal/grain structure used in building a 31-grain microscale RVE shown in Figure 6(c). It is to be noted that the idealized 10-grain RVE is constructed at a much smaller scale (~10 μm) as compared to the 31-grain RVE for demonstration with true micron sized grains which are typical to some explosive materials [7–9]. The microscale RVEs shown in Figures 6(a) and 6(c) are meshed using 3-noded linear triangular finite elements where each grain edge is resolved using 10 coincident node pair across the interface. The constitutive response of these initially coincident node pairs is governed by CNT-polymer nanocomposite based electromechanical cohesive laws which are dependent on the nanocomposite binder electromechanical properties and estimates of initiation and evolution of damage at the microscale.

### *3.1.2. Imperfect Interface Modeling through Cohesive Zones*

The nanocomposite binder medium between the explosive grains is modeled using electromechanical cohesive laws representing the electromechanical response of CNT-polymer nanocomposites through normal and tangential traction-separation laws combined with a normal interfacial resistance-interfacial separation law. These laws are constructed using micromechanics based homogenization techniques to evaluate the initial electromechanical properties of the CNT-polymer nanocomposites in addition to material properties such as experimentally observed cohesive fracture energy.

The cohesive interface response for the mechanical boundary value problem (BVP) is described in terms of bilinear normal and tangential traction-separation response as shown in Figure 7. The normal traction-separation response, shown in Figure 7(a), features an initial region of linearly increasing normal traction as the interface separation increases (A-B). This region represents the part of the interface response where the effective nanocomposite acts like a linear-elastic material for small magnitude of strains with no damage based reduction in the nanocomposite effective stiffness. The local cohesive zone stiffness in the undamaged initial linear elastic region is constant ($\tilde{K}_n^0$). Normal traction increases until it reaches the point of peak traction ($\tilde{t}_n^{\max}$ at B with interface separation, $\Delta\tilde{u}_n^{sw}$) where local cohesive zone damage starts to initiate in the form of a linear reduction in normal interfacial traction from the point of peak traction. The local cohesive zone stiffness at any general point, C, on the traction separation curve is then given by $\tilde{K}_n^C = \tilde{t}_n^C / \Delta\tilde{u}_n^C$, such that $\tilde{K}_n^C \le \tilde{K}_n^0$. The decreasing stiffness of the cohesive interface following the path B-C-D is representative of damaging nanocomposite binder medium where local damage results in reduced interface stiffness. The linear reduction in interfacial normal tractions with increasing interface separation continues until the normal interface separation becomes zero at D, at a normal interface separation of $\Delta\tilde{u}_n^{\max}$, i.e. complete failure of the cohesive zones.

The tangential traction-separation law, shown in Figure 7(b), features a similar bilinear behavior with an initial linear increase in tangential traction with increasing tangential interfacial separation in either direction (A-B). The local tangential stiffness of the cohesive zone in this region is constant and is given by $\tilde{K}_t^0$. However, once the tangential traction reaches the maximum value of $\tilde{t}_t^{\max}$ at B, with an interface separation of $\Delta\tilde{u}_t^{sw}$, the tangential traction undergoes a flat plateau region with constant tangential traction (BC) representing tangential sliding of the interface under frictional contact. The tangential stiffness at any general point is given by $\tilde{K}_t^C = \tilde{t}_t^C / \Delta\tilde{u}_t^C$, such that $\tilde{K}_t^C \le \tilde{K}_t^0$.

In addition to the normal and tangential traction-separa-

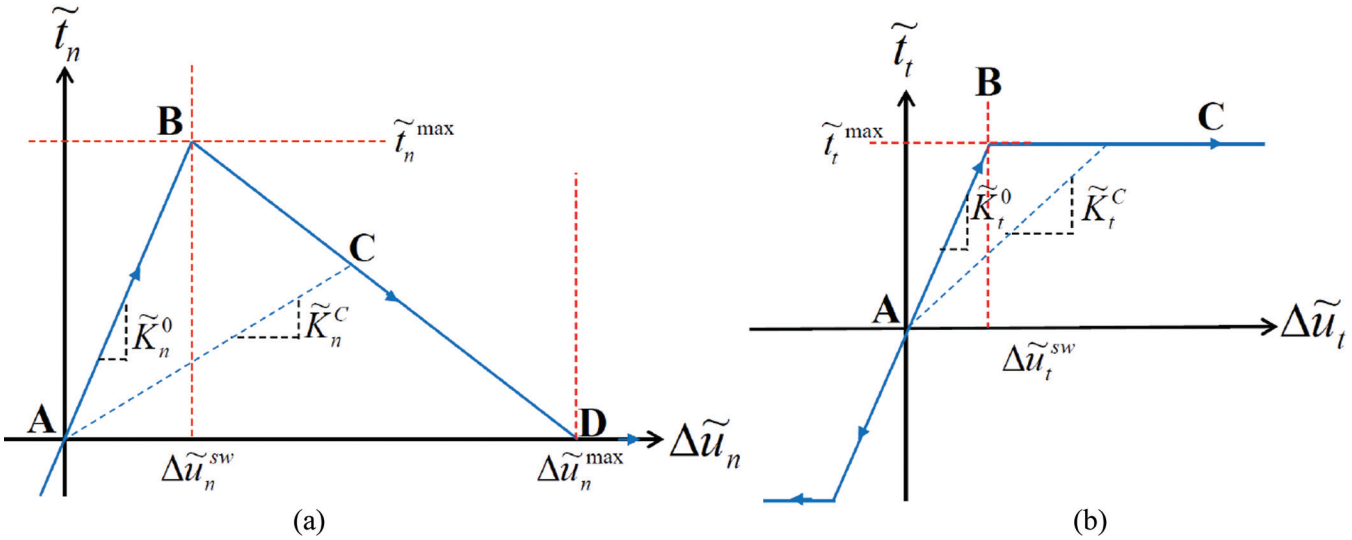


***Figure 7.*** *Schematic of the bilinear traction-separation laws used in the current work in the (a) normal and (b) tangential directions.*

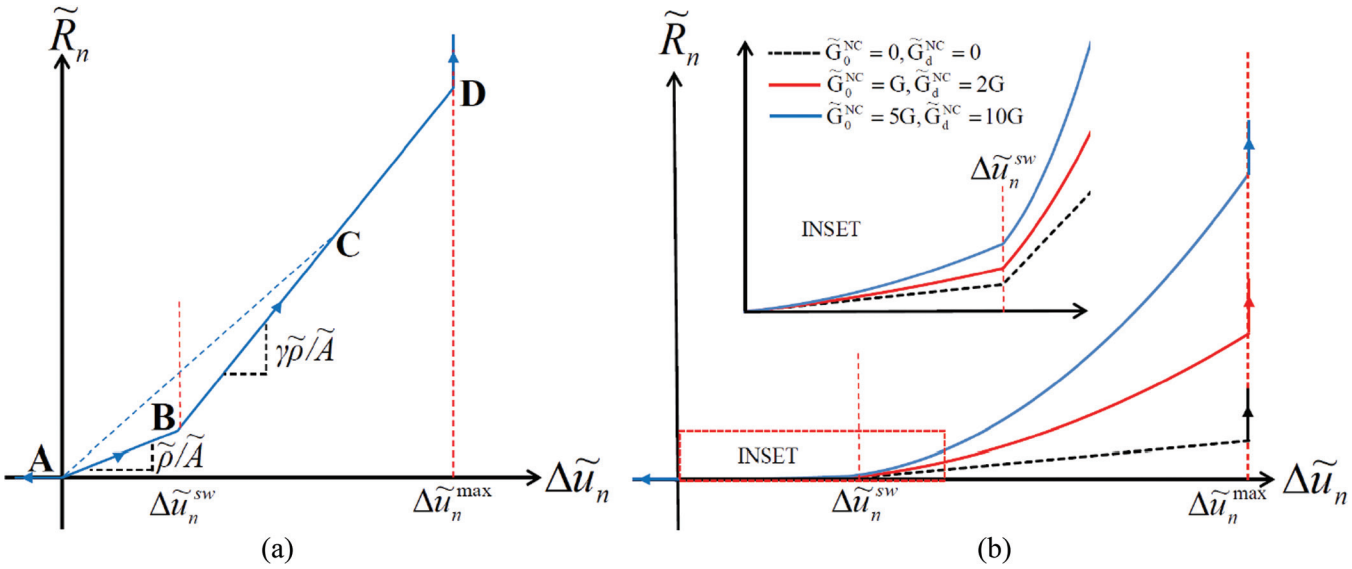


***Figure 8.*** *(a) Schematic of the bilinear interface normal resistance-separation law used in the current work for the coupled electrostatic cohesive zones and (b) the bilinear interface normal resistance-separation law for inherently piezoresistive binder.*

tion laws, electrostatic cohesive zone laws are specified at the explosive grain boundaries in terms of interfacial resistance-normal interface separation laws to allow for current density transfer across the nanocomposite binder interface. The electrostatic cohesive law nominally follows a bilinear response [Figure 8(a)] for a non-piezoresistive binder e.g. pure polymer binder with no CNTs. The interfacial resistance in the initial linear region of the electrostatic cohesive law is given by

$$\tilde{R}(\Delta\tilde{u}_n)=\frac{\tilde{\rho}}{\tilde{A}}\Delta\tilde{u}_n \qquad \Delta\tilde{u}_n \le \Delta\tilde{u}_n^{sw} \tag{1}$$

where $\tilde{A}$ is the effective cross sectional area for the cohesive zone node pair. The normal interface separation $(\Delta\tilde{u}_n)$ acts as the effective length of the polymer ligament connecting the interface. In effect, the interface resistance increases linearly as the interface normal separation increases with a rate given by $\tilde{\rho}/\tilde{A}$. It should be noted that the local resistance of the cohesive zone is dependent on the separation distance, thus, every cohesive zone could possibly have a different current resistance for applied displacement boundary conditions on the inhomogeneous microscale RVE. The local resistivity of the polymer medium $(\tilde{\rho})$, however, remains constant in absence of interfacial damage.

If the normal interface separation becomes larger than $\Delta\tilde{u}_n^{sw}$, the cohesive zone starts to get progressively damaged up to $\Delta\tilde{u}_n^{\max}$, where it gets completely damaged, i.e. becomes an open circuit. The rate of change of resistance with increasing interface separation should be larger than the nominal slope with no interfacial damage to account for the damage induced increase in $\tilde{\rho}/\tilde{A}$ local polymer ligament resistivity. For this study, it is assumed that the increase in resistance with cohesive zone damage follows a linear response with a higher rate of $\gamma\tilde{\rho}/\tilde{A}$ where $\gamma \ge 1$. The symbol, $\gamma$, denotes the increase in rate of change of interfacial resistance with interfacial damage, thus, for an undamaged cohesive zone $\gamma = 1$. The interfacial resistance for interface separation larger than $\Delta\tilde{u}_n^{sw}$ is given by

$$\tilde{R}(\Delta\tilde{u}_n)=\frac{\tilde{\rho}}{\tilde{A}}\Delta\tilde{u}_n^{sw}+\frac{\gamma\tilde{\rho}}{\tilde{A}}(\Delta\tilde{u}_n-\Delta\tilde{u}_n^{sw}) \qquad \Delta\tilde{u}_n \ge \Delta\tilde{u}_n^{sw} \tag{2}$$

The local cohesive zone resistivity on any general point in BD of Figure 8(a) is given by the slope of the line joining the current position on the interfacial resistance-normal separation curve to the origin, and can be expressed as

$$\tilde{\rho}(\Delta\tilde{u}_n)=\tilde{\rho}\frac{\Delta\tilde{u}_n^{sw}}{\Delta\tilde{u}_n}+\gamma\tilde{\rho}\left(1-\frac{\Delta\tilde{u}_n^{sw}}{\Delta\tilde{u}_n}\right) \qquad \Delta\tilde{u}_n \ge \Delta\tilde{u}_n^{sw} \tag{3}$$

In the case where the cohesive zone interface is interpenetrating, i.e. $\Delta\tilde{u}_n < 0$, the interface resistance is fixed at approximately zero, as shown in Figure 8(a). It is to be noted that the bilinear normal traction-separation law shown in Figure 7 and the bilinear interfacial resistance-separation law shown in Figure 8 are coupled through the normal interface separation and represent electromechanical response of the binder medium. It is further noted that only normal current density is allowed across the cohesive zone node pairs through the normal interfacial resistance-normal interface separation laws, however, the model can be readily extended to allow for tangential current density through an appropriate phenomenological model if required.

The discussion of the electrostatic cohesive zones so far has been restricted to nominal non-piezoresistive binder me-

dium e.g. pure polymer. Addition of CNTs to the binder results in the interface response to be inherently piezoresistive, representative of CNT-polymer nanocomposites. Thus, the bilinear normal interface resistance-separation law shown in Figure 8 needs to be modified appropriately to account for the inherent piezoresistivity of the nanocomposite binder medium. By extending Equations (1) and (2) for piezoresistive nanocomposite binder, the interface normal resistance-separation can be mathematically expressed as shown in Equation (4), where $\tilde{\rho}_0$ is the initial unstrained resistivity of the nanocomposite binder, $\delta_n$ is the reference length associated with the normal separation of the cohesive zone, $\tilde{G}_0^{NC}$ and $\tilde{G}_d^{NC}$ are the effective nanocomposite gauge factors before and after the initiation of damage in the nanocomposite. It is to be noted that $\delta_n$ scales normal interface separation into normal interfacial stretch, and thus, relates the normal separation to the local strain in the cohesive zone. In Figure 8(b), the effect of different combinations of $\tilde{G}_0^{NC}$ and $\tilde{G}_d^{NC}$ on the initial bilinear response is studied relating $\tilde{G}_0^{NC}$ and $\tilde{G}_d^{NC}$ to a nominal gauge factor, $G$. The nominal gauge factor, $G$, is dependent on the inherent piezoresisitvity of the interface binder material.

$$\tilde{R}(\Delta\tilde{u}_n)=\begin{cases}0 & \Delta\tilde{u}_n(\tilde{x})\le 0\\ \dfrac{\tilde{\rho}_0}{\tilde{A}}\left[1+\tilde{G}_0^{NC}\dfrac{\Delta\tilde{u}_n}{\delta_n}\right]\Delta\tilde{u}_n & 0\le\Delta\tilde{u}_n\le\Delta\tilde{u}_n^{sw}\\ \dfrac{\tilde{\rho}_0}{\tilde{A}}\left[1+\tilde{G}_0^{NC}\dfrac{\Delta\tilde{u}_n}{\delta_n}\right]\Delta\tilde{u}_n^{sw}+\gamma\dfrac{\tilde{\rho}_0}{\tilde{A}}\left[1+\tilde{G}_d^{NC}\dfrac{\Delta\tilde{u}_n-\Delta\tilde{u}_n^{sw}}{\delta_n}\right](\Delta\tilde{u}_n-\Delta\tilde{u}_n^{sw}) & \Delta\tilde{u}_n^{sw}\le\Delta\tilde{u}_n\le\Delta\tilde{u}_n^{\max}\\ \infty & \Delta\tilde{u}_n^{\max}\le\Delta\tilde{u}_n\end{cases} \tag{4}$$

### 3.1.3. Electromechanical Cohesive Zone Parameter Estimation

The parameters used in construction of the electromechanical cohesive laws determine the response of the nanocomposite binder. While a detailed modeling of the nanocomposite piezoresistive response from the subscales is out of scope of the current work, estimates of the effective properties, reported in the literature and using micromechanics analysis, are used in the current work to construct the electromechanical cohesive laws. As an example, estimates of effective CNT-polymer nanocomposite stiffness components are used to construct the mechanical cohesive law i.e. the initial undamaged cohesive stiffness for normal mode of separation is chosen based on the axial modulus of CNT-polymer nanocomposites while estimates of effective shear modulus is used to find the initial undamaged stiffness of the cohesive law in tangential mode of separation.

The idealized 10-grain RVE [Figure 6(a)] is used in the current work for demonstration of effective piezoresistive response in the nanocomposite bound explosives. Furthermore, parametric studies are conducted by varying the elastic modulus and conductivity of the explosive grains in addition to different nanocomposite piezoresistive response in order to provide an initial assessment of different combinations of properties which lead to the largest piezoresistive response for the composite. For the 10-grain RVE, the strain to initiation of damage and complete nanocomposite failure are used to evaluate the interface separation peak traction and the interface separation at complete failure of the cohesive zone through an appropriate reference length of the cohesive zones. The reference length for the interface is related to the length scale of the microstructure and the binder volume fraction such that integrating over the entire interface with the reference length as cohesive zone thickness provides the volume fraction of the interfacial binder during the averaging process. For the electrostatic cohesive zones, the initial resistivity is assigned using estimates of nanocomposite resistivity [50,52] with the estimates of nanocomposite effective gauge factors [53,54] before and after damage initiation used to allow for the bilinear electrostatic piezoresistive cohesive law to evolve into fully non-linear cohesive zone law [Figure 8(b)]. For the 10-grain RVE, Table 2 summarizes the parameters used in the construction of nanocomposite binder's coupled electromechanical cohesive zone laws along with the material parameters used for the explosive grains, where $E$, $\nu$ and $\rho$ are the linear elastic modulus, Poisson's ratio and resistivity of the explosive grains, respectively. It is to be noted that parametric studies were conducted for some of explosive properties and cohesive zone parameters, and thus, a range is provided for these in Table 2. It is expected that the parametric studies conducted on the 10-grain RVE will provide insight into the effect of grain and binder properties on the NCBX piezoresistive response.

For the microstructure morphology inspired 31-grain microscale RVE, the properties of the explosive grains are fixed with the grains modeled as linear elastic materials with mechanical properties corresponding to HMX crystals [15] with an elastic modulus of 25 GPa and a Poisson's ratio of 0.25. The electrostatic conductivity of the HMX grains are not readily available in the literature, however, PBX conductivity has been reported to be between 300 and 5000 S/m [55]. Based on these estimates for PBX conductivity, a grain conductivity of 1000S/m is used in the current work.

***Table 2. Material Properties for the Explosive Grains and Parameters for the Electromechanical Cohesive Zones used in the Current Work.***

| Type of Property | Parameter | Value |
|---|---|---|
| Explosive grain properties | $E$ | 10–250 GPa |
| | $\nu$ | 0.32 |
| | $\rho$ | 0.01–2.5 Ωm |
| Mechanical cohesive law | $\tilde{K}_n^0$ | 10 GPa |
| | $\Delta\tilde{u}_n^{sw}$ | 0.05 |
| | $\Delta\tilde{u}_n^{\max}$ | 0.50 |
| | $\tilde{K}_t^0$ | 1 GPa |
| | $\Delta\tilde{u}_t^{sw}$ | 0.10 |
| | $\delta_n$ | 0.1 μm |
| Electrostatic cohesive law | $\tilde{\rho}_0$ | 0.1 Ωm |
| | $\tilde{G}_0^{NC}$ | 0–5 |
| | $\tilde{G}_d^{NC}$ | 0–10 |
| | $\gamma$ | 10 |

***Table 3. Effective Electromechanical Properties of CNT-polymer Nanocomposites Calculated using the Mori-Tanaka Method Allowing for Different Orientations of CNT Bundles. Three Different Weight Concentrations (relative to epoxy polymer) are Shown Corresponding to the Experimental Samples. Note that the MWNT Concentrations are Shown here are Relative to Epoxy Polymer.***

| Property | 0.5 wt% | 1 wt% | 2 wt% |
|---|---|---|---|
| Global ($V_f$) | 0.006 | 0.012 | 0.024 |
| Local CNT ($V_f^{CNT_B}$) | 0.4 | 0.4 | 0.4 |
| Bundle ($V_f^B$) | 0.015 | 0.03 | 0.06 |
| Random: $C_{22}^{Eff} = C_{33}^{Eff}$ (GPa) | 8.06 | 9.77 | 11.34 |
| Random: $C_{44}^{Eff}$ (GPa) | 4.95 | 5.93 | 6.77 |
| Random: $\Sigma_{22}^{Eff} = \Sigma_{33}^{Eff}$ (S/m) | 61.16 | 93.68 | 127.62 |
| Aligned: $C_{22}^{Eff}$ (GPa) | 9.39 | 11.74 | 13.94 |
| Aligned: $C_{33}^{Eff}$ (GPa) | 7.59 | 9.27 | 10.92 |
| Aligned: $C_{44}^{Eff}$ (GPa) | 5.55 | 7.29 | 9.16 |
| Aligned: $C_{55}^{Eff}$ (GPa) | 4.4 | 5.51 | 6.69 |
| Aligned: $\Sigma_{22}^{Eff}$ (S/m) | 142.97 | 219.01 | 298.33 |
| Aligned: $\Sigma_{33}^{Eff}$ (S/m) | 1.68 | 2.86 | 4.40 |

The effective properties for the construction of electromechanical cohesive zones are obtained using a more rigorous micromechanics based evaluation of nanocomposite effective properties. The key assumption for the microscale RVE binder medium is that the nanotube bundles, composed of aligned SWCNTs, are identical, well dispersed and aligned/randomly oriented in the polymer matrix. For a given CNT volume fraction within the bundle, in the unstrained state, the mechanical response of the nanoscale bundle is obtained using the Mori-Tanaka method [56] with aligned/randomly oriented CNTs in the polymer medium. The CNT volume fraction within the bundle is chosen to be 0.4 based on some experimental estimates in literature [57]. The corresponding unstrained electrostatic conductivity is obtained using a finite element based micromechanical analysis allowing for electron hopping at the nanoscale [47]. Once the bundle properties are obtained, the Mori-Tanaka method is used to allow for random/aligned orientations of the bundles within the polymer matrix. The effective stiffness and electrostatic conductivity for the microscale RVE is obtained by treating each orientation of a given bundle as a different phase, and averaging over all possible orientations in a consistent manner such that the orientations of nanotube bundles are accounted for [52,53,58–60].

The effective unstrained properties shown in Table 3 are used to construct the initial linear stiffness for the bilinear normal and tangential traction-separation laws and the initial linear resistance-separation law shown in Figure 7 and Figure 8, respectively. As an example, $C_{22}^{Eff}$ is used to construct the initial normal traction-separation law stiffness as $\tilde{K}_0^n = C_{22}^{Eff} / \delta_n$ where $\delta_n$ is the reference length associated with the normal mode of separation. For the 31-grain RVE, a reference length of 47 μm is calculated based on the nanocomposite binder volume fraction of 30%. Similarly, $C_{44}^{Eff}$ is used to construct the initial tangential traction-separation law stiffness, $\tilde{K}_0^t$, for both the random and the aligned cases. The initial resistivity of the cohesive zone used in the normal resistance-separation law is obtained as $\tilde{\rho} = 1/\Sigma_{22}^{Eff}$ for both the random and aligned cases. In addition to the random and aligned cases, an additional case with CNT bundles aligned transverse (or tangential) to the interface is considered. The initial properties for this case are obtained by replacing $C_{22}^{Eff}$, $C_{44}^{Eff}$ and $\Sigma_{22}^{Eff}$ by $C_{33}^{Eff}$, $C_{55}^{Eff}$ and $\Sigma_{33}^{Eff}$, respectively, obtained for the aligned case. It is to be noted that the properties shown in Table 3 are nanocomposite binder properties local to the interface expressed in terms of local cohesive zone coordinate system. In the finite element analysis, the local stiffnesses and conductivities are transformed to the global coordinate system before their influence is added to the global finite element matrices.

In addition to the effective unstrained stiffnesses and conductivities, the initiation and rate of damage for the nanocomposite cohesive zones needs to be estimated in order

to evaluate $\Delta\tilde{u}_n^{sw}$, $\Delta\tilde{u}_t^{sw}$ and $\Delta\tilde{u}_n^{\max}$. These parameters are obtained using cohesive fracture energy estimates for CNT-polymer nanocomposite. It is assumed that the addition of CNTs to the epoxy polymer system does not result in a large change in the cohesive fracture energy such that the polymer cohesive fracture energy (3.2MPa[3] [61], assuming linear elastic brittle material response) can be used. Thereafter, two different cases of bilinear cohesive zone normal traction-separation laws are generated assuming brittle damage and ductile damage of the interface, in absence of direct experimental investigation of damage at the local interface in such composites. For the brittle damage case, cohesive fracture energy is approximated from the given undamaged normal stiffness (chosen to be 10GPa which is nearly representative of each alignment case) by specifying $\Delta\tilde{u}_n^{sw}$ = 0.0225 and $\Delta\tilde{u}_n^{\max}$ = 0.0285. For the ductile damage case, $\Delta\tilde{u}_n^{sw}$ and $\Delta\tilde{u}_n^{\max}$ are chosen to be 0.008 and 0.08, respectively, keeping the cohesive fracture energy of the cohesive zones for normal mode of separation constant at 3.2MPa. For the tangential traction separation law, $\Delta\tilde{u}_t^{sw}$ is assumed to be equal to $\Delta\tilde{u}_n^{sw}$ for all cases. Finally, typical estimates of nanocomposite effective gauge factors before ($\tilde{G}_n^{NC}$) and after ($\tilde{G}_d^{NC}$) damage initiation are chosen based on published work in the literature which are typically reported to be in between 1 and 20 [22–28].

### *3.1.4. Micromechanics Based Averaging for Effective Properties*

The general relationship for a piezoresistive material relates the strain tensor to the relative change in resistivity, i.e. current strain resistivity minus unstrained resistivity ($\Delta\rho$) normalized by the unstrained resistivity ($\rho_0$), as

$$\frac{\Delta\rho_{(i)(j)}}{\Delta\rho^{0}_{(i)(j)}} = \Pi_{ijkl}\varepsilon_{kl} \tag{5}$$

In the current study, it will be assumed that the explosive crystals are not inherently piezoresistive, i.e. all components of the piezoresistive strain tensor are zero. However, due to the piezoresistive nanocomposite binder and local interfacial separation/damage, the effective macroscale material demonstrates an effective piezoresistive response, i.e. $\Pi_{ijkl}^{Eff}$ has non-zero components. The changes in volume averaged resistivities needed to determine the components of the piezoresistive strain tensor are obtained from the averaged representation of Ohm's law which is expanded as

$$\begin{aligned}\langle \hat{J}_1 \rangle &= \Sigma_{11}^{Eff}\langle \hat{E}_1\rangle + \Sigma_{12}^{Eff}\langle \hat{E}_2\rangle \\ \langle \hat{J}_1 \rangle &= \Sigma_{11}^{Eff}\langle \hat{E}_1\rangle + \Sigma_{12}^{Eff}\langle \hat{E}_2\rangle\end{aligned} \tag{6}$$

The components of the effective conductivity tensor are obtained by systematically allowing only one component of the applied electric field to be non-zero, e.g. when $E_1$ is non-zero, the conductivity components $\Sigma_{11}^{Eff}$ and $\Sigma_{21}^{Eff}$ are obtained from Equation (6). The effective conductivity components obtained are then used to evaluate the effective resistivity components. The effective piezoresistive response is presented in terms of relative change in resistivity as a function of applied strain in accordance with Equation (5). For the experimentally obtained microstructure morphology inspired 31-grain *RVE*, the effective response is presented in terms of relative change in resistance to compare with the experiments. The effective resistance ($R^{Eff}$) at a given strain state is evaluated using the effective resistivity as

$$R_{22}^{Eff}(\varepsilon) = \frac{\rho_{22}^{Eff}(\varepsilon) * L^{RVE}}{A^{RVE}} \tag{7}$$

where $L^{RVE}$ is the length of the *RVE* in the direction of applied test electric field, i.e. $x_2$ direction, $A^{RVE}$ is the area transverse to the applied test electric field which is given by the width of the *RVE* in the $x_1$ direction multiplied by the plane strain thickness for the problem.

In order to quantify interfacial damage in the nanoscale *RVE*, an averaged damage parameter ($D_{avg}$) is defined by averaging the local damage in each of the cohesive zone finite element node pairs which constitute the microscale grain boundary interface. The averaged damage parameter is mathematically expressed as

$$D_{avg} = \frac{1}{\tilde{A}^I}\int_{\tilde{A}^I} D(\tilde{x})\, d\tilde{A}^I \tag{8}$$

where $\tilde{x}$ is any point lying along the interface, $\tilde{A}^I$ is the total cohesive zone interface area perpendicular to the direction of normal interface separation, i.e. cohesive zone differential width multiplied by the plane strain thickness, and $D(\tilde{x})$ is the local damage parameter defined at interface location $\tilde{x}$. $D(\tilde{x})$ is defined based on the bilinear mechanical cohesive zone law normal to the interface used in the current study as

$$D(\tilde{x}) = \begin{cases} 1 & \Delta\tilde{u}_n(\tilde{x}) \le \Delta\tilde{u}_n^{sw} \\ 1 - \left[\dfrac{\Delta\tilde{u}_n(\tilde{x}) - \Delta\tilde{u}_n^{sw}}{\Delta\tilde{u}_n^{\max} - \Delta\tilde{u}_n^{sw}}\right] & \Delta\tilde{u}_n^{sw} \le \Delta\tilde{u}_n(\tilde{x}) \le \Delta\tilde{u}_n^{\max} \\ 0 & \Delta\tilde{u}_n^{\max} \le \Delta\tilde{u}_n(\tilde{x}) \end{cases} \tag{9}$$

[3]In the current work, the cohesive fracture energy is found using tensile test results obtained from Epoxy Resin/206 Slow Hardener: Technical Data Sheet [61]. This is done assuming the epoxy binder between the grains acts as ligaments connecting across the interface at the microscale as was done in [13]. The cohesive fracture energy for the interface can then be found using the initial stiffness of the polymer and the strain to failure by evaluating the area under the assumed linear-elastic brittle constitutive law response. The cohesive fracture energy for this case is 0.5 $K^{\text{in}}\varepsilon_f^2$ (in MPa), where $K^{\text{in}}$ is the initial linear elastic stiffness and $\varepsilon_f$ is the strain to failure obtained from the technical data sheet [61].

Integrating the damage state across the entire set of interfaces allows for representation of each cohesive zone in the averaged damage parameter, where every cohesive zone may possibly have a different state of damage depending on the local interface separation.

### 3.2. NCBX Piezoresistive Modeling using Idealized 10-grain RVE

In order to evaluate the NCBX piezoresistive response, ad-hoc electromechanical cohesive laws are constructed based on known estimates of effective CNT-polymer nanocomposite electromechanical properties as shown in Table 2. Once the coupled electromechanical cohesive laws are defined from the nanocomposite effective properties, an idealized representative volume element (RVE) for the microscale grain boundary problem is constructed. For the current work, a 10-grain model of the microscale NCBX is constructed using Voronoi Tessellation as shown in the undeformed state in Figure 9(a). The grains are meshed using linear triangular finite elements such that the 17 cohesive zone edges have 187 initially coincident node pairs across the interface connected through the electromechanical cohesive laws developed. In addition, Figure 9(a) shows the deformed mesh after application of 2% tensile strain in the $x_2$ direction (with a displacement magnification factor of 5) where the cohesive zones at the grain boundaries are observed to separate. In addition to the properties provided in Table 2, the Young's modulus and resistivity of the explosive grains are fixed at 50 GPa and 0.1 Ωm, respectively, for the demonstration case presented in Figure 9. The effective nanocomposite gauge factors before ($\tilde{G}_0^{NC}$) and after ($\tilde{G}_d^{NC}$) the initiation of damage are chosen to be 2 and 4, respectively [53,54].

The electromechanical boundary value problem is solved over the microscale RVE under plane strain assumptions assuming that the grain distribution is sufficiently random so as to result in an effective isotropic response. Local stress component ($\sigma_{22}$) contours and local current density component contours ($J_2$) for the 10-grain problem are shown in Figure 9(b) in the unstrained state along with 1% and 2% applied tension. In the unstrained state, $\sigma_{22}$ is zero everywhere in the domain because of no applied deformation on the RVE and $J_2$ is uniform over the domain because the applied uniform test electric field in the $x_2$ direction results in uniform current density in absence of material inhomogeneities, i.e. cohesive zone separation. As the applied tensile strains are increased, the distribution of grain boundaries leads to localized cohesive zone separation along the edges leading to redistribution of stress and current density pathways. On ap-

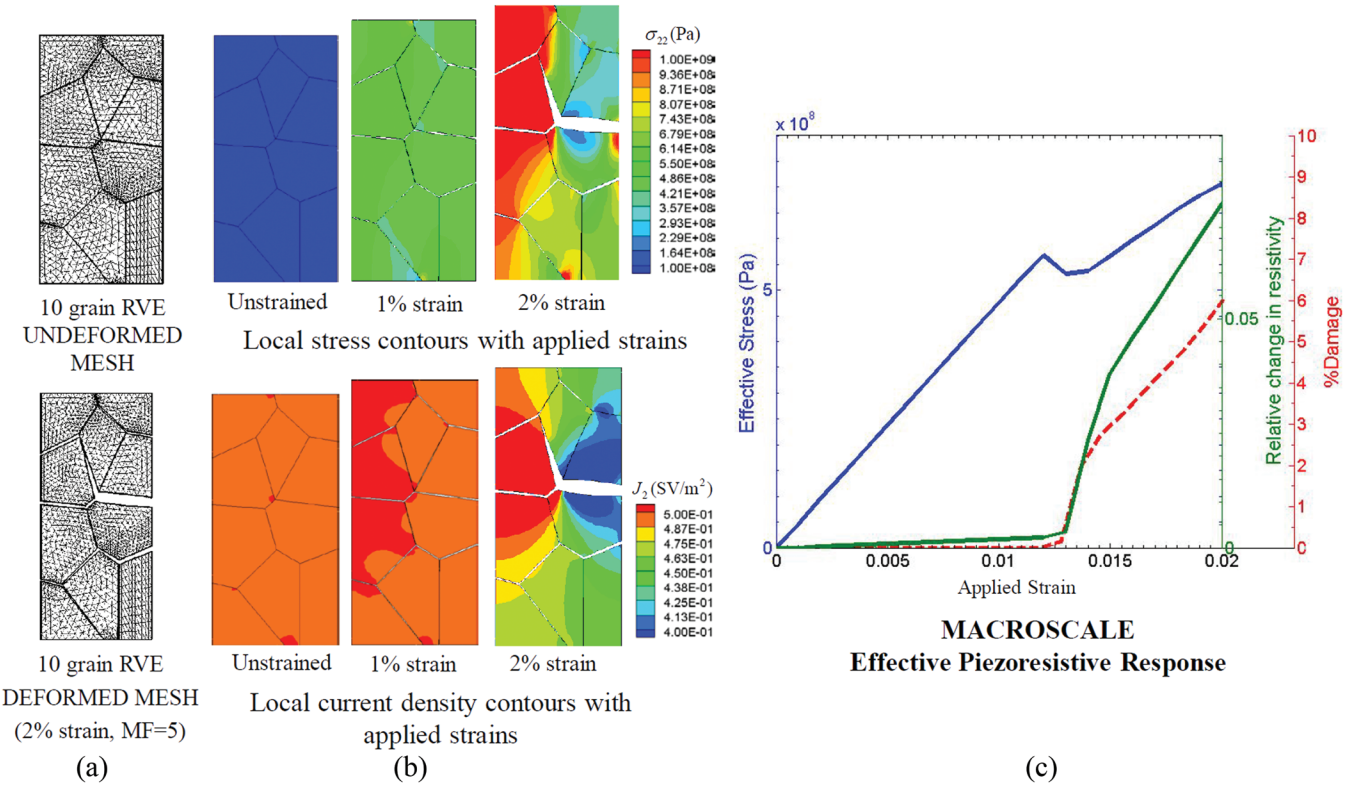


***Figure 9.*** *(a) A sample result from the current grain boundary cohesive zone exploration of NCBX showing the undeformed and deformed meshes with a displacement magnification factor of 5. (b) Local stress and current density contours are presented at different applied strain states. (c) The corresponding effective piezoresistive response and averaged damage index.*

plication of larger strains, some of the current density pathways get completely severed because of cohesive zone damage resulting in smaller current density across the interface. The evolution of the current density pathways in response to separating and damaging interfacial cohesive zones results in an effective piezoresistive response of the microscale RVE shown in Figure 9(c) obtained using micromechanics based energy equivalence.

It is observed from Figure 9(c) that the effective stress component ($\sigma_{22}^{Eff}$) increases linearly from zero on application of tensile strains up to an applied tensile strain of about 1.2%. It is to be noted that there is no damage accumulation at the interfaces in the entire RVE up to 1.2% applied strain which signifies that all of the cohesive zones are still in the initial linear elastic region of the normal traction-separation response. Thus, the initial stiffness of the effective microscale RVE is a function of the explosive crystal stiffness, the normal and tangential cohesive zone initial undamaged stiffnesses and the distribution of nanocomposite binder cohesive zone edges in the microscale RVE. The relative change in resistivity for this initial linear elastic region, in absence of cohesive zone damage is dependent on the initial cohesive zone resistivity and the effective nanocomposite gauge factor before damage initiation, $\hat{G}_0^{NC}$. At an applied tensile strain of about 1.2%, a sharp reduction in $\sigma_{22}^{Eff}$ is observed which can be closely correlated to a sudden increase in the amount of interfacial damage and relative change in effective resistivity ($\Delta\rho_{22}^{Eff}/\rho_{22}^{0}$). This process is accompanied by a rearrangement of local stress contours and in local current density contours in the microscale RVE. For the current case, it is observed that the relative change in resistivity is about 8% in response to 2% applied strain with about 5% interfacial damage accumulation in the RVE. Thus, the result demonstrates that applied deformation induced separation and damage of the binding polymer nanocomposite medium in the microscale NCBX RVE leads to an effective piezoresistive response which can distinguish between the linear elastic region and the damage evolution regime. While the results presented in Figure 9 demonstrate a coupled piezoresistive response in CNT-polymer nanocomposite bonded explosives for a given set of properties, the properties of explosive grain crystals and CNT-polymer nanocomposites can vary over a large range depending on their type and microstructural morphology. Thus, in order to explore the range of piezoresistive response in NCBX materials, parametric studies are conducted over these properties.

The first set of parametric study is conducted by varying the grain stiffness relative to the nanocomposite binder stiffness in order to explore the similarities and differences in cohesive zone separation behavior and associated piezoresistive response. In order to differentiate only between the relative stiffness based piezoresistive response, the resistivity of the explosive grains are set equal to the nanocomposite resistivity provided in Table 2. In addition, the effective nanocomposite gauge factors before ($\tilde{G}_0^{NC}$) and after ($\tilde{G}_d^{NC}$) the initiation of damage are chosen to be 2 and 4, respectively, for all of the cases. The results obtained from the parametric study are presented in Figure 10. Figure 10(a) shows the averaged damage index of the cohesive zones obtained using Equation 8 as a function of applied strain at different ratios of grain stiffness to initial cohesive zone stiffness. For cases where the grains are about the same stiffness as the nanocomposite binder, i.e grain to cohesive zone stiffness ($E_g/E_{cz}$) of 1 and 2, the applied deformation gets distributed between the grains and cohesive zones such that the interface separation between the grain interfaces is less than $\Delta\tilde{u}_n^{sw}$. Thus, the averaged damage index for the entire microscale RVE is 1, i.e. no damage accumulation at the interfaces. However, as the relative stiffness of the grains increases, interfacial damage accumulation is observed in the nanoscale RVE because the applied deformations predominantly result in separation of relatively more compliant interface. The local displacement component ($u_2$) contours for the $E_g/E_{cz}$ ratios of 1 and 25 are presented in Figure 10(c) in both the unstrained and 2% applied strain states. It is observed that for the case with equal stiffnesses, there is insignificant separation in the cohesive zones as compared to the case with $E_g/E_{cz}$ ratio of 25 where the grains act like nearly rigid bodies with minor deformation as the interfacial cohesive zones undergo significantly large normal separation. Figure 10(d) presents the corresponding local stress component ($\sigma_{22}$) contours. Following from the local displacement and stress component contours, at 2% applied strain, the averaged damage index is observed to be 0.94, 0.92 and 0.90 for cases with $E_g/E_{cz}$ ratio of 5, 10 and 25, respectively, i.e. about 6%, 8% and 10% damage accumulation. The effective piezoresistive response of NCBX is presented in Figure 10(b) in terms of relative change in resistivity with applied strain. It is observed that increasing the relative grain stiffness leads to a larger piezoresistive response. For example, the relative change in resistivity at 2% applied strain is observed to be close to zero for the cases with $E_g/E_{cz}$ ratios of 1 and 2 because of small cohesive zone separations. However, the relative change in resistivity is observed to be 0.081, 0.087 and 0.093 for cases where $E_g/E_{cz}$ ratio is 5, 10 and 25, respectively, at 2% applied strain.

In addition to studying the effect of relative stiffness on the effective NCBX piezoresistive response, test cases were designed to explore the effect of relative difference in initial grain conductivity and cohesive zone conductivity. For these test cases, the ratio of grain to cohesive zone stiffness ($E_g/E_{cz}$) is fixed at 5 such that the applied deformations lead to an appreciable amount of interface separation in the microscale RVE. The effective nanocomposite gauge factors before ($\tilde{G}_0^{NC}$) and after ($\tilde{G}_d^{NC}$) the initiation of damage are chosen to be 2 and 4, respectively. Figure 11(a) shows that the averaged damage index for all of these cases follow a similar behavior because the mechanical BVP for all of these cases has the same geometry and mechanical proper-

ties. About 6% damage accumulation is observed in the microscale RVEs at 2% applied strain for each of these cases. The effective piezoresistive response for the microscale RVE is presented in Figure 11(b) in terms of relative change in resistivity for different cases of relative grain conductivity ($S_g/S_{cz}$) as a function of applied strain. It is observed that the case with the largest relative grain conductivity, i.e 25 times the cohesive zone conductivity, exhibits the largest effective piezoresistive response. For example, the case with the $S_g/S_{cz}$ of 25 leads to a relative change in resistivity of 0.43 on application of 2% strain. In contrast, the case with $S_g/S_{cz}$ of 0.1 undergoes a relative change in resistivity of 0.01 on application of 2% strain. The reason for such behavior can be observed from the local electrostatic potential and local current density contours presented in Figure 11(c) and 11(d), respectively, in the undeformed state and at 2% applied strain. It is observed from Figure 11(c) and 11(d) that the local electrostatic potential and current density do not undergo significant redistribution for the case with $S_g/S_{cz}$ of 0.1 even when the grain boundary gets separated by a significant amount due to interfacial damage. For this case, the interface is more conductive, hence, it the acts like a conductive medium and allows insigniffcant hindrance to the current density pathways connecting across the interface. However, as the grains become more conductive, the cohesive zone interface acts as the barrier for current density whereas the grains act predominantly as a conductive medium. Thus, a significant amount of redistribution is observed in the local electrostatic potential and current density as the interfaces separate and accumulate damage. For non-conductive grains (e.g. sugar crystals), however, tangential current density in the binder medium (or explicit polymer binder instead of cohesive interface) may lead to current density pathways through the binder without going through the grains significantly. In the current work such tangential current density pathways which allow for current density only through the binder are not captured in absence of tangential electrostatic cohesive zones and explicit polymer binder modeling.

The piezoresistive response of the nanocomposite binder depends on the microstructural morphology of CNTs within the polymer matrix. A range of gauge factors between 1 and 20 [22–28] are typically reported in the literature for CNT-polymer nanocomposites. Hence, a parametric study is

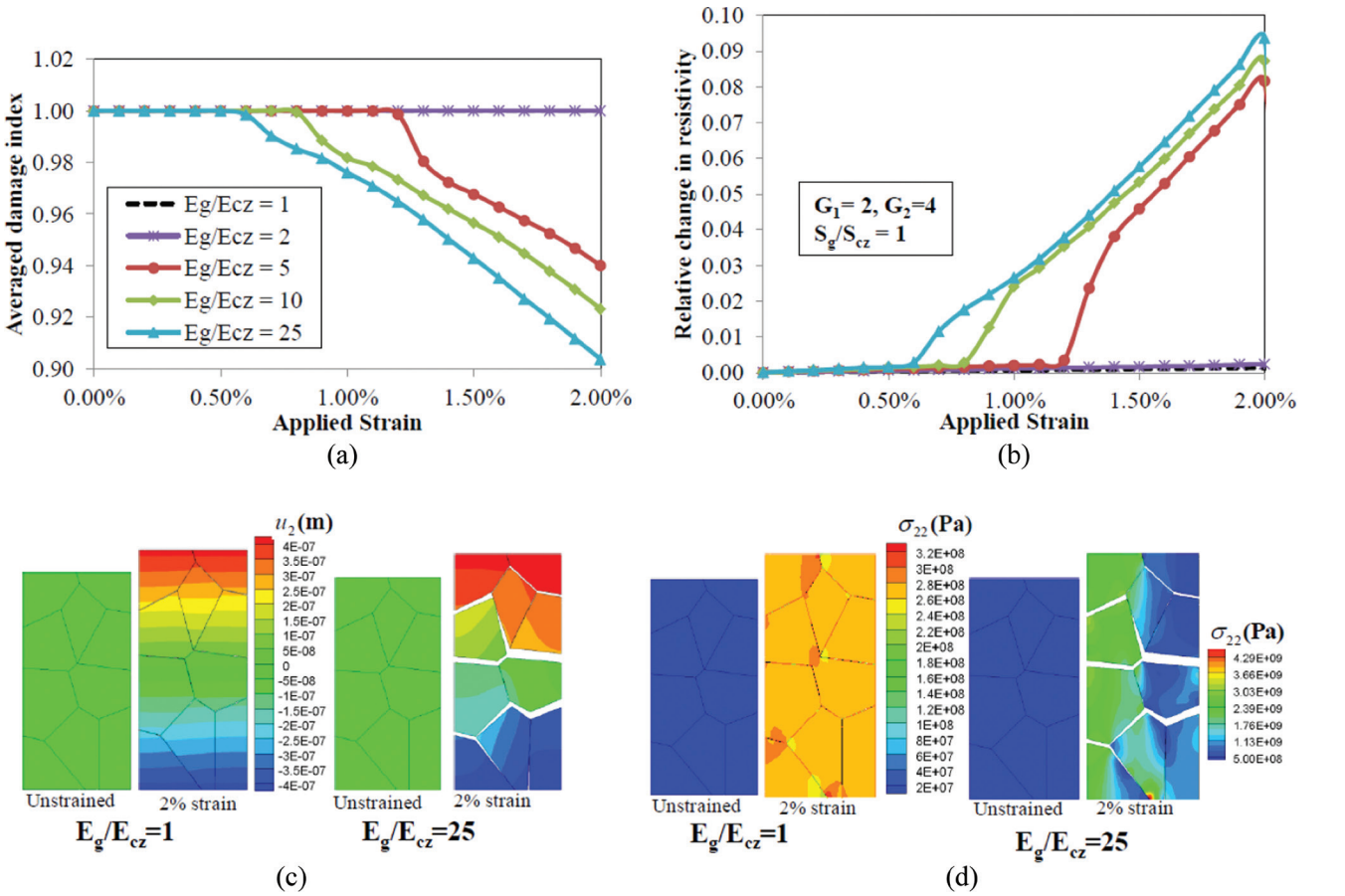


***Figure 10.*** *Comparison of (a) averaged damage index, (b) relative change in resistivity (c) local displacement contours and (d) local stress component contours for the NCBX 10-grain microscale RVE with different relative stiffness of grains and cohesive zones. Note that symbol $E_g$ and $E_{cz}$ are used for the elastic modulus and $S_g$ and $S_{cz}$ for the conductivity of the grains and cohesive zone interface, respectively. $G_1$ and $G_2$ are the effective nanocomposite gauge factors before $(\tilde{G}_0^{NC})$ and after $(\tilde{G}_d^{NC})$ the initiation of nanocomposite damage.*

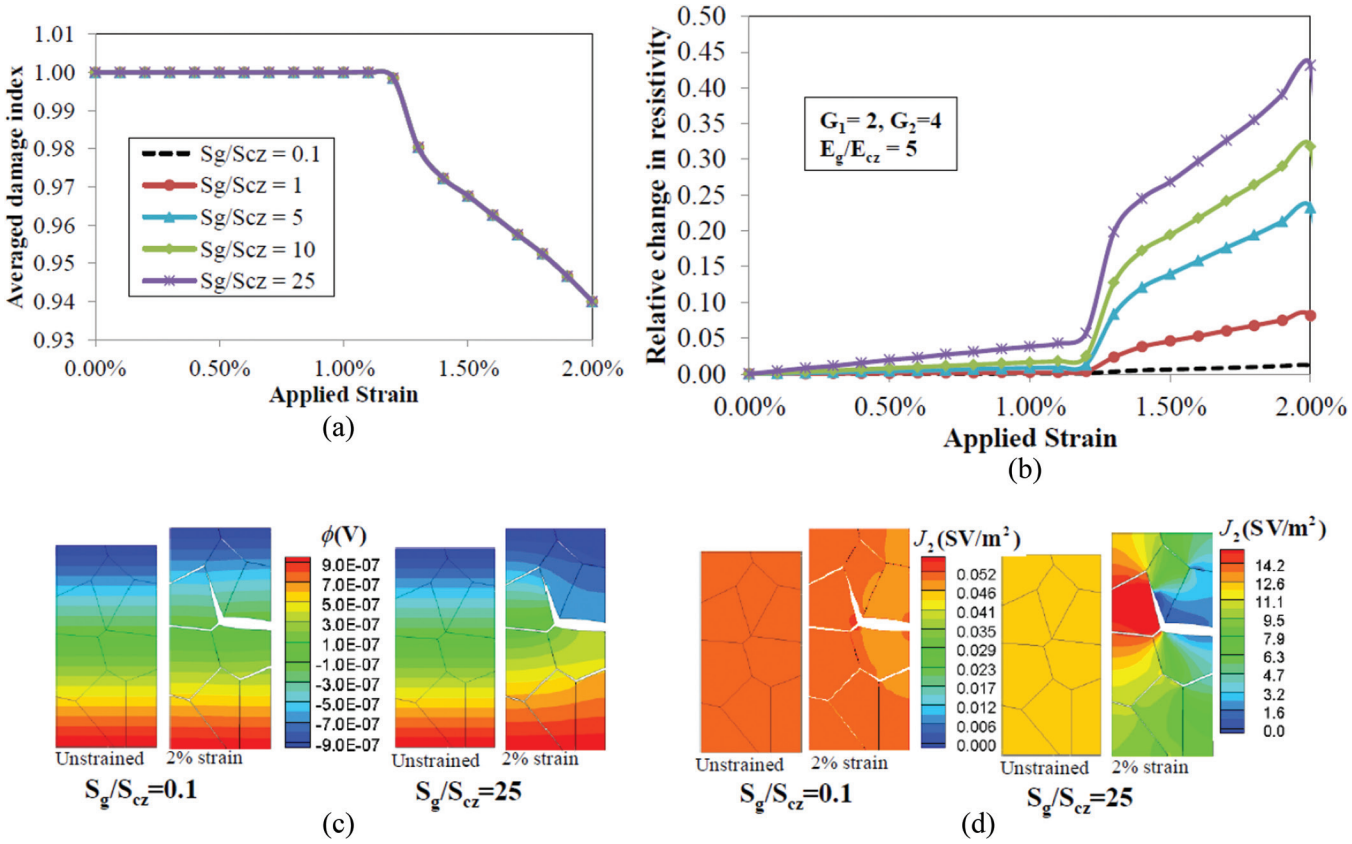


***Figure 11.*** *Comparison of (a) averaged damage index and b) relative change in resistivity (c) local electrostatic potential contours and (d) local current density contours for the NCBX 10-grain microscale RVE with different relative conductivities of grains and cohesive zones. Note that symbol $E_g$ and $E_{cz}$ are used for the elastic modulus and $S_g$ and $S_{cz}$ for the conductivity of the grains and cohesive zone interface, respectively. $G_1$ and $G_2$ are the effective nanocomposite gauge factors before $(\tilde{G}_0^{NC})$ and after $(\tilde{G}_d^{NC})$ the initiation of nanocomposite damage.*

conducted in the current work by varying the effective nanocomposite gauge factors before $(\tilde{G}_0^{NC})$ and after $(\tilde{G}_d^{NC})$ the initiation of damage, keeping the relative grain stiffness at 5 times the cohesive zone stiffness and the relative grain conductivity equal to the cohesive zone. The mechanical BVP for all of these cases is the same, hence, all of the cases undergo same amount of interfacial damage accumulation with applied strain as shown in Figure 12(a). About 6% interfacial damage accumulation is observed for all of these cases at 2% applied strain.

The effective piezoresistive response is presented in Figure 12(b), where the case with largest nanocomposite binder gauge factors before $(\tilde{G}_0^{NC})$ and after $(\tilde{G}_d^{NC})$ the initiation of damage exhibits the largest piezoresistive response. For the case with zero gauge factors before $(\tilde{G}_0^{NC})$ and after $(\tilde{G}_d^{NC})$ the initiation of damage, the effective piezoresistive response is purely governed by the separation and damage of microscale interfaces resulting in a relative change in resistivity of 0.04 at 2% applied strain. In contrast, for the case with $\tilde{G}_0^{NC} = 5$ and $\tilde{G}_d^{NC} = 10$, the effective piezoresistive response additionally depends on the piezoresistive response of the local cohesive zone binder resulting in a relative change in resistivity of 0.12 at 2% applied strain. This observation is tied to the interfacial resistance relation with normal interface separation shown in Equation (4) which specifies that larger gauge factors result in larger change in interfacial resistance.

### 3.3. NCBX Piezoresistive Modeling using 31-grain Microstructure Morphology Inspired RVE

In addition to the 10-grain RVE, the experimental microstructure inspired 31-strain RVE, shown in Figure 6, is subjected to a parametric study to understand the effect of CNT-polymer nanocomposite binder morphology on the effective NCBX piezoresistive response. For the 31-grain RVE, the material properties of the grains are assumed to be constant corresponding to the HMX crystals [15,55] while micromechanics based estimates of effective nanocomposite electromechanical properties (Table 3) are used to construct the cohesive normal and tangential traction-separation and normal resistance-separation curves. Computational model parameters explored parametrically include the (1) effect of ductile versus brittle interfacial damage response at different damage rates, (2) effect of CNT alignment at the interface i.e. normal to the interface, tangential to the interface

or randomly aligned, (3) effect of local CNT volume fraction within the nanocomposite, (4) effect of nanocomposite piezoresistivity.

In order to study the effect of different types of damage, i.e. ductile vs. brittle, electromechanical cohesive laws are constructed for 0.15% wt random CNT alignment at the interface with the gauge factors before ($\tilde{G}_0^{NC}$) and after ($\tilde{G}_d^{NC}$) the initiation of damage to be 2 and 4, respectively. The effective initial undamaged electromechanical properties $C_{22}^{Eff}$, $C_{44}^{Eff}$ and $\Sigma_{22}^{Eff}$ for the nanocomposite are presented in Table 3 and are used as estimates for the random alignment case, are used as estimates of initial slopes of the normal and tangential traction-separation and the normal resistance-separation laws respectively. Finally, the brittle and ductile damage cases are approximated by specifying $\Delta\tilde{u}_n^{sw} = 0.0225$, $\Delta\tilde{u}_n^{\max} = 0.0285$ and $\Delta\tilde{u}_n^{sw} = 0.008$, $\Delta\tilde{u}_n^{\max} = 0.08$, respectively, keeping the separation energy (i.e. cohesive fracture energy) constant as described in Section 3.1.3. The comparison of the brittle vs ductile response is presented in Figure 13 in terms of the effective stress-strain behavior [Figure 13(a)] and relative change in effective resistance [Figure 13(b)] where the resistance of the RVE is calculated using Equation (7). In addition, local stress and current density contours are provided in the direction of applied strains/test electric fields, i.e. $x_2$ direction, in Figure 13(c) and 13(d).

The effective stress-strain response for the ductile and brittle damage cases presented in Figure 13(a) undergoes an initial linear increase in effective stress for both the ductile and brittle damage cases while the local cohesive interface follows a linear elastic response everywhere in the RVE. At about 0.5% applied tensile strain, the ductile damage case starts to deviate from the linear elastic behavior because of initiation of local damage and reduction in local stiffness in some of the cohesive zones as indicated by the averaged damage index which starts to decrease from its initial value of 1. The local strain associated with damage initiation of the nanocomposite binder interface is much smaller for the ductile cohesive zones ($\Delta\tilde{u}_n^{sw} = 0.0008$) as compared to the brittle cohesive zones ($\Delta\tilde{u}_n^{sw} = 0.0225$) which leads to a faster damage initiation in the local cohesive zones. Similarly, the effective stress-strain response for the brittle case deviates from the linear elastic behavior at about 1% strain along with a reduction in the corresponding averaged damage index. Once damage initiates in the local cohesive zones, the effective stress-strain response for the ductile and brittle damage cases evolves with significantly different effective stress states for a given applied strain state. For example, at 2% applied strain state, the effective stress for the brittle and ductile damage cases is observed to be 36 MPa and 135 MPa, respectively, with about 20% damage accumulation for both cases. The differences observed in the effective stress at a given strain state can also be observed in Figure 13(c)which shows the local stress component ($\sigma_{22}$) contours in the 31-grain RVE for the ductile and brittle damage cases in the unstrained state and at 1% and 2.3% applied tensile strain. It is observed that the local interface separation and damage paths are slightly different for the two cases because of differences in local interface damage behaviors. In addition, at 2% applied strain state, the stress carrying columns for the ductile case are weaker as compared to the brittle damage case leading to the observed difference in effective stress. It is noted that the effective stress-strain response for the brittle damage case follows a more ductile behavior because while the local damage is brittle the effective response is dependent on collective behavior of grains and interfaces.

It is worth noting that the relative change in effective resistance for the ductile and brittle cases, shown in Figure 13(b), starts to increase from zero (in the unstrained state) much before an observed deviation from the linear elastic mechanical behavior. It is observed that the deviation in the relative change in resistance starts to capture the local interfacial damage faster than the stress-strain response, es-

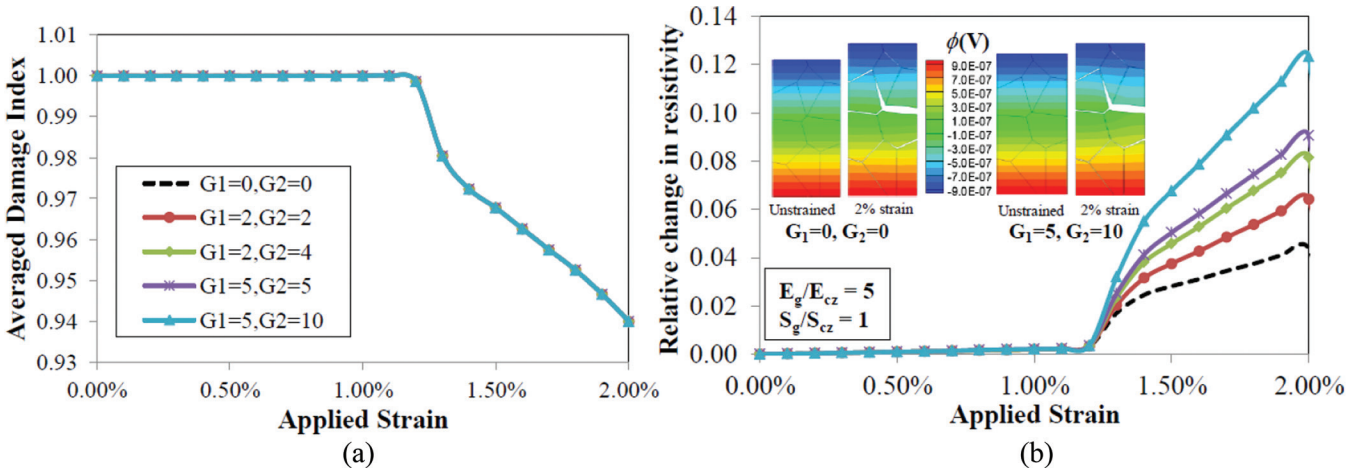


***Figure 12.*** *Comparison of (a) averaged damage index and (b) relative change in resistivity for the NCBX 10-grain microscale RVE with different effective nanocomposite binder gauge factors before ($\tilde{G}_0^{NC}$) and after ($\tilde{G}_d^{NC}$) the initiation of damage. $G_1$ and $G_2$ are the effective nanocomposite gauge factors before ($\tilde{G}_0^{NC}$) and after ($\tilde{G}_d^{NC}$) the initiation of nanocomposite damage.*

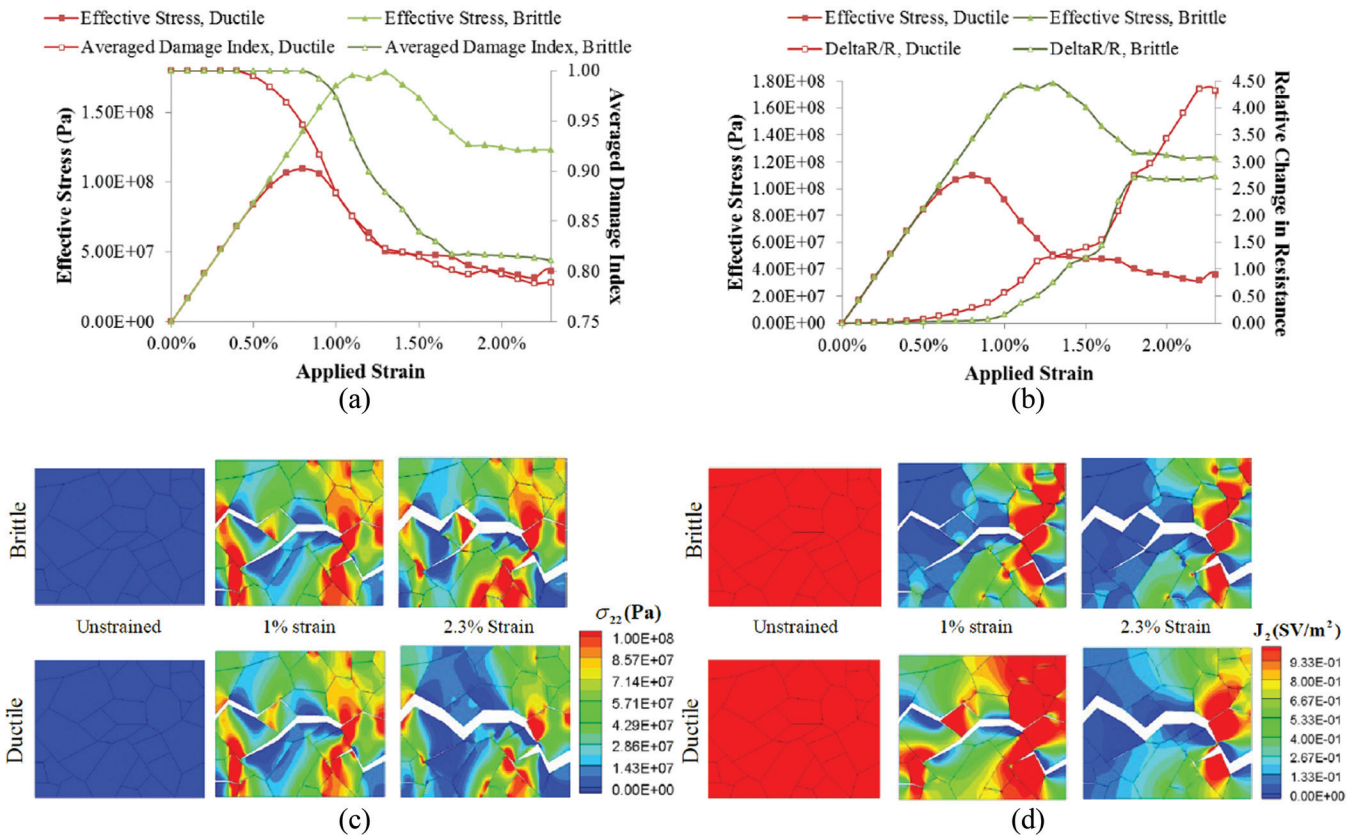


***Figure 13.*** *Comparison of ductile and brittle interfacial damage on the effective piezoresistive response with 0.15% wt random CNT alignment at the interface with the gauge factors before ($\tilde{G}_0^{NC}$) and after ($\tilde{G}_d^{NC}$) the initiation of damage chosen to be 2 and 4, respectively. (a) Effective stress-strain response along with the evolution of averaged damage index, (b) Relative change in effective resistance along with the effective stress-strain response for comparison, (c) the local stress component ($\sigma_{22}$) contours in the 31-grain RVE for the ductile and brittle damage cases in the unstrained state, at 1% and 2% applied tensile strain, and (d) local current density contours show a difference in the evolution of current density ($J_2$) carrying pathways for the two cases in the unstrained state, at 1% and 2% applied tensile strain.*

pecially for the brittle damage case, where the stress-strain response is linear up to 1% applied strain whereas the relative change in resistance starts to increase significantly at around 0.5% applied strain. The rate of increase of relative change in effective resistance is observed to be sensitive to the initiation and evolution of damage in the local cohesive zones such that the ductile case has a larger change in resistance at an applied strain of 1% because of larger damage accumulation. At 1% applied strain, while the brittle damage case undergoes about 7.4% increase in resistance, the ductile damage case undergoes about 37% increase with about 12% and 3% averaged interfacial damage for the ductile and brittle damage cases, respectively. Figure 13(d) shows the local current density contours demonstrate the difference in the evolution of current density ($J_2$) carrying pathways for the two cases in the unstrained state and at 1% and 2.3% applied tensile strain.

The ductile damage case was further studied by changing the local orientation of the CNTs in the nanocomposite binder interface at a volume fraction of 0.15% wt and with the gauge factors before ($\tilde{G}_0^{NC}$) and after ($\tilde{G}_d^{NC}$) the initiation of damage to be 2 and 4, respectively. Three different local orientation cases are considered in the current work i.e. randomly oriented, aligned normal to the interface and aligned tangential/parallel to the interface. The local orientation distribution of CNTs leads to differences in effective undamaged nanocomposite electromechanical properties used to construct the cohesive laws. These effective electromechanical properties are obtained using the micromechanics based Mori-Tanaka method as illustrated in Section 3.1.3 with properties for the aligned and randomly oriented CNTs listed in Table 3. The aligned (normal to interface) properties are transformed by replacing $C_{22}^{Eff}$, $C_{44}^{Eff}$ and $\Sigma_{22}^{Eff}$ by $C_{33}^{Eff}$, $C_{55}^{Eff}$ and $\Sigma_{33}^{Eff}$, respectively, to identify the electromechanical properties for the transverse alignment case.

The effective stress-strain response for the three alignment cases is shown in Figure 14(a) along with the evolution of averaged damage index. The initial linear elastic stiffness for the three cases is observed to be different as the local interfaces have different initial stiffness such that the aligned case has the largest stiffness (9.39 GPa), followed by the random case (8.06 GPa) and transverse alignment case (7.39 GPa). As such, the effective composite stiffnesses for the aligned, random and transverse cases are observed to be 18.0

GPa, 17.1 GPa and 16.5 GPa, respectively, i.e. largest for larger degree of alignment normal to the interface. Following from the initial stiffness , the peak stress is largest for the aligned case and is observed to be around 1% applied strain for each of the three cases. The averaged damage index is observed to follow a similar evolution for the three cases with about 22% damage observed at 2.3% applied strain.

The relative change in effective resistance for the three alignment cases is presented in Figure 14(b). A larger difference is observed in the relative change in resistance with applied strain for the three cases in comparison to the corresponding stress-strain response because while the different orientations cause slight differences in the effective undamaged interface stiffnesses, they lead to much larger differences in undamaged effective conductivities, as observed from Table 3. The unstrained interface conductivity is larger with a larger degree of alignment normal to the interface i.e. the aligned case (142.97 S/m) is most conductive followed by random (61.16 S/m) and transverse (1.68 S/m) cases. However, the small undamaged conductivity for the transverse case leads to a larger relative difference between the grain (1000 S/m) and interface conductivities. In addition, the more compliant transverse alignment (in comparison to the grains) leads to larger interface separation. Thus, following from the discussion of Figure 11 in Section 3.2, the largest change in effective resistance is observed for the transverse alignment case followed by the random and aligned cases. For example, at 2.3% applied strain, the relative change in resistance is observed to be 244%, 435% and 566% for the aligned, random and transverse cases, respectively. The results indicate that while a larger degree of alignment normal to the interface may improve the mechanical stiffness of the material, transverse alignment leads to a larger piezoresistive response for strain and damage sensing.

The random local CNT orientation case with ductile damage was further studied with different weight concentrations (volume fractions) of CNTs in the nanocomposite binder having the gauge factors before $(\tilde{G}_0^{NC})$ and after $(\tilde{G}_d^{NC})$ the initiation of damage to be 2 and 4, respectively. The effective undamaged electromechanical properties for each weight concentration, i.e. 0.5%, 1% and 2%, are listed in Table 3 along with the corresponding volume fractions. The effective stress-strain response for the three cases is shown in Figure 15(a) along with the corresponding evolution of averaged damage index. The effective unstrained interface stiffness is larger for larger weight concentration of CNTs in the nanocomposite resulting in a larger initial effective composite stiffness for the 0.6%wt case. The evolution of stress-strain curve follows a similar behavior for the three cases with larger observed stresses in the 0.6%wt case for a given strain state followed by 0.3%wt and 0.15%wt. The averaged damage index starts to deviate from its initial value of 1 around 0.5% strain and about 22% average damage is observed at 2.3% applied strain for all three cases.

The corresponding relative change in resistance for the three cases with different weight concentrations are shown in Figure 15(b). The local conductivity of the unstrained interface obtained from Mori-Tanaka method is smallest for the 0.15%wt (61.16S/m, 0.5%wt relative to epoxy) case followed by 0.3%wt (93.68S/m, 1%wt relative to epoxy) and 0.6%wt (127.62S/m, 2%wt relative to epoxy) cases. The 0.15%wt case undergoes the largest change in effective resistance with applied strains because the relative difference between the grain (1000 S/m) and interface conductivities is highest for this case. At 2.3% applied strain, a 435%, 300% 250% increase in resistance is observed for the 0.15%wt, 0.3%wt and 0.6%wt, respectively. Thus, a larger weight concentration of CNTs leads to a larger initial effective stiffness, but a smaller weight concentration may produce a larger effective piezoresistive response for NCBX materials.

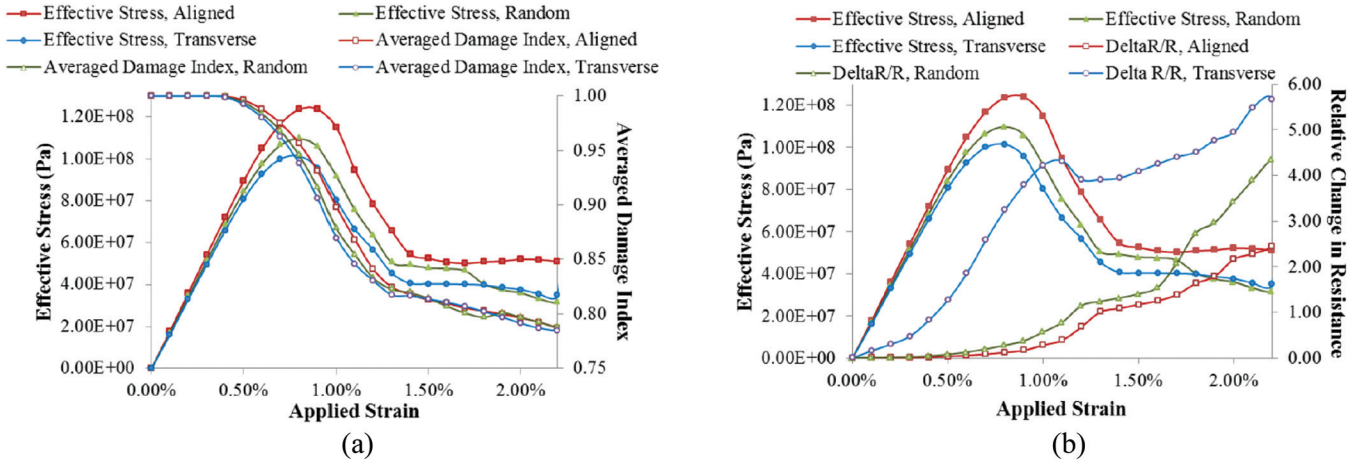


***Figure 14.*** *Effect of local orientation of the CNTs in the nanocomposite binder interface, i.e. aligned, random and transverse, at a weight concentration of 0.15% wt and with the gauge factors before* $(\tilde{G}_0^{NC})$ *and after* $(\tilde{G}_0^{NC})$ *the initiation of damage chosen to be 2 and 4, respectively. (a) Effective stress-strain response along with the evolution of averaged damage index, (b) Relative change in effective resistance along with the effective stress-strain response for comparison.*

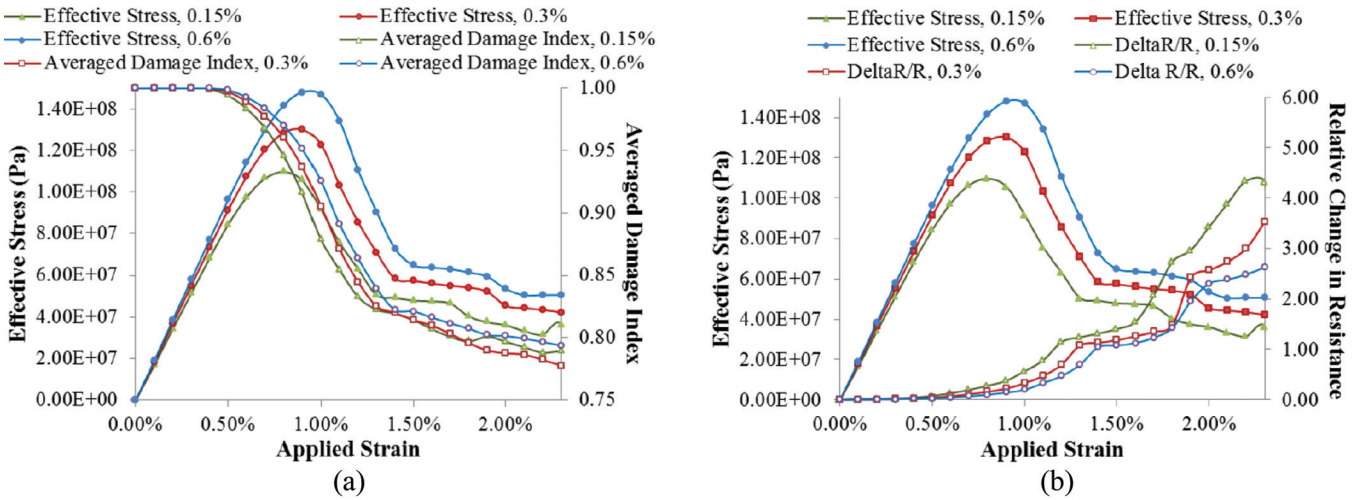


***Figure 15.*** *Effect of local weight concentration of the randomly oriented CNTs in the nanocomposite binder interface undergoing ductile damage with the gauge factors before* $(\tilde{G}_0^{NC})$ *and after* $(\tilde{G}_d^{NC})$ *the initiation of damage chosen to be 2 and 4, respectively. (a) Effective stress-strain response along with the evolution of averaged damage index, (b) Relative change in effective resistance along with the effective stress-strain response for comparison.*

In the discussion so far, the gauge factors before and after the initiation of damage have been chosen to be 2 and 4, respectively, based on some typical values in the literature. These values were kept constant even when the orientation and volume fraction of CNTs were varied to explore the difference in response by varying one set of microstructural features/response. However, a typical nanocomposite will exhibit different effective piezoresistive response as the volume fractions and orientations of CNTs is changed. In particular, the effective piezoresistive response of nanocomposite with transverse alignment of CNTs has been observed to be stronger than the random and aligned cases [29,53]. Thus, the transverse case for 0.15%wt with ductile damage is further studied by increasing $(\tilde{G}_0^{NC}, \tilde{G}_d^{NC})$ from (2,4) to (5,10) and (20,40) along with a baseline case with no nanocomposite piezoresistivity (0,0), i.e. the purely geometric and damage dependent case. The effective stress-strain response, shown in Figure 16(a), is observed to be the same for all of these cases as the mechanical problem has the same properties. Local interfacial damage is observed to initiate at about 0.5% applied strain with approximately 22% average interfacial damage observed at 2.3% applied strain.

The relative change in effective resistance increases as the nanocomposite effective gauge factors are increased as shown in Figure 16(b). At 1% applied strain, the relative change in resistance is observed to be 1.83%, 2.46% and 6.06% larger for the (2,4), (5,10) and (20,40) cases, respectively, as compared to the baseline (0,0) case. The observed increase in resistance, however, is much smaller than that observed for the 10-grain RVE presented in Figure 12(b).

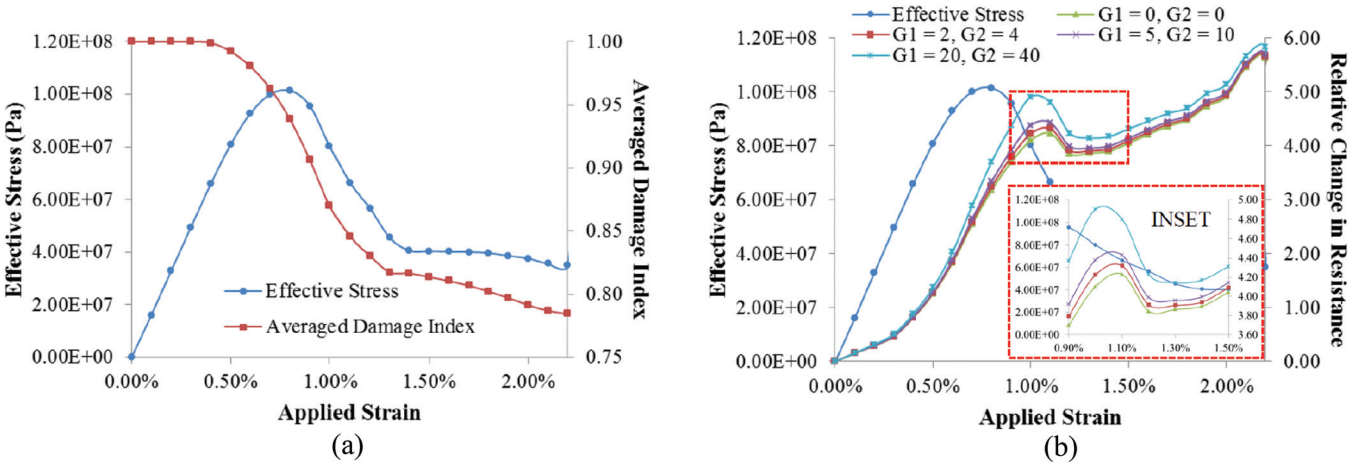


***Figure 16.*** *Effect of nanocomposite binder gauge factors before* $(\tilde{G}_0^{NC})$ *and after* $(\tilde{G}_d^{NC})$ *the initiation of damage for 0.15%wt transversely oriented CNTs in the nanocomposite binder interface undergoing ductile damage. (a) Effective stress-strain response along with the evolution of averaged damage index, (b) Relative change in effective resistance along with the effective stress-strain response for comparison.* $G_1$ *and* $G_2$ *are the effective nanocomposite gauge factors before* $(\tilde{G}_0^{NC})$ *and after* $(\tilde{G}_d^{NC})$ *the initiation of nanocomposite damage.*

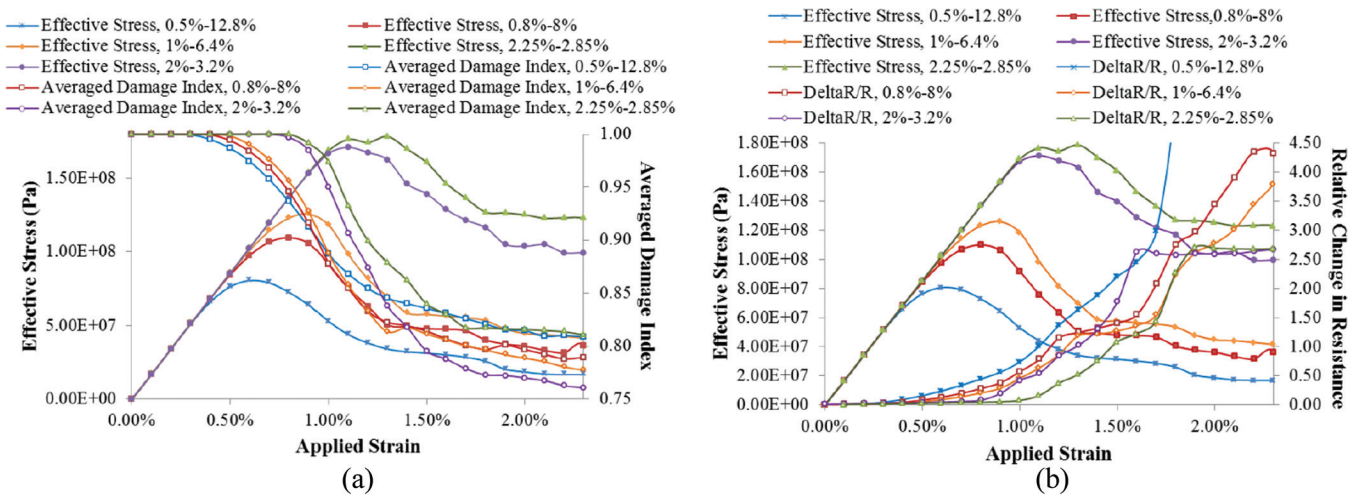


***Figure 17.*** *Comparison of damage rate going from ductile to brittle interfacial damage (with constant cohesive fracture energy) on the effective piezoresistive response with 0.15% wt (relative to epoxy) random CNT alignment at the interface with the gauge factors before* $(\tilde{G}_0^{NC})$ *and after* $(\tilde{G}_d^{NC})$ *the initiation of damage to be 2 and 4, respectively. (a) Effective stress-strain response along with the evolution of averaged damage index, (b) Relative change in effective resistance along with the effective stress-strain response for comparison.*

For the 10-grain RVE, there were only 2 grains across the width of the sample. A change in local interface resistance was reflected better in the effective response. For the 31-grain RVE there are several additional pathways that the current density can travel through. Thus, the effect of local interface piezoresistive response does not lead to as large a change in effective piezoresistive response. It is to be noted that at about 1% applied strain, the relative change in resistance is observed to decrease slightly because local damage of the cohesive zone leads to rearrangement of current carrying pathways through the 31-grain RVE.

Finally, the surface treatment of the grains during processing could affect the interfacial separation and damage between the grains and the polymer interface similar to how functionalized CNT interfaces lead to different interfacial response in CNT-polymer nanocomposites [62]. Thus, a damage rate comparison is presented in Figure 17 with three other interfacial damage rates in addition to the ductile and brittle damage discussed earlier. The separation energy for each of these cases is kept constant equal to the polymer cohesive fracture energy (3.2 MPa) assuming that the CNTs do not change it significantly. For each of these cases, the interface nanocomposite binder has the 0.15%wt randomly oriented CNTs with an undamaged and damaged effective gauge factors of 2 and 4, respectively. The effective stress-strain response for each of these cases is presented in Figure 17(a) along with the evolution of averaged damage index. It is observed that the cases with faster damage initiation deviate from the initial linear elastic response faster and the corresponding averaged damage index deviates faster from the initial value of 1 at smaller applied strain, i.e. going from more ductile to more brittle like damage. The evolution of damage index does not necessarily follow the order for all strain states because of localized rearrangements in microstructure as damage develops at the local interfaces as was similarly illustrated in the discussion for Figure 13 where a comparison of brittle vs. ductile damage was presented. The evolution of relative change in resistance follows from the evolution of averaged damage index such that faster damage initiation leads to larger relative change in resistance, in general. However, some deviations from this trend are observed at different states of applied strain which can be closely correlated to the evolution of averaged damage index. In conclusion, while the more brittle like damage leads to larger values of peak stress, the effective piezoresistive response of ductile damage cases capture the effect of local interfacial damage better.

### 3.4. Comparison of Computational Modeling and Experimental Investigation

While the experimentally observed and computationally obtained effective behavior is similar in terms of regions of deviation from linear elastic response with damage progression and larger damage sensitivity of the relative change in resistivity, some differences between the two are observed such as (1) smaller experimentally obtained NCBX initial stiffness (2) smaller peak stresses observed experimentally, and (3) smaller relative change in resistivity observed experimentally for a given strain state and weight concentration of CNTs. For example, the peak stress observed in the experimental results (Figure 5) was between 3 and 5 MPa, whereas those computationally obtained from the 31-grain RVE were observed to be between 75 and 150 MPa (Section 3). Similarly, the experimentally observed relative change in resistance was observed to be typically smaller than 1 at 2% applied strain in comparison to the computationally obtained range between 2 and 6 for 2% strain for the 31-grain RVE.

Some of these differences could possibly be reduced by lifting some of the modeling idealizations which include (1) allowing for tangential current density through the interface, (2) modeling of the polymer binder region explicitly and (3) more accurate microstructure characterization of the CNT-polymer nanocomposite to build RVEs for the nanocomposite interface. On the other hand, there remains a large degree of uncertainty regarding the identification of accurate material properties for NCBX under the processing conditions employed in preparing the surrogate samples characterized in Section 2, such as uncertainty regarding (1) degree of uncured matrix pockets due to constrained curing of the polymer matrix, (2) voids in nanocomposite binder which may require degassing, and (3) interfacial bonding strength between the polymer nanocomposite and sugar crystals. Thus, in order to explore possible reasons for these differences in further detail, the model inputs are treated as tunable parameters in an effort to better reproduce experimental results using the 31-grain RVE.

In tuning the material properties, some of the properties were fixed initially, e.g. the mechanical properties of the grains were fixed at the properties obtained for HMX from the literature as indicated in Section 3.1.3. The remaining model input parameters were varied. For example, the electrostatic conductivity of the grains was reduced from the nominal value of 1000S/m estimated for HMX grains (as indicated in Section 3.1.3) as the sugar particles are believed to be less conductive. In absence of estimates of sugar grain conductivity a smaller grain conductivity of 1E-3S/m is used herein. The mechanical properties of the effective nanocomposite binder were reduced significantly to reduce the large initial stiffness and the peak stress obtained from the computational model. The nanocomposite axial stiffness was chosen to be 0.3 GPa in comparison to ~10 GPa used earlier for the 31-grain model, while the shear modulus was chosen to be 0.15 GPa. The conductivity of the nanocomposite binder medium was fixed at the derived value (61.16 S/m) for the case where randomly aligned 0.5% weight concentrations of CNTs were used. A ductile mode of damage was assumed with rates of damage adjusted such that a $\Delta\tilde{u}_n^{sw}$ of 0.007 and a $\Delta\tilde{u}_n^{\max}$ of 0.013 was used in order to match the applied strain at which the peak stress would occur. The choice of initial stiffness and damage rates significantly reduces the cohesive fracture energy of the interface from 3.2 MPa to 0.0136 MPa. Finally, the bilinear electrostatic cohesive law damage rate parameter ($\gamma$) was reduced from its nominal value of 10 to 2, while the nanocomposite binder gauge factors before and after the initiation of damage were fixed at their nominal value of 2 and 4.

The effective stress-strain and relative change in resistance generated after calibrating the model are shown in Figure 18 along with the experimentally obtained results for the 0.3%wt MWNT concentration results shown earlier in Figure 5. An initial stiffness of 1.46 GPa is obtained from

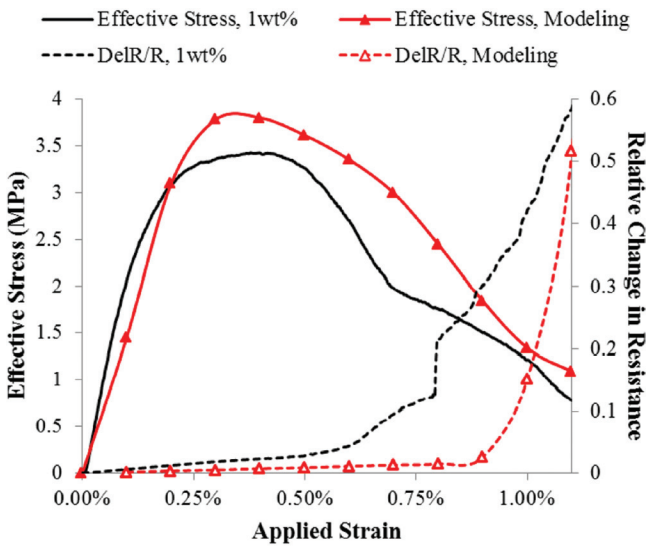


***Figure 18.*** *Comparison of the stress-strain and relative change in resistance response with applied strain obtained from the experimental investigation (0.3%wt) and the calibrated 31-grain computational model.*

the model, which is significantly smaller than the initial stiffnesses for cases presented in Section 3.3 before calibration, as compared to 2.59 GPa obtained experimentally. A peak stress of 3.8 MPa was obtained computationally which compares well to the 3.40 MPa obtained experimentally. The relative change in resistance obtained computationally undergoes and initial linear increase, however the rate of increase is much smaller for the model as compared to the experiment. The relative change in resistance at a strain state of 1.1%, however, is close to 0.5 for both cases. Overall, while exact replication of the experimental results is difficult given the complex interdependence of the effective response on the material properties as illustrated in Section 3.3, the calibrated model is much closer to the experimentally observed behavior.

Some key conclusions which can be made based on this calibration exercise include (1) the interface stiffness and cohesive fracture energy of the nanocomposite binder is significantly smaller as compared to estimated values indicating weak interfacial bonding between the polymer and grains and/or initial voids/cracks in the polymer binder, and (2) the sugar grains are non-conductive which does not compare well with estimates of HMX conductivity indicating that while sugar grains may be a good mechanical surrogate for HMX, they may be less suitable as a surrogate electrically.

## 4. CONCLUSION

In the current work, experimental investigation of MWNT-sugar-epoxy hybrid nanocomposites was performed to assess their microstructure morphology, effective con-

ductivity and deformation based effective piezoresistive response. Additionally, 2-scale hierarchal computational micromechanics based modeling framework was developed to assess the variations in effective piezoresistive response based on differences in material parameters and properties to explore the design space for NCBX materials. The key experimental observation from the current exploration of NCBX piezoresistivity include

- The neat sugar-epoxy samples are non-conductive and addition of MWNTs increases the effective conductivity of the composite,
- The stress-strain response MWNT-sugar-epoxy hybrid nanocomposites undergoes a ductile failure behavior going through the initial linear elastic behavior, formation of microcracks leading to reduction in composite stiffness and finally macrocracks result in eventual failure,
- The relative change in resistance captures the effect of microcracks and macrocracks earlier than the stress strain response resulting in gauge factors between 5–10 before significant macrocrack formation and over 50 at composite failure.

In addition, the some of the key observations made from the computational modeling include

- Effective NCBX piezoresistive response is largely dependent on the relative difference in the explosive grains and nanocomposite interface properties,
- A larger relative grain stiffness and conductivity as compared to the nanocomposite binder results in a larger NCBX piezoresistive response,
- Ductile mode of interfacial damage leads to smaller peak stresses and larger relative change in resistance as compared to brittle interfacial damage,
- Alignment of CNTs transverse (tangential) to the interface and smaller CNT volume fractions lead to smaller mechanical stiffness but a larger piezoresistive response, and
- A larger inherent piezoresistivity of the nanocomposite binder results in a larger effective NCBX piezoresistivity.

The initial piezoresistive testing of surrogate MWNT-sugar-epoxy hybrid nanocomposites indicates that addition of CNTs to the polymer binder can lead to piezoresistive response based deformation and damage sensing. In addition, the current work computationally explores the microstructure design space of NCBX materials which is expected to be helpful in material design with optimized piezoresistive response.

## 5. ACKNOWLEDGEMENT

The authors would like to acknowledge the support of Air Force Office of Scientific Research (grant FA9550-12-1-0205) in the Dynamic Materials and Interactions Program and Virginia Tech's Institute for Critical Technology and Applied Science (ICTAS) Junior Faculty Collaborative (JFC) Seed Award. The authors would like to acknowledge Dr. Michael Butler for providing us an access to use Instron Tensile Frame in The Frith Freshman Design Laboratory at Virginia Tech. In addition, the authors' acknowledge Advanced Research Computing (ARC) at Virginia Tech for providing computational resources and technical support. Finally, the authors would also like to acknowledge many constructive conversations with Naveen Prakash at Virginia Tech in developing some of the ideas presented herein.

## 6. REFERENCES

[1] R. Peeters, Characterization of plastic-bonded explosives, *Journal of Reinforced Plastics and Composites 1* (2) (1982) 131–140. http://dx.doi.org/10.1177/073168448200100204

[2] C. Liu, D. G. Thompson, Crack initiation and growth in pbx 9502 high explosive subject to compression, *Journal of Applied Mechanics 81* (10) (2014) 101004. http://dx.doi.org/10.1115/1.4028087

[3] C. Liu, D. G. Thompson, Macroscopic crack formation and extension in pristine and artificially aged pbx 9501, in: *Proceeding of the 14th International Detonation Symposium Coeur d'Alene, Idaho, USA*, 2010.

[4] C. Liu, M. Stouta, B. Asay, Stress bridging in a heterogeneous material, *Engineering Fracture Mechanics 67* (1) (2000) 1–20. http://dx.doi.org/10.1016/S0013-7944(00)00041-2

[5] C. Liu, P. J. Rae, C. Cady, M. Lovato, Damage and fracture of high-explosive mock subject to cyclic loading, in: *Conference Proceedings of the Society for Experimental Mechanics Series, Vol. 3 of Mechanics of Time-Dependent Materials and Processes in Conventional and Multifunctional Materials*, 2011, pp. 151–157. http://dx.doi.org/10.1007/978-1-4614-0213-8_23

[6] F. Ruz-Nuglo, L. Groven, J. Puszynski, Additive manufacturing for energetic components and materials, in: *Proceedings 50th AIAA/ASME/SAE/ASEE Joint Propulsion Conference, Additive Manufacturing for Energetic Components and Materials, Cleveland, OH, USA,* 2014. http://dx.doi.org/10.2514/6.2014-3894

[7] J. Paripovic, P. Davies, Identification of the dynamic behavior of surrogate explosive materials, in: *Proceedings of the ASME 2013 International Design Engineering Technical Conferences and Computers and Information in Engineering Conference IDETC/CIE, Portland, Oregon, USA*, 2013. http://dx.doi.org/10.1115/detc2013-12755

[8] J. O. Mares, J. K. Miller, N. D. Sharp, D. S. Moore, D. E. Adams, L. J. Groven, J. F. Rhoads, S. F. Son, Thermal and mechanical response of pbx 9501 under contact excitation, *Journal of Applied Physics 113* (084904). http://dx.doi.org/10.1063/1.4793495

[9] J. K. Miller, D. C. Woods, J. F. Rhoads, Thermal and mechanical response of particulate composite plates under inertial excitation, *Journal of Applied Physics 116* (244904). http://dx.doi.org/10.1063/1.4904439

[10] S. J. P. Palmer, J. E. Field, J. M. Huntley, Deformation, strengths and strains to failure of polymer bonded explosives, *Proceedings of the Royal Society of London Series A—Mathematical Physical and Engineering Sciences 440* (1993) 399–419. http://dx.doi.org/10.1098/rspa.1993.0023

[11] P. J. Rae, H. T. Goldrein, S. J. P. Palmer, J. E. Field, A. L. Lewis, Quasi-static studies of the deformation and failure of beta-hmx based polymer bonded explosives, *Proceedings of the Royal Society of London Series A—Mathematical Physical and Engineering Sciences 458* (2002) 743–762. http://dx.doi.org/10.1098/rspa.2001.0894

[12] Y.-R. Kim, D. Allen, G. Seidel, Damage-induced modeling of elastic-

viscoelastic randomly oriented particulate composites, *Journal of Engineering Materials and Technology 128* (2006) 18–27. http://dx.doi.org/10.1115/1.2127960

[13] G. Seidel, D. Allen, K. Helms, S. Groves, A model for predicting the evolution of damage in viscoelastic particle-reinforced composites, *Mechanics of Materials 37* (2005) 163–178. http://dx.doi.org/10.1016/j.mechmat.2004.01.002

[14] A. Barua, M. Zhou, A lagrangian framework for analyzing microstructural level response of polymer-bonded explosives, *Modelling and Simulation in Materials Science and Engineering 19* (5) (2011) 055001. http://dx.doi.org/10.1088/0965-0393/19/5/055001

[15] A. Barua, Mesoscale computational prediction and quantification of thermomechanical ignition behavior of polymer-bonded explosives (pbxs), Dissertation, Georgia Institute of Technology (2013).

[16] A. Barua, M. Zhou, Computational analysis of temperature rises in microstructures of hmxestane pbxs, *Computational Mechanics 52* (1) (2013) 151–159. http://dx.doi.org/10.1007/s00466-012-0803-x

[17] R. Panchadhara, K. A. Gonthier, Mesoscale analysis of volumetric and surface dissipation in granular explosive induced by uniaxial deformation waves, *Shock Waves 21* (1) (2011) 43–61. http://dx.doi.org/10.1007/s00193-010-0287-6

[18] S. Chakravarthy, K. A. Gonthier, R. Panchadhara, Analysis of mesoscale heating by piston supported waves in granular metalized explosive, *Modelling and Simulation in Materials Science and Engineering 21* (5) (2013) 055016. http://dx.doi.org/10.1088/0965-0393/21/5/055016

[19] D. Hardin, J. Rimoli, M. Zhou, Analysis of thermomechanical response of polycrystalline hmx under impact loading through mesoscale simulations, *AIP Advances 4* (9) (2014) 097136. http://dx.doi.org/10.1063/1.4896699

[20] J. E. Field, Hot spot ignition mechanisms for explosives, *Accounts of Chemical Research 25* (11) (1992) 489–496. http://dx.doi.org/10.1021/ar00023a002

[21] Y. Horie, Hot spots, high explosives ignition, and material microstructure, Materials Science Forum 767.

[22] K. Loh, J. Lynch, N. Kotov, Conformable single-walled carbon nanotube thin film strain sensors for structural monitoring, in: *Proceedings of the 5th International Workshop on Structural Health Monitoring, Stanford, CA*, 2005, pp. 1–8.

[23] X. Song, S. Liu, Z. Gan, Q. Lu, H. Cao, H. Yan, Controllable fabrication of carbon nanotubepolymer hybrid thin film for strain sensing, *Microelectronic Engineering* (2009) In Press. http://dx.doi.org/10.1016/j.mee.2009.04.012

[24] M. H. G. Wichmann, S. T. Buschhorn, J. Gehrmann, K. Schulte, Piezoresistive response of epoxy composites with carbon nanoparticles under tensile load, *Physical Review B 80* (2009) 245437–1 to 245437–8. http://dx.doi.org/10.1103/PhysRevB.80.245437

[25] J. Lu, M. Lu, A. Bermak, Y.-K. Lee, Study of piezoresistance effect of carbon nanotube-pdms composite materials for nanosensors, *Proceedings of the 7th IEEE International Conference on Nanotechnology* (2007) 1240–1243.

[26] I. Kang, Y. Heung, J. Kim, J. Lee, R. Gollapudi, S. Subramaniam, S. Narasimhadevara, D. Hurd, G. Kirikera, V. Shanov, M. Schulz, D. Shi, J. Boerio, S. Mall, M. Ruggles-Wren, Introduction to carbon nanotube and nanofiber smart materials, *Composites Part B: Engineering 37* (6) (2006) 382–394. http://dx.doi.org/10.1016/j.compositesb.2006.02.011

[27] I. Kang, M. Schulz, J. Kim, V. Shanov, D. Shi, A carbon nanotube strain sensor for structural health monitoring, *Smart Materials and Structures 15* (2006) 737–748. http://dx.doi.org/10.1088/0964-1726/15/3/009

[28] J. H. Kang, C. Park, J. A. Scholl, A. H. Brazin, N. M. Holloway, Piezoresistive characteristics of single wall carbon nanotube/polyimide nanocomposites, *Journal of Polymer Science B 47* (2009) 994–1003. http://dx.doi.org/10.1002/polb.21705

[29] E. Sengezer, G. Seidel, Experimental characterization of damage evolution in carbon nanoubepolymer nanocomposites, in: *Proceedings of 56th AIAA/ASME/ASCE/AHS/ASC Structures, Structural Dynamis and Materials Conference at AIAA SciTech, Kissimmee, FL*, 2015.

[30] E. C. Sengezer, G. D. Seidel, R. J. Bodnar, Phenomenological characterization of fabrication of aligned pristine-swnt and cooh-swnt nanocomposites via dielectrophoresis under ac electric field, *Polymer Composites 36* (7) (2015) 1266{1279.

[31] L. Gao, E. Thostenson, Z. Zhang, T.-W. Chou, Coupled carbon nanotube network and acoustic emission monitoring for sensing of damage development in composites, *Carbon 47* (5) (2009) 1381–1388. http://dx.doi.org/10.1016/j.carbon.2009.01.030

[32] T. Theodosiou, D. Saravanos, Numerical investigation of mechanisms affecting the piezoresistive properties of cnt-doped polymers using multi-scale models, *Composites Science and Technology 70* (9) (2010) 1312{1320.

[33] C. Li, T.-W. Chou, Modeling of damage sensing in fiber composites using carbon nanotube networks, *Composites Science and Technology 68* (2008) 3373–3379. http://dx.doi.org/10.1016/j.compscitech.2008.09.025

[34] F. Du, R. Scogna, W. Zhou, S. Brand, J. Fischer, K. Winey, Nanotube networks in polymer nanocomposites: Rheology and electrical conductivity, *Macromolecules 37* (2004) 9048–9055. http://dx.doi.org/10.1021/ma049164g

[35] C. Li, E. T. Thostenson, T.-W. Chou, Dominant role of tunneling resistance in the electrical conductivity of carbon nanotubebased composites, *Applied Physics Letters 91* (2007) 223114–1 to 223114–3. http://dx.doi.org/10.1063/1.2819690

[36] N. Hua, Y. Karube, C. Yan, Z. Masuda, H. Fukunaga, Tunneling effect in a polymer/carbon nanotube nanocomposite strain sensor, *Acta Materialia 56* (2008) 2929–2936. http://dx.doi.org/10.1016/j.actamat.2008.02.030

[37] G. Yin, N. Hu, Y. Karube, Y. Liu, Y. Li, H. Fukunaga, A carbon nanotube/polymer strain sensor with linear and anti-symmetric piezoresistivity, *Journal of Composite Materials 45* (12) (2011) 1315–1323. http://dx.doi.org/10.1177/0021998310393296

[38] Y. Yu, G. Song, L. Sun, Determinant role of tunneling resistance in electrical conductivity of polymer composites reinforced by well dispersed carbon nanotubes, *Journal of Applied Physics 108* (2010) 084319–1 to 084319–5. http://dx.doi.org/10.1063/1.3499628

[39] X. Sun, M. Song, Highly conductive carbon nanotube/polymer nanocomposites achievable?, *Macromolecular Theory and Simulations 18* (2009) 155–161. http://dx.doi.org/10.1002/mats.200800091

[40] A. Rochefort, F. Lesage, D. R. Salahub, P. Avouris, Conductance of distorted carbon nanotubes, *Physical Review B 60* (1999) 13824–13830. http://dx.doi.org/10.1103/PhysRevB.60.13824

[41] T. C. Theodosiou, D. A. Saravanos, Piezoresistive behavior of cnt nanocomposites using atomistic and micromechanics models, *Proceedings SPIE Smart Structures and Materials—Behavior and Mechanics of Multifunctional Materials and Composites 7289* (10) (2009) 728918–1 to 728918–10. http://dx.doi.org/10.1117/12.816943

[42] L. Megalini, D. S. Saito, E. J. Garcia, A. J. Hart, B. L. Wardle, Impedance of aligned carbon nanotube arrays and polymeric nanocomposites, *Journal of Nano Systems and Technology 1* (1) (2009) 1–16.

[43] J. Cao, Q. Wang, H. Dai, Electromechanical properties of metallic, quasimetallic, and semiconducting carbon nanotubes under stretching, *Physical Review Letters 90* (15) (2003) 157601–1–4. http://dx.doi.org/10.1103/PhysRevLett.90.157601

[44] T. Tombler, C. Zhou, L. Alexseyev, J. Kong, H. Dai, L. Liu, C. Jayanthi, M. Tang, S.-Y.Wu, Reversible electromechanical characteristics of carbon nanotubes under local-probe manipulation, *Nature 405* (2000) 769–772. http://dx.doi.org/10.1038/35015519

[45] B. Hu, N. Hu, Y. Li, K. Akagi, W. Yuan, T.Watanabe, Y. Cai, Multi-scale numerical simulations on piezoresistivity of cnt/polymer nanocomposites, *Nanoscale Research Letters 7* (402) (2012) 1–11. http://dx.doi.org/10.1186/1556-276x-7-402

[46] Y. Kuronuma, T. Takeda, Y. Shindo, F. Narita, Z. Wei, Electrical resistance-based strain sensing in carbon nanotube/polymer composites under tension: Analytical modeling and experiments, *Composites Science and Technology 72* (2012) 1678{1682.

[47] A. Chaurasia, G. Seidel, Computational micromechanics analysis of electron hopping induced conductive paths and associated macroscale piezoresistive response in carbon nanotube-polymer nanocomposites, *Journal of Intelligent Material Systems and Structures 15* (17) (2014) 2141–2164. http://dx.doi.org/10.1177/1045389X13517314

[48] A. Chaurasia, X. Ren, G. Seidel, Computational micromechanics analysis of electron hopping and interfacial damage induced piezoresistive response in carbon nanotube-polymer nanocomposites, *Journal of Smart Materials and Structures 23* (075023) (2014) 1–23. http://dx.doi.org/10.1088/0964-1726/23/7/075023

[49] D. Hammerand, G. Seidel, D. Lagoudas, Computational micromechanics of clustering and interphase effects in carbon nanotube composites, *Mechanics of Advanced Materials and Structures 14* (2007) 277–294. http://dx.doi.org/10.1080/15376490600817370

[50] G. D. Seidel, D. C. Lagoudas, A micromechanics model for the electrical conductivity of nanotube-polymer nanocomposites, *Journal of Composite Materials 43* (9) (2009) 917–925. http://dx.doi.org/10.1177/0021998308105124

[51] W. Bauhofer, J. Kovacs, A review and analysis of electrical percolation in carbon nanotube polymer composites, *Composites Science and Technology 69* (2008) 1486–1498. http://dx.doi.org/10.1016/j.compscitech.2008.06.018

[52] G. Seidel, A. Puydupin-Jamin, Analysis of clustering, interphase region, and orientation effects on the electrical conductivity of carbon nanotube polymer nanocomposites via computational micromechanics, *Mechanics of Materials 43* (2011) 755–774. http://dx.doi.org/10.1016/j.mechmat.2011.08.010

[53] A. Chaurasia, G. Seidel, Computational micromechanics analysis of electron hopping induced piezoresistive response in carbon nanotube-polymer nanocomposites, no. AIAA 2013-1731, Boston, Massachusetts, USA, 2013, pp. 1–23.

[54] A. Oliva-Aviles, F. Aviles, V. Sosa, Electrical and piezoresistive properties of multi-walled carbon nanotube/polymer composite films aligned by an electric field, *Carbon 49* (2011) 2989–2997. http://dx.doi.org/10.1016/j.carbon.2011.03.017

[55] D. G. Tasker, V. H. Whitley, J. L. Mace, S. J. Pemberton, T. D. Sandoval, R. J. Lee, Electromagnetic effects on explosive reaction and plasma, in: *Proceedings of 14th International Detonation Symposium, Coeur d'Alene, Idaho, 2010*.

[56] T. Mori, K. Tanaka, Average stress in matrix and average elastic energy of materials with misfitting inclusions, *Acta Metallurgica 21* (1973) 571–574. http://dx.doi.org/10.1016/0001-6160(73)90064-3

[57] F. Li, H. M. Cheng, S. Bai, G. Su, M. S. Dresselhaus, Tensile strength of single-walled carbon nanotubes directly measured from their macroscopic ropes, *Applied Physics Letters 77* (20) (2000) 3161–3163. http://dx.doi.org/10.1063/1.1324984

[58] N. Marzari, M. Ferrari, Textural and micromorphological effects on the overall elastic response of macroscopically anisotropic composites, *Journal of Applied Mechanics 59* (1992) 269–275. http://dx.doi.org/10.1115/1.2899516

[59] P. Entchev, D. Lagoudas, Modeling porous shape memory alloys using micromechanical averaging techniques, *Mechanics of Materials 34* (2002) 1–24. http://dx.doi.org/10.1016/S0167-6636(01)00088-6

[60] G. Odegard, T. Gates, K. Wise, C. Park, E. Siochi, Constitutive modeling of nanotube-reinforced polymer composites., *Composites Science and Technology 63* (2003) 1671–1687. http://dx.doi.org/10.1016/S0266-3538(03)00063-0

[61] W. System, 105 Epoxy Resin/206 Slow Hardener: Technical Data Sheet, Gougeon Brothers, Inc., Gougeon Brothers, Inc, P.O. Box 908, Bay City, MI 48707 (October 2014).

[62] Y. Li, G. Seidel, Multiscale modeling of functionalized interface effects on the effective elastic material properties of cnt-polyethylene nanocomposites, *Computational Materials Science 107* (2015) 216–234. http://dx.doi.org/10.1016/j.commatsci.2015.05.006

# GUIDE TO AUTHORS

## SUBMISSION CHECKLIST FOR AN ORIGINAL SUBMISSION

*Please ensure your final submission contains the following items:*

**Cover Letter:** All submissions must be accompanied by a cover letter addressed to the Editor. The cover letter should start at the first page of the submission. The cover letter pages should not be numbered. Include the complete contact information for the corresponding author (name, affiliation, email, phone, fax, address); Provide a list of potential reviewers for the manuscript. Include the name, email, and institution. A minimum of four and maximum of six names should be provided. Of these at least two names must be from the US. If desired, you can also provide a list of individuals or institutions that you DO NOT want to review the manuscript; The cover letter must also include a declaration from the corresponding author, on behalf of all authors, that the work is original and has not previously been submitted to another journal for publication. If the results contained in the article have previously appeared in a magazine, conference proceedings, or a thesis/dissertation, this should be clearly stated; If any copyrighted material has been used in the manuscript, mention it in the cover letter and include proof of permission to re-use the copyrighted material; Disclose any conflict of interest with any persons or organizations that may be personal or financial in nature and that may affect or influence either your work or their work.

**Types of Articles:** Full length articles, review articles, and short letters will be accepted for publication. Authors interested in writing review articles should first contact the Editor.

**Manuscript:** Abstract, Keywords, Main Text, Figures, Tables, Acknowledgements, References

**In addition, please note the following:** Name your submission using the last name of the corresponding author, for e.g. Wang.pdf; Make sure the main text is in a single column format and checked for both spelling and grammar. All pages must be consecutively numbered; Make sure all symbols and equations appear properly in the final PDF document; If copyrighted material is used in the manuscript, please make sure permission has been previously obtained from the copyright holder. Proof of permission will need to be sent to the journal along with the submission; Color figures will appear in color in the online version of the article and in grayscale in the print version of the article.

**Word-processing Software:** Articles can be prepared using any word-processing software. However submissions must only be in the form of a single PDF document.

**Article Structure and Hierarchy:** The structure of the article should closely follow this order: Title, Authors, Affiliations, Abstract, Keywords, Corresponding author contact information, Main text (e.g. Introduction, Setup/Methodology, Results, Discussion, Conclusions), Acknowledgements, References, Figures, Tables, Appendix.

**Title:** The title must clearly distinguish between work that is experimental and numerical in nature. For e.g., "An Experimental Investigation of . . ." or "Numerical Modeling of . . .". Use sentence case for the title, i.e. do not capitalize all letters. Avoid the use of abbreviations and refrain from using commercial names. For e.g., use Finite Element Analysis instead of FEA.

**Author Names and Affiliations:** Provide the author's entire first and last name. Middle names, if any, can be included as an initial. Below the list of author names, provide the entire postal address for each affiliation that includes the department, organization, street address, zip or postal code, and country. Use lower case alphabetical superscripts to relate each author to each affiliation. These superscripts should appear after each author's name and before each affiliation listing. The corresponding author should be identified by a * superscript that appears after the alphabetical superscripts, for e.g., John Wu a,b,*. If any of the authors have changed their affiliation, then provide as a footnote on the title page the new affiliation for the author. The affiliation must correspond to the place where majority of the work was performed.

**Main Text:** There is no page or word limit. The text should be in a single column with one-and-a-half or double line spacing and a minimum font size of 10 pt. Use of Times New Roman, Arial, or Calibri fonts are preferred. Each new paragraph must be clearly identified using either a tab indent or a blank line. Figures and tables, including their captions, should appear on separate pages at the end of the manuscript, and should not be inserted within the text. Number all pages consecutively in the manuscript and place the page number at the top right of each page.

**Abstract:** The abstract is meant to serve as a stand-alone version of the manuscript. It should be kept as brief as possible and concisely state the objective of the research, the principal results, and major conclusions.

**Keywords:** Select a minimum of three and a maximum of five keywords. Keywords should preferably be between one to three words. Do not include phrases or commercial names.

**Corresponding Author Contact Information:** Provide the official email address, phone number, and fax number of the corresponding author below the list of keywords or as a footnote in the title page. One corresponding author must be clearly identified for each manuscript and will be sole point of contact between the Editor/Journal and the authors.

**Headings and Subheadings:** Heading and subheadings in the article should be identified using a decimal system. Main headings appear as (1, 2, 3,…), sub-headings as (1.1, 1.2, 2.1,…), and sub-sub-headings as (1.1.1, 1.1.2, 2.1.1, . . .). Avoid any further division of sub-headings. The abstract is not numbered. All headings and sub-headings must appear in bold font in the text. The font size of the main headings must be 2 pt higher than the main text, for example if the main text has a 10 pt font size then the main headings must have a 12 pt font size. The font size of all lower-level headings must be the same as the main text.

**Figures:** Figures must appear on separate pages at the end of the manuscript and before the tables. Do not include more than two figures on each page. A descriptive figure caption, consecutively numbered, must accompany each figure and be placed below the figure. If symbols or abbreviations are used in the figure, explain them in the caption. If text is used inside a figure, use regular fonts and a large enough font size so that the text appears legible even if the figure is reduced in size for the final proof. Refer to each figure in the main text as Figure (1) or Figure (1.1). After the article is accepted for publication, if some of the figures embedded in the Word or PDF submissions are not of high enough quality, the journal manager will ask the corresponding author to provide high-resolution figures, for which separate instructions will be sent. All color figures will be converted to grayscale for the print version, but will appear in color in the online version. If a figure contains solid plot lines of different colors, make sure each plot line is clearly labeled so that it can be properly interpreted in the grayscale version.

**Tables:** Tables must appear on separate pages at the end of the manuscript and after the figures. Each table must appear on a separate page. Include a table heading above each table and number them consecutively using Roman numerals. Refer to each table in the main text as Table (I), Table (II), and so forth. Do not duplicate data between the figures and tables unless absolutely required. Tables comprising non-essential or large data sets should be placed in the Appendix if possible and appear as Table (A.I), Table (A.II), Table (B.II), and so forth.

**Equations:** Equations should appear within the main text, but must be separated from the text with a blank line both above and below the equation. Each equation should be followed by an equation number that is enclosed in rounded brackets and situated at the right hand margin of the page. Refer to each equation in the main text as Equation (1) or Equation (1.1). Describe the list of symbols used in each equation either in the text immediately following the equation or collectively in a separate table just after the abstract and just before the main text. This table does not need to be numbered. Its title should be 'List of Symbols'.

**Units:** Use the international system of units (SI) and follow internationally accepted nomenclature and conventions. If any other system of units is used, which is strongly discouraged, then provide the SI equivalent of the quantity in rounded brackets, i.e. ( )

**Permission to Re-Use Copyrighted Material:** The author(s) of the article are solely responsible for obtaining permission from copyright holders to re-use verbatim and without significant change images, tables, graphs, and text excerpts in excess of 200 words. Forms for obtaining such permission can be obtained from the journal's Editor or Publisher. All required permissions must be submitted to the journal at the time of manuscript submission. Further the use of such copyrighted material must be clearly indicated in the cover letter.

**Copyright Transfer:** Once the Editor determines the article has been accepted for publication, a copyright form will be sent to the Corresponding Author requesting release of the copyright to the Publisher, DEStech Publications, Inc. It is assumed that the Corresponding Author will sign the copyright form on behalf of all other authors. Corresponding Authors are asked to return this form promptly, within 48 hours, since the article cannot be published until it is received. All accepted articles will be copyrighted in the name of the Publisher. After transfer of copyright the author retains certain rights to use the article for non-commercial and instructional purposes as well as personal presentations within the author's research group.

**Open Access and Supplementary Data:** At this time we do not offer the possibility of open access and the inclusion of supplementary data. However since the articles do not have any word or page limit, supplementary data can either be included within the main set of figures and tables or within the appendix.

**Acknowledgements:** Acknowledgements appear before the list of references. Please acknowledge the funding source for your work. If you received no funding for your work, mention so in the cover letter. You can also acknowledge the role of anyindividuals or organizations that contributed to your work.

**References:** All references in the text should be consecutively numbered and appear within square brackets (e.g. [1] or Last Name et al. [1]). Ensure that all cited references in the text appear in the list of references at the end of the manuscript and vice-versa. The use of reference management software such as *EndNote* or *RefWorks* is encouraged. The format of the reference in the list of references is left to the author, since it will later be converted to the required format by the journal. However each reference in the list must contain all author names (either as the full name, or the last name and first initial of the first name), article title, full journal name (do not abbreviate), volume number, issue number, start and end page numbers, and year of publication. If complete bibliographic details are not available, the DOI number or the words 'In Press' can be used which imply the article has been accepted for publication. The use of unpublished works and personal communications as a reference is prohibited. The uses of web references is discouraged, but when necessary include the entire URL, date the webpage was last accessed, and any other pertinent information.

**Note:** The article may be rejected if it is determined that the author has not conducted a thorough literature review of previous works, or has simply cited old references instead of citing current and/or recent works.

**Appendix:** All text, figures, and tables belonging to the appendix must collectively appear in the appendix and should not be included within the main text and along with the main figures and tables. Identify each appendix as A, B, C, and so forth. Each figure in the appendix should be numbered as (A.1), (A.2), (B.1), and so forth while each table should be numbered as (A.I), (A.II), (B.I), and so forth. Once again, follow this order for each appendix: appendix main text, appendix figures, and appendix tables.

**Author Inquiries and Contact Information:** All inquiries related to the submission of the article should be directed to the Editor, Gaurav Nilakantan (Nilakantan@destechpub.com or gaurav.nilakantan@usc.edu); all inquiries related to processing of the article should be directed to the Journal Manager, Steve Spangler (sspangler@destechpub.com).